Flinders University

Geospatial Modelling of Three-dimensional Structure and Ecohydrological Processes of Semi-arid Woodlands

By

Wenjie Liu

Thesis
Submitted to Flinders University
for the degree of

Doctor of Philosophy
College of Science and Engineering
January 17, 2024

TABLE OF CONTENTS

ABSTRACT

Semi-arid woodlands are important part of terrestrial ecosystems. Woodlands not only provide provisioning services (timber, fuel, food), but also regulating services like soil stabilization, air and water quality improvement, local microclimate regulation, and carbon sequestration. In the face of escalating climate change and human activities, conservation and sustainable management are vital for ensuring the long-term resilience of these ecosystems.

Remote sensing technology enables large-scale, high-frequency monitoring of terrestrial ecosystem dynamics. However, widely utilized satellite missions such as MODIS, Landsat, and Sentinel offer only low to moderate resolution data, while high-resolution imagery, although available, is prohibitively expensive. Additionally, all these satellite systems are prone to cloud contamination, leading to data gaps. Those factors constrain our ability to accurately observe woodland ecosystems at the tree scale. Moreover, current approaches to remote sensing-based ecosystem monitoring often simplify woodlands by treating them as flat surfaces, with a predominant focus on canopy-level processes, thereby neglecting the complex physical interactions occurring beneath the canopy.

The overarching aim of this study is to explore the above mentioned challenges and investigate the three-dimensional structure and ecohydrological processes of the semi-arid woodlands. Understanding woodland 3D structure is crucial for monitoring forest changes, supporting carbon emission reduction initiatives, enhancing forest fire management, and providing essential data for climate adaptation and sustainable forest management. Besides, forest canopy significantly influences the radiation transmission thereby controls the sub-canopy surface energy budget. Exploring the overstory vegetation attributes improves our knowledge of understorey ecohydrological processes, which enhances our comprehension of the overall ecosystem's energy and water balance.

In the first part of this research, the role of local environments in shaping vegetation attributes within semi-arid woodlands is investigated. Topographic factors such as elevation, slope, and aspect are crucial in determining the distribution, composition, and structure of vegetation. The objective of this study is to quantify how topography influences vegetation attributes and identify the key driving factors. Understanding these relationships is important for improving our ability to predict vegetation dynamics and inform reforestation and afforestation efforts in semi-arid regions.

The second part aims to develop a radiation model for simulating the distribution of solar radiation within the woodland’s understorey surface. By incorporating local topographic features and canopy shading effects, this model provides a detailed representation of how solar radiation is distributed beneath the canopy across varying environmental conditions. The accurate simulation of

understorey radiation is crucial for understanding microclimate dynamics and the subsequent impact on vegetation growth and ecosystem processes.

The third part of this research is on modelling and mapping understorey evapotranspiration (ET), which are fundamental to the water balance and energy flux within woodland ecosystems. The study aims to quantify understorey ET and assess its contribution to the overall water flux of semi-arid woodlands. This detailed mapping of ET processes will enhance our understanding of water resource dynamics in these ecosystems and support the development of more effective conservation and management strategies.

In summary, this study offers a comprehensive analysis of the influence of topography on the structure of the studied semi-arid woodlands. It also provides valuable insights into the distribution patterns of solar radiation and ET within these ecosystems. The research framework and methodology developed in this study can be transferred to other regions, enabling broader applications. These findings contribute to guiding sustainable management practices, helping to ensure the resilience of semi-arid woodlands in the face of environmental challenges.

DECLARATION

I certify that this thesis:

1. does not incorporate without acknowledgment any material previously submitted for a degree or diploma in any university

2. and the research within will not be submitted for any other future degree or diploma without the permission of Flinders University; and

3. to the best of my knowledge and belief, does not contain any material previously published or written by another person except where due reference is made in the text.

Signed.....Wenjie Liu.....

Date.....20/09/2024.....

ACKNOWLEDGEMENTS

I would like to sincerely acknowledge and thank all those who have helped me throughout my PhD journey.

First and foremost, I extend my profound gratitude to my supervisor, Prof. Huade Guan, for his invaluable guidance, unwavering support, and encouragement over the past three years. His extensive knowledge and the countless hours he devoted to discussing research ideas have greatly expanded my understanding of the field. His thoughtful concern for my personal well-being made it much easier for me to adjust to living far from home.

I am also deeply grateful to my co-supervisors, Prof. Okke Batelaan and Prof. Patrick Hesp, for their insightful advice, thorough feedback on my research, and valuable suggestions and encouragement during challenging times.

My sincere thanks go to those who generously offered their time and assistance, including Prof. David Bruce, Prof. Greg Falzon, Prof. Hugo Gutierrez-Jurado, Robert Keane, and Lawrence Burk. Their expertise and support have been essential to my research. I also want to express my deep appreciation to my groupmates—Ajiao Chen, Yifei Zhou, Zecheng Zhang, Zhongli Liu, and Liping Pan—and visiting scholars Zidong Luo, Jianfeng Gou, Yajun Zhou, Xia Li, Wenjing Yang, and Pu Wang, for their guidance, support, engaging academic discussions, assistance during field trips, and the many joyful moments we shared. I will always cherish these memories.

I gratefully acknowledge Flinders University and the China Scholarship Council for their financial support and the opportunities they provided, which were crucial for the successful completion of my studies.

Finally, I wish to express my heartfelt gratitude to my parents for their love, support, and encouragement throughout this journey. Their unwavering belief in me has given me the strength and motivation to keep going.

LIST OF FIGURES

LIST OF TABLES

1 INTRODUCTION

1.1 Significance of semi-arid woodlands

Semi-arid areas cover around 18% of Earth's land surface, and within these regions, woodlands make up a substantial proportion (Rotenberg & Yakir, 2010). Those woodlands significantly contribute to preserving soil stability (Sharafatmandrad & Khosravi Mashizi, 2021), maintaining biodiversity (Zhang et al., 2023), regulating local microclimate, and contribute to global land carbon sink (Anderson-Teixeira et al., 2012). Its conservation and sustainable management are vital to maintaining the resilience of these ecosystems, particularly amidst growing environmental pressures and climate change (García-Ruiz et al., 2011; Vilà-Cabrera et al., 2018).

Specifically, semi-arid woodlands support local livelihoods and regional economic development. It effectively prevents land degradation by regulating the water cycle and reducing soil erosion. Additionally, these ecosystems are crucial for maintaining biodiversity by providing food, thermal shelter, and supporting species migration.

However, semi-arid woodlands are increasingly threatened by both human activities and climate change. On one hand, anthropogenic impacts such as deforestation and urbanization lead to habitat fragmentation, soil erosion, and a decline in biodiversity, severely degrading these ecosystems (Zhao et al., 2005; Villarino et al., 2017; McPhillips et al., 2019; Schoener, 2022). On the other hand, climate change induces ecosystem degradation by disrupting precipitation patterns and intensifying the occurrence of extreme events, resulting in more severe droughts and increased tree mortality (Huang et al., 2016; C. Xu et al., 2017). With the increasing degradation of semi-arid woodlands, it is essential to develop and apply effective techniques for measuring, mapping, and monitoring forest parameters. This data must be generated at appropriate scales to support and enhance conservation and management efforts (David et al., 2022).

1.2 Threats on semi-arid woodlands

1.2.1 Deforestation

Deforestation refers to the transformation of forest/woodland into a permanent non-forested land use (Van Kooten & Bulte, 2000). Key anthropogenic drivers include urbanization, agricultural expansion, industrial development, timber trading, and mineral exploration (Santos et al., 2020). Deforestation changes the global energy exchange through micrometeorological processes and increases atmospheric CO_2 concentration (Okia, 2012). The consequential global warming leads to abnormal weather patterns, resulting in hotter and drier conditions, which escalate the risks of drought, desertification, and the displacement of dominant vegetation regimes. (Lawrence & Vandecar, 2015). In global scale, Hansen et al. (2013) mapped around 230 million hectares of

forest cover loss from 2000 to 2012 but only 80 million hectares of new forest cover gained. The extent and driver of deforestation drivers varies across different countries and regions.

In Australia, deforestation has profoundly impacted the terrestrial environment since European colonization (Bradshaw, 2012). Despite various policy reforms intended to control deforestation, Australia experienced high deforestation rates at the beginning of the 21st century (Evans, 2016). Legislation in Queensland and New South Wales initially reduced large scale clearing, but recent policy changes have raised concerns about a potential resurgence in deforestation (Evans, 2016; Boer, 2024; Macintosh et al., 2024).

A critical area of concern is the deforestation of Australia's semi-arid woodlands which characterized by sparse tree cover and adaptation to dry conditions. For instance, the woodlands of the Riverina and Murray-Darling Basin have suffered significant losses due to agricultural expansion and land clearing, impacting ecological communities dominated by species like Buloke, Slender Cypress Pine, and Grey Box (Cheal et al., 2011).

1.2.2 Water stress from climate change

Global water resources are increasingly under strain, with water scarcity now widespread across most arid and semi-arid regions(Vörösmarty et al., 2010; Mekonnen & Hoekstra, 2016). Climate change is projected to aggravate existing water scarcity, leading to more frequent and severe droughts, and complicating water management efforts (Hosseinizadeh et al., 2015; Kahil et al., 2015; Wilson et al., 2018). Recent droughts in Australia (2001-2009), the western United States (2012), and southern Europe (2012) highlight the substantial impact of such events on regions already facing water scarcity (Van Dijk et al., 2013; Diffenbaugh et al., 2015; Crocetti et al., 2020).

The impacts of water scarcity are particularly pronounced in semi-arid woodlands, where the balance between water availability and ecosystem health is delicate (Reynolds et al., 2007; Maestre et al., 2016). In these regions, the lack of sufficient water reduces vegetation cover and increases vulnerability to desertification (D’Odorico et al., 2013). The interplay between water scarcity and land degradation creates a feedback loop where reduced vegetation cover leads to greater soil erosion, further diminishing the land's capacity to retain moisture and sustain plant growth. Water scarcity also threatens biodiversity in these ecosystems, which are often home to species uniquely adapted to survive in dry conditions. Prolonged droughts and changing climate patterns can push these species to their limits, causing population reductions or even local extinctions (Allen et al., 2015; Maron et al., 2015). The decline in biodiversity can trigger a domino effect on ecosystem functionality, impacting everything from soil health to the availability of resources for human and animal populations.

Climate change induced water scarcity has also intensified the frequency and severity of bushfires, posing a significant threat to semi-arid woodlands (Duffy et al., 2019; Kirchmeier‐Young et al.,

2019). Prolonged warmer and drier conditions are expected to reduce fuel moisture and lengthen fire seasons, leading to more frequent and extensive bushfires that result in higher tree mortality (Goss et al., 2020). Additionally, water stress caused by climate change creates unfavorable post-fire recovery conditions in arid and semi-arid woodlands, resulting in lower seedling densities and increased regeneration failures, ultimately diminishing the resilience of these ecosystems (Enright et al., 2015; Stevens‐Rumann et al., 2018). For example, the 2019-2020 'Black Summer' bushfire in southeast Australia exemplifies the impact of climate change on bushfire dynamics, as the unprecedented scale and intensity of the fires were driven by the hottest and driest year on record, with exceptionally dry fuel loads and compounded effects of multiple climate modes, significantly escalating fire risk and severity in the region (Abram et al., 2021).

1.3 Knowledge gaps for improved management of semi-arid woodlands

In regards of the threats posed by deforestation and the stress from climate change, it is imperative that we take actions to better protect and manage semi-arid woodlands. From a research perspective, there are currently two critical knowledge gaps:

1) understanding how vegetation attributes are controlled by topography.

2) monitoring surface ecohydrological processes.

Firstly, afforestation and reforestation initiatives can be highly effective in restoring native vegetation. The potential of afforestation/reforestation for carbon sequestration has been widely studied and acknowledged (Nilsson & Schopfhauser, 1995; Niu & Duiker, 2006; Doelman et al., 2020). Surprisingly, in arid and semi-arid regions, afforestation/reforestation has shown remarkable potential for carbon sequestration (McNicol et al., 2018; Yosef et al., 2018).

However, their success depends on a nuanced understanding of local environmental constraints and strategic decision-making. For instance, poorly designed projects can result in unintended consequences, as seen in northwestern China, where afforestation efforts exacerbated environmental degradation due to mismatched tree species and local conditions (Cao et al., 2010). Similarly, critiques of Australia's native forest regeneration carbon offset projects question their limited impact on vegetation cover and carbon sequestration, calling for more robust planning and evaluation frameworks (Macintosh et al., 2024). Given these complexities, ecohydrological models can serve as critical decision-support tools for designing and implementing afforestation and reforestation projects. By integrating spatially variable factors such as topography, soil moisture, and climatic conditions, such models can enable the prediction of vegetation growth patterns and water dynamics. They can provide insights into the trade-offs between ecological benefits and water availability, guiding project planners towards sustainable outcomes. Previous studies have shown that forest restoration effects can be significantly influenced by the local environment, and

topography plays an important role in producing spatially variable local environmental conditions (Sattler et al., 2014; Hong et al., 2020; X. Zhang et al., 2020). Section 1.3.1 reviews the current knowledge on topography's influence on vegetation growth and attributes and outlines the existing problem.

Another critical aspect of afforestation and reforestation is the potential competition for water between ecosystems and human society (Kahil et al., 2016). While the primary objective of tree planting is to enhance community well-being, it can paradoxically become detrimental if the water uptake by woodlands diminishes the water resources available to local populations (Hoek van Dijke et al., 2022; Zan et al., 2024). Moreover, the reduction in precipitation and the intensification of extreme events caused by climate change in semi-arid regions necessitate highly accurate and comprehensive monitoring of these fragile ecosystems. Such monitoring is essential for implementing proactive strategies to mitigate ecosystem degradation. Addressing these challenges requires an advanced understanding of surface ecohydrological processes. Section 1.3.2 reviews the literature on surface ecohydrological processes and identifies key research gaps that require further investigation.

1.3.1 Topography controls on vegetation

Vegetation is an indispensable component of natural ecosystems and can serve as an indicator for monitoring ecosystem status (X. Fang et al., 2018). In semi-arid region, vegetation plays a key role in ameliorating local climate (Huryna & Pokorný, 2016), preventing desertification (Lee et al., 2019), and enhancing local biodiversity (Li et al., 2004). The impact of climate factors like precipitation and temperature on vegetation growth has been widely researched, but the relationship between them is often nonlinear and may vary from region to region (Lamchin et al., 2018; Li et al., 2018; Lamchin et al., 2020). While in the scale of hectares to km^2 where the same regional climate condition is shared, topography is the major factor that influence vegetation attributes, especially in mountainous areas (Douville et al., 2000; Baudena et al., 2008; Hwang et al., 2011). By altering the timing and amount of energy inputs and available water of land surface, topography can impact the vegetation growth, soil development, and biogeochemical fluxes.

Research in Australia has highlighted the critical role of topography in shaping vegetation patterns. Kirkpatrick and Bridle (1998) analyzed floristic and environmental data for Australian alpine vegetation and found that while climatic factors dominate floristic variation at broader scales, topography becomes the key driver at finer scales. Yadav et al. (2022) investigated the relationship between landscape topography, geology, and vegetation attributes in a wet eucalypt forest, and the results suggest that topography and geology data can partially predict vegetation density. In a native eucalypt woodland catchment, previous studies have revealed distinctive patterns of tree water stress, root zone moisture dynamics, leaf nutrient contents, and tree water

use, many of which are closely related to topography (X. Xu et al., 2017, 2019; Xu et al., 2022; H. Wang et al., 2024).

In summary, these studies have significantly advanced our understanding of the impact of topography on vegetation attributes. However, these studies often rely on analysis of medium-resolution remote sensing data (e.g. 30 - 500 m), or observation of discrete points, which may not adequately capture the detailed topographic variations that significantly influence vegetation patterns. Moreover, many of these studies are pixel-based rather than tree-based, which limits their ability to account for individual tree characteristics and their responses to micro-topographic changes. This represents a key knowledge gap, as tree-based approaches that utilize high-resolution data could provide more detailed insights into the relationship between vegetation and topography, ultimately improving our understanding of regional vegetation patterns. Such detailed studies could effectively guide afforestation and reforestation efforts, leading to more economically viable and efficient carbon sequestration strategies. By integrating high-resolution geospatial data into these studies, we can better inform land management practices.

1.3.2 Surface ecohydrological processes

1.3.2.1 Energy and water balance in ecohydrology

Energy and water balance are two key components in ecohydrology research. The equation for land surface energy balance illustrates how net radiation (R_n) partitions among sensible heat flux (H), latent heat flux (λE), and soil heat flux (G). During daytime, the land surface receives heat from net radiation; a minor fraction of this energy is absorbed by the soil, while the majority is returned to the atmosphere as sensible heat (through conduction and convection) and latent heat (related to evapotranspiration (ET)). The land surface water balance equation, as shown in equation 1.2, describes how precipitation in a catchment turns to different components. It includes variables such as precipitation (P), runoff (R), ET, and the change in soil water and groundwater storage (ΔS). ET (or the latent heat flux) serves as a key component in the water and energy balance within soil-plant-atmosphere continuum. It consists of evaporation and transpiration. Evaporation occurs on water surfaces, wet canopy, and exposed soil. Transpiration starts with the root water uptake, followed by water moving from roots and stems to the leaves and then vaporizing to the atmosphere. Accurately quantifying ET is crucial to effective water, agricultural, and ecosystem management.

$$R_n = H + \lambda\mathrm{E} + \mathrm{G} \tag{1.1}$$

$$P = R + ET + \Delta S \tag{1.2}$$

High temporal-resolution ET measurements, utilizing equipment like lysimeters, sap flow, and eddy covariance, have provided valuable insights into ecohydrological sciences and enhanced our comprehension of ET processes. Various techniques are available for quantifying ET. For instance, the watershed water balance method, which calculates ET as the difference between precipitation inputs and streamflow outputs, is often most applicable for long-term averages, particularly when changes in water storage are negligible (Senay et al., 2011). Conversely, sap flow and eddy covariance methods, which estimate ET at finer temporal scales, show good agreement with other techniques in uniform stands with extensive coverage but tend to be less accurate in complex terrain or areas with small or uneven coverage, such as canopy gaps (Wullschleger et al., 1998; Ewers et al., 2002; Barker et al., 2009). However, direct measurement of ET at larger scales and in heterogenous landscapes remains impractical due to the operational challenges of deploying dense networks of such instruments, and point observations are inadequate for fully capturing the spatial variability of regional land surfaces (Mueller et al., 2011).

1.3.2.2 Advances in remote sensing for ET monitoring

Remote sensing is widely acknowledged as a promising tool for its potential in ET estimation, as it enables the collection of spatially and temporally continuous data on key biophysical parameters that influence ET (Li et al., 2009). Since the 1980s, numerous methods have been proposed, leveraging a range of satellite observations for ET estimation (Zhang et al., 2016). For example, the water balance method can be simple to perform for catchments and requires only precipitation and runoff data, but it cannot obtain gridded ET values and is sensitive to precipitation data errors (Long et al., 2014; Wan et al., 2015). The Penman-Monteith model is a process-based method for ET mapping. It requires a large amount of meteorological data input such as radiation, air temperature, vapor pressure deficit, and vegetation cover information (Mu et al., 2007; Leuning et al., 2008; Zhang et al., 2009). The Priestley-Taylor model is built based on a semi-empirical relationship and is a simplification of the Penman-Monteith model (Flint & Childs, 1991). The Surface Energy Balance (SEB) model requires less meteorological data input and can estimate ET for different surface layers. While the estimation is highly sensitive to surface temperature accuracy. The surface temperature and vegetation Index (Ts-VI) space model uses the spatial variation of surface temperature, and the internal relationship derived from Ts-VI space to partition Rn into sensible and latent heat. Compared to the SEB models, the Ts-VI model is less sensitive to Ts error. However, the semi-empirical relationships established within the Ts-VI space may not always be reliable or consistent (Zhang et al., 2016). Recent advancements in Unmanned Aerial Vehicle (UAV) provides an opportunity to monitor surface ET at sub-meter resolution for local hydrological research (Acharya et al., 2021; Mokhtari et al., 2021; Yan et al., 2023). However, current approaches to remote sensing-based ET estimation often oversimplify woodlands by treating them as flat surfaces, with a predominant focus on canopy-level processes, thereby neglecting the complex physical interactions occurring beneath the canopy.

1.3.2.3 Understorey contributions to woodland ecosystems ET

Forests and woodlands generally comprise two unique layers: an overstory consisting primarily of tall trees, and an understorey made up of shrubs, grasses, and mosses. These layers are often considered separately in ecosystem research because of differences in their photosynthetic capacities, carbon turnover rates, and adaptations to changing climate conditions (Marques & Oliveira, 2004; Kim et al., 2016; Liu et al., 2017). Much emphasis has been placed on the overstory in forest ecosystems, as it significantly influences light availability, microclimate variables, and water balance through processes like ET and rainfall interception (Blanken et al., 1998; Messier et al., 1998; Aussenac, 2000; Clinton, 2003).

The understorey layer also plays a significant role in woodland ecosystems. This layer, comprising both vascular and nonvascular plants, is crucial for maintaining ecosystem functions, including nutrient cycling, water retention, and carbon sequestration (Bartels & Chen, 2013; Deng et al., 2023). Additionally, the understorey provides essential habitat and food sources for various animal species, particularly soil arthropods and large herbivores (Fisher, 2000).

The interaction between the understorey and overstory is crucial in shaping the structure and function of woodland ecosystems (Deng et al., 2023). Some studies have shown that removing understorey vegetation can lead to significant increases in photosynthetic rate and nutrient use efficiency (including nitrogen and phosphorus) in both coniferous species and broadleaved species. However, these changes were often accompanied by a decrease in water use efficiency (Hébert et al., 2010). The effects were most pronounced in the upper canopy, while photosynthetic rate in the middle and lower canopy leaves remained largely unaffected (Kobayashi et al., 2006). Conversely, other studies have found no impact on photosynthetic capacity when understorey vegetation is removed (R. Li et al., 2020; Yifan et al., 2020).

The interdependence between understorey and overstory layers extends significantly to ET processes. Although understorey ET is typically lower than that of the overstory, it constitutes a significant component of the overall woodland water balance, directly influencing the microclimate and soil moisture conditions that sustain overstory trees (Baldocchi & Meyers, 1998; Wilson et al., 2000). Factors such as plant species composition, density, and the microclimatic conditions shaped by the overstory canopy heavily dictate the rate of understorey ET (Simonin et al., 2007).

Understanding the dynamics of understorey ET is essential for accurate ecosystem modeling and effective forest management. In forest and woodland ecosystems, the combined ET from both layers can lead to significant water loss, impacting soil moisture availability for both understorey and overstory plants (Wilson & Baldocchi, 2000; Goulden & Bales, 2014). Recent studies have emphasized the significant contribution of understorey ET to the total forest water flux. For example, Yepez et al. (2003) used stable isotope measurements to determine that understorey ET accounts for 30% of the total ecosystem ET in a semi-arid savanna woodland environment. Iida et

al. (2009) found that mean daily understorey ET represents approximately one third of total ecosystem ET in a Siberian boreal forest based on eddy covariance measurements. Similarly, Wolf et al. (2024) investigated above- and below-canopy ET in a montane forest using concurrent eddy covariance measurements and found that understorey ET accounts for 45% of total ecosystem ET.

Recent attention to understorey ET has highlighted its critical role in forest/woodland ecosystems, yet existing research predominantly relies on localized observations, either at a single point or integrated over a limited area. Due to the pronounced spatial heterogeneity of the understorey environment, these localized measurements can introduce uncertainties when scaling up estimates of understorey ET to larger areas. A major knowledge gap lies in effectively detecting the spatial distribution of understorey ET. Addressing this challenge necessitates a comprehensive understanding of the spatial distribution of environmental variables within the understorey. Improved spatially explicit methods and models that account for these heterogeneous conditions are essential for accurate assessments and better management of semi-arid woodland water resources.

1.4 Objectives

The aim of this study is to advance our understanding of vegetation attributes, understorey solar radiation, and understorey ET processes in semi-arid woodlands. To achieve this aim, the study focuses on three primary objectives:

Objective 1: Investigate woodland vegetation attributes in relation to topography in hilly areas.

The first objective is to examine how topography influences vegetation attributes in hilly regions. This is achieved by utilizing high-resolution ALS and hyperspectral data to capture detailed spatial patterns of vegetation. The study aims to quantify the extent to which topography influences vegetation attributes and identify key topographic variables that determine vegetation distribution, composition, and structure.

Objective 2: Develop a solar radiation model for woodland understorey radiation in complex terrain.

The second objective focuses on the development of a solar radiation model to simulate the temporal and spatial distribution of incident radiation in the forest/woodland environments. Solar radiation is a fundamental driver of ecohydrological processes. Existing models often lack the capability to simulate understorey radiation and are limited to clear-sky conditions. To address this, the Double-Shading Transposition (DST) model is proposed, which incorporates local topographic and canopy shading effects to accurately model understorey radiation. This model is crucial for improving the accuracy of understorey ET simulations.

Objective 3: Model and map semi-arid woodland understorey ET.

The third objective is to model and map understorey ET in semi-arid regions. ET is a critical factor in understanding the water balance of ecosystems. However, existing studies often focus primarily on overstory ET, neglecting the contributions of the understorey surface. This study utilizes the Maximum Entropy Production (MEP) model to quantify understorey ET in two semi-arid woodlands, thereby enhancing our understanding of the role of understorey layer in overall ecosystem water dynamics and informing better water management practices.

By addressing these objectives, this study aims to provide an improved understanding of the distinct influences of topography on vegetation attributes, the dynamics of understorey radiation, and the critical contributions of understorey ET to ecosystem water balance.

1.5 Thesis structure

The structure of the thesis is shown below:

Chapters	Chapter Title	Main Content
1	Introduction	Background, research objectives, and thesis structure.
2	Geospatial modelling of vegetation-topography relationships	This chapter investigates the influence of topography on vegetation attributes in complex terrains within a representative semi-arid environment.
3	Solar radiation modelling	This chapter focuses on the development of a distributed understorey shortwave radiation model.
4	Understorey evapotranspiration modelling and mapping	This chapter establishes a robust framework for understorey ET mapping and analyses the factors that influence ET.
5	Conclusion	Conclusions and future research interests.
Appendix	Spatiotemporal delineation of bushfire in semi-arid area	Methodological improvements for bushfire detection and post-fire recovery monitoring in semi-arid areas.

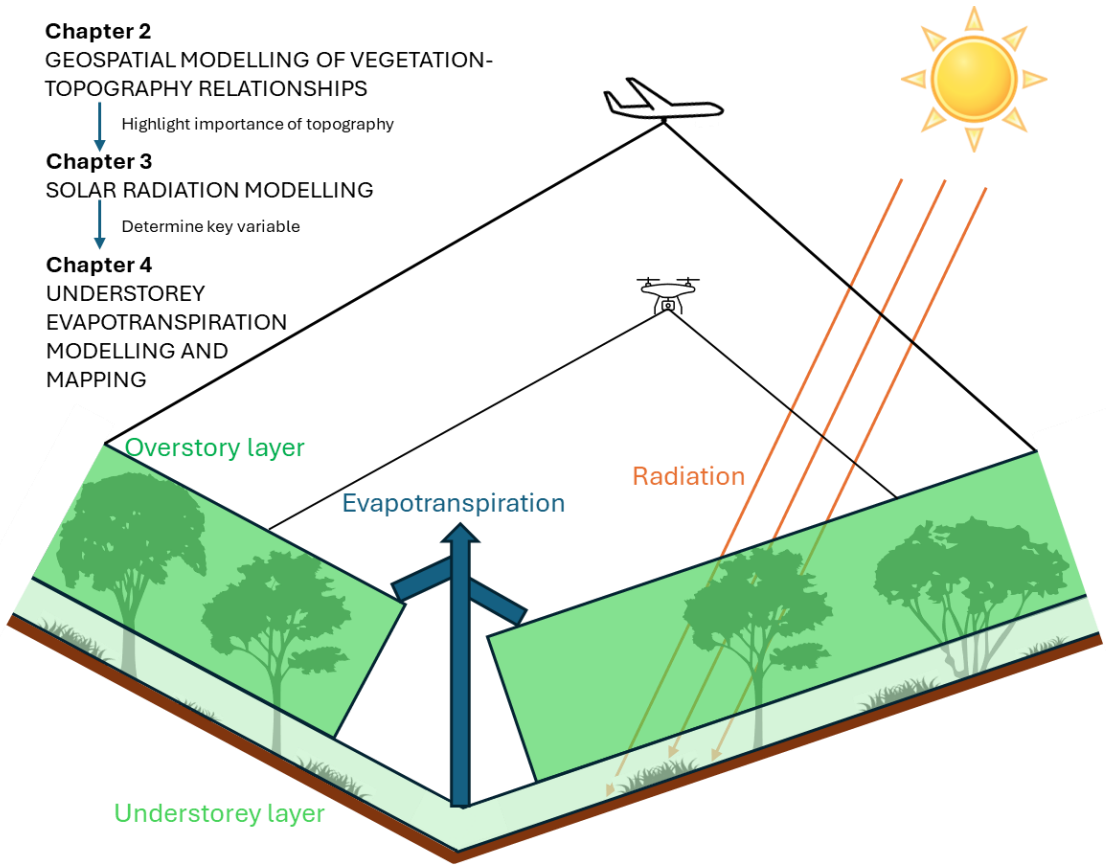

Figure 1.1 Graphic abstract of the thesis structure

Figure 1.1 illustrates the connections between the three main chapters of this study.

Chapter 2 investigates the influence of topography on vegetation attributes within a semi-arid catchment. The findings highlight that topographic factors significantly affect vegetation attributes such as tree height and NDVI. The analysis reveals that areas with varying sunlight exposure and hydrological conditions exhibit distinct patterns of vegetation attributes. These topographic effects are crucial for understanding the spatial distribution of vegetation and its response to environmental changes, informing targeted conservation and restoration strategies.

Transitioning from the overstory to the understorey, **Chapter 3** introduces the development of the DST model, which integrates shading effects from both topographic features and the vegetation canopy. This chapter examines a critical variable for understanding understorey surface dynamics.

Chapter 4 focuses on the distributed modelling of understorey ET using the MEP model. This analysis is based on net radiation, surface temperature, and specific humidity. The chapter also details the data acquisition methods and the approach for estimating understorey temperature using UAV-based thermal imagery. Additionally, it explores the contribution of understorey ET to the total ecosystem ET in two representative semi-arid regions and examines the factors influencing this contribution.

In **Appendix A1**, we examine traditional remote sensing methods for delineating bushfires and monitoring post-fire recovery in semi-arid woodlands. The findings indicate that NDVI is more effective than other indices for detecting burned areas in these regions. However, using remote sensing indices to monitor post-fire recovery proves to be less reliable due to the complex and variable responses of the understorey layer. This highlights the need for a more comprehensive understanding of the 3D structure of woodlands.

1.6 Publications

Liu, W., Guan, H., Gutiérrez-Jurado, H. A., Banks, E. W., He, X., & Zhang, X. (2022). Modelling quasi-three-dimensional distribution of solar irradiance on complex terrain. *Environmental Modelling & Software*, 149, 105293.

Liu, W., Guan, H., Hesp, P. A., & Batelaan, O. (2023). Remote sensing delineation of wildfire spatial extents and post-fire recovery along a semi-arid climate gradient. *Ecological Informatics*, 78, 102304.

Integrating the Maximum Entropy Production model and airborne imagery for understorey evapotranspiration mapping (currently under review in *Journal of Hydrology*).

1.7 References

Abram, N. J., Henley, B. J., Sen Gupta, A., Lippmann, T. J., Clarke, H., Dowdy, A. J., Sharples, J. J., Nolan, R. H., Zhang, T., & Wooster, M. J. (2021). Connections of climate change and variability to large and extreme forest fires in southeast Australia. *Communications Earth & Environment*, *2*(1), 1-17.

Acharya, B. S., Bhandari, M., Bandini, F., Pizarro, A., Perks, M., Joshi, D. R., Wang, S., Dogwiler, T., Ray, R. L., & Kharel, G. (2021). Unmanned aerial vehicles in hydrology and water management: Applications, challenges, and perspectives. *Water Resources Research*, *57*(11), e2021WR029925.

Allen, C. D., Breshears, D. D., & McDowell, N. G. (2015). On underestimation of global vulnerability to tree mortality and forest die‐off from hotter drought in the Anthropocene. *Ecosphere*, *6*(8), 1-55.

Anderson-Teixeira, K. J., Snyder, P. K., Twine, T. E., Cuadra, S. V., Costa, M. H., & DeLucia, E. H. (2012). Climate-regulation services of natural and agricultural ecoregions of the Americas. *Nature Climate Change*, *2*(3), 177-181.

Armstrong, A., Quinton, J., Francis, B., Heng, B., & Sander, G. (2011). Controls over nutrient dynamics in overland flows on slopes representative of agricultural land in North West Europe. *Geoderma*, *164*(1-2), 2-10.

Aussenac, G. (2000). Interactions between forest stands and microclimate: ecophysiological aspects and consequences for silviculture. *Annals of forest science*, *57*(3), 287-301.

Baldocchi, D., & Meyers, T. (1998). On using eco-physiological, micrometeorological and biogeochemical theory to evaluate carbon dioxide, water vapor and trace gas fluxes over vegetation: a perspective. *Agricultural and forest Meteorology*, *90*(1-2), 1-25.

Barker, C. A., Amiro, B. D., Kwon, H., Ewers, B. E., & Angstmann, J. L. (2009). Evapotranspiration in intermediate‐aged and mature fens and upland black spruce boreal forests. *Ecohydrology: Ecosystems, Land and Water Process Interactions, Ecohydrogeomorphology*, *2*(4), 462-471.

Bartels, S. F., & Chen, H. Y. (2013). Interactions between overstorey and understorey vegetation along an overstorey compositional gradient. *Journal of Vegetation Science*, *24*(3), 543-552.

Baudena, M., d'Andrea, F., & Provenzale, A. (2008). A model for soil‐vegetation‐atmosphere interactions in water‐limited ecosystems. *Water Resources Research*, *44*(12).

Blanken, P., Black, T., Neumann, H., Den Hartog, G., Yang, P., Nesic, Z., Staebler, R., Chen, W., & Novak, M. (1998). Turbulent flux measurements above and below the overstory of a boreal aspen forest. *Boundary-Layer Meteorology*, *89*, 109-140.

Boer, H. (2024). Deliberate disproportionate policy outcomes and regulating deforestation in Queensland, Australia. *Australian Journal of Public Administration*, *83*(1), 50-68.

Bradshaw, C. J. (2012). Little left to lose: deforestation and forest degradation in Australia since European colonization. *Journal of Plant Ecology*, *5*(1), 109-120.

Brooks, P. D., Chorover, J., Fan, Y., Godsey, S. E., Maxwell, R. M., McNamara, J. P., & Tague, C. (2015). Hydrological partitioning in the critical zone: Recent advances and opportunities for developing transferable understanding of water cycle dynamics. *Water Resources Research*, *51*(9), 6973-6987.

Cao, S., Tian, T., Chen, L., Dong, X., Yu, X., & Wang, G. (2010). Damage caused to the environment by reforestation policies in arid and semi-arid areas of China. *Ambio*, *39*, 279-283.

Cheal, D., Lucas, A., & Macaulay, L. (2011). National recovery plan for Buloke Woodlands of the Riverina and Murray Darling Depression Bioregions. *Department of Sustainability and Environment, Melbourne, Victoria, Australia*.

Clinton, B. D. (2003). Light, temperature, and soil moisture responses to elevation, evergreen understory, and small canopy gaps in the southern Appalachians. *Forest Ecology and Management*, *186*(1-3), 243-255.

Crocetti, L., Forkel, M., Fischer, M., Jurečka, F., Grlj, A., Salentinig, A., Trnka, M., Anderson, M., Ng, W.-T., & Kokalj, Ž. (2020). Earth Observation for agricultural drought monitoring in the Pannonian Basin (southeastern Europe): current state and future directions. *Regional environmental change*, *20*, 1-17.

Curtis, P. G., Slay, C. M., Harris, N. L., Tyukavina, A., & Hansen, M. C. (2018). Classifying drivers of global forest loss. *Science*, *361*(6407), 1108-1111.

D'Odorico, P., Bhattachan, A., Davis, K. F., Ravi, S., & Runyan, C. W. (2013). Global desertification: Drivers and feedbacks. *Advances in water resources*, *51*, 326-344.
David, R. M., Rosser, N. J., & Donoghue, D. N. (2022). Improving above ground biomass estimates of Southern Africa dryland forests by combining Sentinel-1 SAR and Sentinel-2 multispectral imagery. *Remote sensing of Environment*, *282*, 113232.
Deng, J., Fang, S., Fang, X., Jin, Y., Kuang, Y., Lin, F., Liu, J., Ma, J., Nie, Y., & Ouyang, S. (2023). Forest understory vegetation study: current status and future trends. *Forestry Research*, *3*(1).
Diffenbaugh, N. S., Swain, D. L., & Touma, D. (2015). Anthropogenic warming has increased drought risk in California. *Proceedings of the National Academy of Sciences*, *112*(13), 3931-3936.
Doelman, J. C., Stehfest, E., van Vuuren, D. P., Tabeau, A., Hof, A. F., Braakhekke, M. C., Gernaat, D. E., van den Berg, M., van Zeist, W. J., & Daioglou, V. (2020). Afforestation for climate change mitigation: Potentials, risks and trade‐offs. *Global change biology*, *26*(3), 1576-1591.
Douville, H., Planton, S., Royer, J. F., Stephenson, D., Tyteca, S., Kergoat, L., Lafont, S., & Betts, R. (2000). Importance of vegetation feedbacks in doubled‐CO2 climate experiments. *Journal of Geophysical Research: Atmospheres*, *105*(D11), 14841-14861.
Dubs, B., Furley, P., Proctor, J., & Ratter, J. (1992). Nature and dynamics of forest-savanna boundaries. In.
Duffy, P. B., Field, C. B., Diffenbaugh, N. S., Doney, S. C., Dutton, Z., Goodman, S., Heinzerling, L., Hsiang, S., Lobell, D. B., & Mickley, L. J. (2019). Strengthened scientific support for the Endangerment Finding for atmospheric greenhouse gases. *Science*, *363*(6427), eaat5982.
Endalamaw, A., Bolton, W. R., Young-Robertson, J. M., Morton, D., Hinzman, L., & Nijssen, B. (2017). Towards improved parameterization of a macroscale hydrologic model in a discontinuous permafrost boreal forest ecosystem. *Hydrology and Earth System Sciences*, *21*(9), 4663-4680.
Enright, N. J., Fontaine, J. B., Bowman, D. M., Bradstock, R. A., & Williams, R. J. (2015). Interval squeeze: altered fire regimes and demographic responses interact to threaten woody species persistence as climate changes. *Frontiers in Ecology and the Environment*, *13*(5), 265-272.
Evans, M. C. (2016). Deforestation in Australia: drivers, trends and policy responses. *Pacific Conservation Biology*, *22*(2), 130-150.
Ewers, B., Mackay, D., Gower, S., Ahl, D., Burrows, S., & Samanta, S. (2002). Tree species effects on stand transpiration in northern Wisconsin. *Water Resources Research*, *38*(7), 8-1-8-11.
Fan, Y., Clark, M., Lawrence, D. M., Swenson, S., Band, L., Brantley, S. L., Brooks, P. D., Dietrich, W. E., Flores, A., & Grant, G. (2019). Hillslope hydrology in global change research and earth system modeling. *Water Resources Research*, *55*(2), 1737-1772.
Fang, X., Zhu, Q., Ren, L., Chen, H., Wang, K., & Peng, C. (2018). Large-scale detection of vegetation dynamics and their potential drivers using MODIS images and BFAST: A case study in Quebec, Canada. *Remote sensing of Environment*, *206*, 391-402.
Fisher, D. (2000). Effects of vegetation structure, food and shelter on the home range and habitat use of an endangered wallaby. *Journal of Applied Ecology*, *37*(4), 660-671.
Flint, A. L., & Childs, S. W. (1991). Use of the Priestley-Taylor evaporation equation for soil water limited conditions in a small forest clearcut. *Agricultural and forest Meteorology*, *56*(3-4), 247-260.
Florinsky, I. V., & Kuryakova, G. A. (1996). Influence of topography on some vegetation cover properties. *Catena*, *27*(2), 123-141.
García-Ruiz, J. M., López-Moreno, J. I., Vicente-Serrano, S. M., Lasanta–Martínez, T., & Beguería, S. (2011). Mediterranean water resources in a global change scenario. *Earth-Science Reviews*, *105*(3-4), 121-139.
Goss, M., Swain, D. L., Abatzoglou, J. T., Sarhadi, A., Kolden, C. A., Williams, A. P., & Diffenbaugh, N. S. (2020). Climate change is increasing the likelihood of extreme autumn wildfire conditions across California. *Environmental Research Letters*, *15*(9), 094016.
Goulden, M., Anderson, R., Bales, R., Kelly, A., Meadows, M., & Winston, G. (2012). Evapotranspiration along an elevation gradient in California's Sierra Nevada. *Journal of Geophysical Research: Biogeosciences*, *117*(G3).
Goulden, M. L., & Bales, R. C. (2014). Mountain runoff vulnerability to increased evapotranspiration with vegetation expansion. *Proceedings of the National Academy of Sciences*, *111*(39), 14071-14075.

Hansen, M. C., Potapov, P. V., Moore, R., Hancher, M., Turubanova, S. A., Tyukavina, A., Thau, D., Stehman, S. V., Goetz, S. J., & Loveland, T. R. (2013). High-resolution global maps of 21st-century forest cover change. *Science*, *342*(6160), 850-853.
Hébert, F., Thiffault, N., Ruel, J.-C., & Munson, A. D. (2010). Ericaceous shrubs affect black spruce physiology independently from inherent site fertility. *Forest Ecology and Management*, *260*(2), 219-228.
Hoek van Dijke, A. J., Herold, M., Mallick, K., Benedict, I., Machwitz, M., Schlerf, M., Pranindita, A., Theeuwen, J. J., Bastin, J.-F., & Teuling, A. J. (2022). Shifts in regional water availability due to global tree restoration. *Nature Geoscience*, *15*(5), 363-368.
Hong, S., Yin, G., Piao, S., Dybzinski, R., Cong, N., Li, X., Wang, K., Peñuelas, J., Zeng, H., & Chen, A. (2020). Divergent responses of soil organic carbon to afforestation. *Nature Sustainability*, *3*(9), 694-700.
Hosseinizadeh, A., SeyedKaboli, H., Zareie, H., Akhondali, A., & Farjad, B. (2015). Impact of climate change on the severity, duration, and frequency of drought in a semi-arid agricultural basin. *Geoenvironmental Disasters*, *2*, 1-9.
Huang, J., Ji, M., Xie, Y., Wang, S., He, Y., & Ran, J. (2016). Global semi-arid climate change over last 60 years. *Climate Dynamics*, *46*, 1131-1150.
Huryna, H., & Pokorný, J. (2016). The role of water and vegetation in the distribution of solar energy and local climate: a review. *Folia geobotanica*, *51*, 191-208.
Hwang, T., Song, C., Vose, J. M., & Band, L. E. (2011). Topography-mediated controls on local vegetation phenology estimated from MODIS vegetation index. *Landscape ecology*, *26*, 541-556.
Iida, S. i., Ohta, T., Matsumoto, K., Nakai, T., Kuwada, T., Kononov, A. V., Maximov, T. C., van der Molen, M. K., Dolman, H., & Tanaka, H. (2009). Evapotranspiration from understory vegetation in an eastern Siberian boreal larch forest. *Agricultural and forest Meteorology*, *149*(6-7), 1129-1139.
Kahil, M. T., Dinar, A., & Albiac, J. (2015). Modeling water scarcity and droughts for policy adaptation to climate change in arid and semiarid regions. *Journal of Hydrology*, *522*, 95-109.
Kahil, M. T., Dinar, A., & Albiac, J. (2016). Cooperative water management and ecosystem protection under scarcity and drought in arid and semiarid regions. Water Resources and Economics, 13, 60-74.
Kim, D., Oren, R., & Qian, S. S. (2016). Response to CO 2 enrichment of understory vegetation in the shade of forests. *Global change biology*, *22*(2), 944-956.
Kirchmeier‐Young, M. C., Gillett, N. P., Zwiers, F. W., Cannon, A. J., & Anslow, F. (2019). Attribution of the influence of human‐induced climate change on an extreme fire season. *Earth's Future*, *7*(1), 2-10.
Kirkpatrick, J., & Bridle, K. (1998). Environmental relationships of floristic variation in the alpine vegetation of southeast Australia. *Journal of Vegetation Science*, *9*(2), 251-260.
Kobayashi, T., Miki, N., Kato, K., Kubo, T., Nishimura, S.-i., Uemura, S., Ono, K., Sumida, A., Ohta, T., & Hara, T. (2006). Understory removal increases carbon gain and transpiration in the overstory of birch (Betula ermanii) stands in northern Hokkaido, Japan: trends in leaf, shoot, and canopy. Proceedings of international workshop on H2O and CO2 exchange in Siberia,
Kundzewicz, Z. W. (2007). Global freshwater resources for sustainable development. *Ecohydrology & Hydrobiology*, *7*(2), 125-134.
Lamchin, M., Lee, W.-K., Jeon, S. W., Wang, S. W., Lim, C. H., Song, C., & Sung, M. (2018). Long-term trend and correlation between vegetation greenness and climate variables in Asia based on satellite data. *Science of the Total Environment*, *618*, 1089-1095.
Lamchin, M., Wang, S. W., Lim, C.-H., Ochir, A., Pavel, U., Gebru, B. M., Choi, Y., Jeon, S. W., & Lee, W.-K. (2020). Understanding global spatio-temporal trends and the relationship between vegetation greenness and climate factors by land cover during 1982–2014. *Global Ecology and Conservation*, *24*, e01299.
Lawrence, D., & Vandecar, K. (2015). Effects of tropical deforestation on climate and agriculture. *Nature Climate Change*, *5*(1), 27-36.
Lee, D. B., Ferdowsi, B., & Jerolmack, D. J. (2019). The imprint of vegetation on desert dune dynamics. *Geophysical Research Letters*, *46*(21), 12041-12048.
Leuning, R., Zhang, Y., Rajaud, A., Cleugh, H., & Tu, K. (2008). A simple surface conductance model to estimate regional evaporation using MODIS leaf area index and the Penman‐Monteith equation. *Water Resources Research*, *44*(10).

Li, L., Zhang, Y., Liu, L., Wu, J., Wang, Z., Li, S., Zhang, H., Zu, J., Ding, M., & Paudel, B. (2018). Spatiotemporal patterns of vegetation greenness change and associated climatic and anthropogenic drivers on the Tibetan Plateau during 2000–2015. *Remote Sensing*, *10*(10), 1525.
Li, R., Han, J., Guan, X., Chi, Y., Zhang, W., Chen, L., Wang, Q., Xu, M., Yang, Q., & Wang, S. (2020). Crown pruning and understory removal did not change the tree growth rate in a Chinese fir (Cunninghamia lanceolata) plantation. *Forest Ecology and Management*, *464*, 118056.
Li, X. R., Xiao, H. L., Zhang, J. G., & Wang, X. P. (2004). Long-term ecosystem effects of sand-binding vegetation in the Tengger Desert, northern China. *Restoration Ecology*, *12*(3), 376-390.
Li, Z.-L., Tang, R., Wan, Z., Bi, Y., Zhou, C., Tang, B., Yan, G., & Zhang, X. (2009). A review of current methodologies for regional evapotranspiration estimation from remotely sensed data. *Sensors*, *9*(05), 3801-3853.
Liu, Y., Liu, R., Pisek, J., & Chen, J. M. (2017). Separating overstory and understory leaf area indices for global needleleaf and deciduous broadleaf forests by fusion of MODIS and MISR data. *Biogeosciences*, *14*(5), 1093-1110.
Long, D., Longuevergne, L., & Scanlon, B. R. (2014). Uncertainty in evapotranspiration from land surface modeling, remote sensing, and GRACE satellites. *Water Resources Research*, *50*(2), 1131-1151.
Macintosh, A., Butler, D., Larraondo, P., Evans, M. C., Ansell, D., Waschka, M., Fensham, R., Eldridge, D., Lindenmayer, D., & Gibbons, P. (2024). Australian human-induced native forest regeneration carbon offset projects have limited impact on changes in woody vegetation cover and carbon removals. *Communications Earth & Environment*, *5*(1), 149.
Maestre, F. T., Eldridge, D. J., Soliveres, S., Kéfi, S., Delgado-Baquerizo, M., Bowker, M. A., García-Palacios, P., Gaitán, J., Gallardo, A., & Lázaro, R. (2016). Structure and functioning of dryland ecosystems in a changing world. *Annual review of ecology, evolution, and systematics*, *47*(1), 215-237.
Maron, M., McAlpine, C. A., Watson, J. E., Maxwell, S., & Barnard, P. (2015). Climate-induced resource bottlenecks exacerbate species vulnerability: a review. *Diversity and Distributions*, *21*(7), 731-743.
Marques, M., & Oliveira, P. E. A. (2004). Phenology of canopy and understory species of two Coastal Plain Forests in Southern Brazil. *Brazilian Journal of Botany*, *27*, 713-723.
McNab, W. H. (1993). A topographic index to quantify the effect of mesoscale landform on site productivity. *Canadian Journal of Forest Research*, *23*(6), 1100-1107.
McNicol, I. M., Ryan, C. M., & Mitchard, E. T. (2018). Carbon losses from deforestation and widespread degradation offset by extensive growth in African woodlands. *Nature communications*, *9*(1), 3045.
McPhillips, L., Earl, S., Hale, R., & Grimm, N. (2019). Urbanization in arid central Arizona watersheds results in decreased stream flashiness. *Water Resources Research*, *55*(11), 9436-9453.
Mekonnen, M. M., & Hoekstra, A. Y. (2016). Four billion people facing severe water scarcity. *Science advances*, *2*(2), e1500323.
Messier, C., Parent, S., & Bergeron, Y. (1998). Effects of overstory and understory vegetation on the understory light environment in mixed boreal forests. *Journal of Vegetation Science*, *9*(4), 511-520.
Mokhtari, A., Ahmadi, A., Daccache, A., & Drechsler, K. (2021). Actual evapotranspiration from UAV images: A multi-sensor data fusion approach. *Remote Sensing*, *13*(12), 2315.
Morton, D. C., DeFries, R. S., Shimabukuro, Y. E., Anderson, L. O., Arai, E., del Bon Espirito-Santo, F., Freitas, R., & Morisette, J. (2006). Cropland expansion changes deforestation dynamics in the southern Brazilian Amazon. *Proceedings of the National Academy of Sciences*, *103*(39), 14637-14641.
Mu, Q., Heinsch, F. A., Zhao, M., & Running, S. W. (2007). Development of a global evapotranspiration algorithm based on MODIS and global meteorology data. *Remote sensing of Environment*, *111*(4), 519-536.
Mueller, B., Seneviratne, S. I., Jimenez, C., Corti, T., Hirschi, M., Balsamo, G., Ciais, P., Dirmeyer, P., Fisher, J., & Guo, Z. (2011). Evaluation of global observations-based evapotranspiration datasets and IPCC AR4 simulations. *Geophysical Research Letters*, *38*(6).
Nilsson, S., & Schopfhauser, W. (1995). The carbon-sequestration potential of a global afforestation program. *Climatic change*, *30*(3), 267-293.

Niu, X., & Duiker, S. W. (2006). Carbon sequestration potential by afforestation of marginal agricultural land in the Midwestern US. *Forest Ecology and Management*, *223*(1-3), 415-427.
Okia, C. A. (2012). *Global perspectives on sustainable forest management*. BoD–Books on Demand.
Osborne, B. B., Nasto, M. K., Asner, G. P., Balzotti, C. S., Cleveland, C. C., Sullivan, B. W., Taylor, P. G., Townsend, A. R., & Porder, S. (2017). Climate, topography, and canopy chemistry exert hierarchical control over soil N cycling in a Neotropical lowland forest. *Ecosystems*, *20*(6), 1089-1103.
Pelletier, J. D., Barron-Gafford, G. A., Gutiérrez-Jurado, H., Hinckley, E. L. S., Istanbulluoglu, E., McGuire, L. A., Niu, G. Y., Poulos, M. J., Rasmussen, C., & Richardson, P. (2018). Which way do you lean? Using slope aspect variations to understand Critical Zone processes and feedbacks. *Earth Surface Processes and Landforms*, *43*(5), 1133-1154.
Polglase, P., Reeson, A., Hawkins, C., Paul, K., Siggins, A., Turner, J., Crawford, D., Jovanovic, T., Hobbs, T., & Opie, K. (2013). Potential for forest carbon plantings to offset greenhouse emissions in Australia: economics and constraints to implementation. *Climatic change*, *121*, 161-175.
Porder, S., & Hilley, G. E. (2011). Linking chronosequences with the rest of the world: predicting soil phosphorus content in denuding landscapes. *Biogeochemistry*, *102*(1), 153-166.
Reynolds, J. F., Smith, D. M. S., Lambin, E. F., Turner, B., Mortimore, M., Batterbury, S. P., Downing, T. E., Dowlatabadi, H., Fernández, R. J., & Herrick, J. E. (2007). Global desertification: building a science for dryland development. *Science*, *316*(5826), 847-851.
Rotenberg, E., & Yakir, D. (2010). Contribution of semi-arid forests to the climate system. *Science*, *327*(5964), 451-454.
Santos, C. A. G., do Nascimento, T. V. M., & da Silva, R. M. (2020). Analysis of forest cover changes and trends in the Brazilian semiarid region between 2000 and 2018. *Environmental Earth Sciences*, *79*(18), 418.
Sattler, D., Murray, L. T., Kirchner, A., & Lindner, A. (2014). Influence of soil and topography on aboveground biomass accumulation and carbon stocks of afforested pastures in South East Brazil. *Ecological Engineering*, *73*, 126-131.
Schoener, G. (2022). Impact of urbanization and stormwater infrastructure on ephemeral channel transmission loss in a semiarid watershed. *Journal of Hydrology: Regional Studies*, *41*, 101089.
Senay, G., Leake, S., Nagler, P., Artan, G., Dickinson, J., Cordova, J., & Glenn, E. (2011). Estimating basin scale evapotranspiration (ET) by water balance and remote sensing methods. *Hydrological Processes*, *25*(26), 4037-4049.
Seymour, F., & Harris, N. L. (2019). Reducing tropical deforestation. *Science*, *365*(6455), 756-757.
Sharafatmandrad, M., & Khosravi Mashizi, A. (2021). Temporal and spatial assessment of supply and demand of the water-yield ecosystem service for water scarcity management in arid to semi-arid ecosystems. *Water Resources Management*, *35*(1), 63-82.
Simonin, K., Kolb, T., Montes-Helu, M., & Koch, G. (2007). The influence of thinning on components of stand water balance in a ponderosa pine forest stand during and after extreme drought. *Agricultural and forest Meteorology*, *143*(3-4), 266-276.
Stevens-Rumann, C. S., Kemp, K. B., Higuera, P. E., Harvey, B. J., Rother, M. T., Donato, D. C., Morgan, P., & Veblen, T. T. (2018). Evidence for declining forest resilience to wildfires under climate change. *Ecology letters*, *21*(2), 243-252.
Sullivan, P. L., Price, R. M., Ross, M. S., Stoffella, S. L., Sah, J. P., Scinto, L. J., Cline, E., Dreschel, T. W., & Sklar, F. H. (2016). Trees: a powerful geomorphic agent governing the landscape evolution of a subtropical wetland. *Biogeochemistry*, *128*(3), 369-384.
Swetnam, T. L., Brooks, P. D., Barnard, H. R., Harpold, A. A., & Gallo, E. L. (2017). Topographically driven differences in energy and water constrain climatic control on forest carbon sequestration. *Ecosphere*, *8*(4), e01797.
Tai, X., Mackay, D. S., Anderegg, W. R., Sperry, J. S., & Brooks, P. D. (2017). Plant hydraulics improves and topography mediates prediction of aspen mortality in southwestern USA. *New Phytologist*, *213*(1), 113-127.
Van Dijk, A. I., Beck, H. E., Crosbie, R. S., De Jeu, R. A., Liu, Y. Y., Podger, G. M., Timbal, B., & Viney, N. R. (2013). The Millennium Drought in southeast Australia (2001–2009): Natural and human causes and implications for water resources, ecosystems, economy, and society. *Water Resources Research*, *49*(2), 1040-1057.

Van Kooten, G. C., & Bulte, E. H. (2000). *The economics of nature: managing biological assets*.
Vilà-Cabrera, A., Coll, L., Martínez-Vilalta, J., & Retana, J. (2018). Forest management for adaptation to climate change in the Mediterranean basin: A synthesis of evidence. *Forest Ecology and Management*, *407*, 16-22.
Villarino, S. H., Studdert, G. A., Baldassini, P., Cendoya, M. G., Ciuffoli, L., Mastrángelo, M., & Piñeiro, G. (2017). Deforestation impacts on soil organic carbon stocks in the Semiarid Chaco Region, Argentina. *Science of the Total Environment*, *575*, 1056-1065.
Vörösmarty, C. J., McIntyre, P. B., Gessner, M. O., Dudgeon, D., Prusevich, A., Green, P., Glidden, S., Bunn, S. E., Sullivan, C. A., & Liermann, C. R. (2010). Global threats to human water security and river biodiversity. *Nature*, *467*(7315), 555-561.
Wan, Z., Zhang, K., Xue, X., Hong, Z., Hong, Y., & Gourley, J. J. (2015). Water balance‐based actual evapotranspiration reconstruction from ground and satellite observations over the conterminous U nited S tates. *Water Resources Research*, *51*(8), 6485-6499.
Wang, H., Guan, H., Xu, X., Gao, L., Gutiérrez-Jurado, H. A., & Simmons, C. T. (2024). Topographic regulations on ecohydrological dynamics in a montane forest catchment and the implications for plant adaptation to environment. *Journal of Hydrology*, 131412.
Wilson, K. B., & Baldocchi, D. D. (2000). Seasonal and interannual variability of energy fluxes over a broadleaved temperate deciduous forest in North America. *Agricultural and forest Meteorology*, *100*(1), 1-18.
Wilson, K. B., Hanson, P. J., & Baldocchi, D. D. (2000). Factors controlling evaporation and energy partitioning beneath a deciduous forest over an annual cycle. *Agricultural and forest Meteorology*, *102*(2-3), 83-103.
Wilson, S. D., Schlaepfer, D. R., Bradford, J. B., Lauenroth, W. K., Duniway, M. C., Hall, S. A., Jamiyansharav, K., Jia, G., Lkhagva, A., & Munson, S. M. (2018). Functional group, biomass, and climate change effects on ecological drought in semiarid grasslands. *Journal of Geophysical Research: Biogeosciences*, *123*(3), 1072-1085.
Wolf, S., Paul-Limoges, E., Sayler, D., & Kirchner, J. W. (2024). Dynamics of evapotranspiration from concurrent above-and below-canopy flux measurements in a montane Sierra Nevada forest. *Agricultural and forest Meteorology*, *346*, 109864.
Wullschleger, S. D., Hanson, P. J., & Tschaplinski, T. J. (1998). Whole-plant water flux in understory red maple exposed to altered precipitation regimes. *Tree Physiology*, *18*(2), 71-79.
Xu, C., Liu, H., Anenkhonov, O. A., Korolyuk, A. Y., Sandanov, D. V., Balsanova, L. D., Naidanov, B. B., & Wu, X. (2017). Long‐term forest resilience to climate change indicated by mortality, regeneration, and growth in semiarid southern S iberia. *Global change biology*, *23*(6), 2370-2382.
Xu, X., Guan, H., Skrzypek, G., & Simmons, C. T. (2017). Response of leaf stable carbon isotope composition to temporal and spatial variabilities of aridity index on two opposite hillslopes in a native vegetated catchment. *Journal of Hydrology*, *553*, 214-223.
Xu, X., Guan, H., Skrzypek, G., & Simmons, C. T. (2019). Root‐zone moisture replenishment in a native vegetated catchment under Mediterranean climate. *Hydrological Processes*, *33*(18), 2394-2407.
Xu, X., Guan, H., Skrzypek, G., & Williams, D. G. (2022). Topographical influences on foliar nitrogen concentration and stable isotope composition in a Mediterranean-climate catchment. *Ecological informatics*, *68*, 101569.
Yadav, B., Lucieer, A., Jordan, G., & Baker, S. (2022). Using topographic attributes to predict the density of vegetation layers in a wet eucalypt forest. *Australian Forestry*, *85*(1), 25-37.
Yan, C., Xiang, J., Qin, L., Wang, B., Shi, Z., Xiao, W., Hayat, M., & Qiu, G. Y. (2023). High temporal and spatial resolution characteristics of evaporation, transpiration, and evapotranspiration from a subalpine wetland by an advanced UAV technology. *Journal of Hydrology*, *623*, 129748.
Yepez, E. A., Williams, D. G., Scott, R. L., & Lin, G. (2003). Partitioning overstory and understory evapotranspiration in a semiarid savanna woodland from the isotopic composition of water vapor. *Agricultural and forest Meteorology*, *119*(1-2), 53-68.
Yifan, C., Xiaoli, F., Huimin, W., Xiaoqin, D., Liang, K., Fusheng, C., & Wensheng, B. (2020). Effects of understory removal on growth rate of middle-aged Chinese fir with different dbh classes.
Yosef, G., Walko, R., Avisar, R., Tatarinov, F., Rotenberg, E., & Yakir, D. (2018). Large-scale semi-arid afforestation can enhance precipitation and carbon sequestration potential. *Scientific reports*, *8*(1), 996.

Zan, B., Ge, J., Mu, M., Sun, Q., Luo, X., & Wei, J. (2024). Spatiotemporal inequality in land water availability amplified by global tree restoration. *Nature Water*, 1-12.
Zhang, K., Kimball, J. S., Mu, Q., Jones, L. A., Goetz, S. J., & Running, S. W. (2009). Satellite based analysis of northern ET trends and associated changes in the regional water balance from 1983 to 2005. *Journal of Hydrology*, *379*(1-2), 92-110.
Zhang, K., Kimball, J. S., & Running, S. W. (2016). A review of remote sensing based actual evapotranspiration estimation. *Wiley interdisciplinary reviews: Water*, *3*(6), 834-853.
Zhang, X., Adamowski, J. F., Liu, C., Zhou, J., Zhu, G., Dong, X., Cao, J., & Feng, Q. (2020). Which slope aspect and gradient provides the best afforestation-driven soil carbon sequestration on the China's Loess Plateau? *Ecological Engineering*, *147*, 105782.
Zhang, Y., Tariq, A., Hughes, A. C., Hong, D., Wei, F., Sun, H., Sardans, J., Peñuelas, J., Perry, G., & Qiao, J. (2023). Challenges and solutions to biodiversity conservation in arid lands. *Science of the Total Environment*, *857*, 159695.
Zhao, W. Z., Xiao, H. L., Liu, Z. M., & Li, J. (2005). Soil degradation and restoration as affected by land use change in the semiarid Bashang area, northern China. *Catena*, *59*(2), 173-186.

2 GEOSPATIAL MODELLING OF VEGETATION-TOPOGRAPHY RELATIONSHIPS

Abstract

Woodlands play a vital role in global water and carbon cycles but face significant threats from human activities and climate change. Understanding the relationship between topography and vegetation attributes is crucial for the effective management and conservation of these ecosystems, particularly in semi-arid regions where topography strongly influences water availability and microclimate. This study leverages high-resolution airborne remote sensing data, including LiDAR and NDVI, to explore vegetation-topography relationships across multiple spatial scales. By addressing limitations in previous studies, such as low-resolution imagery and pixel-based sampling errors, this research provides a detailed understanding of how topographic factors shape vegetation structure. The findings offer valuable insights for guiding afforestation and reforestation strategies in semi-arid environments, contributing to improved restoration efforts and sustainable woodland management.

2.1 Introduction

Woodlands play important roles in global water and carbon cycle, and its future management is key to international efforts to abate climate change (Coomes et al., 2017). However, they are increasingly threatened by human activities such as deforestation and climate change-induced droughts (Zhao et al., 2005; Huang et al., 2016; Villarino et al., 2017; McPhillips et al., 2019; Khosravi Mashizi & Sharafatmandrad, 2021; Schoener, 2022; Zeratsion et al., 2024; Zhu et al., 2024). To protect and preserve these ecosystems, it is essential to develop and implement effective techniques for measuring, mapping, and monitoring woodland dynamics.

Understanding woodland vegetation attributes is crucial for effective management and conservation efforts. Advanced remote sensing techniques, particularly Light Detection and Ranging (LiDAR), have proven to be highly effective in capturing detailed vegetation structure (Hawbaker et al., 2009; Guo et al., 2017). LiDAR data can be used to derive precise measurements of tree height, crown area, and diameter at breast height (DBH), which are essential for estimating above-ground biomass, a key indicator of carbon storage in woodland ecosystems (Stone & Haywood, 2006; Clark & Schweitzer, 2016; Valbuena et al., 2016). In addition to LiDAR, satellite imagery can provide valuable information on vegetation status through vegetation indices. One of the most commonly used indices is the Normalized Difference Vegetation Index (NDVI), which is calculated using the red and near-infrared bands of the electromagnetic spectrum. NDVI is widely utilized to assess vegetation health, monitor drought conditions, and estimate primary productivity (Ji & Peters, 2003; Nayak et al., 2016; Xie & Fan, 2021; Mehmood et al., 2024). By analysing changes in vegetation attributes over time, researchers

can track the impact of environmental stressors on woodland ecosystems, making it a powerful tool for long-term vegetation monitoring.

However, to fully understand the dynamics of woodland ecosystems, it is essential to explore the relationship between topography and vegetation attributes. Topography, including factors such as elevation, slope, and aspect, significantly influences vegetation distribution, structure, and health (Baudena et al., 2008; Hwang et al., 2011). Modelling the relationship between topography and vegetation is crucial for understanding how the topography induced soil, moisture, nutrition, and microclimate conditions affect vegetation growth. This modelling effort is particularly important in semi-arid woodlands, where water availability and microclimatic conditions are closely linked to topographical variation (Maestre et al., 2016). Understanding these relationships is also crucial for guiding afforestation and reforestation strategies, as topographic factors play a significant role in determining the suitability of species and the success of restoration efforts. For example, Sattler et al. (2014) highlights the complex relationship between aboveground biomass accumulation and topography in South East Brazil. Luo et al. (2021) demonstrates the impact of topography on forest indices within afforestation catchments in the Chinese Loess Plateau. These findings emphasize the importance of further research to deepen our understanding of topography-vegetation interactions, which is vital for improving restoration strategies and ensuring the sustainable management of woodland ecosystems.

Previous studies have explored the relationship between topography and vegetation attributes (Hwang et al., 2011; Elliott et al., 2015; Yang et al., 2020). However, there are notable limitations in the current research. First, many studies rely on low to medium-resolution satellite imagery, which may not capture the fine-scale topographical features that influence vegetation. High-resolution remote sensing data, such as those obtained from airborne platforms, are less commonly used but are crucial for identifying microscale topographical influences on vegetation. Furthermore, the pixel-based sampling method commonly employed in remote sensing can be affected by mixed pixels, where multiple vegetation types or land cover classes are represented within a single pixel (Ferraz et al., 2016; Coomes et al., 2017). This can introduce errors into models, leading to inaccurate predictions of vegetation attributes.

Another issue for spatial analysis of topography-vegetation relationship is the spatial non-stationarity. Traditional regression models, such as ordinary linear regression, generate "global" estimates under the assumption that both the coefficients and intercepts remain constant across the entire study area. However, this assumption can be problematic, as the relationship between environmental variables and remote sensing responses often varies with geographic location (Foody, 2005; Li et al., 2010; Su et al., 2012). When global methods are applied, the accuracy of remote sensing in assessing surface environmental variables can be greatly reduced due to spatial non-stationarity. To effectively address this issue, local techniques like geographically weighted

regression (GWR) offer a more suitable alternative. GWR allows the relationship between variables to vary spatially, providing a more nuanced and precise result.

In this study, we aim to address these gaps by leveraging high-resolution airborne remote sensing data to explore the following key objectives:

1) Evaluating the explanatory power of topography on vegetation attributes across different spatial scales and using both pixel-based and tree-based sampling methods, to identify the scale and method for which vegetation attributes are most responsive to topographical variation.

2) Examining the impact of spatial non-stationarity on the relationships of topography and vegetation.

3) Identifying the main driving factors that control vegetation attributes.

The findings will provide critical insights into how topographic factors influence vegetation structure and offer a foundation for developing targeted afforestation and reforestation strategies in semi-arid regions. By focusing on the nuanced role of topography, this study contributes to advancing vegetation management and restoration efforts tailored to semi-arid environments.

2.2 Methodology

2.2.1 Study area

The study area is a relatively steep vegetated catchment (~0.15 km^2) located at Mount Wilson (138.64° E, 35.21° S) in South Australia (Figure 2.1). The Mount Wilson site characterized as Mediterranean climate, which experiences cold, wet winters (May–July) and hot, dry summers (December–February). The mean annual rainfall and mean annual temperature are around 700 mm and 14 °C according to Australia's Bureau of Meteorology (http://www.bom.gov.au/). The rainfall distribution is highly uneven, with the majority occurring during the winter months and a pronounced dry season in summer. This seasonal imbalance results in periods of significant water deficit, especially during summer, which aligns with characteristics typical of semi-arid environments. The catchment is predominantly covered by native vegetation, with minimal human disturbance. The dominant vegetation species include *Eucalyptus leucoxylon*, *Eucalyptus fasciculosa*, and *Eucalyptus viminalis* (X. Xu et al., 2019). The catchment is characterized by rugged topography, with an average slope of 20 degrees, and features two slopes with contrasting aspects.

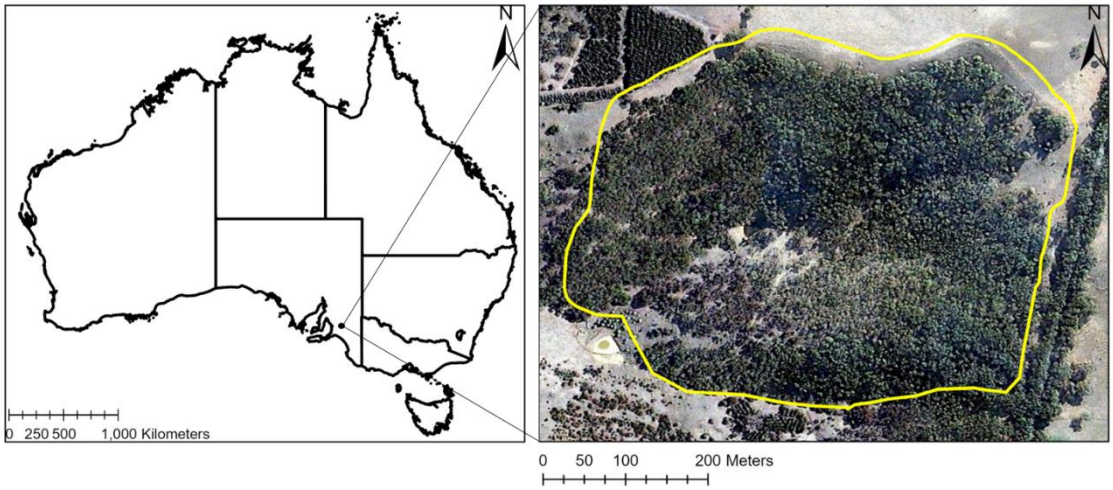

Figure 2.1 Overview of the study areas. Yellow line depicts the study area. The true colour image (20/02/2014) is collected from World Imagery dataset in ARCGIS Pro.

2.2.2 Airborne data collection and processing

2.2.2.1 Data collection

Airborne surveys were conducted by Airborne Research Australia (ARA). A Diamond HK 36 TTC-ECO sailplane was used as the flying platform. The LiDAR survey was conducted on June 16, 2013, using a Riegl Q560 laser scanner. The data were obtained as a discretised point cloud with an average point density of 73 point/m^2. By using the ARCGIS Pro software (https://pro.arcgis.com/), points were classified into ground and non-ground points and the digital terrain model (DTM), digital surface model (DSM), and canopy height model (CHM) were generated at 1, 5, 10 m resolution. For the non-ground points, a two-stage cut-pursuit clustering algorithm was applied to preliminary segment the point cloud into spatial connected clusters (Xi & Hopkinson, 2022), and a manual segment was performed in CloudCompare software (https://www.cloudcompare.org/) to refine the result into individual tree. There is in total 2702 trees been identified in this catchment (Figure 2.2).

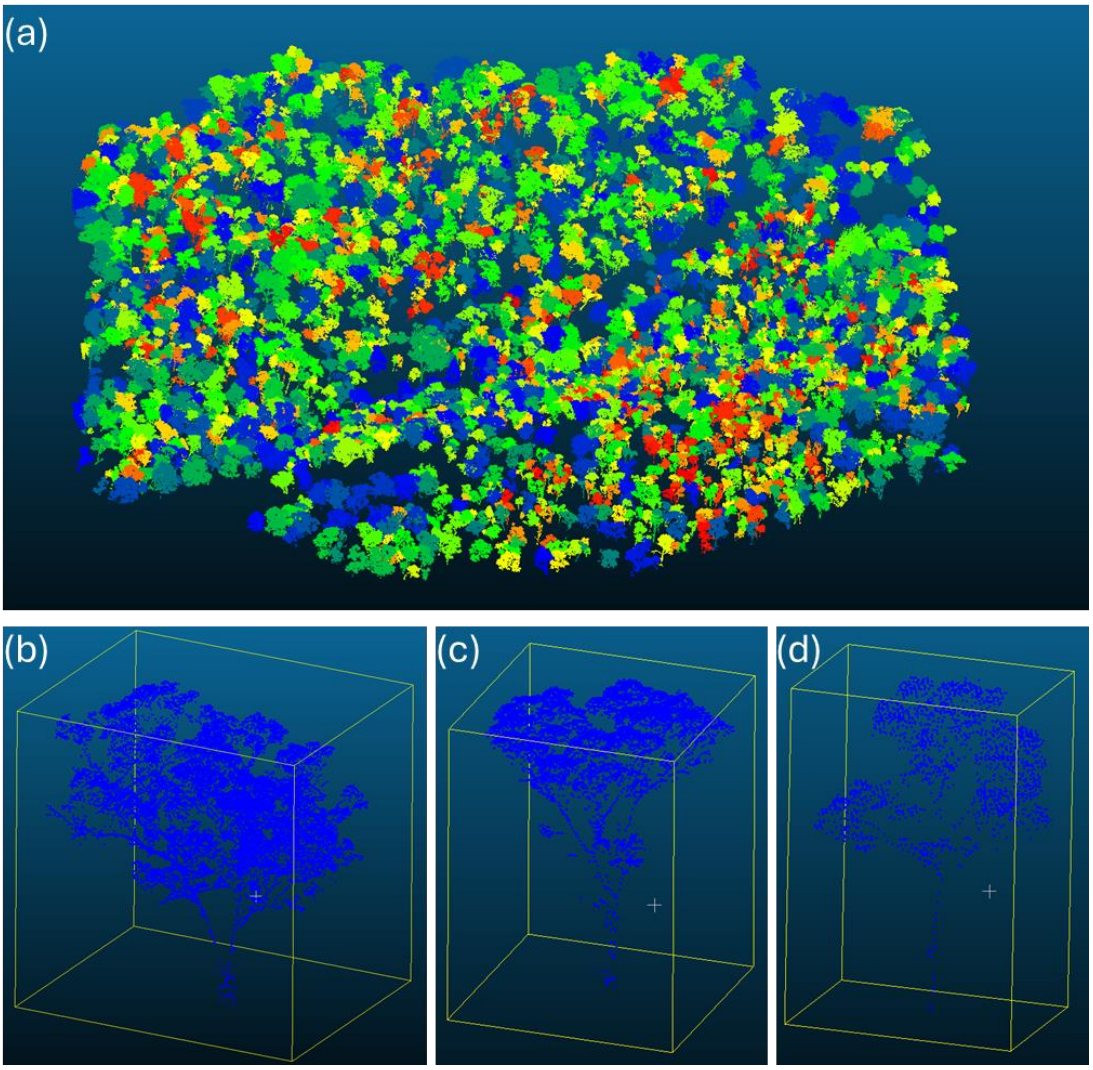

Figure 2.2 Tree segmentation of the study area. (b), (c), and (d) are three examples of identified individual tree.

The hyperspectral data was collected on November 04, 2013, using Specim AISA Eagle 2 VNIR hyperspectral line scanner and Hawk SWIR hyperspectral line scanner for 400-999nm and 1000-2500nm spectral band. The raw data were processed by ARA's specialized team.

2.2.2.2 Variables derivation

In this study, we extracted eight topographic variables from DTM to characterize the terrain attribute. Elevation values were extracted from the DTM as their original grid values. Slope and aspect were calculated using the least squares method (Hengl & Reuter, 2008). Aspect is clockwise in degrees from north (0°) and converted to sine and cosine components to represent east-west (Eastness) and north-south (Northness) orientations (Deng et al., 2007). Mean curvature was calculated to quantify the convexity or concavity of the landscape using the equation given by Zevenbergen and Thorne (1987). A positive mean curvature value indicates a convex surface, such as the top of a hill, while a negative value signifies a concave surface, like a valley. Mean

radiation accounts for the potential solar radiation (kWh/m^2) received by the surface during a year considering the topographic shading, slope facing, and solar elevation. The Topographic Position Index (TPI) used to determine the relative position of each point on the landscape (e.g., ridge or valley). For simplicity, the TPI was calculated use a 15×15 cells moving window for neighbouring searching across different scales. The Topographic Wetness Index (TWI) was calculated to assess soil moisture potential based on slope and upstream contributing area (O'Callaghan & Mark, 1984).

The correlation matrices of topographic variables are calculated at three different resolutions (1m, 5m, and 10m) (Table 2.1-2.3). Overall, most variables exhibit low correlations with each other, but in some cases, such as northness and radiation, the correlations are relatively high (with correlation coefficients of 0.83, 0.84, and 0.86 at different resolutions). Despite the high correlation between northness and radiation, both variables were retained because they each represent distinct and crucial aspects of the terrain (Deng et al., 2007). Northness directly captures the terrain's orientation, which is vital for understanding directional influences on vegetation and microclimate. On the other hand, radiation is a key factor in determining surface energy balance and microclimate conditions, influencing processes like evapotranspiration and soil moisture retention (Ďuračiová & Pružinec, 2022). By including both variables, we ensure a more nuanced analysis of how topography affects ecological processes, allowing us to better understand the interplay between terrain orientation, solar exposure, and their combined effects on vegetation patterns and ecosystem dynamics.

Table 2.1 Correlation matrix of topography variables (1m)

	Elevation	Slope	Eastness	Northness	Curvature	Radiation	TWI
Slope	-0.35						
Eastness	-0.26	0.21					
Northness	-0.02	-0.02	-0.45				
Curvature	0.05	0.00	0.01	0.00			
Radiation	0.21	-0.46	-0.54	0.83	0.02		
TWI	0.01	-0.24	-0.03	-0.03	-0.09	0.08	
TPI	0.25	-0.07	0.00	0.01	0.43	0.09	-0.23

Table 2.2 Correlation matrix of topography variables (5m)

	Elevation	Slope	Eastness	Northness	Curvature	Radiation	TWI
Slope	-0.36						
Eastness	-0.29	0.31					
Northness	-0.01	-0.04	-0.48				
Curvature	0.20	0.03	0.00	0.01			
Radiation	0.21	-0.46	-0.56	0.84	0.06		
TWI	-0.13	-0.33	-0.14	0.00	-0.51	0.10	
TPI	0.49	-0.18	-0.01	0.02	0.56	0.18	-0.46

Table 2.3 Correlation matrix of topography variables (10m)

	Elevation	Slope	Eastness	Northness	Curvature	Radiation	TWI
Slope	-0.33						
Eastness	-0.28	0.33					
Northness	-0.01	-0.04	-0.49				
Curvature	0.28	0.05	-0.01	0.01			
Radiation	0.21	-0.43	-0.56	0.86	0.08		
TWI	-0.22	-0.41	-0.16	0.00	-0.64	0.10	
TPI	0.41	-0.05	0.00	0.02	0.88	0.15	-0.62

For pixel-based analysis, four vegetation attribute variables were derived: tree height, NDVI, leaf area index (LAI), and tree density. Tree height was extracted from the canopy height model (CHM), which is the difference between LiDAR derived DTM and DSM. The CHM was smoothed with a low pass filter to remove the sharp changes in height within crowns (Coomes et al., 2017). NDVI was calculated using Equation 2.1 based on the hyperspectral imagery (Tucker, 1979). LAI is an indicator of vegetation canopy density, representing the total one-sided green leaf area per unit ground surface area. The LAI was estimated from LiDAR based on the Beer-Lambert law (Equation 2.2) (Wang & Fang, 2020). Tree density was calculated using kernel density tool in ARCGIS Pro software.

$$NDVI = \frac{NIR - Red}{NIR + Red} \tag{2.1}$$

$$LAI = -\frac{1}{k}\ln(N_{ground}/N_{total}) \tag{2.2}$$

where Red and NIR stand for the spectral reflectance measurements acquired in the red (640-670 nm) and near-infrared (850-880 nm) bands. N_{ground} is the count of LiDAR return points from the ground level, N_{total} is the total count of return LiDAR points, and k is the extinction coefficient.

For tree-based analysis, the tree height was calculated based on the point cloud of each tree segment. NDVI and LAI were derived using the geometric centroid of each tree segment and the corresponding NDVI and LAI maps at different resolutions. Crown volume of trees was calculated using a voxel-based approach applied to point cloud data (Phattaralerphong & Sinoquet, 2005). Although the tree trunks were also included in the calculations, their contribution to the overall volume is minimal and can be considered negligible for the purpose of this analysis.

2.2.3 Regression methods

To explore the relationships between vegetation attributes and potential topographic variables, both linear and non-linear regressions were analysed. For the linear model, stepwise linear regression (SLR) was employed (Draper, 1998). A bidirectional method, including forward selection and backward elimination, was used to refine the model (Wang et al., 2016). The statistical significance of the final regression model was evaluated using an F-test, where variables were included at a significance level of 0.05 and excluded at 0.1. The coefficient of determination (R^2) and adjusted R^2 were calculated for model evaluation. R^2 indicates the proportion of variance in the dependent variable explained by the selected predictors and adjusted R^2 accounts for additional model complexity, which can be used for model comparison between different sampling methods.

Multiscale Geographically Weighted Regression (MGWR) model was employed to analyse the potential spatial non-stationarity relationship between topography and vegetation attributes. MGWR is an improved version of the GWR model. Unlike GWR, which has a single optimal bandwidth for all variables, MGWR allows each variable to have its own spatial smoothing level. This flexibility overcomes the limitations of GWR by allowing each variable to have its own distinct bandwidth. The model formula is as follows:

$$y_i = \beta_0(u_i, v_i) + \sum_{k=1}^{K} \beta_k(u_i, v_i)\, x_{ik} + \varepsilon_i \tag{2.3}$$

Where x_i and y_i *are* the independent and dependent variable at location *i*. (u_i,v_i) are the coordinates of location *i*, β_0 and β_k are the intercept and coefficient. *K* is the number of independent variables and ε_i is the error term. The golden section search algorithm based on Akaike information criterion minimization is used for variables bandwidth optimization (Fotheringham et al., 2009).

Random forest (RF) regression was applied to identify the potential non-linear relationships between topography variables and vegetation attributes. RF regression is a machine learning technique that uses an ensemble of decision trees to make predictions. Each tree in the forest is trained on a random subset of the data, and the final prediction is made by averaging the predictions of all the trees. This method helps to reduce overfitting and improves the model's accuracy by capturing a wide range of patterns in the data. Random forest regression is particularly effective when dealing with complex datasets with many variables. To ensure optimal model performance, hyperparameter tuning was conducted on the training set using a comprehensive grid search strategy coupled with cross-validation. The hyperparameters targeted for optimization included the number of decision trees, the maximum depth of the trees, the

minimum number of samples required for a split, and the minimum number of samples required at a leaf node.

Shapley additive explanations (SHAP) was used to interpret RF regression models by quantifying the contribution of each feature to the model's predictions (Lundberg & Lee, 2017). Unlike traditional feature importance methods, SHAP values are based on game theory and provide a unified measure that fairly attributes the impact of each feature on the model's output, regardless of the feature interactions. By assigning each feature an importance score, SHAP allows for a more nuanced understanding of how individual variables influence the model's predictions. Partial dependence plot (PDP) was used to visualize the relationship between specific features and the model's predicted outcomes, allowing for the interpretation of how changes in these features influence predictions while accounting for the effects of other variables (Goldstein et al., 2015).

2.2.4 Spatial cluster analysis

Anselin Local Moran's I (LMI) was employed to identify statistically significant spatial clusters and outliers within the study area (Anselin, 1995). For each sample of the input vegetation attributes, the LMI value, z-score, and pseudo p-value were calculated. A positive LMI value indicates that the sample shares similar high or low attribute values with its neighbouring samples, while a negative LMI value indicates that the sample and its neighbouring samples have dissimilar values. The z-scores and pseudo p-values help determine the statistical significance of these clusters and outliers. Four types of spatial patterns can occur: high-high (HH), low-low (LL) clusters, and high-low (HL), low-high (LH) outliers. The analysis was conducted using the Cluster and Outlier Analysis tool in ARCGIS Pro software. The spatial relationships were modelled based on inverse Euclidean distance, and spatial weights are standardized to mitigate potential bias from an uneven distribution of spatial neighbours.

To evaluate the differences of topographical variables between clustered variables, we employed the Mann-Whitney U test, a non-parametric test suitable for comparing two independent samples when the data does not follow a normal distribution (Fay & Proschan, 2010). The 0.01 significance level was adopted in this study. The rank-biserial correlation was calculated as a measure of effect size. It evaluates the magnitude of the difference between clusters. The effect sizes were interpreted according to Cohen's guidelines: Small to moderate differences ($0.1 \leqslant |\text{effect size}| < 0.5$) suggest limited practical significance. Large differences ($|\text{effect size}| \geqslant 0.5$) suggest substantial practical significance (Cohen, 1988).

2.3 Results and Discussion

2.3.1 Scale and sample method comparison

Table 2.4 and 2.5 present the regression results for tree height, NDVI, LAI, tree density, and crown volume across different scales (1 m, 5 m, and 10 m), with R^2 and adjusted R^2 values provided. The results indicate that only tree height and NDVI achieve relatively strong linear relationships with topographic factors, whereas LAI, tree density, and crown volume show much weaker correlations. Besides, the 5-m and 10-m sampling methods show significant improvements over the 1-m scale, suggesting that vegetation attributes are more sensitive to terrain data when aggregated over 5-10 meters. This is likely because larger sampling scales smooth out local variations and noise, allowing a more consistent relationships between topography and vegetation attributes.

Comparing the adjusted R^2 values, it is evident that the regression performance improves significantly with the tree-based sampling method compared to the pixel-based method. Coomes et al. (2017) shows that tree-based method is less accurate at estimating aboveground carbon density than the best-performing area-based model due to the inaccurate detection of individual tree. However, they still consider the tree-based method to be a promising approach. Our result here supports Coomes's idea that the tree-based sampling is similar to well-established field-based approaches for vegetation attributes measurement.

Table 2.4 Accuracy of the SLR models based on pixel samples

Vegetation attributes	1 m		5 m		10 m	
	R^2	Adj R^2	R^2	Adj R^2	R^2	Adj R^2
Tree height	0.24	0.24	0.31	0.31	0.31	0.31
NDVI	0.27	0.27	0.32	0.32	0.40	0.40
LAI	0.03	0.03	0.04	0.04	0.04	0.04
Tree density	0.11	0.11	0.15	0.14	0.14	0.13

Table 2.5 Accuracy of the SLR models based on tree samples

Vegetation attributes	1 m		5 m		10 m	
	R^2	Adj R^2	R^2	Adj R^2	R^2	Adj R^2
Tree height	0.34	0.33	0.42	0.42	0.42	0.42
NDVI	-	-	0.47	0.46	0.55	0.55
LAI	0.05	0.04	0.08	0.07	0.07	0.06
Crown volume	0.01	0.01	0.02	0.02	0.02	0.02

2.3.2 Linear and non-linear models testing results

Data derived from tree-based sample at the 5-m scale were used as input as it is proved to have better performance in section 2.3.1. Although the 10-m data exhibited enhanced performance in the SLR, the limited sample size at this resolution made it suboptimal for the RF regression, which is designed to handle larger datasets efficiently. Two data selection methods are applied: for random sampling, the whole dataset was randomly divided into training and testing subsets with an equal split (1:1 ratio). For spatial block sampling, the input data was spatially divided into training and testing sets to assess the model's spatial generalizability.

Table 2.6 shows the training and testing results of the SLR and RF regression. For the random sample test, the RF regression model performed well on the training set for all vegetation attributes, with R^2 values exceeding 0.8. However, the model's performance declined on the testing set, which is indicative of overfitting. Overfitting occurs when the model becomes too complex and starts to capture noise rather than the underlying data distribution (Meyer et al., 2018). The SLR achieves lower R^2 on the training set. However, it maintained a more consistent performance between the training and testing sets, suggesting that the SLR model was less sensitive to noise. This consistency highlights that while the SLR may not capture the complexity of the relationships between variables as effectively as the RF model, it avoids the risk of overfitting, leading to more stable predictions. Ultimately, the results indicate that both models performed similarly on the testing set, despite their differences in complexity.

For the spatial block test, the testing R^2 values dropped significantly for the RF regression model, suggesting that the model struggled to generalize when it is applied to new spatial areas. This

suggests that while the RF model can capture patterns within a specific spatial region, its ability to predict vegetation attributes across different spatial areas is limited. Similarly, the spatial block sampling has been conducted for the SLR. The testing R^2 values also showed a noticeable decline compared to the training R^2, when compared with the random sample test. The results from the spatial block test highlight that the relationship between vegetation attributes and topography in this watershed is not stationary and exhibits significant spatial heterogeneity.

These findings indicate that when using a global model to assess the influence of topography on vegetation attributes, both SLR and RF regression effectively explain tree height and NDVI (~34% for tree height and ~49% for NDVI in the testing set). However, the significant drop in testing accuracy compared to training accuracy for RF regression (a reduction of 56% for tree height and 39% for NDVI) suggests that the model suffers from overfitting. This implies that the simpler SLR model performs comparably to Random Forest in capturing vegetation-topography relationships, highlighting the need for caution when applying machine learning methods to spatial analysis.

When the objective is for spatial prediction, the predictive capabilities of both methods are less satisfactory (~20% for tree height and ~30% for NDVI) compared to their strong performance on the training set. This disparity underscores the presence of considerable spatial non-stationarity in the relationship between topography and vegetation attributes. Further investigation is required to incorporate spatial patterns in the data, which could lead to a more nuanced understanding and improved modelling of this relationship.

Table 2.6 Model training and testing result of SLR and RF regression (LAI and CV are not shown metrics not included due to poor model interpretability)

	Vegetation attributes	Randon sample		Spatial block sample	
		Training R^2	Testing R^2	Training R^2	Testing R^2
SLR	Tree Height	0.36	0.35	0.40	0.23
	NDVI	0.46	0.45	0.34	0.30
RF regression	Tree Height	0.89	0.33	0.89	0.21
	NDVI	0.92	0.53	0.91	0.31

2.3.3 Controlling factors analysis results

2.3.3.1 Linear regression results

The coefficients for the topographic factors in predicting tree height and NDVI provide insights into the relationship between these topographical variables and vegetation attributes (Table 2.7).

According to the SLR model, the most influential factor for tree height is TPI, with a negative coefficient (-0.359, explaining 37.7% of the variance), indicating that higher topographic positions, which are more exposed and less able to retain moisture, tend to have shorter trees. Northness also plays a significant role, which shows a significant negative correlation (-1.612, explaining 31.9% of the variance). This suggests that north-facing slopes, which receive more direct and intense sunlight throughout the day in the Southern Hemisphere, may experience higher evapotranspiration demands and increased water stress, potentially leading to reduced tree height. Elevation is also an influential factor, with a negative coefficient (-0.019, explaining 14.3% of the variance). Elevation reflects the overall height variation across the catchment, indicating that areas with higher elevation within the catchment tend to have shorter trees. Eastness and TWI also contribute marginally to the model, with eastness showing a positive correlation (0.545, explaining 8.7% of the variance) and TWI a positive correlation (0.163, explaining 7.4% of the variance). Eastness suggests that east-facing slopes, which receive gentler morning sunlight, create a more favourable environment for tree growth, resulting in taller trees. TWI indicates that areas with higher water accumulation support taller trees due to the increased availability of water.

For NDVI, eastness is the most significant variable, with a positive correlation (0.062, explaining 23.5% of the variance). Slope is the next most influential factor, showing a negative correlation (-0.005, explaining 21.0% of the variance), suggesting that steeper slopes might experience more soil erosion and water runoff, reducing vegetation density. Similar to tree height, NDVI shows negative correlation with both TPI (-0.008, explaining 19.7% of the variance) and northness (-0.042, explaining 19.4% of the variance). The influence of radiation and elevation are relatively small. Northness could already explain most of the radiation related variation of NDVI.

Table 2.7 Coefficients and variable contributions of SLR

Vegetation attributes	Coefficients								
	Elevation	Slope	Eastness	Northness	Curvature	Radiation	TWI	TPI	Constant
Tree Height	-0.019 (14.3%)	-	0.545 (8.7%)	-1.612 (31.9)	-	-	0.163 (7.4%)	-0.359 (37.7%)	17.157
NDVI	4.060×10^{-4} (7.3%)	-0.005 (21.0%)	0.062 (23.5%)	-0.042 (19.4%)	-	-7.730×10^{-5} (9.1%)	-	-0.008 (19.7%)	0.773

Table 2.8 shows the results of MGWR model for tree height and NDVI. The significant rate tells the percentage of the local models in which the variable is significant. The results suggest that accounting for spatial heterogeneity can lead to more accurate models compared to using a global SLR model (Table 2.5). For the tree height model, the result consists well with the SLR model, with the most significant variables to be TPI and northness. Figure 2.3 (a), (b) show the coefficient distribution of TPI and northness. Consistent with the results in Table 2.7, the MGWR model shows that TPI and northness are negatively correlated with tree height.

For explaining NDVI spatial variability, TPI, northness, elevation, and eastness are significant variables in the MGWR model, with a significance rate above 40%. Figure 2.6 (c)-(f) show the coefficients of topographical variables. The variable importance and the signs of the regression coefficients for TPI, northness, and eastness are similar to those in the SLR model. In Figure 2.6 (e), It is worth noting that the relationship between NDVI and elevation is strongly influenced by elevation itself, that in low elevation region, NDVI is negatively correlated with elevation, and in high elevation region, it turns to be positive correlation. The spatial non-stationarity observed in the relationship between elevation and NDVI helps explain the relatively insignificant contribution of elevation in SLR model. This suggests that, at the tree level, the influence of elevation on NDVI differs from that of other variables. The contrasting trends indicate that the effect of elevation on NDVI is not solely related to controlling water flow direction. Instead, it may also be associated with other factors such as wind speed, soil properties, and microclimatic conditions, which vary with elevation and impact NDVI across different regions.

Table 2.8 Statistical description of MGWR model coefficient. Radiation and mean curvature are excluded in MGWR model as the model is sensitive to multicollinearity

	Tree height				NDVI			
Variables	Mean	Min	Max	Sig. rate (%)	Mean	Min	Max	Sig. rate (%)
Elevation	-0.05	-0.63	0.32	5.34	0.17	-0.45	1.04	51.42
Slope	0.01	-0.22	0.41	9.73	-0.07	-0.42	0.15	16.90
Eastness	0.05	-0.36	0.88	9.34	0.21	-0.27	0.92	41.63
Northness	-0.25	-0.55	0.08	55.48	-0.27	-0.67	0.19	65.04
TWI	0.01	0.00	0.02	0	0.02	0.01	0.02	0
TPI	-0.38	-0.59	-0.11	87.16	-0.28	-0.60	-0.03	84.49
R^2			0.52		R^2		0.60	

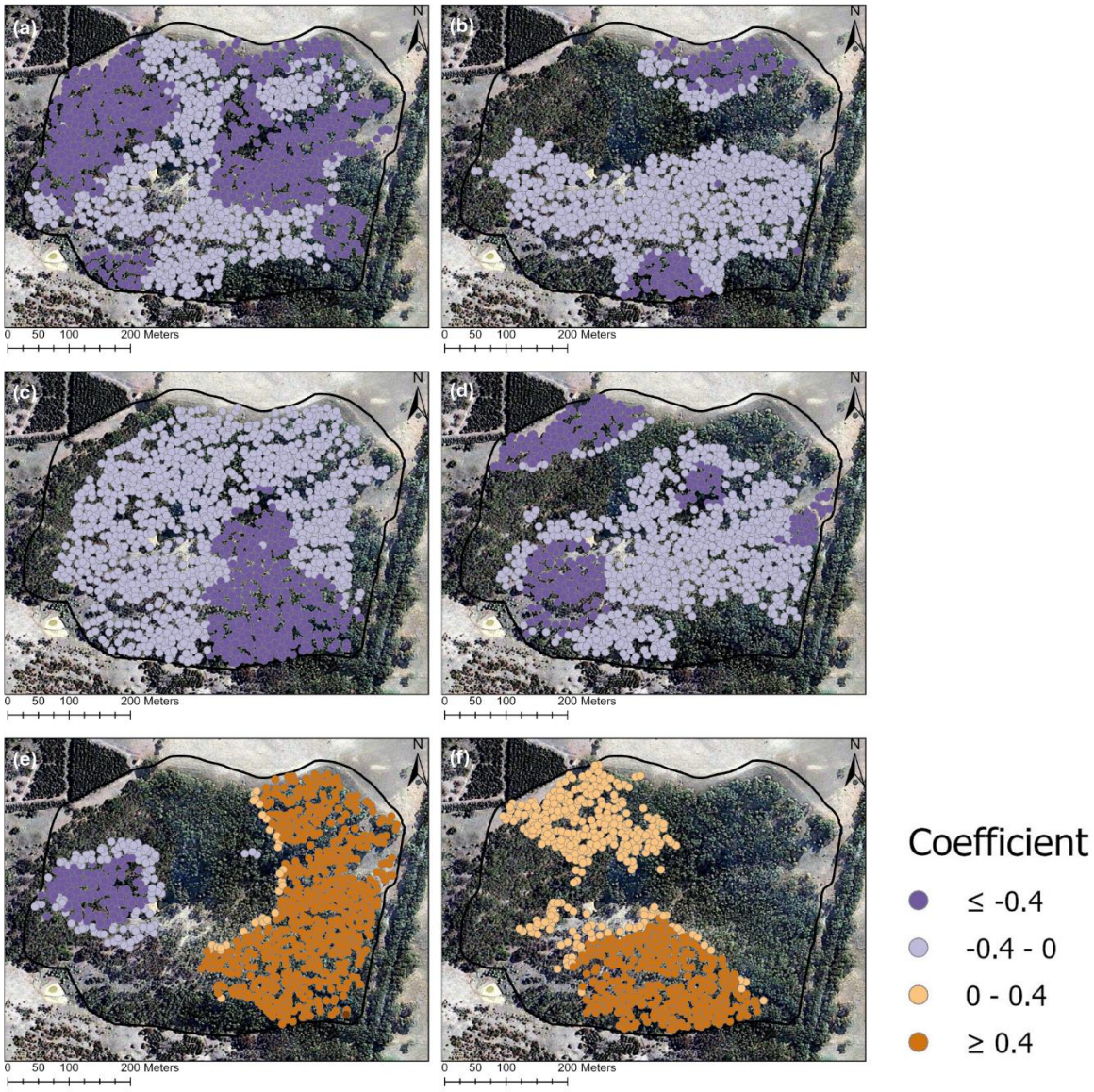

Figure 2.3 Spatial distribution of scaled coefficients. (a) and (b) show the coefficients of TPI and northness for tree height. (c) - (f) show the coefficients of TPI, northness, elevation, and eastness for NDVI (Variables with significance rates below 20% are not shown).

2.3.3.2 Spatial clustering and RF regression results

Figure 2.4 shows spatial clustering of four vegetation attributes. The clusters are identified using LMI, which highlights areas with significant spatial aggregation of HH and LL values. The HL and LH outlier account for a minimal proportion and were excluded from the analysis. Tree Height and NDVI exhibit very similar spatial pattern, with LL clusters predominantly on northwest-facing slopes and HH clusters on southeast-facing slopes. The spatial patterns for LAI and Crown Volume are less distinct.

Figure 2.5 presents a detailed comparison of topographic variables between HH and LL clusters. Each row corresponds to a different attribute. The effect size from the Mann–Whitney test is displayed, which quantify the differences between groups. For tree height and NDVI, all

topographic variables show significant differences between the HH and LL clusters (p-value < 0.01). Tree height, in particular, displays large differences in elevation, northness, eastness, radiation, TWI, and TPI. Similarly, NDVI also shows large differences in northness, eastness, and radiation, underscoring the importance of slope orientation and sunlight exposure on vegetation growth and health. In contrast, for LAI and crown volume, although some topographic variables show significant differences between clusters, the effect sizes are generally low to moderate. This suggests that topography has a less pronounced influence on these attributes.

Figure 2.4 Spatial distribution of High-High and Low-Low clusters of vegetation attributes based on the LMI analysis.

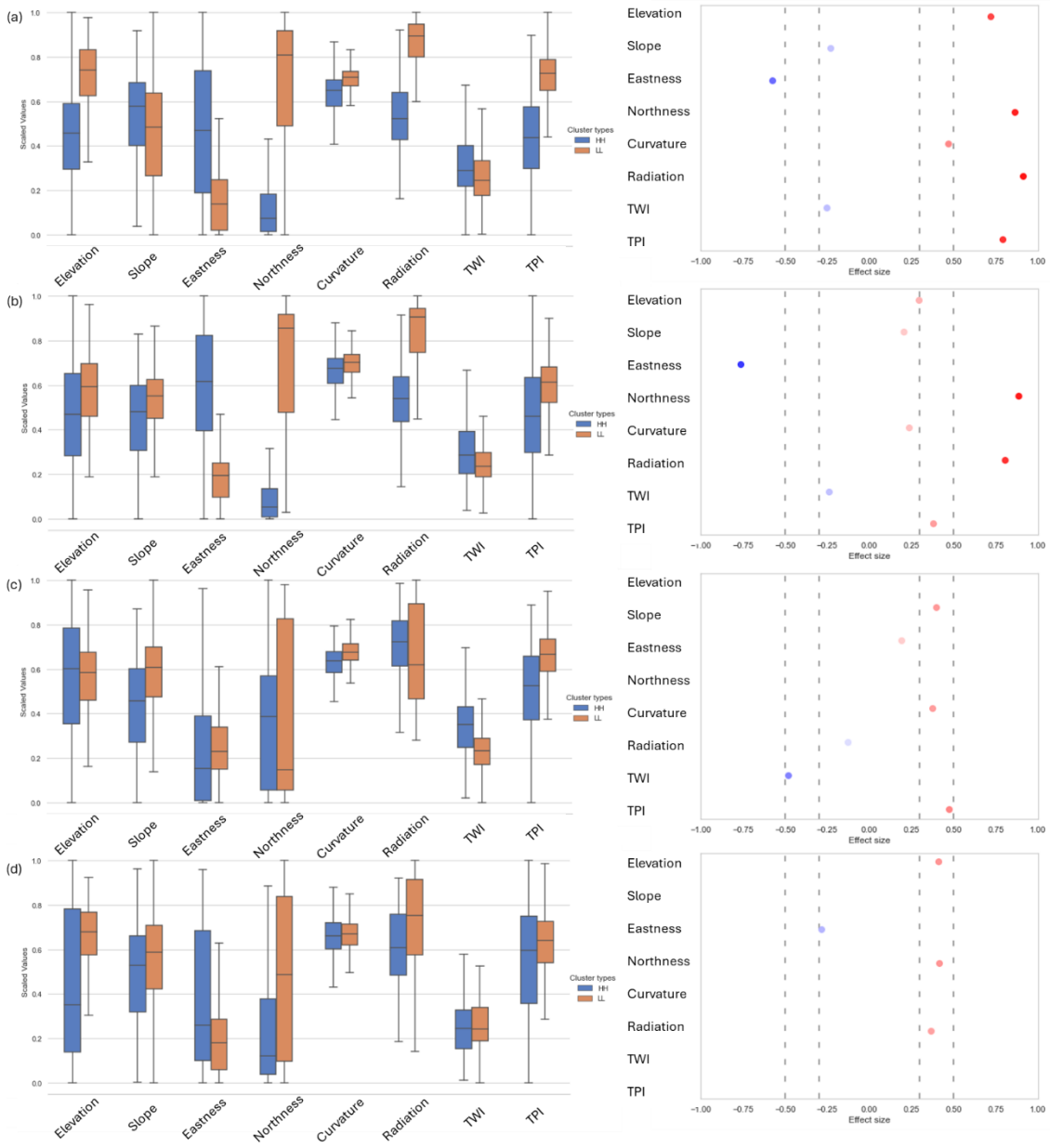

Figure 2.5 Boxplots of spatial clustered topographical factors according to different vegetation attributes ((a)-(d) are tree height, NDVI, LAI, and crown volume). The right side are the corresponding effect size of statistic test (no significant variables are not shown).

Spatially clustered significant data were used as inputs for the RF model to reduce potential noise. The results indicate that the R^2 values for tree height and NDVI on the training set were 0.86 and 0.87, respectively, while on the testing set, they reached 0.62 and 0.71. This suggests that spatial clustering can effectively reduce underlying noise in the variables.

PDP for the top four most important variables, based on SHAP importance, are shown in Figures 2.6 and 2.7. The results demonstrate that for tree height, TPI, northness, and eastness have a notable influence. TPI emerged as the most significant factor in the model, with a nearly linear negative correlation. The PDP for northness and eastness show that tree height is generally lower

on north-facing and west-facing slopes. This relationship is not strictly linear, with the most significant changes occurring in the mid-range of the gradient. For NDVI, northness and eastness exert the strongest influence. The gradient from south to north shows that NDVI remains higher within the slope aspect range of 120 to 240 degrees. Regarding east-west slope orientation, NDVI tends to stay elevated as long as the slope faces no more than 30 degrees westward.

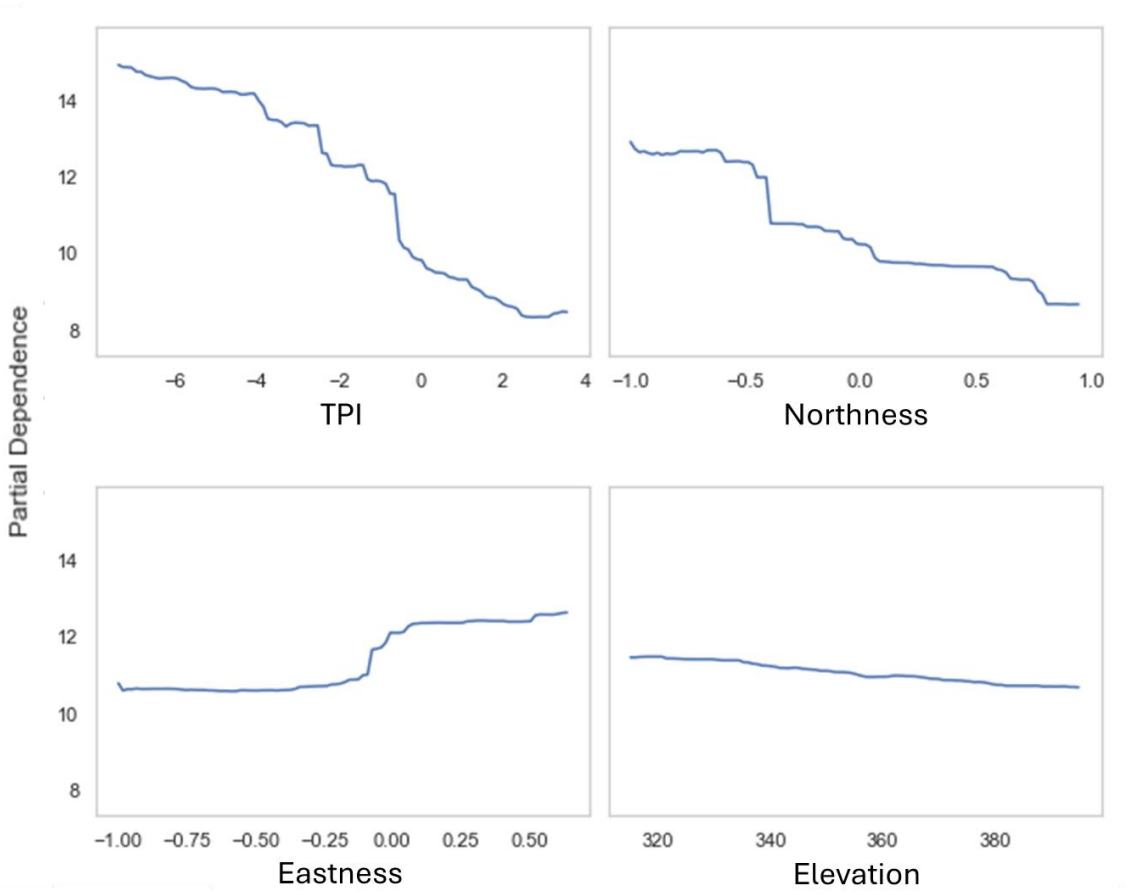

Figure 2.6 Partial dependence plot between tree height and topographical factors. The plots are ranked based on SHAP importance, with the top four variables presented.

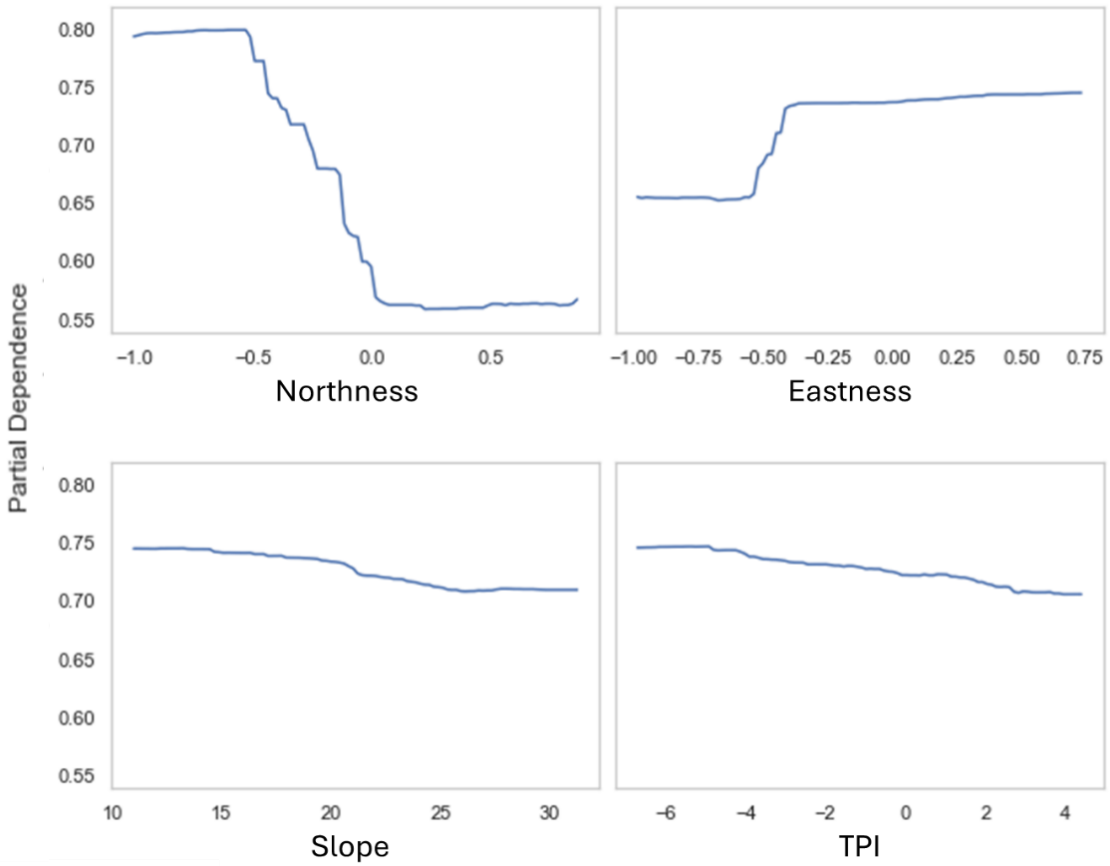

Figure 2.7 Partial dependence plot between NDVI and topographical factors. The plots are ranked based on SHAP importance, with the top four variables presented.

In summary, for tree height, the SLR, MGWR, and RF regression consistently identify the same controlling factors: TPI and northness. This indicates that tree height is primarily influenced by local water convergence and the amount of direct solar radiation. For NDVI, both SLR and RF highlight that northness, eastness, slope, and TPI are the most influential factors. This suggests that, at the tree scale, NDVI is more sensitive to soil moisture conditions, which are significantly affected by these factors. MGWR also shows a high impact of TPI, northness, and eastness on NDVI but reveals the spatial non-stationarity of the relationship between topographical factors and NDVI. TWI is not significant in all models, indicating that, at the scale of this study, tree height and NDVI are not necessarily related to the water flow path.

No significant linear or non-linear relationships were found between topographical factors and LAI, suggesting that the factors influencing the spatial heterogeneity of LAI vary with species composition and forest type. This is consistent with findings from other studies; for instance, Bequet et al. (2012) reported that the spatial variability of LAI was linked to the diameter at breast height (DBH) of large trees (DBH > 30 cm) across different forest types. These observations suggest that plant functional types, such as life-history stages or size classes, are likely connected to LAI's spatial heterogeneity. Zhu et al. (2016) indicates that small-scale variability in LAI within

Chinese subtropical forests is primarily governed by factors like stem number, crown coverage, species composition (proportion of evergreen coniferous and deciduous species), and forest type, with these factors changing seasonally. Liu et al. (2018) conducted research in temperate forests, demonstrating that LAI is shaped by a combination of biotic and abiotic factors, such as tree density, species composition, crown coverage, soil temperature, and soil moisture content.

For the crown volume, existing literature indicates that tree growth experiments across different density and competition levels show that tree height growth remains relatively stable across a wide range of stand densities, from solitary trees to dense stands. In contrast, tree crown and stem diameter growth are highly sensitive to competition (Pretzsch et al., 2015). Compared to the influence of topography, crown volume is more strongly affected by competition among trees.

2.4 Conclusion

This study has provided a comprehensive analysis of the relationships between vegetation attribute and fine-scale topographical factors in a semi-arid woodland environment. By employing both linear and non-linear regression methods, including SLR, MGWR, and RF regression, this research has illuminated the critical role of topography in influencing vegetation structure.

1) The results demonstrate that vegetation attributes are particularly sensitive to topographical factors at the 5-10m scale, with tree height and NDVI showing the strongest relationships. The tree-based sampling method used in this study proved to be more effective than traditional pixel-based methods, capturing the spatial variability of vegetation attributes more accurately and leading to more reliable models.
2) The study also highlighted the significance of spatial non-stationarity in modelling vegetation attributes, especially for relationship between topographic factors and NDVI. Compared to global models, the MGWR model not only shows a significant improvement in explanatory power but also identifies influential variables that may be overlooked due to spatial non-stationarity. Our results also indicate that when there is spatial non-stationarity in the data, the accuracy of both SLR and RF regression is significantly affected, with RF being more prone to overfitting due to noise. Therefore, we recommend using simpler linear models or applying noise removal before employing machine learning models to minimize model errors.
3) Key driving factors for vegetation attributes were identified: TPI and northness significantly influence tree height, while northness, eastness, slope, and TPI significantly influence NDVI. TPI, in particular, was found to have a nearly linear negative correlation with tree height, while slope orientation (northness and eastness) was crucial for both tree height and NDVI, reflecting the importance of sunlight exposure and microclimatic conditions. For LAI, tree density, and crown volume, no direct relationship with topography was evident at tree level scales.

Beyond the descriptive findings, this research offers a foundation for optimizing afforestation and reforestation strategies in semi-arid woodlands by leveraging the relationships between topography and vegetation attributes. The strong correlation between tree height and TPI suggests that areas with lower TPI values, such as valleys, could be prioritized for planting taller tree species to maximize productivity in water-accumulating zones, while areas with higher TPI (hills) may require drought-resistant species adapted to lower water availability. Similarly, the importance of northness and eastness highlights the role of slope orientation in determining vegetation structure. Afforestation on south-facing slopes (in the semi-arid regions of the southern hemisphere) is more efficient, as the reduced water stress creates optimal conditions for the growth, while east-facing slopes might support tree growth due to morning insolation and cooler microclimates. The study's demonstration of the spatial non-stationarity in NDVI-topography relationships, as captured by the MGWR model, suggesting that planting strategies should consider localised conditions rather than relying solely on broad-scale patterns. By integrating these findings, afforestation and reforestation efforts can be tailored to enhance vegetation establishment and resilience in semi-arid environments.

The findings of this research have important implications for the management and conservation of semi-arid woodlands. By enhancing our understanding of how topography influences vegetation attributes, this study contributes to more informed and effective strategies for afforestation, reforestation, and the broader goal of maintaining healthy and resilient woodland ecosystems.

2.5 References

Anselin, L. (1995). Local indicators of spatial association—LISA. *Geographical analysis*, *27*(2), 93-115.

Baudena, M., d'Andrea, F., & Provenzale, A. (2008). A model for soil‐vegetation‐atmosphere interactions in water‐limited ecosystems. *Water Resources Research*, *44*(12).

Bequet, R., Campioli, M., Kint, V., Muys, B., Bogaert, J., & Ceulemans, R. (2012). Spatial variability of leaf area index in homogeneous forests relates to local variation in tree characteristics. *Forest Science*, *58*(6), 633-640.

Clark, S. L., & Schweitzer, C. J. (2016). Stand dynamics of an oak woodland forest and effects of a restoration treatment on forest health. *Forest Ecology and Management*, *381*, 258-267.

Cohen, J. (1988). Differences between correlation coefficients. *Statistical power analysis for the behavioral sciences*.

Coomes, D. A., Dalponte, M., Jucker, T., Asner, G. P., Banin, L. F., Burslem, D. F., Lewis, S. L., Nilus, R., Phillips, O. L., & Phua, M.-H. (2017). Area-based vs tree-centric approaches to mapping forest carbon in Southeast Asian forests from airborne laser scanning data. *Remote sensing of Environment*, *194*, 77-88.

Deng, Y., Chen, X., Chuvieco, E., Warner, T., & Wilson, J. P. (2007). Multi-scale linkages between topographic attributes and vegetation indices in a mountainous landscape. *Remote sensing of Environment*, *111*(1), 122-134.

Draper, N. (1998). *Applied regression analysis*. McGraw-Hill. Inc.

Ďuračiová, R., & Pružinec, F. (2022). Effects of terrain parameters and spatial resolution of a digital elevation model on the calculation of potential solar radiation in the mountain environment: A case study of the Tatra mountains. *ISPRS International Journal of Geo-Information*, *11*(7), 389.

Elliott, K. J., Miniat, C. F., Pederson, N., & Laseter, S. H. (2015). Forest tree growth response to hydroclimate variability in the southern Appalachians. *Global change biology*, *21*(12), 4627-4641.

Fay, M. P., & Proschan, M. A. (2010). Wilcoxon-Mann-Whitney or t-test? On assumptions for hypothesis tests and multiple interpretations of decision rules. *Statistics surveys*, *4*, 1.

Ferraz, A., Saatchi, S., Mallet, C., & Meyer, V. (2016). Lidar detection of individual tree size in tropical forests. *Remote sensing of Environment*, *183*, 318-333.

Foody, G. M. (2005). Mapping the richness and composition of British breeding birds from coarse spatial resolution satellite sensor imagery. *International Journal of Remote Sensing*, *26*(18), 3943-3956.

Fotheringham, A. S., Brunsdon, C., & Charlton, M. (2009). Geographically weighted regression. *The Sage handbook of spatial analysis*, *1*, 243-254.

Goldstein, A., Kapelner, A., Bleich, J., & Pitkin, E. (2015). Peeking inside the black box: Visualizing statistical learning with plots of individual conditional expectation. *journal of Computational and Graphical Statistics*, *24*(1), 44-65.

Guo, X., Coops, N. C., Tompalski, P., Nielsen, S. E., Bater, C. W., & Stadt, J. J. (2017). Regional mapping of vegetation structure for biodiversity monitoring using airborne lidar data. *Ecological informatics*, *38*, 50-61.

Hawbaker, T. J., Keuler, N. S., Lesak, A. A., Gobakken, T., Contrucci, K., & Radeloff, V. C. (2009). Improved estimates of forest vegetation structure and biomass with a LiDAR‐optimized sampling design. *Journal of Geophysical Research: Biogeosciences*, *114*(G2).

Hengl, T., & Reuter, H. I. (2008). *Geomorphometry: concepts, software, applications* (Vol. 33). Elsevier.

Huang, J., Ji, M., Xie, Y., Wang, S., He, Y., & Ran, J. (2016). Global semi-arid climate change over last 60 years. *Climate Dynamics*, *46*, 1131-1150.

Hwang, T., Song, C., Vose, J. M., & Band, L. E. (2011). Topography-mediated controls on local vegetation phenology estimated from MODIS vegetation index. *Landscape ecology*, *26*, 541-556.

Ji, L., & Peters, A. J. (2003). Assessing vegetation response to drought in the northern Great Plains using vegetation and drought indices. *Remote sensing of Environment*, *87*(1), 85-98.

Khosravi Mashizi, A., & Sharafatmandrad, M. (2021). Water regulation and soil retention services in semiarid ecosystems of southeastern Iran, 2018–2020. *International Journal of Environmental Science and Technology*, *18*(12), 3979-3994.

Li, S., Zhao, Z., Miaomiao, X., & Wang, Y. (2010). Investigating spatial non-stationary and scale-dependent relationships between urban surface temperature and environmental factors using geographically weighted regression. *Environmental Modelling & Software*, *25*(12), 1789-1800.
Liu, Z., Jiang, F., Zhu, Y., Li, F., & Jin, G. (2018). Spatial heterogeneity of leaf area index in a temperate old-growth forest: Spatial autocorrelation dominates over biotic and abiotic factors. *Science of the Total Environment*, *634*, 287-295.
Lundberg, S. M., & Lee, S.-I. (2017). A unified approach to interpreting model predictions. *Advances in neural information processing systems*, *30*.
Luo, D., Jin, Z., Yu, Y., & Chen, Y. (2021). Effects of topography on planted trees in a headwater catchment on the Chinese Loess Plateau. *Forests*, 12(6), 792.
Maestre, F. T., Eldridge, D. J., Soliveres, S., Kéfi, S., Delgado-Baquerizo, M., Bowker, M. A., García-Palacios, P., Gaitán, J., Gallardo, A., & Lázaro, R. (2016). Structure and functioning of dryland ecosystems in a changing world. *Annual review of ecology, evolution, and systematics*, *47*(1), 215-237.
McPhillips, L., Earl, S., Hale, R., & Grimm, N. (2019). Urbanization in arid central Arizona watersheds results in decreased stream flashiness. *Water Resources Research*, *55*(11), 9436-9453.
Mehmood, K., Anees, S. A., Muhammad, S., Hussain, K., Shahzad, F., Liu, Q., Ansari, M. J., Alharbi, S. A., & Khan, W. R. (2024). Analyzing vegetation health dynamics across seasons and regions through NDVI and climatic variables. *Scientific reports*, *14*(1), 11775.
Meyer, H., Reudenbach, C., Hengl, T., Katurji, M., & Nauss, T. (2018). Improving performance of spatio-temporal machine learning models using forward feature selection and target-oriented validation. *Environmental Modelling & Software*, *101*, 1-9.
Nayak, R., Mishra, N., Dadhwal, V., Patel, N., Salim, M., Rao, K., & S Dutt, C. (2016). Assessing the consistency between AVHRR and MODIS NDVI datasets for estimating terrestrial net primary productivity over India. *Journal of Earth System Science*, *125*, 1189-1204.
O'Callaghan, J. F., & Mark, D. M. (1984). The extraction of drainage networks from digital elevation data. *Computer vision, graphics, and image processing*, *28*(3), 323-344.
Phattaralerphong, J., & Sinoquet, H. (2005). A method for 3D reconstruction of tree crown volume from photographs: assessment with 3D-digitized plants. *Tree Physiology*, *25*(10), 1229-1242.
Pretzsch, H., Biber, P., Uhl, E., Dahlhausen, J., Rötzer, T., Caldentey, J., Koike, T., Van Con, T., Chavanne, A., & Seifert, T. (2015). Crown size and growing space requirement of common tree species in urban centres, parks, and forests. *Urban forestry & urban greening*, *14*(3), 466-479.
Schoener, G. (2022). Impact of urbanization and stormwater infrastructure on ephemeral channel transmission loss in a semiarid watershed. *Journal of Hydrology: Regional Studies*, *41*, 101089.
Stone, C., & Haywood, A. (2006). Assessing canopy health of native eucalypt forests. *Ecological Management & Restoration*, *7*, S24-S30.
Su, Y.-F., Foody, G. M., & Cheng, K.-S. (2012). Spatial non-stationarity in the relationships between land cover and surface temperature in an urban heat island and its impacts on thermally sensitive populations. *Landscape and Urban Planning*, *107*(2), 172-180.
Tucker, C. J. (1979). Red and photographic infrared linear combinations for monitoring vegetation. *Remote sensing of Environment*, *8*(2), 127-150.
Valbuena, R., Heiskanen, J., Aynekulu, E., Pitkänen, S., & Packalen, P. (2016). Sensitivity of above-ground biomass estimates to height-diameter modelling in mixed-species West African woodlands. *PloS one*, *11*(7), e0158198.
Villarino, S. H., Studdert, G. A., Baldassini, P., Cendoya, M. G., Ciuffoli, L., Mastrángelo, M., & Piñeiro, G. (2017). Deforestation impacts on soil organic carbon stocks in the Semiarid Chaco Region, Argentina. *Science of the Total Environment*, *575*, 1056-1065.
Wang, M., Wright, J., Brownlee, A., & Buswell, R. (2016). A comparison of approaches to stepwise regression on variables sensitivities in building simulation and analysis. *Energy and Buildings*, *127*, 313-326.
Wang, Y., & Fang, H. (2020). Estimation of LAI with the LiDAR technology: A review. *Remote Sensing*, *12*(20), 3457.
Sattler, D., Murray, L. T., Kirchner, A., & Lindner, A. (2014). Influence of soil and topography on aboveground biomass accumulation and carbon stocks of afforested pastures in South East Brazil. *Ecological Engineering*, 73, 126-131.

Xi, Z., & Hopkinson, C. (2022). 3D graph-based individual-tree isolation (Treeiso) from terrestrial laser scanning point clouds. *Remote Sensing*, *14*(23), 6116.
Xie, F., & Fan, H. (2021). Deriving drought indices from MODIS vegetation indices (NDVI/EVI) and Land Surface Temperature (LST): Is data reconstruction necessary? *International Journal of applied earth observation and geoinformation*, *101*, 102352.
Xu, X., Guan, H., Skrzypek, G., & Simmons, C. T. (2019). Root‐zone moisture replenishment in a native vegetated catchment under Mediterranean climate. *Hydrological Processes*, *33*(18), 2394-2407.
Yang, J., El-Kassaby, Y. A., & Guan, W. (2020). The effect of slope aspect on vegetation attributes in a mountainous dry valley, Southwest China. *Scientific reports*, *10*(1), 16465.
Zeratsion, B. T., Gebreslassie, A., Gebrewahid, Y., Berhe, D. H., Manaye, A., Gebru, K. M., & Kifle, B. (2024). Community perceptions towards the ecosystem services of urban forests in Mekelle, Tigray, Ethiopia. *Discover Sustainability*, *5*(1), 166.
Zevenbergen, L. W., & Thorne, C. R. (1987). Quantitative analysis of land surface topography. *Earth Surface Processes and Landforms*, *12*(1), 47-56.
Zhao, W. Z., Xiao, H. L., Liu, Z. M., & Li, J. (2005). Soil degradation and restoration as affected by land use change in the semiarid Bashang area, northern China. *Catena*, *59*(2), 173-186.
Zhu, W., Xiang, W., Pan, Q., Zeng, Y., Ouyang, S., Lei, P., Deng, X., Fang, X., & Peng, C. (2016). Spatial and seasonal variations of leaf area index (LAI) in subtropical secondary forests related to floristic composition and stand characters. *Biogeosciences*, *13*(12), 3819-3831.
Zhu, X., Si, J., He, X., Jia, B., Zhou, D., Wang, C., Qin, J., & Liu, Z. (2024). Effects of long-term afforestation on soil water and carbon in the Alxa plateau. *Frontiers in Plant Science*, *14*, 1273108.

3 SOLAR RADIATION MODELLING

Abstract

Solar radiation, driving land-atmosphere interactions and terrestrial carbon assimilation, varies both temporally and spatially due to surface gradient, slope aspect and vegetation shading. Here we present a double-shading transposition model (DST) for simulating temporal and spatial distribution of downwelling shortwave solar radiation. The DST model considers influences of both topographic and canopy structure on radiation transmission. It simulates sub-hourly radiation distribution on and beneath vegetation canopy for any weather conditions. The model is tested against observations at two opposite-facing slopes. The simulated above-canopy radiation compares well with the observed data. The simulated under-canopy daily insolation highly correlates with observed radiation with an r of 0.95 and 0.94, at the two slopes, respectively. The model provides a convenient and effective tool for simulating spatial and temporal variation of solar radiation on mountainous areas with vegetation cover and has great potential in ecohydrological modelling and catchment management.

3.1 Introduction

Solar radiation on Earth's surface drives hydrological cycles, powers meteorological systems, and sustains ecosystems. As a key variable in hydrological and meteorological models, it largely determines the land surface energy balance and governs plenty of surface processes (Sheng et al., 2009; Wild, 2009; Antonanzas-Torres et al., 2019). Spatial variation of incident radiation also regulates vegetation spatial patterns, especially in water-limited areas (Gutiérrez-Jurado & Vivoni, 2013; Y. Fan et al., 2019).

Solar radiation is emitted from the sun, with an average temperature of 6000 ˚K. Over 95% of the solar energy is made up of shortwave radiation (wavelength range of 0.29 – 3 μm), which constitutes the largest component of the land surface energy balance (Kumar et al., 1997; Duffie & Beckman, 2013). For simplicity, the term 'radiation' in this paper denotes shortwave radiation. When solar radiation penetrates through the atmosphere, part of it that is not direct radiation is scattered in various directions and becomes diffuse radiation. On a rugged surface, radiation reflected from the surroundings can also contribute to the total radiation at a surface point (Duffie & Beckman, 2013).

The clear sky model is a radiation transfer for estimating solar radiation on Earth's surface. This model calculates radiation under clear sky conditions, representing the upper limit of real radiation on Earth's surface (Lefèvre et al., 2013; Antonanzas-Torres et al., 2019). In a clear sky model, the process begins with calculating extraterrestrial radiation for a specific location, considering latitude and time. The model then incorporates atmospheric interactions with solar radiation (McKenney,

1999). Clear sky models simulate radiation transfer processes in the atmosphere and interactions with various atmospheric components. Atmospheric molecules such as water vapor, oxygen, and ozone absorb solar radiation, converting it into heat, while other gases and particulates scatter radiation in all directions (Kumar et al., 1997). These effects are integrated into the radiation transfer model to estimate the radiation reaching the Earth's surface.

Clear sky models have several limitations that can restrict their application. For instance, a key challenge is the lack of data needed to accurately parameterize radiation transfer simulations through the atmosphere (Badescu et al., 2012). More critically, clear sky models do not account for cloud effects, which significantly impact radiation transmission. This limitation confines their use to areas or times with minimal cloud cover. In some regions, cloudiness can intercept up to 80% of down-welling solar radiation (Serrano et al., 2015; Kambezidis et al., 2016). To address this shortcoming, efforts have been made to incorporate cloud effects into radiation transfer models by quantifying cloud optical depth, thereby extending the clear sky model to account for all conditions (Tang et al., 2016). However, monitoring the spatial and temporal variations of cloud distribution and properties remains challenging due to the sparse and heterogeneous nature of observation stations (Zajaczkowski et al., 2013).

To address these issues, transposition models, which rely on point radiation measurements, have been developed (Liu & Jordan, 1963; Yang, 2016). A transposition model uses observed radiation on a horizontal surface to simulate radiation on a tilted surface over a specific area (Gueymard & Myers, 2008). This model incorporates the surface geometry and solar zenith angle to perform its calculations. One common application of transposition models is in optimizing the placement of flat-panel photovoltaic arrays (Khatib et al., 2015; Yang, 2016). These models can generate solar radiation distribution maps for any given time period. Additionally, transposition models require fewer variables than all-condition models, though they do depend on measured radiation on a horizontal plane at a nearby location (referred to as the reference radiation). By using concurrently measured radiation, transposition models can be applied under any weather conditions.

Shading effects can significantly influence surface solar radiation, creating substantial temporal and spatial variability, particularly in complex terrain (Zou et al., 2007; Marsh et al., 2012; S. Zhang et al., 2020). Most previous studies have focused on the impact of topography on solar radiation, constructing models based on landscape components and structures derived from digital elevation models (DEM) (Dozier, 1980; Dubayah & Rich, 1995; Kumar et al., 1997). Recently, research has expanded to explore the spatial and temporal variation of solar radiation in urban environments. For example, Yu et al. (2009) examined the spatiotemporal variability of solar radiation in downtown Houston, Texas, and developed a solar flux model for urban vegetation planning and management. Liang et al. (2014) introduced a 3D method for computing and visualizing urban solar radiation using image-space data representation. Erdélyi et al. (2014) proposed a numerical

model to simulate the distribution of direct and diffuse radiation in urban settings. These studies have primarily addressed the shading effects from surrounding terrain or artificial structures on solar radiation distribution.

Vegetation can partially intercept solar radiation that would otherwise reach the ground, altering the patterns of incident radiation in forested and vegetated areas. Understanding the amount of radiation reaching the top of the vegetation and the ground surface beneath the tree canopy is crucial for ecohydrological investigations in complex terrains, where small changes in energy balance can significantly impact vegetation and water flux dynamics (Metzen et al., 2019). Seyednasrollah and Kumar (2014) developed a shortwave radiation model for snowmelt prediction that calculates radiation transmission based on the path length of the solar beam as it passes through gaps in the forest canopy. However, this model estimates incident radiation only at a single point. With the advent of high-resolution topographic data from photogrammetry and light detection and ranging (LiDAR) technology, detailed 3D landscape structures are becoming more accessible, enhancing the potential for incorporating detailed surfaces into earth system models (Crosby et al., 2020). For instance, Gutiérrez-Jurado and Vivoni (2013) investigated the effects of topography and vegetation on annual and seasonal irradiance on opposing hillslopes in New Mexico by combining LiDAR-derived digital surface models with a distributed solar radiation model. Bode et al. (2014) estimated sub-canopy radiation transmittance using a light penetration index derived from LiDAR data. Peng et al. (2014) introduced a spatiotemporally explicit 3D ray-tracing model to analyse spatiotemporal patterns of understorey light density. Nyman et al. (2017) evaluated four sub-canopy radiation models and found that the model based on path-length simulation performed best.

Although these methods use LiDAR data or the length of solar rays crossing the vegetation canopy for canopy transmission calculations. However, characterizing the light attenuation effect based only on the path-length attribute is insufficient since the light attenuation along its transmission path through the crown is also affected by the non-random distribution of foliage elements (Zeng et al., 2019). The leaf area index (LAI), which quantifies leaf density within the canopy, could be used to parameterize light attenuation effects through the canopy. Despite this, few solar radiation models incorporate LAI to enhance radiation estimates in vegetated areas. Additionally, existing distributed solar radiation models either operate under clear sky conditions or require local cloudiness data. An all-weather distributed 3D solar radiation model remains to be developed.

This chapter presents the development of a solar radiation model for simulating the temporal and spatial distribution of incident radiation on and beneath a vegetated surface for any weather conditions based on a reference point shortwave irradiance measurement. Both the topographic shading and vegetation canopy shading are considered. In order to simulate the canopy shading, the DEMs (including the digital terrain model (DTM), which is the elevation of bare earth and the

digital surface model (DSM), which is the elevation of all objects including vegetation) and the LAI are used. One-year's shortwave irradiance data above-canopy and net radiation data below canopy on two opposite-facing slopes (polar-facing and equator-facing slopes) of a steep vegetated catchment at Mount Wilson, South Australia is used to evaluate the model's performance.

3.2 Model description

The model proposed here is a transposition model based on a reference station of unshaded radiation that incorporates the local topographic and canopy shading effects. We refer to this model as the double-shading transposition (DST) model. The model is developed based on the conceptualization shown in Figure 3.1.

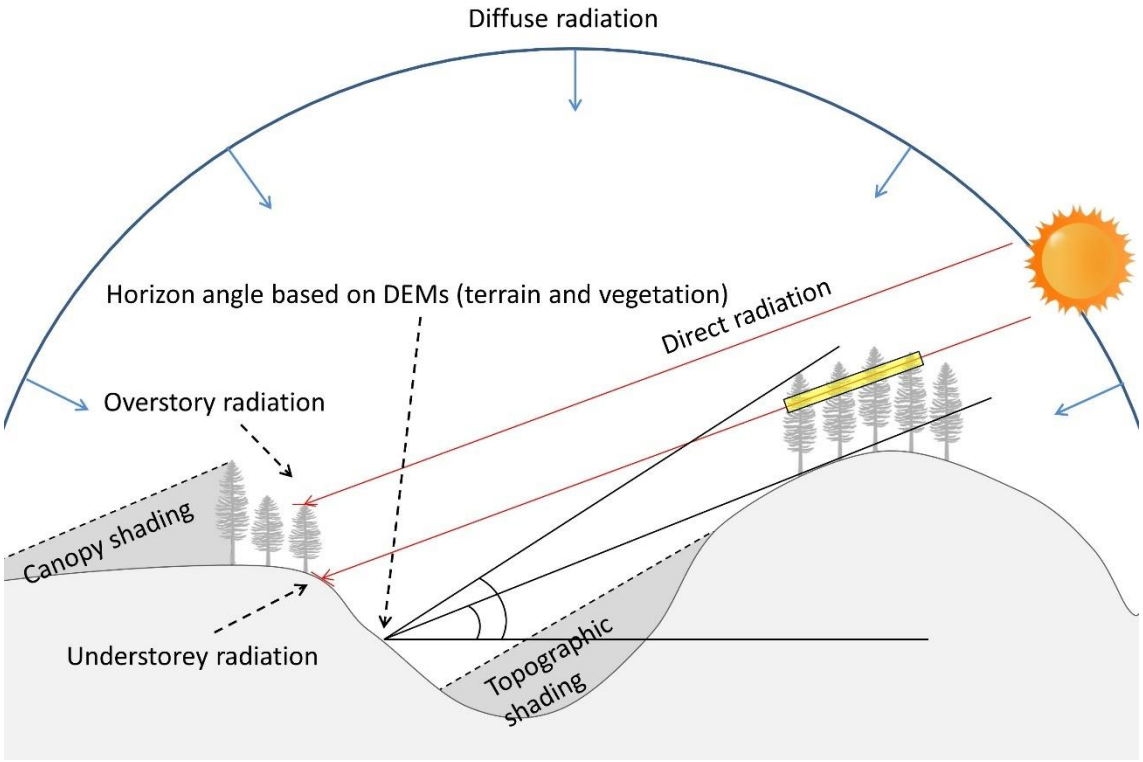

Figure 3.1 Conceptual diagram of the solar radiation transmission; the red arrows represent direct radiation, the blue arrows represent diffuse radiation, the yellow box represents the path depth that solar radiation travels through the canopy. The horizon angle based on Digital Elevation Models are terrain horizon angle and vegetation horizon angle.

Topographic shading can be caused by the surface itself (self-shading) and the surrounding features. The self-shading results from surface orientation and it can be calculated with the solar altitude angle, solar azimuth angle, and slope and aspect derived from DTM (Duffie & Beckman,

2013). The surrounding terrain shading is complex since it results from multiple features interacting with and intercepting light from various directions. To estimate when shading occurs as a result of the surrounding terrain, horizon angles are calculated using the DEMs at the solar azimuth and are compared with the solar altitude angle. The horizon angle in a direction is defined as the angle between the horizontal plane and the upper view edge of elevated terrain in that direction (Ruiz-Arias et al., 2010). If at the time of interest, the terrain horizon angle at the solar azimuth direction is larger than the solar altitude angle, the surface is shaded by the terrain and has no direct radiation. If the solar altitude angle is between the terrain and vegetation horizon angles, the surface is shaded by vegetation canopy, which will be explained later.

Different from direct radiation, diffuse radiation comes from all directions from the sky. Usually, the sky view factor is adopted to estimate the topography effect on diffuse radiation in solar radiation models (Li et al., 2016). However, since the diffuse radiation does not distribute isotropically in the hemisphere, it is inaccurate to simply use the sky view factor to calculate the diffuse radiation. Moreover, the sky view factor only accounts for diffuse radiation reduction from the topography effect and is therefore not suitable for simulating the shading effect that is caused by penetrable objects such as vegetation canopy. In the DST model, we calculated the anisotropic diffuse radiation, and the attenuation of diffuse radiation is estimated based on the canopy structure.

The incident solar radiation on the land surface may be partially obstructed by vegetation canopy. As can be seen in Figure 3.1, the incident direct radiation on both above- and under-canopy can be obstructed by vegetation occurring in the beam direction. To simulate the process of light traveling through the canopy, the canopy is considered as a turbid medium (Da Silva et al., 2008). To detect the spatial variation of the forest structure, the DSM is employed. Since it can capture the morphologies of the vegetation above the land surface, we combined it with LAI to estimate the transmittance of solar ray crossing the canopy according to the Beer-Lambert law (Ross, 2012). For direct radiation at a certain point in time, the canopy transmittance is calculated for the direction in which the solar ray comes in contact with the canopy surface at that moment. The canopy transmittance of diffuse radiation is estimated according to the mean canopy transmittance value for all directions of the hemisphere.

A flowchart for the DST model is shown in Figure 3.2. The model requires the following data: (1) Time and location information, including the start and end dates, and the latitude and longitude, (2) Topography and vegetation data, including DEMs and LAI, and (3) Reference radiation data on a horizontal surface, free of the shading effects, which shares the same sky condition with the area of interest with solar radiation to be simulated. Given that direct radiation and diffuse radiation behave differently in the two shading processes, a decomposition model is adopted to partition the observed global radiation at the reference station into direct and diffuse components (Ridley et al., 2010).

The incident solar radiation on a surface at a given point in time is related to the solar geometric and the topography factors of the receiving surface at that instance. Similar to other radiation models, the DST model starts from calculating the solar geometry and topographic features. For an inclined surface, the reflected radiation from surrounding terrain is also considered in the DST model.

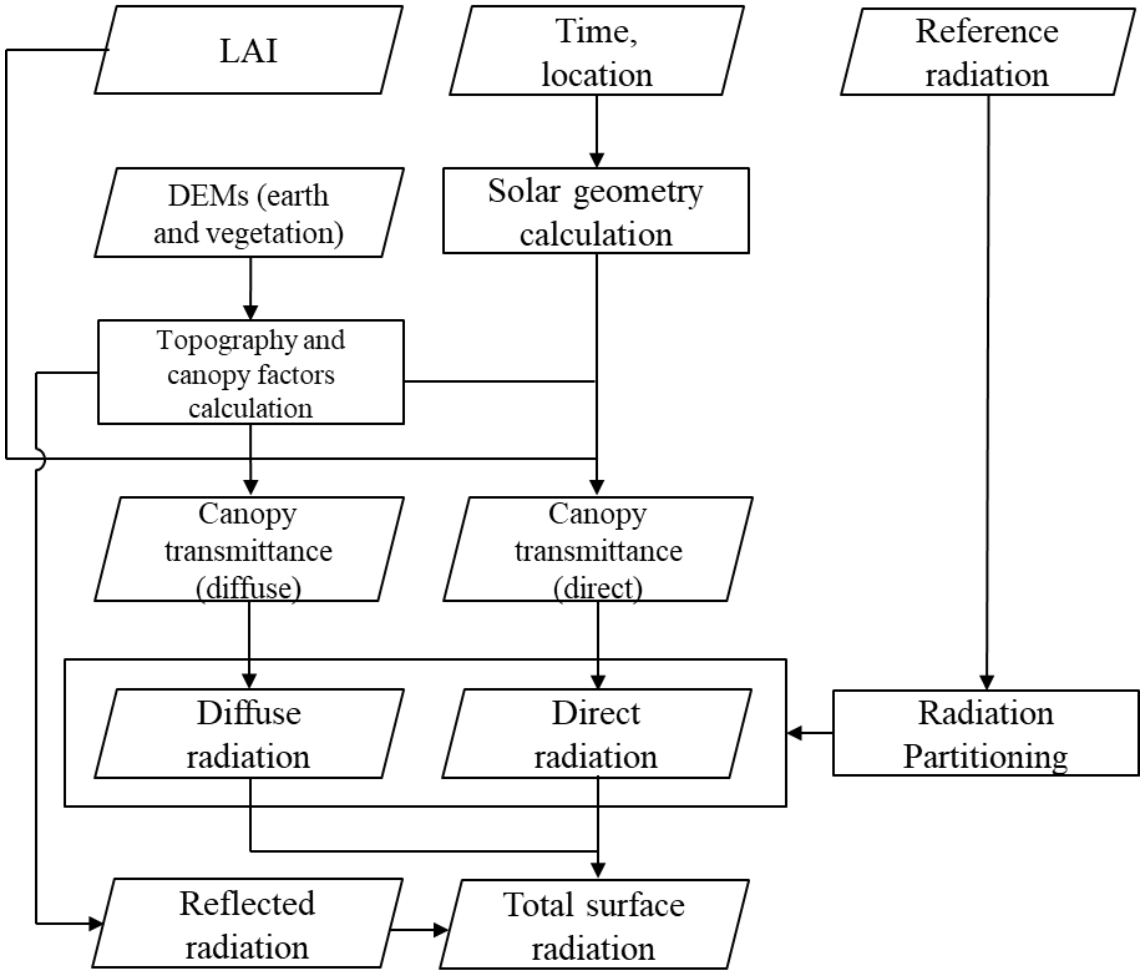

Figure 3.2 Flowchart showing the model process.

3.3 Methodology

3.3.1 Study area and data collection

The study area is same with chapter 2. Figure 3.3 show the study area and weather station installation location. The maximum irradiance (radiation flux, W/m^2) in summer can be up to 1200 W/m^2, but in winter it is about 600 W/m^2 (based on a reference station detailed later). In addition to this temporal variation, spatial variation of solar irradiation is more complicated due to steep

topography relief and slope-induced variation in vegetation cover (X. Xu et al., 2017). This spatial variability provides a range of conditions to test the proposed DST model.

Three radiation stations were installed. One is located in an open area at the top edge of the catchment. Hereafter referred to as the reference station. This station measured the unshaded, shortwave solar radiation with a CM3 Pyranometer (Kipp & Zonen). The two other sites were located on two opposite-facing hill slopes of the small catchment, one with an equator-facing slope (EFS) and the other with a polar-facing slope (PFS). For these sites, CNR4 Net Radiometer (Kipp & Zonen) was installed at an elevation of 12 meters above the ground and measured both upwelling and downwelling shortwave and longwave radiation (i.e. above the tree canopy). In addition, a NR Lite2 Net Radiometer (Kipp & Zonen) was installed at 1.7 m above the ground, under the tree canopy, to measure understorey net radiation at both sites.

Radiation data was recorded from April 04, 2013 to April 05, 2014, with a 30-minute sample interval. The quality control process includes the following rules: (1) Missing or incomplete data is excluded; (2) Recorded radiation exceeding extraterrestrial radiation is excluded; (3) For the measured above-canopy radiation, a 3-point (1hour) moving average is adopted. For measured under-canopy net radiation, the negative values are eliminated and a 5-point (2 hours) moving average is adopted, since a high frequency variation exists in the measured data due to temporal variation of canopy shadow casting.

Radiation data for 361 days is available from the reference station as model input. The data recorded at the EFS and PFS sites is used for model validation. At the EFS site, radiation measurements above the canopy cover 343 days, while at the PFS site, it covers 208 days. For measurements beneath the tree canopy, half-hourly net radiation data is available for 313 days at the EFS site and 339 days at the PFS site.

The DTM, DSM, and LAI data were derived from airborne LiDAR data (detailed in chapter 2) with a spatial resolution of 0.5 m.

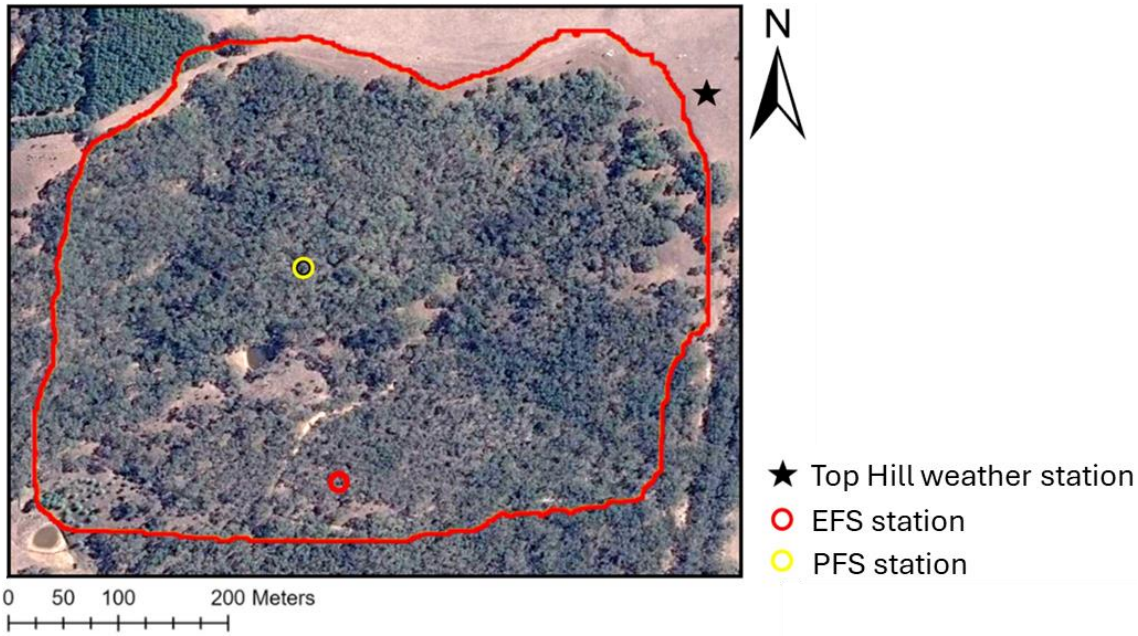

Figure 3.3 The study area and geographical location of weather stations.

3.3.2 Basic equations

3.3.2.1 Solar geometry

The sun's position in the sky needs to be calculated for each time interval, which can be expressed by solar altitude angle and solar azimuth angle. Solar altitude angle, α_s is the angle between a horizontal plane and the line to the sun, and solar azimuth angle, γ_s is the angular displacement from south of the projection of direct radiation on the horizontal plane (Duffie & Beckman, 2013):

$$\sin \alpha_s = \cos \varphi \cos \delta \cos \omega + \sin \varphi \sin \delta \tag{3.1}$$

$$\gamma_s = \text{sign}(\omega) \left(\pi - \cos^{-1} \left(\frac{\sin \alpha_s \sin \varphi - \sin \delta}{\cos \alpha_s \cos \varphi} \right) \right) + \pi \tag{3.2}$$

$$\delta = 23.45 \sin \left(360 \frac{284 + n}{365} \right) \tag{3.3}$$

where φ is the latitude in radians, δ is the solar declination (Equation 3.3), and ω is the hour angle, which equals zero at the solar noon and varies at the rate of 15° per hour, negative in the morning, positive in the afternoon, the sign function equals to +1 if ω is positive and is equal to −1 if ω is

negative. *n* is the day of year. The solar azimuth angle γ_s ranges from 0 to 2π, zero facing south, and increasing in a counterclockwise direction.

3.3.2.2 Radiation partition

In most cases, only the total radiation is available. Boland et al. (2001) proposed a method to estimate the diffuse fraction based on a logistical function. This method establishes correlation among diffuse fraction, clearness index, and the solar time. The clearness index is defined as the ratio of total radiation on a horizontal surface to extraterrestrial radiation (Reindl et al., 1990). With the solar constant, time and location information, the extraterrestrial radiation can be precisely calculated for any instantaneous time point (Duffie & Beckman, 2013). Ridley et al. (2010) improved the diffusion fraction method with more predictors for better performance, which is referred to as the Boland-Ridley-Lauret (BRL) model. The radiation partitioning model is:

$$K_d = \frac{1}{1 + \exp\left(\beta_0 + \beta_1 k_t + \beta_2 AST + \beta_3 \alpha_s + \beta_4 K_t + \beta_5 \psi\right)} \tag{3.4}$$

where K_d is the diffuse fraction, k_t and K_t are the sub-hourly and daily clearness index (calculated based on the reference station data), AST is the apparent solar time, ψ is a persistence factor and (β_0, β_1,…, β_5) are the coefficients adopted from Ridley et al. (2010).

3.3.2.3 Topography shading

Terrain horizon angle is required to determine whether topography shading occurs or not. In this instance, for a given point, the horizon angle should be calculated for all possible solar azimuth angles, which is computationally expensive. To this end, a rapid calculation algorithm is employed in this study after Dozier et al. (1981). The DEMs data is transformed into matrix form such that it could be rotated, and the horizon angle calculated in forward and backward directions for each pixel. The shading relationship is described using the discrete Heaviside step function $\mathrm{f}(x)$ (Ruiz-Arias et al., 2010):

$$\mathrm{f}(x) = \begin{cases} 0, & x < 0 \\ 1, & x \geq 0 \end{cases} \tag{3.5}$$

The variable x in Equation 3.5 is the difference between solar altitude angle and the horizon angle in the solar azimuth direction (H_{γ_s}). Once the solar altitude angle, α_s and solar azimuth angle, γ_s are determined, the estimated direct radiation is calculated as:

$$\hat{r}_b = \mathrm{f}(\alpha_s - H_{\gamma_s}) r_b \tag{3.6}$$

r_b is the partitioned direct radiation.

3.3.2.4 Canopy shading

When the DSM is used in the horizon angle calculation, it results in a threshold for determining whether canopy shading may occur. Canopy shading on direct radiation occurs if the solar altitude angle falls between the terrain and vegetation horizon angles. When this occurs, the estimated direct radiation can be calculated as:

$$\hat{r}_b = \tau_b r_b \tag{3.7}$$

$$\tau_b = \exp(-k \cdot LAD \cdot L) \tag{3.8}$$

where $\hat{r}_b$ is the estimated direct radiation travelling through the canopy, τ_b is the canopy transmittance of beam radiation, *k* is the extinction coefficient, *LAD* is the leaf area density (m^2/m^3), and *L* is the penetrating distance that light crossing the canopy.

The extinction coefficient, *k* depends on light direction and leaf inclination distribution. Previous studies suggest that it is a function of solar altitude angle assuming a spherical leaf angle distribution (Campbell & Norman, 1998; Timlin et al., 2014):

$$G = \frac{0.5}{\sin \alpha_s} \tag{3.9}$$

The *LAD* is defined as the ratio of leaf area to crown volume (Da Silva et al., 2012). In this study, we evenly distribute leaves in a grid. Although canopy leaves tend to distribute at the upper part of a tree height at any given pixel, given that a solar beam traveling through the canopy at different

heights intercepts several pixels along its path (Figure 3.4), this approximation has potential to capture the canopy shading effect on beam radiation. The leaf area density can then be expressed by LAI:

$$LAD = \frac{LAI}{canopy\ height} \tag{3.10}$$

Since the DEMs data include the height information of the land surface and canopy, the canopy height for each grid cell can be estimated from the differential value between the DTM and DSM.

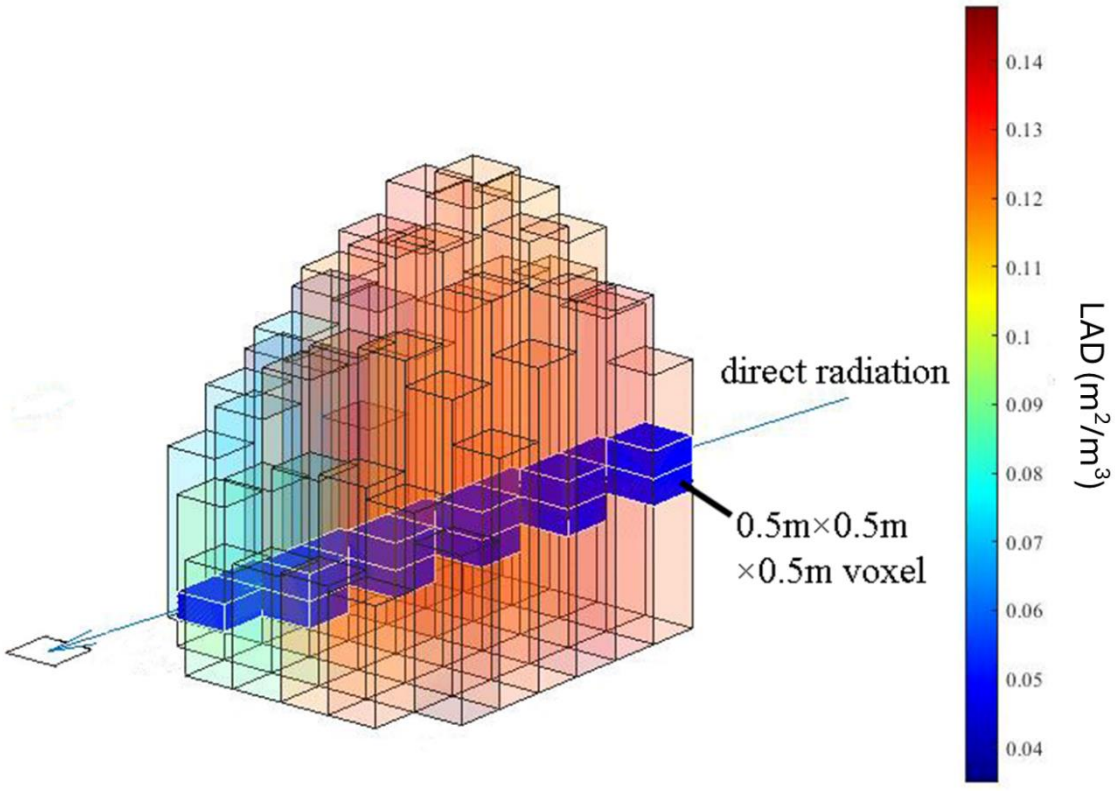

Figure 3.4 Diagram of the canopy shading effect (voxels) along a solar beam path towards a target surface, with an assumption that leaf area is evenly distributed over the whole canopy height at each pixel.

To calculate the distance that the solar ray penetrates through the canopy, a ray tracing method, known as the voxel traverse algorithm, is adopted (Amanatides & Woo, 1987; Musselman et al., 2013). Firstly, a 3-D domain, consisting of cubic volumes (voxel) is constructed according to the size of the study area. In this study, the DEMs data include 730×998 pixels and the maximum height is 427 m, such that the 3-D domain has 730×998×854 elements. Having adequate voxel

numbers ensured greater accuracy of distance estimation, but it is computationally inefficient for a large number of voxels. The resolution of the DEMs data in this study is 0.5 m, so the height of each voxel is set to 0.5 m (Figure 3.4). According to the height information in the DEMs data, the voxels are defined as three types: above the canopy, between the canopy and land surface, and below the land surface. Once the point of interest is identified and light direction defined, the ray tracing algorithm determines the positions of all voxels through which the light travels and the total distance.

For each time interval, the solar altitude angle and solar azimuth angle are calculated for each grid cell and converted to a direction vector. Then, the horizon angle is calculated based on the DSM and compared to the corresponding solar altitude angle to determine whether the grid cell is shaded by canopy. Only those shaded pixels are included in the transmittance calculation to ensure computational efficiency. The averaged LAD is calculated according to the voxel position and LAI data. The canopy transmittance of direct radiation for each shaded grid is calculated using Equation 3.8.

The canopy can also attenuate the diffuse radiation. Unlike the direct radiation, it comes from all directions without a certain source. Two factors affect the intensity of the diffuse radiation from the sky:

(1) It has been found that the distribution of diffuse radiation is anisotropic, especially in cloudy day (Kondratyev & Manolova, 1960). An anisotropic model proposed by Hay (1993) is employed for its simplicity and accuracy. The formulation gives by:

$$d = (1 - \mathrm{A}_I)\cos^2\frac{\beta}{2} + \mathrm{A}_I\frac{\cos\alpha}{\sin\alpha_s} \tag{3.11}$$

where *d* is the diffuse factor (ranging from 0 to 1), A_I is the "anisotropy index" expressed as $\mathrm{A}_I = I/I_{sc}$, I is the normal incident direct radiation and I_{sc} is the solar constant, β is the surface slope. The incident angle α between sun light and the normal to that surface can be calculated as (Duffie & Beckman, 2013):

$$\begin{aligned}\cos\alpha = {} & \sin\delta\sin\varphi\cos\beta - \sin\delta\cos\varphi\sin\beta\cos\gamma \\ & + \cos\delta\cos\varphi\cos\beta\cos\omega + \cos\delta\sin\varphi\sin\beta\cos\gamma\cos\omega \\ & + \cos\delta\sin\beta\sin\gamma\sin\omega\end{aligned} \tag{3.12}$$

where γ is the surface aspect, other symbols are explained in Section 3.2.1.

(2) The surrounding canopy attenuates the diffuse radiation from all directions. In that case, the canopy transmittance of diffuse radiation, τ_d is approximated by averaging the canopy transmittance over the whole hemisphere (de Castro & Fetcher, 1998). In this research, four azimuth (west, east, north, and south) and three altitude angles (30˚, 60˚ and 90˚) are selected for calculation.

The estimated diffuse radiation can be calculated as:

$$\hat{r}_d = d\tau_d r_d \tag{3.13}$$

where r_d is the partitioned diffuse radiation.

3.3.3 Total radiation over and understorey

The model is designed to estimate the incident solar radiation above and under the canopy. For overstory radiation, the reference height is derived from the DSM data and the received surface is set to be horizontal. The canopy shading mainly comes from surrounding canopy that is higher than itself.

$$\hat{r}_a = \hat{r}_{b,a} + \hat{r}_{d,a} \tag{3.14}$$

$\hat{r}_{b,a}$ and $\hat{r}_{d,a}$ are the estimated direct and diffuse radiation for overstory.

For the understorey radiation, since the land surface is inclined, the slope and aspect of land surface are considered. In this study, the reference radiation data from a weather station is received on a horizontal surface, and therefore, the direct radiation is restored to the correct solar direction at that point in time. A geometric factor, $R = \cos\alpha \,/\, \sin\alpha_s$ is applied for the direct radiation.

In complex terrain, the radiation reflected from the surrounding terrain should be included in the calculation. A common adopted formulation is employed here to describe the reflected radiation (Gueymard, 2009):

$$r_r = \rho\mu r_R \tag{3.15}$$

$$\mu = \frac{1 - \cos\beta}{2} \tag{3.16}$$

where r_r is the reflected radiation, ρ is the foreground albedo (in a forest area, ρ assumes to be 0.2), μ is the reflection factor, and r_R is the global radiation on a horizontal surface.

The under-canopy radiation is calculated follows:

$$\hat{r}_u = R\hat{r}_{b,u} + \hat{r}_{d,u} + r_r \tag{3.17}$$

$\hat{r}_{b,u}$ and $\hat{r}_{d,u}$ are the estimated direct and diffuse radiation for under-canopy condition.

3.3.4 Model validation

The DST estimate of direct canopy transmittance is evaluated against the calculated transmittance based on the EFS and PFS observations. Additionally, we calculated the transmittance based on LiDAR point cloud data for comparison (Musselman et al., 2013). The method consists of a voxel-based canopy structure model and a ray trace model. Firstly, the study area is assigned a certain vertical dimension defined by the elevation difference between the highest value of the DSM in the domain and the lowest value of the DTM. The airborne scanning LiDAR data points are distributed in the voxel space according to the 3D LIDAR laser return geographical coordinates. Each voxel is assigned a value corresponding to the number of laser point returns contained within that voxel extent. Voxels within which no returns are recorded are set a value of zero. Then, a voxel traversal algorithm is applied to calculate the laser point returns along the direct solar ray direction for each surface grid. The direct beam canopy transmittance $\tau_{i,j}(t)$ is computed as:

$$\tau_{i,j}(t) = 1 - \frac{\min\left(return_{i,j}(t), P\right)}{P} \tag{3.18}$$

where $return_{i,j}(t)$ represents the accumulated LiDAR laser point returns along the solar ray path to surface point *(i, j)*, at time step *t*. *P* is the maximum return parameter that represents the upper limit of accumulated point returns, above which full canopy attenuation of the incoming solar direct beam is assumed. Musselman et al. (2013) calibrates the *P* parameter using 12 hemispherical photographs. A *P* parameter value of 42 produced a minimum mean absolute difference value. The *P* is set to 105 for the transmittance calculation in our study, according to the ratio of the point return density between our data and the data of Musselman et al. (2013).

Both the DST model and the point-cloud model estimated canopy transmittance are tested against the observed estimation. The direct shortwave canopy transmittance can be calculated as the ratio of the under-canopy radiation and the above canopy direct radiation (Milenković et al., 2017):

$$\tau = \frac{r_{b,a}}{r_{b,u}} \tag{3.19}$$

Since the understorey shortwave radiation was not measured in this study area, an empirical equation considering both the surface temperature and Earth–Sun distance is adopted to convert the understorey net radiation to downwelling shortwave radiation (Jiang et al., 2015):

$$R_n = a_1 R_s + a_2 T + a_3 d_r + a_4 \tag{3.20}$$

where R_n is the net radiation, R_s is the downwelling shortwave radiation, T is air temperature, d_r is the inverse relative Earth-Sun distance and a_1, a_2, a_3, and a_4 are coefficients. The air temperature T was measured at both sites. To minimize the effect of diffuse radiation and topography shading in the observation, only data between the daylight hours of 10:00 and 14:00 and has the diffuse fraction K_d less than 0.3 is considered. Then the daily average is calculated for evaluating the model performance.

Several indexes are selected for model evaluation. Two metrics are evaluated for the transmittance estimate comparison: the mean error (ME) and mean absolute error (MAE). The MAE shows the absolute error between the model result and the observation. The ME determines whether the model result underestimates or overestimates the transmittance. For the radiation simulation evaluation, the correlation coefficient R, between the model simulation and site observation (both offset by the observed radiation at the reference station) is calculated. Additionally, the relative error of the sub-hourly and daily radiation is evaluated by calculating the mean absolute percentage error (MAPE) and mean absolute percent deviation (MAPD) (Jackson et al., 2019):

$$MAPE = \frac{1}{n}\sum_{i=1}^{n}\left|\frac{y_i - x_i}{r_i}\right| \tag{3.21}$$

$$MAPD = \frac{\sum_{i=1}^{n}|y_i - x_i|}{\sum_{i=1}^{n}|r_i|} \tag{3.22}$$

where *n* is the number of radiation data according to the simulated time interval in one day. y_i and x_i are the simulated data and observed data, r_i is the radiation data of the reference station.

3.4 Results and Discussion

3.4.1 Comparison of the transmittance estimates

The ME and MAE of the direct radiation transmittance at EFS and PFS sites are calculated to evaluate the DST model performance and the point-cloud based model against the observation-based transmittance according to Equation 3.19 (Table 3.1). The error metrics are calculated for four seasons.

The MAE values of the DST model are smaller than the point-cloud based model. There are two improvements on the DST model, which makes the DST estimated transmittance consistent with the observations. Firstly, the DST model includes the light penetration distance among canopy for estimating the transmittance. For both EFS and PFS sites, a significant difference is observed for summer in which the ME of the point-cloud based model is larger than that of the DST model. The ME negative values for summer suggest that the point-cloud based model tends to overestimate the transmittance while the DST model underestimates the transmittance. The airborne LiDAR only scans the forest canopy from above and therefore there is obstruction by higher canopy elements that reduces the probability of lower elements to be sampled (Popescu & Zhao, 2008). As a result, the point cloud tends to have a larger distribution at the top of the canopy whilst the lower-level canopy has less point samples even though it may have a dense leaf cover. This leads to some apparent “hollows” in LiDAR point cloud data in the central and lower parts of the canopy.

The solar altitude angle is higher from late spring to early autumn, which means the solar rays penetrate the canopy close to a near vertical direction. Under this circumstance, the DST model uses the light penetration distance from the incident point on the canopy to the land surface, while the point-cloud based model takes the point-cloud information primarily representing the top of the canopy. This could explain why the point-cloud based model tends to overestimate transmittance in summer.

Secondly, the DST model incorporates the information of LAI to estimate the transmittance. As can be seen in Table 3.1, the point-cloud based model has a reduced level of performance for the PFS site, with a much higher ME and MAE than for the NFS in spring, summer and autumn. However, the level of error is not found in the DST model. Chapter 2 demonstrates that NDVI, which represents vegetation cover, is elevated in the polar facing slope is higher than the equator facing slope. As a result, the direct shortwave canopy transmittance in the SFS is lower than the NFS (data are not shown in paper for simplicity). This could amplify the overestimated error created by the feature of point-cloud data that tend to accumulate on the upper layer of canopy. In winter, the MAE of the point-cloud based model decreases significantly. As the solar altitude angle decreases

in winter, the incident solar rays entering the canopy are at a lower angle, minimizing the effect of the “hollows” of the point-cloud. The better performance of the DST model in both the NFS and the SFS sites indicate that the LAI information can improve the accuracy of transmittance estimation for the different facing slopes.

To further demonstrate the difference of the two models in simulating transmittance for different facing slopes, Figure 3.5 shows the direct radiation transmittance estimates of the two models for three days (summer: January 12, 2014, spring: April 10, 2013 and winter; July 11, 2013) at 2 pm. For the summer day in which the solar altitude angle at 2 pm is 71.48˚, the point-cloud based model estimates high transmittance (over 0.8) for almost the entire study area, while the DST model estimate shows that the transmittance is lower and there is a distinct difference between the equator facing (south-east section) and polar facing (north-west section) slopes (Figure 3.5). Since the equator facing slope has less overstory vegetation cover (according to chapter 2), the DST estimate captures the real situation, while the point-cloud based model fails. For the spring day, the solar altitude angle is 45.58˚ at 2 pm. As the solar altitude angle is smaller, the difference in the transmittance for the two opposite slopes is shown in the point-cloud based model, but not as much as that from the DST model. In winter, the solar altitude angle is 32.04˚ at 2 pm and there is an obvious difference in transmittance for the two opposite facing slopes which could be determined in the point-cloud based model.

In summary, the DST model tends to perform better than the point-cloud based model with a smaller MAE from the observation-based estimated transmittance. By using information of LAI and the penetration distance, the DST model performance can be used to estimate the canopy transmittance.

Table 3.1 ME and MAE of the direct canopy transmittance, estimated from the point-cloud based model and DST model

Method			spring	summer	autumn	winter
Point-cloud based model	EFS	ME	0.04	0.12	0.10	0.04
		MAE	0.10	0.14	0.18	0.07
	PFS	ME	0.35	0.36	0.24	0.01
		MAE	0.35	0.36	0.25	0.08
DST model	EFS	ME	-0.06	-0.05	0.01	-0.03
		MAE	0.10	0.09	0.11	0.07
	PFS	ME	-0.04	-0.09	-0.03	-0.04
		MAE	0.09	0.13	0.04	0.04

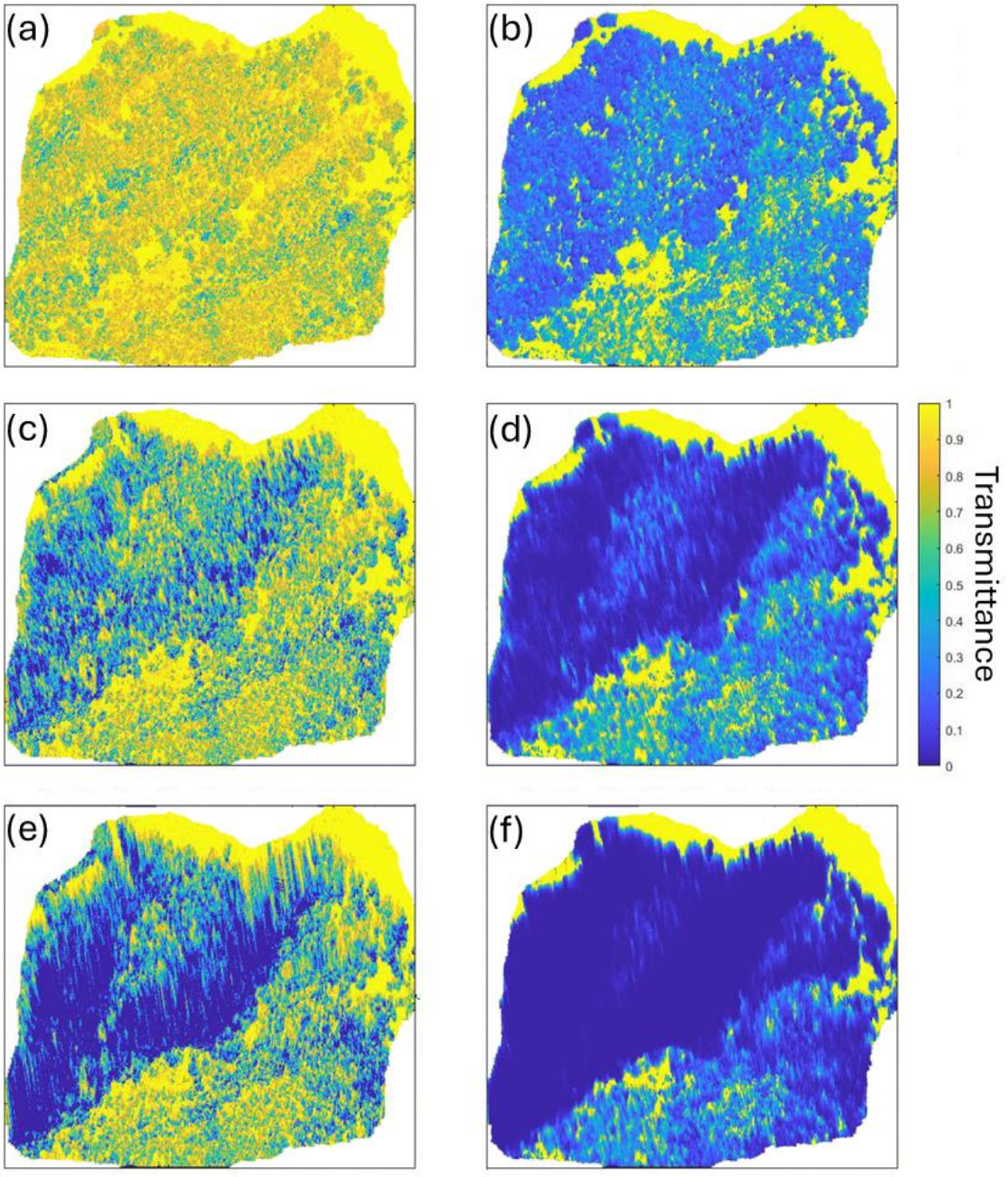

Figure 3.5 Modelled canopy transmittance for direct shortwave radiation on (a) and (b) January 12, 2014, (c) and (d) April 10, 2013, (e) and (f) July 11, 2013 estimated from the point-cloud based model (left) and the DST model (right).

3.4.2 Overstory radiation

The 30-minute radiation values of the observed sites (EFS and PFS) are calculated for eight representative clear and cloudy days in four seasons. The results are compared to the site observations to evaluate the model's capability in radiation simulation. A 3-point (equivalent to one hour) moving average is applied to observations and simulations at both sites to minimize the disturbance from temporal variation of sky conditions. In order to remove the apparent effect of the daytime radiation cycle, which is irrelevant of the model quality, the offset radiation values are

calculated. The offset radiation values are the difference between the site observation/model simulation and the reference station radiation (Figure 3.6). The correlation coefficient r between the offset values of observation and simulation is calculated for performance evaluation (Table 3.2). The MAPE and MAPD are also calculated to examine the relative error.

At the EFS site, the model simulations (red solid line) do not improve much, as the offset values are not consistent with the observed one (red dotted line). From Figure 3.6 (a) (b), we can find lower values appear at about 8:00 am for the simulations while the observations close to zero. That means it is shaded in the model at the moment, which is not correct for the real situation. The R of the offset value in site observation and model simulation of EFS show relative low values for almost all the seasons in any weather, suggesting that the shading situation estimates of the EFS site do not perform well. Since the altitude of the EFS site is higher in the study area, there is very little shade during the daytime. As a result, at the top of the canopy, the NFS site can receive almost same radiation as the reference station. Thus, the DST model improvement is not clear.

At the PFS site, a clear improvement is found in the model simulation. The difference in reference station and site observation (blue dotted line) shows significant variation, with extreme low values happen in around 3:00-5:00 pm for most of the examined days. Negative offset values indicate there are shading occurrences. As can be seen in Figure 3.6, the model simulation highly correlated with the observation. The r values of SFS site also maintain high values for most of examined days (Table 3.2). The results show that DST model can well capture the shading effects on PFS site, especially for the situation with obvious shading occurrence.

Compared to the EFS site, there are more shading occurrence on the PFS site. The results show that the DST model performs better on the PFS site. While for the EFS site, since there are fewer shading occurrences, the above-canopy radiation is consistent with the reference station data. The model simulated radiation is also close to the real situation as the offset values are close to zero for most of the time intervals, with the MAPE and MAPD indexes show low values for all the seasons and weather conditions, suggesting that the relative error between the observed and simulated radiation is small. In general, the proposed radiation model is able to accurately simulate the overstory radiation for both slopes.

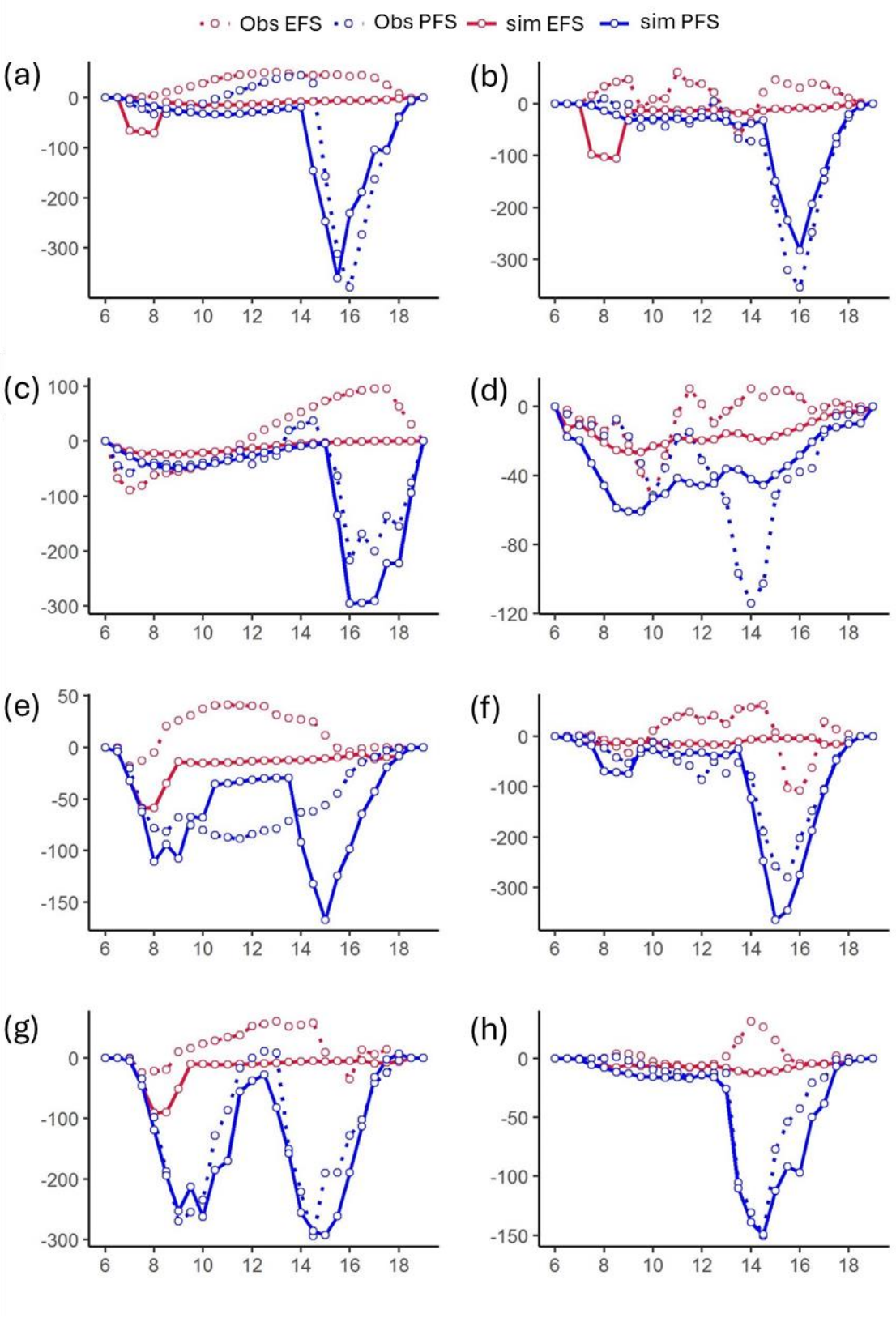

Figure 3.6 The overstory radiation values of site observation and model simulation offset by the reference station radiation. A three-point (equivalent to one hour) moving average is applied and plotted at a 30-minute interval for selected clear (left) and cloudy (right) days for four seasons (from top to bottom, spring, summer, autumn and winter), the x axis is the hour of the day.

Table 3.2 The correlation coefficient R, and two relative error statistics of the offset values between site observation and model simulation for overstory radiation

		Clear day				Cloudy day			
		spring	summer	autumn	winter	spring	summer	autumn	winter
EFS	R	0.34	0.87	0.19	0.39	-0.18	0.47	-0.38	-0.58
	MAPE	0.12	0.12	0.12	0.16	0.16	0.05	0.16	0.10
	MAPD	0.09	0.08	0.16	0.21	0.07	0.07	0.12	0.15
PFS	R	0.85	0.95	0.39	0.94	0.98	0.41	0.97	0.96
	MAPE	0.08	0.07	0.09	0.11	0.09	0.03	0.13	0.08
	MAPD	0.08	0.05	0.11	0.10	0.05	0.05	0.10	0.10

3.4.3 Understorey radiation

The under-canopy radiation values (offset by the reference station global radiation) are calculated for the same days as in Section 4.2 and compared with the observed net radiation based shortwave radiation data. The R is calculated to evaluate the correlation between model simulation and observation, and the MAPE and MAPD are calculated to evaluate the relative error (Table 3.3).

The results show that the model simulation is well correlated with observed radiation at both the EFS and PFS sites. As can be seen in Figure 3.7, the shading exists for the entire daytime hours at both sites since the offset values are negative for all the seasons and weather conditions. For the EFS site, the offset values are less negative than the PFS site, suggesting that the shading effect in the EFS is weaker than in the PFS. This is likely to be a result of the sparser overstory vegetation cover on the EFS. For both the NFS and SFS sites, the R values are above 0.8 for almost all the examined days. One exception is the clear day in summer, where the model simulation on the EFS largely underestimates the radiation, resulting in a lower R. While the MAPE and MAPD is 0.29 and 0.16, respectively, this indicates that the error is relatively small comparing to the total incident radiation. The underestimation could also be found in spring, which is discussed later in Section 4.4.

Comparing to the overstory radiation, a large improvement on r for the understorey radiation simulation can be found for the EFS site, which demonstrates the capability of the DST model in simulating the canopy shading effect. The MAPE and MAPD are larger than the above-canopy

radiation simulation, but it is still within an acceptable range (MAPE less than 0.34 and MAPD less than 0.18).

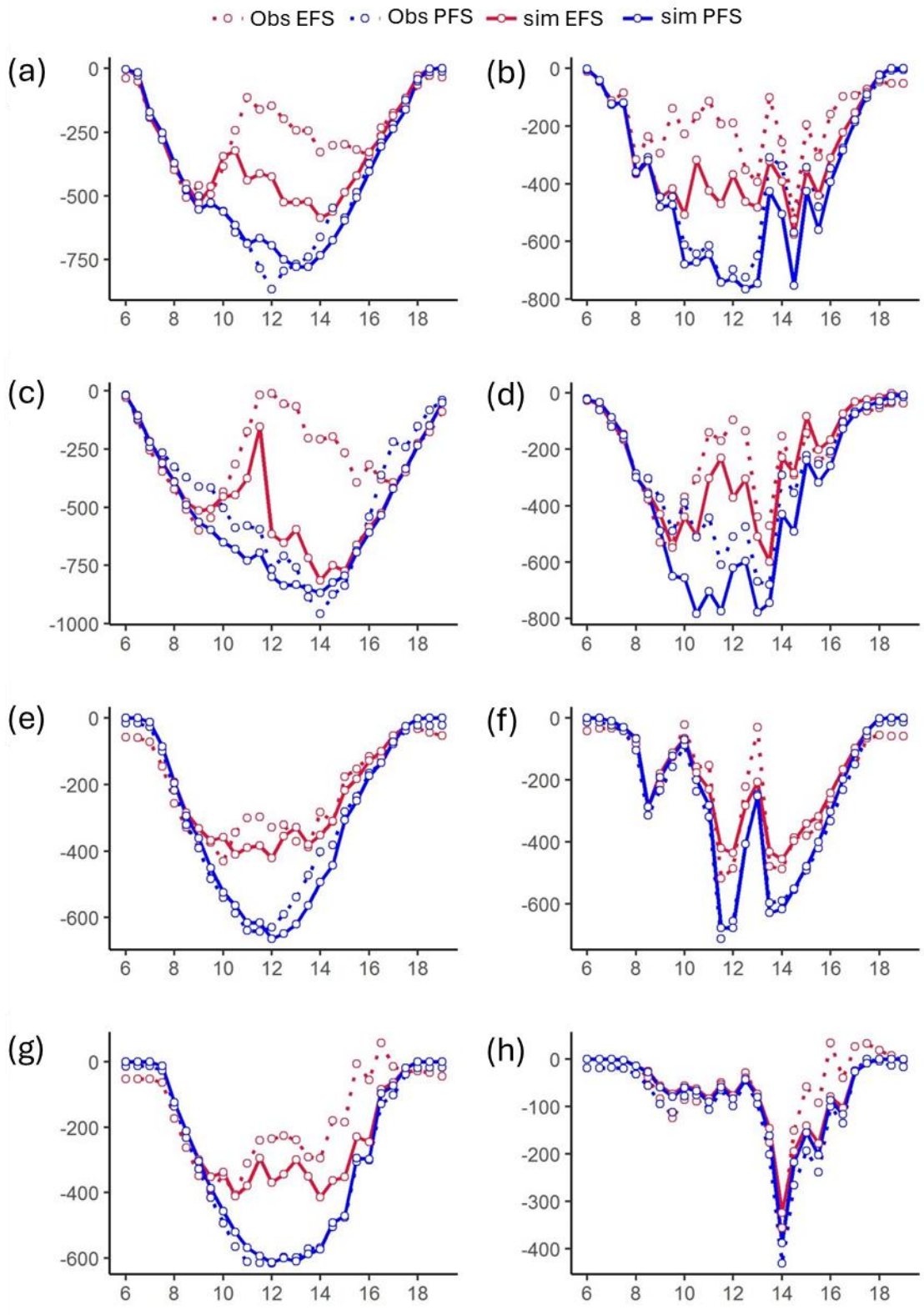

Figure 3.7 The understorey radiation values of site observation and model simulation offset by the reference station radiation. A five-point (equivalent to two hours) moving average is applied and plotted at a 30-minute interval for selected clear (left) and cloudy (right) days for four seasons (from top to bottom, spring, summer, autumn and winter), the x axis is the hour of the day.

Table 3.3 The correlation coefficient R, and two relative error statistics of the offset values between site observation and model simulation for understorey radiation

		Clear day				Cloudy day			
		spring	summer	autumn	winter	spring	summer	autumn	winter
EFS	R	0.69	0.29	0.94	0.82	0.82	0.87	0.94	0.87
	MAPE	0.19	0.29	0.10	0.30	0.26	0.16	0.13	0.32
	MAPD	0.06	0.16	0.07	0.02	0.09	0.18	0.08	0.12
PFS	R	0.98	0.96	0.98	0.99	0.98	0.97	0.99	0.99
	MAPE	0.22	0.34	0.09	0.21	0.26	0.13	0.11	0.24
	MAPD	0.06	0.13	0.08	0.02	0.09	0.18	0.05	0.13

3.4.4 Annual understorey insolation

Daily insolation (MJ/m^2) is the total amount of solar radiation energy received over a given surface area during a day. One year of under canopy insolation data is simulated and compared with the understorey shortwave radiation data. Figure 3.8 shows the daily insolation simulations of the EFS and PFS from April 2013 to April 2014 and the correlation coefficient. A seven-day interval is used for the canopy transmittance calculation to reduce the computation cost (i.e. data storage and processing time), while still capturing the solar geometry variation.

The results of daily insolation over one year show a strong consistency between the simulation and measured data. Compared to the reference radiation (black line), both simulated results of the EFS and PFS sites are much closer to the observation-based estimated radiation at both sites. For the four seasons, the simulated radiation is lower than observation from spring (starting from September 01, 2013) to the end of summer (ending by February 29, 2014). For the remaining days, the simulated radiation is very close to the observation. The most possible reason for this is that the LiDAR derived LAI used in the model are obtained in June 2013. If there are more representative data corresponding to the different seasons as input, the model performance would greatly be improved. In general, the r between observation and the simulation is 0.95 for the EFS and 0.94 for the PFS, indicating that the DST model is capable of simulating the understorey daily insolation.

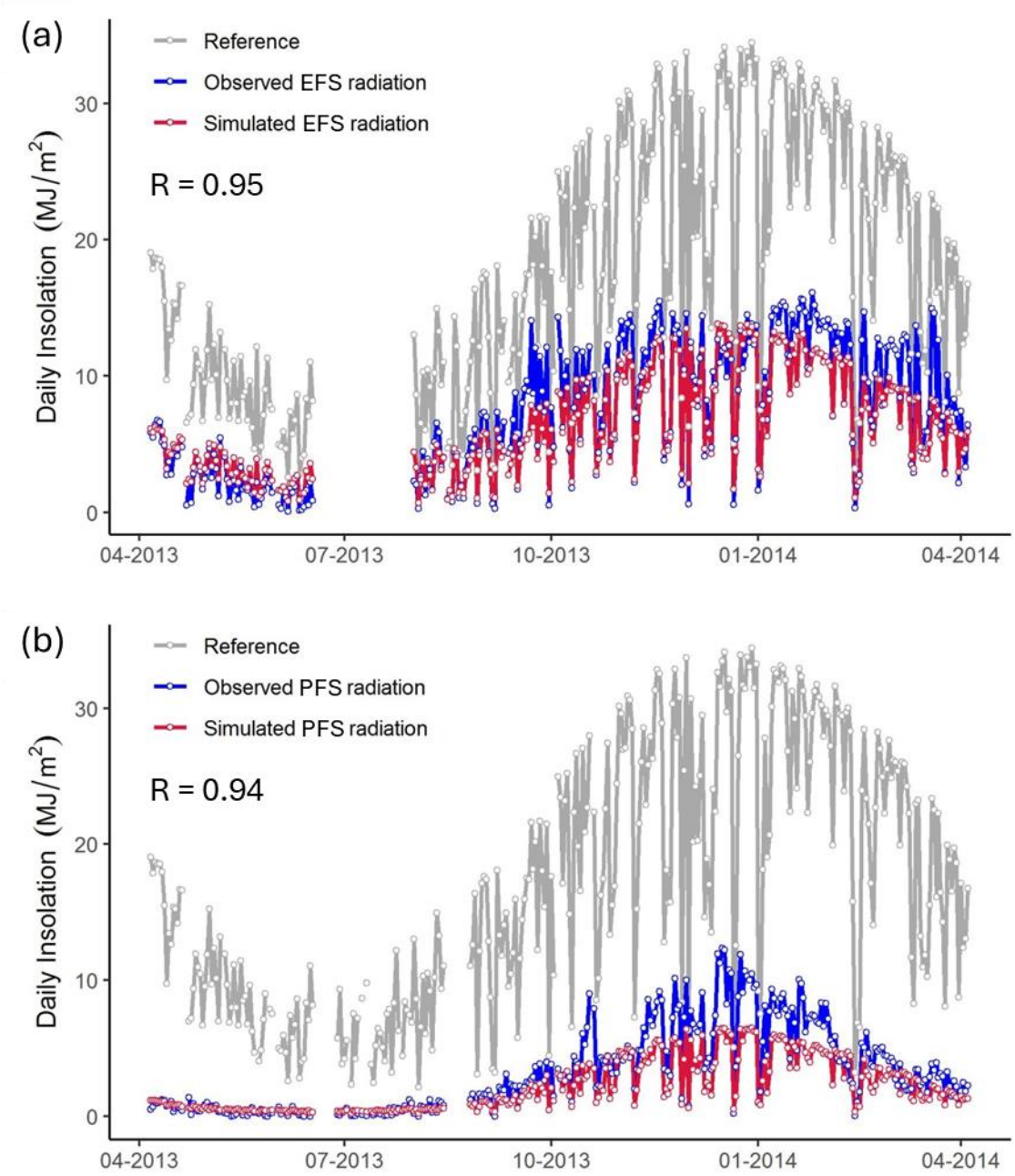

Figure 3.8 Simulated daily understorey insolation (MJ/m^2) in comparison to observed radiation and the reference radiation: (a) EFS and (b) PFS sites.

3.4.5 Spatial distribution of over and understorey radiation

Figure 3.9 shows the simulated daily insolation of the whole study area. In Figure 3.9, we can see that the simulated radiation on the top of canopy is similar to that in a flat unshaded surface. The difference in simulated insolation between different parts of the catchment is small. For the understorey radiation, the amount of radiation in the northwest area of the catchment is significantly lower than in the southeast. Two factors may account for the difference. 1) The topography effect influences the incident radiation. The northwest area of the catchment is facing south-east with a slope ranging from 10-30˚, while the southeast area of the catchment is facing

north with a slope ranging from 20-30˚. Since the study area is in South Australia and the latitude is about 35°S, the sun rises and moves in the northern sky of the area. Hence, the incident angle of the northwest area of the catchment would be much higher than that of the southeast. For example, the impact of the incident angle to radiation is shown in Figure 3.9 (b), where the black circle area is an exposed area with no shading and faces north with a slope of around 25°. The radiation of this area would be the same as in the northeast corner (around 13 MJ/m^2) if it is a flat surface. However, in Figure 3.9 (a), the simulated insolation is about 15 MJ/m^2. As the circled area is towards sun's position, the incident angle would be smaller than that for a horizontal surface, which explains why the simulated daily radiation on this surface is larger than a horizontal one. 2) Dense overstory vegetation was observed at the northwest area of the catchment (According to chapter 2). Therefore, there would be more radiation being obstructed by the tree canopy.

10,000 sample points for different slope orientations (equator facing and polar facing) are randomly selected (Figure 3.10). Since the data do not meet the parametric statistic test assumptions of normality and homogeneity of variance, the Kruskal-Wallis test is conducted to compare the effect of canopy shading on the incident radiation. There is a significant difference in incident radiation between the different facing slopes and positions ($p<0.001$). The pairwise comparison results indicate that the average insolation for the overstory insolation for both EFS and PFS are significantly different from that of the understorey insolation. For the overstory insolation, the EFS and PFS are significantly different ($p<0.001$) while with similar mean values (11.14 MJ/m^2 for EFS and 10.37 MJ/m^2 for PFS). For under-canopy insolation, the average insolation for EFS (mean=6.28 MJ/m^2) is significantly larger than from the PFS (mean=2.35 MJ/m^2) with $p<0.001$. The difference in mean value for the under-canopy radiation between the two sites is larger than that of the overstory radiation. This large difference in understorey radiation may help explain the contrasting understorey vegetation between the two slopes in this dry-summer climate site (Figure 3.11).

For the simulated overstory insolation, the maximum and upper quartiles of EFS and PFS are close to each other. However, the minimum and lower quartiles for PFS are smaller than EFS, indicating that the upper limit of insolation has no difference for the two opposite hill slopes. More canopy shading exists on the PFS since it is polar facing, which results in the difference in minimum and lower quartiles. The simulated understorey insolation is generally lower than the overstory insolation as expected. However, on the EFS, the maximum of the simulated understorey insolation is even larger than the simulation of overstory insolation. The slope orientation accounts for this discrepancy since the equator facing slope can receive more irradiance than a horizontal plane. Here the simulated overstory insolation is meant for a horizontal plane above the canopy. It may be different from the insolation the canopy actually receives due to a possible difference in solar incident angles to the canopy between the two slopes. The current DST model does not

simulate this difference. Altogether these results suggest that the DST model can well simulate the spatial variability of solar radiation distribution over and understorey surface on complex terrain.

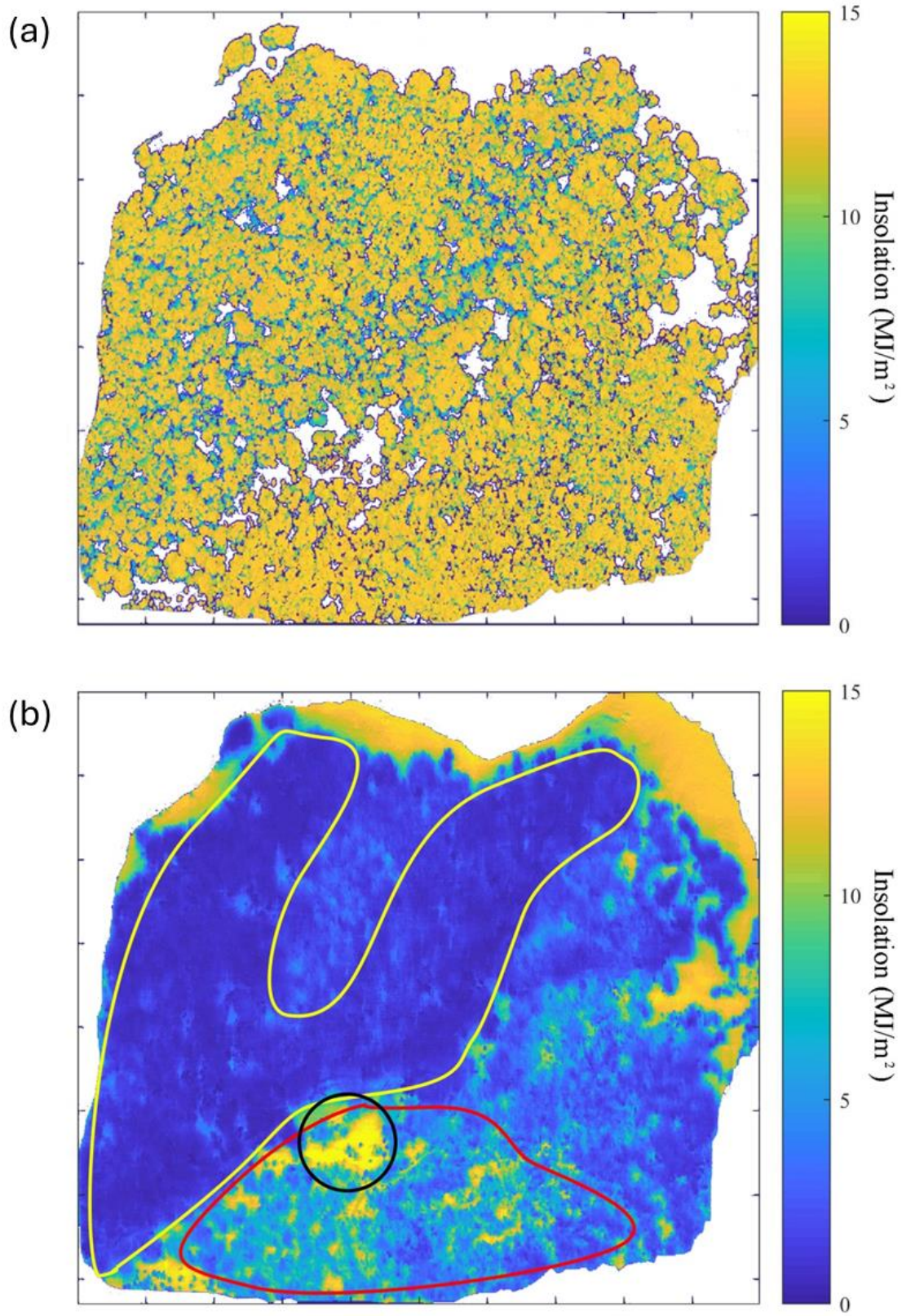

Figure 3.9 The simulated daily insolation (MJ/m2) of the study area on 14 April 2014 for (a) overstory and (b) understorey. The area marked in red has north facing slopes, and the area marked in yellow has south facing slopes. The black circle identifies an open area with no shading and faces north with a slope of around 25°.

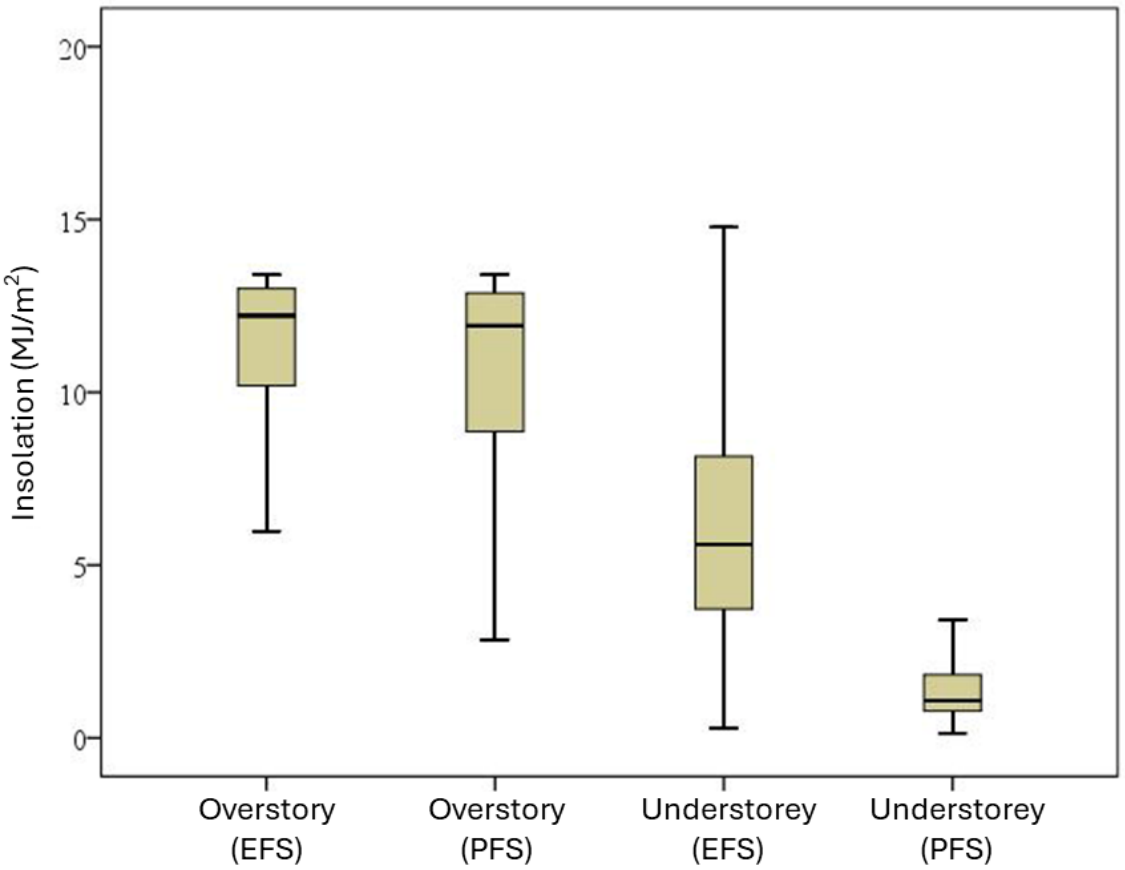

Figure 3.10 Statistics of simulated daily insolation (MJ/m2) of randomly selected 10,000 grid cells of the study area on 14 April 2014 for over and understorey of the equator facing vs. polar facing slopes of the catchment.

Figure 3.11 Photos showing the understorey conditions of the (a) EFS and (b) PFS sites, taken on 4 June 2020.

3.5 Conclusion

This chapter introduces the method development and validation of the DST model. This model is proposed to simulate the spatial and temporal distribution of actual shortwave radiation in woodlands for both overstory and understorey layers. The model simulations, in general, agree well with the observations. For the understorey surface, a significant difference in daily insolation is found for opposite north and south slope orientation. Those finding indicate that the DST model is capable to capture the shading effect caused by topographic and vegetation canopy.

Being able to simulate radiation fields in areas of complex terrain with variable vegetation cover opens a diverse set of possibilities for soil scientists, ecologists, hydrologists, geomorphologists, and other earth scientists for which accurate estimations of surface energy loads are important. For example, our model provides a key variable for hydrologist to examine ET patterns below and under the canopy conditions in a distributed way. Other potential uses include insolation simulation to help to accurately find thermal shelters (canopies that shelter an animal from microclimatic extremes) in the forest, which has been increasingly studied in biological investigations due to global warming (Melin et al., 2014).

In this study, the estimated understorey radiation serves as a critical input for modelling understorey ET (see chapter 5). By accurately capturing the radiation dynamics beneath the canopy, the DST model enhances our understanding of ecohydrological processes in forest/woodland environments and provides an effective tool for ecosystem water resources management.

3.6 References

Amanatides, J., & Woo, A. (1987). A fast voxel traversal algorithm for ray tracing. Eurographics,
Antonanzas-Torres, F., Urraca, R., Polo, J., Perpiñán-Lamigueiro, O., & Escobar, R. (2019). Clear sky solar irradiance models: A review of seventy models. *Renewable and Sustainable Energy Reviews*, *107*, 374-387.
Badescu, V., Gueymard, C. A., Cheval, S., Oprea, C., Baciu, M., Dumitrescu, A., Iacobescu, F., Milos, I., & Rada, C. (2012). Computing global and diffuse solar hourly irradiation on clear sky. Review and testing of 54 models. *Renewable and Sustainable Energy Reviews*, *16*(3), 1636-1656.
Bode, C. A., Limm, M. P., Power, M. E., & Finlay, J. C. (2014). Subcanopy Solar Radiation model: Predicting solar radiation across a heavily vegetated landscape using LiDAR and GIS solar radiation models. *Remote Sensing of Environment*, *154*, 387-397. https://doi.org/https://doi.org/10.1016/j.rse.2014.01.028
Boland, J., Scott, L., & Luther, M. (2001). Modelling the diffuse fraction of global solar radiation on a horizontal surface. *Environmetrics: The official journal of the International Environmetrics Society*, *12*(2), 103-116.
Campbell, G. S., & Norman, J. M. (1998). The light environment of plant canopies. In *An introduction to environmental biophysics* (pp. 247-278). Springer.
Crosby, C. J., Arrowsmith, J. R., & Nandigam, V. (2020). Zero to a trillion: advancing earth surface process studies with open access to high-resolution topography. In *Developments in Earth Surface Processes* (Vol. 23, pp. 317-338). Elsevier.
Da Silva, D., Balandier, P., Boudon, F., Marquier, A., & Godin, C. (2012). Modeling of light transmission under heterogeneous forest canopy: an appraisal of the effect of the precision level of crown description. *Annals of forest science*, *69*(2), 181-193.
Da Silva, D., Boudon, F., Godin, C., & Sinoquet, H. (2008). Multiscale framework for modeling and analyzing light interception by trees. *Multiscale Modeling & Simulation*, *7*(2), 910-933.
de Castro, F., & Fetcher, N. (1998). Three dimensional model of the interception of light by a canopy. *Agricultural and Forest Meteorology*, *90*(3), 215-233. https://doi.org/https://doi.org/10.1016/S0168-1923(97)00097-X
Dozier, J. (1980). A clear-sky spectral solar radiation model for snow-covered mountainous terrain. *Water Resources Research*, *16*(4), 709-718. https://doi.org/https://doi.org/10.1029/WR016i004p00709
Dozier, J., Bruno, J., & Downey, P. (1981). A faster solution to the horizon problem. *Computers & Geosciences*, *7*(2), 145-151.
Dubayah, R., & Rich, P. M. (1995). Topographic solar radiation models for GIS. *International Journal of Geographical Information Systems*, *9*(4), 405-419. https://doi.org/10.1080/02693799508902046
Duffie, J. A., & Beckman, W. A. (2013). *Solar engineering of thermal processes*. John Wiley & Sons.
Erdélyi, R., Wang, Y., Guo, W., Hanna, E., & Colantuono, G. (2014). Three-dimensional SOlar RAdiation Model (SORAM) and its application to 3-D urban planning. *Solar energy*, *101*, 63-73. https://doi.org/https://doi.org/10.1016/j.solener.2013.12.023
Fan, Y., Clark, M., Lawrence, D. M., Swenson, S., Band, L. E., Brantley, S. L., Brooks, P. D., Dietrich, W. E., Flores, A., Grant, G., Kirchner, J. W., Mackay, D. S., McDonnell, J. J., Milly, P. C. D., Sullivan, P. L., Tague, C., Ajami, H., Chaney, N., Hartmann, A., . . . Yamazaki, D. (2019). Hillslope Hydrology in Global Change Research and Earth System Modeling. *Water Resources Research*, *55*(2), 1737-1772. https://doi.org/https://doi.org/10.1029/2018WR023903
Gueymard, C. A. (2009). Direct and indirect uncertainties in the prediction of tilted irradiance for solar engineering applications. *Solar energy*, *83*(3), 432-444. https://doi.org/https://doi.org/10.1016/j.solener.2008.11.004
Gueymard, C. A., & Myers, D. R. (2008). Validation and ranking methodologies for solar radiation models. In *Modeling solar radiation at the earth's surface* (pp. 479-510). Springer.
Gutiérrez-Jurado, H. A., & Vivoni, E. R. (2013). Ecogeomorphic expressions of an aspect-controlled semiarid basin: II. Topographic and vegetation controls on solar irradiance. *Ecohydrology*, *6*(1), 24-37. https://doi.org/https://doi.org/10.1002/eco.1263
Hay, J. E. (1993). Calculating solar radiation for inclined surfaces: Practical approaches. *Renewable Energy*, *3*(4), 373-380. https://doi.org/https://doi.org/10.1016/0960-1481(93)90104-O

Jackson, E. K., Roberts, W., Nelsen, B., Williams, G. P., Nelson, E. J., & Ames, D. P. (2019). Introductory overview: Error metrics for hydrologic modelling–A review of common practices and an open source library to facilitate use and adoption. *Environmental Modelling & Software*, *119*, 32-48.
Jiang, B., Zhang, Y., Liang, S., Wohlfahrt, G., Arain, A., Cescatti, A., Georgiadis, T., Jia, K., Kiely, G., & Lund, M. (2015). Empirical estimation of daytime net radiation from shortwave radiation and ancillary information. *Agricultural and Forest Meteorology*, *211*, 23-36.
Kambezidis, H., Psiloglou, B., Karagiannis, D., Dumka, U., & Kaskaoutis, D. (2016). Recent improvements of the Meteorological Radiation Model for solar irradiance estimates under all-sky conditions. *Renewable Energy*, *93*, 142-158.
Khatib, T., Mohamed, A., Mahmoud, M., & Sopian, K. (2015). Optimization of the tilt angle of solar panels for Malaysia. *Energy sources, part A: Recovery, utilization, and environmental effects*, *37*(6), 606-613.
Kondratyev, K. J., & Manolova, M. (1960). The radiation balance of slopes. *Solar energy*, *4*(1), 14-19.
Kumar, L., Skidmore, A. K., & Knowles, E. (1997). Modelling topographic variation in solar radiation in a GIS environment. *International Journal of Geographical Information Science*, *11*(5), 475-497.
Lefèvre, M., Oumbe, A., Blanc, P., Espinar, B., Gschwind, B., Qu, Z., Wald, L., Schroedter-Homscheidt, M., Hoyer-Klick, C., Arola, A., Benedetti, A., Kaiser, J. W., & Morcrette, J. J. (2013). McClear: a new model estimating downwelling solar radiation at ground level in clear-sky conditions. *Atmos. Meas. Tech.*, *6*(9), 2403-2418. https://doi.org/10.5194/amt-6-2403-2013
Li, X., Zhang, S., & Chen, Y. (2016). Error assessment of grid-based diffuse solar radiation models. *International Journal of Geographical Information Science*, *30*(10), 2032-2049. https://doi.org/10.1080/13658816.2016.1155215
Liang, J., Gong, J., Li, W., & Ibrahim, A. N. (2014). A visualization-oriented 3D method for efficient computation of urban solar radiation based on 3D–2D surface mapping. *International Journal of Geographical Information Science*, *28*(4), 780-798. https://doi.org/10.1080/13658816.2014.880168
Liu, B. Y., & Jordan, R. C. (1963). The long-term average performance of flat-plate solar-energy collectors: with design data for the US, its outlying possessions and Canada. *Solar energy*, *7*(2), 53-74.
Marsh, C. B., Pomeroy, J. W., & Spiteri, R. J. (2012). Implications of mountain shading on calculating energy for snowmelt using unstructured triangular meshes. *Hydrological Processes*, *26*(12), 1767-1778.
McKenney, D. W. (1999). Calibration and sensitivity analysis of a spatially-distributed solar radiation model. *International Journal of Geographical Information Science*, *13*(1), 49-65. https://doi.org/10.1080/136588199241454
Metzen, D., Sheridan, G. J., Benyon, R. G., Bolstad, P. V., Griebel, A., & Lane, P. N. (2019). Spatio-temporal transpiration patterns reflect vegetation structure in complex upland terrain. *Science of the Total Environment*, *694*, 133551.
Milenković, M., Wagner, W., Quast, R., Hollaus, M., Ressl, C., & Pfeifer, N. (2017). Total canopy transmittance estimated from small-footprint, full-waveform airborne LiDAR. *ISPRS Journal of Photogrammetry and Remote Sensing*, *128*, 61-72.
Musselman, K. N., Margulis, S. A., & Molotch, N. P. (2013). Estimation of solar direct beam transmittance of conifer canopies from airborne LiDAR. *Remote Sensing of Environment*, *136*, 402-415.
Nyman, P., Metzen, D., Hawthorne, S. N. D., Duff, T. J., Inbar, A., Lane, P. N. J., & Sheridan, G. J. (2017). Evaluating models of shortwave radiation below Eucalyptus canopies in SE Australia. *Agricultural and Forest Meteorology*, *246*, 51-63. https://doi.org/https://doi.org/10.1016/j.agrformet.2017.05.025
Peng, S., Zhao, C., & Xu, Z. (2014). Modeling spatiotemporal patterns of understory light intensity using airborne laser scanner (LiDAR). *ISPRS Journal of Photogrammetry and Remote Sensing*, *97*, 195-203. https://doi.org/https://doi.org/10.1016/j.isprsjprs.2014.09.003
Popescu, S. C., & Zhao, K. (2008). A voxel-based lidar method for estimating crown base height for deciduous and pine trees. *Remote Sensing of Environment*, *112*(3), 767-781.
Reindl, D. T., Beckman, W. A., & Duffie, J. A. (1990). Diffuse fraction correlations. *Solar energy*, *45*(1), 1-7.
Ridley, B., Boland, J., & Lauret, P. (2010). Modelling of diffuse solar fraction with multiple predictors. *Renewable Energy*, *35*(2), 478-483.

Ross, J. (2012). *The radiation regime and architecture of plant stands* (Vol. 3). Springer Science & Business Media.
Ruiz-Arias, J. A., Cebecauer, T., Tovar-Pescador, J., & Šúri, M. (2010). Spatial disaggregation of satellite-derived irradiance using a high-resolution digital elevation model. *Solar energy*, *84*(9), 1644-1657.
Serrano, D., Marín, M., Núñez, M., Gandía, S., Utrillas, M., & Martínez-Lozano, J. (2015). Relationship between the effective cloud optical depth and different atmospheric transmission factors. *Atmospheric Research*, *160*, 50-58.
Seyednasrollah, B., & Kumar, M. (2014). Net radiation in a snow-covered discontinuous forest gap for a range of gap sizes and topographic configurations [https://doi.org/10.1002/2014JD021809]. *Journal of Geophysical Research: Atmospheres*, *119*(17), 10,323-310,342. https://doi.org/https://doi.org/10.1002/2014JD021809
Sheng, J., Wilson, J. P., & Lee, S. (2009). Comparison of land surface temperature (LST) modeled with a spatially-distributed solar radiation model (SRAD) and remote sensing data. *Environmental Modelling & Software*, *24*(3), 436-443. https://doi.org/https://doi.org/10.1016/j.envsoft.2008.09.003
Tang, W., Qin, J., Yang, K., Liu, S., Lu, N., & Niu, X. (2016). Retrieving high-resolution surface solar radiation with cloud parameters derived by combining MODIS and MTSAT data. *Atmos. Chem. Phys.*, *16*(4), 2543-2557. https://doi.org/10.5194/acp-16-2543-2016
Timlin, D. J., Fleisher, D. H., Kemanian, A. R., & Reddy, V. R. (2014). Plant density and leaf area index effects on the distribution of light transmittance to the soil surface in maize. *Agronomy Journal*, *106*(5), 1828-1837.
Wild, M. (2009). Global dimming and brightening: A review. *Journal of Geophysical Research: Atmospheres*, *114*(D10). https://doi.org/https://doi.org/10.1029/2008JD011470
Xu, X., Guan, H., Skrzypek, G., & Simmons, C. T. (2017). Response of leaf stable carbon isotope composition to temporal and spatial variabilities of aridity index on two opposite hillslopes in a native vegetated catchment. *Journal of Hydrology*, *553*, 214-223.
Yang, D. (2016). Solar radiation on inclined surfaces: Corrections and benchmarks. *Solar energy*, *136*, 288-302.
Yu, B., Liu, H., Wu, J., & Lin, W.-M. (2009). Investigating impacts of urban morphology on spatio-temporal variations of solar radiation with airborne LIDAR data and a solar flux model: a case study of downtown Houston. *International Journal of Remote Sensing*, *30*(17), 4359-4385. https://doi.org/10.1080/01431160802555846
Zajaczkowski, J., Wong, K., & Carter, J. (2013). Improved historical solar radiation gridded data for Australia. *Environmental Modelling & Software*, *49*, 64-77. https://doi.org/https://doi.org/10.1016/j.envsoft.2013.06.013
Zeng, K., Zheng, G., Ma, L., Ju, W., & Pang, Y. (2019). Modelling Three-Dimensional Spatiotemporal Distributions of Forest Photosynthetically Active Radiation Using UAV-Based Lidar Data. *Remote Sensing*, *11*(23), 2806. https://www.mdpi.com/2072-4292/11/23/2806
Zhang, S., Li, X., & She, J. (2020). Error assessment of grid-based terrain shading algorithms for solar radiation modeling over complex terrain. *Transactions in GIS*, *24*(1), 230-252.
Zou, C. B., Barron-Gafford, G. A., & Breshears, D. D. (2007). Effects of topography and woody plant canopy cover on near-ground solar radiation: Relevant energy inputs for ecohydrology and hydropedology. *Geophysical Research Letters*, *34*(24).

4 UNDERSTOREY EVAPOTRANSPIRATION MODELLING AND MAPPING

Abstract

While extensive research has focused on evapotranspiration (ET) from forest canopies, the spatial distributions of ET in the understorey remain poorly understood. This study developed a method to estimate spatially distributed understorey ET by integrating the Maximum Entropy Production (MEP) model with airborne thermal surveys. Validation against ground-truth data showed good model accuracy (R^2 = 0.93, RMSE = 0.03 mm/h), confirming its efficacy across different land cover types, including open and understorey areas. The results revealed significant spatial heterogeneity in understorey ET, with distinct responses observed in areas of varying vegetation cover and topographic attributes. This method provides a solution for investigating vertical water consumption in forests and woodlands, contributing to assessing ecosystem water use efficiency and improving water resource and vegetation management strategies.

4.1 Introduction

ET is a land-surface process of coupled energy and water fluxes. ET returns water from the soil and plants into the atmosphere, which is the major component of the terrestrial water balance (Allen et al., 2005; Poon & Kinoshita, 2018). While considerable research effort has been dedicated to studying ET at the forest canopy level, the role of the understorey surface has received less attention (Iida et al., 2020). This gap is especially notable in understanding the spatial distributions of ET across the surface layer of forest/woodland ecosystems. Monitoring understorey ET is challenging due to diverse vegetation types, variable light conditions, and distinct microclimates from the ambient environment. The conventional methods of ET measurement often overlook understorey ET, focusing instead on the more accessible overstory canopy levels.

Numerous methods have been proposed to measure ET or its components. Field-based techniques such as gas exchange chamber, sap flow, and soil weighing lysimeter directly measure plant transpiration and soil evaporation at the plant scale (Yang et al., 2000; Liu et al., 2002; Stannard & Weltz, 2006; Pieters et al., 2022). Bowen ratio systems, eddy covariance (EC) towers, and large-aperture scintillometers are the state-of-art techniques for ET measurement at the field scale (Wolf et al., 2008; Zhang et al., 2008; Zhang et al., 2014; Anapalli et al., 2018). However, the implementation of above-mentioned methods can be costly and challenging, and these methods have limitations when the surface is heterogenous and topographically complex.

With the advancement of remote sensing technology, a variety of models have been developed to utilize satellite imagery for estimating and mapping ET across a wide range of spatial and temporal

scales (Chen & Liu, 2020; Acharya et al., 2021; Anderson et al., 2024). Among them, the surface energy balance (SEB) models are most widely used to simulate actual surface ET combined with remote sensing land surface temperature (LST) data (Taheri et al., 2022). The basic assumption of an SEB model is that the net surface energy is partitioned into sensible, latent, and soil heat flux. LST serves as an important input for estimating latent heat flux. One-layer and two-layer SEB models have been widely used to provide ET estimates (Bastiaanssen et al., 1998; Allen et al., 2007; Sun et al., 2009; Yang et al., 2015). Yet, satellite remote sensing LST data are only reliable under clear-sky conditions (Zhang et al., 2016). And the accuracy of the SEB models is strongly affected by model parameters such as surface resistance (Ter Steege et al., 2013; Hu et al., 2014; D. Xu et al., 2019; Taheri et al., 2022).

Recently, the development of Unmanned Aerial Vehicle (UAV) provides new opportunities for mapping surface heat flux at decimetre scale (Hoffmann et al., 2016). For example, Ramin Heidarian et al. (2022) use the ETLook model to monitor farmland ET by fusing UAV and Landsat imagery. Mokari et al. (2022) use UAV-based thermal imagery combined with a modified Senay's model to estimate real-time pecan water consumption and actual ET. Feng et al. (2022); Yan et al. (2023) use a tri-temperature model together with UAV based thermal imagery to estimate the actual ET in unban and wetland environments.

Although accurate estimates of ecosystem ET are important for water balance studies, the partition of ET into its components (over- and understorey vegetation) for gaining a deeper understanding of the water use of different vegetation species is challenging. Previous studies have found significant but variable contribution of the understorey to the total forest ET (Landuyt et al., 2019). For instance, stable isotope measurements indicate that understorey ET accounts for 30% of the total ecosystem ET in a semi-arid savanna woodland (Yepez et al., 2003). Eddy covariance measurements show that one third (45%) of total ecosystem ET in a Siberian boreal forest (montane forest) comes from understorey (Iida et al., 2009; Wolf et al., 2024). Point scale ET measurements using EC and stable isotope method do not provide the spatial distribution of ET in heterogeneous understorey environments. Meanwhile, the existing remote sensing techniques cannot directly measure understorey processes. Consequently, modelling and mapping ET of understorey vegetation in forested regions remains challenging.

The objectives of this chapter are to 1) establish a robust and effective method for estimating understorey surface ET using airborne thermal imagery and the Maximum Entropy Production (MEP) model with net radiation and surface temperature for the understorey surface; and 2) investigate the contribution of understorey ET to the total ecosystem ET for two typical settings and understand influence factors. This research will enhance our understanding of hydrological dynamics in the understorey layer for improving water management and ecological conservation practices.

4.2 Methodology

4.2.1 Study area and stations

The first study area is located in a floodplain (140.58°E, 34.35°S) located at Bookpurnong and a vegetated catchment (138.64° E, 35.21° S) at Mount Wilson in South Australia (Figure 4.1). The Bookpurnong floodplain, a subset of the Murray-Darling system. is located within the semi-arid inland of Australia with a heterogeneous vegetation cover and long-term average annual rainfall of 265 mm (Doble et al., 2005). Three representative areas were selected for ET monitoring and mapping characterized by distinct vegetation species: (1) *Eucalyptus camaldulensis*, commonly known as River Red Gum (RRG); (2) *Muehlenbeckia florulenta* (Lignum); and (3) small bushes *Sclerolaena sp.* (Bindyi) and *Atriplex sp.* (Saltbush). In this study, these areas are referred to as the RRG understorey, the Lignum, and the Subshrub site, respectively. The RRG understorey comprises woody vegetation, short herbaceous plants, and bare soil. The second study area is the Mount Wilson site introduced in Chapter 2.

Five MEP stations were installed, each equipped with a NR Lite2 Net Radiometer (positioned at 1.5 meters), an Apogee SI-111SS Infrared Radiometer (at 1.5 meters), and a Vaisala HMP155 temperature/humidity sensor (at 0.3 meters) to measure net radiation, surface temperature, and near-surface air humidity/temperature at 30-minute resolution. Downwelling shortwave radiation was recorded for both the Bookpurnong and Mount Wilson sites in an open area. At Bookpurnong, data were recorded from October 2021 through October 2023, with an interruption during late 2022 to early 2023 due to a flooding event. At Mount Wilson, data were collected from April 2013 to July 2014 on two hillslopes with opposite orientation, referred to as the equator-facing slope (EFS) and the polar-facing slope (PFS).

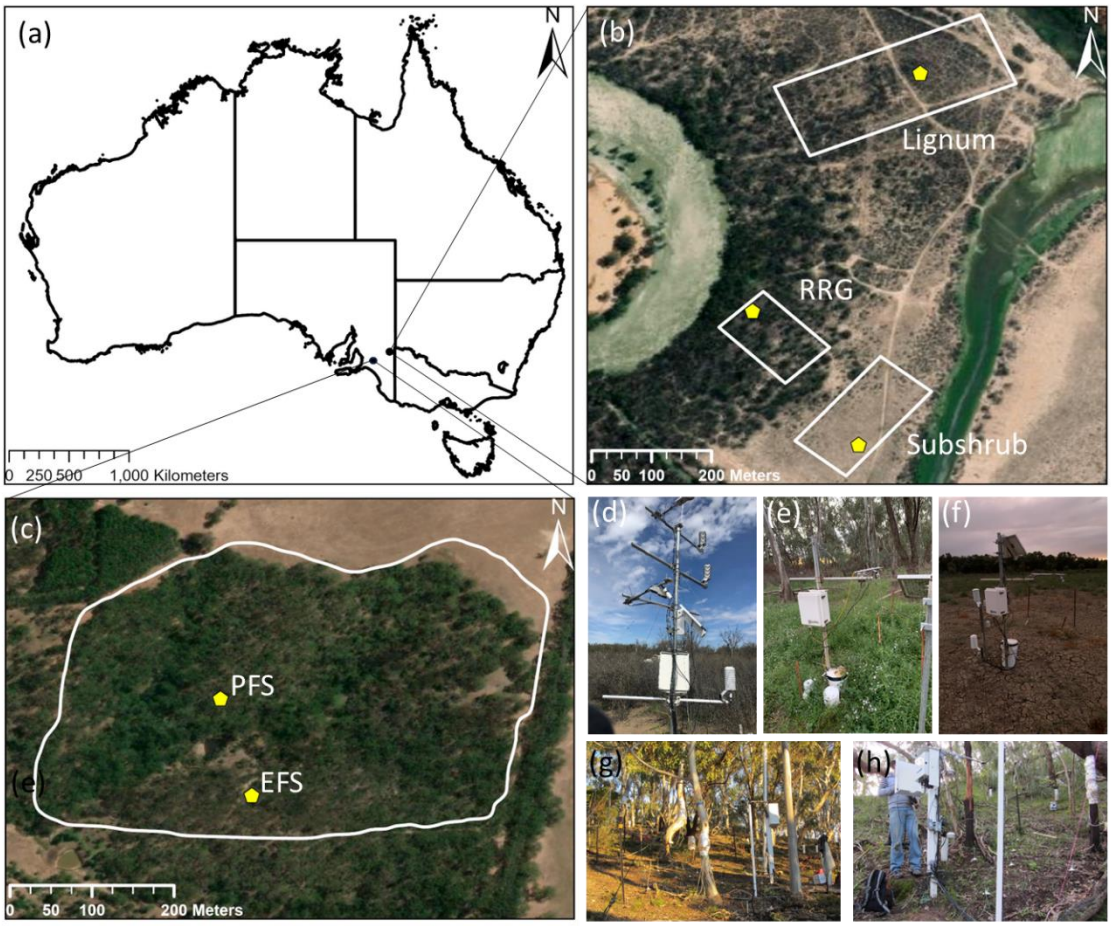

Figure 4.1 (a) Overview of the study areas within Australia. (b) and (c) the location of Bookpurnong and Mount Wilson sites, with yellow pentagons marking the Maximum Entropy Production station locations and white line indicating the drone survey areas. (d), (e), (f), (g) and (h) are the station photos of Lignum, RRG, Subshrub, EFS, and PFS, respectively.

4.2.2 Airborne remote sensing data

Airborne remote sensing data were collected for both study areas. For the Bookpurnong floodplain, a DJI Matrice 300RTK drone was used as the flying platform. A TrueView 410 3DIS laser scanner (LiDAR) mounted on the drone captured forest structure data on March 3, 2022. The LiDAR data was then processed in EVO software to generate 3D point clouds to show the forest structure. Leaf area index (LAI) is calculated based on Equation 2.2. Thermal data were collected using a DJI Zenmuse H20T camera to capture surface-emitted thermal radiation in a single 8-14 µm band. For the Lignum and Subshrub sites, the flight height was 60 m above ground, with a corresponding thermal image resolution of approximately 5 cm. For the River Red Gum understorey site, the flight height was 40 m for a higher spatial resolution to resolve the overstory canopy (approximately 3 cm). The temperature measured by the thermal camera reflects the spectral thermal energy emitted from the surface target pixel through the air column between the pixel and camera. The emissivity of sensed objects was assumed to be 0.95 (Hook et al., 1992). The ambient humidity and temperature measured at corresponding stations were applied to correct for atmosphere using

the DJI Thermal SDK package (https://www.dji.com/downloads/softwares/dji-thermal-sdk). An image mosaic was created using Pix4D mapper software following the standard workflow for thermal camera imagery.

At the Mount Wilson site, airborne surveys were conducted by Airborne Research Australia (ARA). A Diamond HK 36 TTC-ECO sailplane was used as the flying platform. The LiDAR survey was conducted on June 16, 2013, using a Riegl Q560 laser scanner. Thermal data were collected using a FLIR A615 thermal camera at a 750 m height with around 25 cm spatial resolution. The raw data were processed by ARA's specialised team. Table 4.1 lists the details of all thermal survey in two study areas.

Table 4.1 Thermal imagery acquisition information

Study areas	Aircraft model	Thermal camera	Survey area (m^2)	Flight height AGL (m)	Spatial resolution (cm)	Acquisition date
Lignum	DJI Matrice 300	DJI Zenmuse H20T	124×308	60	5	2022/03/04 2022/05/07 2023/09/13 2023/10/18
Subshrub	DJI Matrice 300	DJI Zenmuse H20T	91×183	60	5	2022/03/04 2022/04/10 2022/05/07 2022/06/25 2023/09/13 2023/10/18
RRG	DJI Matrice 300	DJI Zenmuse H20T	85×130	40	3	2022/03/04 2022/04/10 2022/05/07 2022/06/25 2023/09/13 2023/11/17
Mount Wilson	Diamond HK 36 TTC-ECO	FLIR A615	500×350	750	25	2013/11/04 2013/11/18

4.2.3 Satellite remote sensing data

Satellite remote sensing based monthly 30 m ET data was obtained from CSIRO MODIS Reflectance-based Scaling Evapotranspiration (CMRSET) (Guerschman et al., 2009; Guerschman et al., 2022) using optical remote sensing data from MODIS, VIIRS, Landsat, and Sentinel-2 combined with ground meteorological data and calibrated against EC data from 30 flux towers across Australia covering diverse land covers and climates (Guerschman et al., 2022).

4.2.4 ET mapping based on the maximum entropy production model

In this study, surface ET is estimated using the MEP model (Wang & Bras, 2009; Wang & Bras, 2011), which has been increasingly used for modelling surface energy budget and monitoring ET (Wang et al., 2017; Li et al., 2019; D. Xu et al., 2019; Yang et al., 2022; Jia et al., 2023). The MEP model partitions net radiation over land surface into sensible (H), latent (E), and ground (G) heat flux:

$$E = B(\sigma)H \tag{4.1}$$

$$B(\sigma) = 6\left(\sqrt{1+\frac{11}{36}\sigma} - 1\right) \tag{4.2}$$

$$\sigma = \left(\frac{\lambda^2}{c_p R_v}\frac{q_s}{T_s^2}\right) \tag{4.3}$$

$$G = \frac{B(\sigma)}{\sigma}\frac{I_s}{I_o}H|H|^{-\frac{1}{6}} \tag{4.4}$$

where $B(\sigma)$ is the reciprocal of the Bowen ratio as a function of the dimensionless parameter σ in terms of specific humidity q_s and air temperature T_s close to the evaporating surface, λ is the latent heat of vaporisation based on surface temperature, c_p is the heat capacity of air, R_v is ideal gas constant of water vapour, I_s and I_o are the thermal inertia associated with ground and sensible heat flux, respectively.

The MEP model uses three input variables: net radiation, surface temperature, and surface-specific humidity. Mapping the spatial distribution of these variables under woodland/forest

canopies to estimate understorey ET is challenging due to the mixture of overstorey and understorey pixels in airborne remote sensing imagery. To address this, we developed methods for mapping understorey surface temperature, net radiation, and surface-specific humidity. Structural data, such as LAI and canopy height, were derived from LiDAR datasets, while thermal data were obtained from drone thermal imagery. These datasets were then integrated to estimate understorey ET.

4.2.4.1 Understorey surface temperature

Drone-based thermal imagery captures the composite temperature signals from both the overstory canopy and understorey vegetation, making it challenging to directly extract the signals of understorey surface temperature (Cheung et al., 2021). To address this issue, a combined approach utilizing thermal imagery from drones and LiDAR data was employed in this study to estimate the understorey surface temperature. The conceptual model of the Land Surface Temperature (LST) and Vegetation Index (VI) space demonstrates a strong negative correlation between LST and VI (Gillies et al., 1997; Holzman et al., 2014). Numerous studies have shown that when the data encompasses a wide range of fractional vegetation cover and soil moisture conditions, the scatterplot of LST and VI often has a triangular shape (Carlson et al., 1994; Sun, 2015). This triangular pattern arises because as the VI increases, the soil thermal signal becomes increasingly masked by the overlying vegetation, leading to decreasing temperature. Conversely, when soil moisture is high, LST decreases, resulting in similar temperature profiles for both bare soil and vegetated surfaces (Nemani et al., 1993).

The understorey surface temperature can be estimated using the VI-Ts space approach when vegetation indices are replaced by LAI to effectively capture the spatial distribution of overstory vegetation as the LAI-Ts space has a similar triangular pattern to that of the VI-Ts space. Assuming the impact of soil moisture on temperature is uniform across the relatively small areas, surface temperature is predominantly influenced by the overstory canopy shading. In this triangular space (Figure 4.2), the lower edge (blue line) represents the consistent temperature of the canopy less affected by LAI variations. The upper edge (red line) reflects bare soil temperature strongly influenced by overstory LAI. Given that the actual understorey surface includes various grasses, litter, and shrubs and the upper edge temperature results from direct sunlight exposure, mean temperature is used for each LAI interval (orange dots) as the representative understorey surface temperature. We then obtained a regression equation to link LAI and understorey surface temperature. Upon the relationship is built, a LiDAR-derived Canopy Height Model (CHM) was utilized to separate over and understorey surface (Gaulton & Malthus, 2010). For pixels with taller vegetation cover over 5 m, the understorey surface temperature is estimated based on the relationship.

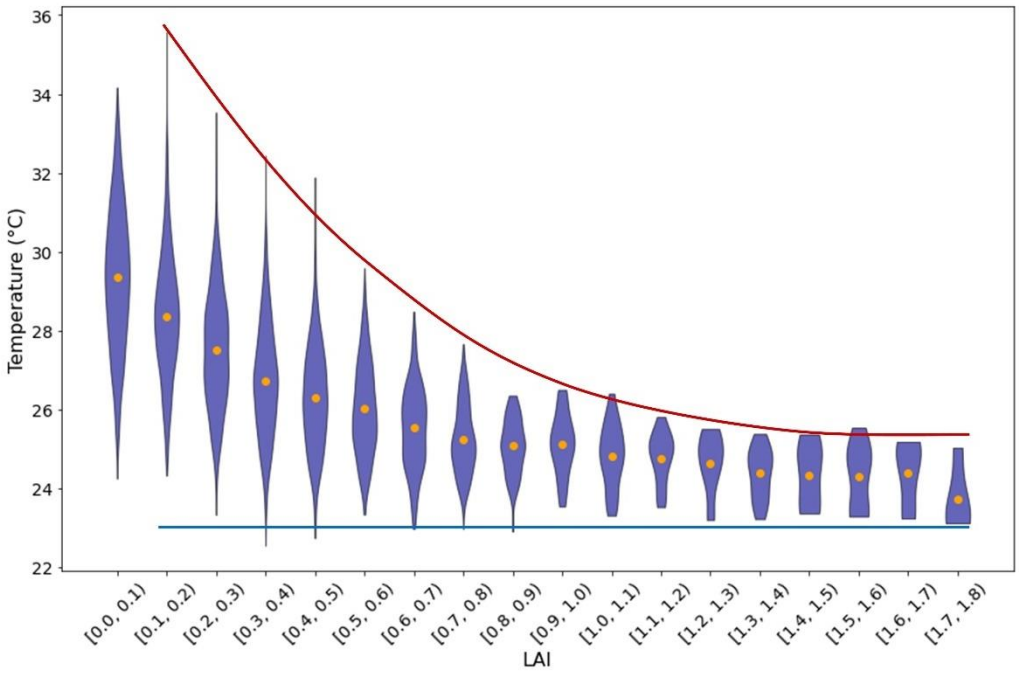

Figure 4.2 Violin plots of temperature for pixel groups, categorized by 0.1 LAI intervals, generated from drone thermal imagery (March 4, 2022) and LiDAR-derived LAI data (March 3, 2022) at the RRG site.

The estimates of the understorey temperature are validated against radiative transfer model and field observations. The temperature distribution of natural forests is simulated using the Large-scale Environmental Remote Sensing and Image Simulation model (LESS), a sophisticated ray-tracing 3D radiative transfer model simulating remote sensing spectral and temperature images (Qi et al., 2019). Figure 4.3 depicts the virtual scene of a 100 x 100 m area with 180 tree crowns with LAI ranging from 0.1 to 3.6. The simulated drone thermal image is created at 14 μm wavelength from a height of 60 meters with high spatial resolution of 0.1 m, while the surface temperature data at 1 m resolution is also simulated. Actual surface temperature data was collected using a Fluke TIS55+ Thermal Imaging Camera, and the corresponding LAI was measured with an LP80 LAI Ceptometer during a drone survey on November 17, 2023. The temperature measurements and the drone survey were carried out simultaneously for direct comparison.

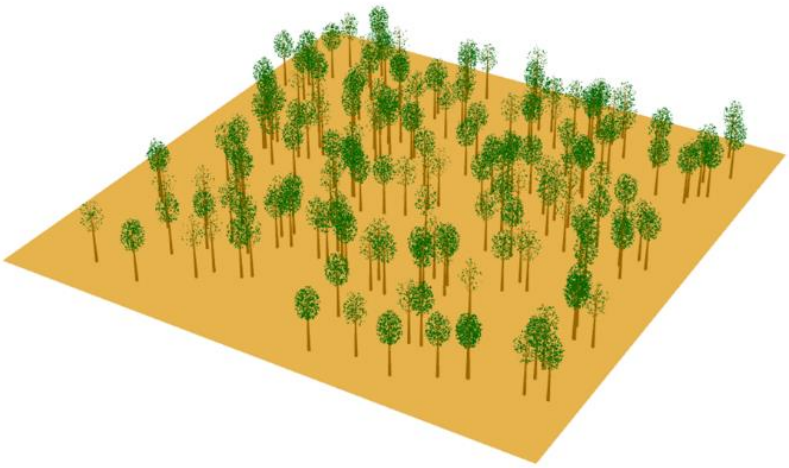

Figure 4.3 Virtual forest scene to assess the accuracy of understorey temperature estimation.

4.2.4.2 Net radiation

The net radiation at the understorey surface was simulated from:

$$R_n = (1 - \alpha_{surf})R_s + \varepsilon_{surf}\varepsilon_{atm\_adj}\sigma T_a^4 - \varepsilon_{surf}\sigma T_s^4 \quad (4.5)$$

where α_{surf} is the surface albedo (0.25), R_s is the downwelling shortwave radiation, ε_{surf} is the surface emissivity (0.95), ε_{atm_adj} is the LAI adjusted atmosphere emissivity for the RRG understorey area (ε_{atm_adj} = (1-*LAI*) * ε_{atm} +*LAI* * ε_{surf}, where ε_{atm} is assumed to be 0.85) for the Lignum and Subshrub areas, overstory LAI is zero, σ is Stefan-Boltzmann constant (5.67×10^{-8} $Wm^{-2}K^{-4}$), and T_a and T_s are the air and surface temperature. A double-shading transposition (DST) model is employed to estimate the downwelling shortwave radiation under vegetation cover (Liu et al., 2022) using the following inputs: (1) Time and location information; (2) Topography and vegetation data, including digital terrain model (DTM) data, digital surface model (DSM) data, and LAI data; and (3) Reference radiation data on a horizontal surface, free of shading effects under the same sky condition over the study area.

4.2.4.3 Surface specific humidity

Surface specific humidity is a critical variable for evapotranspiration modelling using the MEP method. However, obtaining high-resolution surface specific humidity data is challenging due to its dependence on heterogeneous ground features. In this study, a method was developed to predict surface-specific humidity based on surface radiative temperature, and ambient

micrometeorological variables. Stepwise linear regression was employed to establish predictive models, using data from both the Bookpurnong and Mount Wilson sites as inputs. The details of the model development and performance evaluation are provided in a separate article (Gou et al., with Wenjie as the second author; currently under review).

4.2.5 ET temporal upscaling

Since drone-based ET mapping only provides data at the survey times, it is essential to upscale the instantaneous ET to monthly ET (Yang et al., 2013). We assume that the ratio of monthly ET to instantaneous ET remain unchanged for areas with similar vegetation cover. This assumption allows the combination of spatially continuous map of instantaneous ET with temporally continuous point-scale ET observations to produce monthly ET maps. For the surfaces without overstory vegetation (Lignum and Subshrub areas), the observed ratio of monthly to instantaneous ET from the corresponding station is used to upscale the instantaneous ET map to monthly ET map (Equation 4.6). For the understorey area, the instantaneous to monthly ET ratio is adjusted in terms of LAI (Equation 4.7).

$$\frac{ET^{m}{}_{(i,j)}}{ET^{t}{}_{(i,j)}} = \frac{ET^{m}{}_{(S/L)}}{ET^{t}{}_{(S/L)}} \tag{4.6}$$

$$\frac{ET^{m}{}_{(i,j)}}{ET^{t}{}_{(i,j)}} = \frac{LAI_{(i,j)}}{LAI_{(R)}}\frac{ET^{m}{}_{(R)}}{ET^{t}{}_{(R)}} + (1 - \frac{LAI_{(i,j)}}{LAI_{(R)}})\frac{ET^{m}{}_{(S)}}{ET^{d}{}_{(S)}} \tag{4.7}$$

where $ET^{m}{}_{(i,j)}$ and $ET^{t}{}_{(i,j)}$ are the monthly and instantaneous ET at location (i,j), *S*, *L*, and *R* refer to the Subshrub, Lignum, and RRG understorey station measurement respectively. This ET upscaling method is specifically applied to the Bookpurnong area to support the analysis of flood impacts.

4.3 Results and Discussion

4.3.1 MEP derived ET based on the station's measurement

Figure 4.4 (a) shows daily MEP ET at the Bookpurnong site from October 2021 to November 2023 with data missing from October 21, 2022, to May 26, 2023 due to flooding. Daily ET of Lignum site varied from below 0.5 mm to around 3 mm with a mean daily ET of 1 mm for the period of October 2021 to October 2022. ET at the Subshrub and RRG understorey sites was measured from

October 2021 to February 2024 with data missing from November 4, 2022, to March 31, 2023 due to flooding. The daily ET at these two sites was generally lower than that at the Lignum site with mean daily ET values of 0.79 mm and 0.52 mm from October 2021 to October 2022, respectively. Figure 4.4 (b) shows daily MEP ET at the Mount Wilson site from May 2013 to July 2024. The average daily ET was 0.72 mm at the EFS site and 0.36 mm at the PFS site from May 2013 to May 2014.

Generally, ET from all sites have pronounced seasonal cycles characterized by higher daily ET during the summer months and lower ET in autumn and winter consistent with the seasonal cycles of temperature and solar radiation. Understorey ET is generally lower than the open surface due to limited radiation input and lower wind speed. The distinct difference between the EFS and PFS sites illustrates the impact of topography on ET through solar radiation, particularly during winter when ET at the PFS site decreases to nearly zero due to low solar angles, while ET at the EFS site maintains at 0.25 mm.

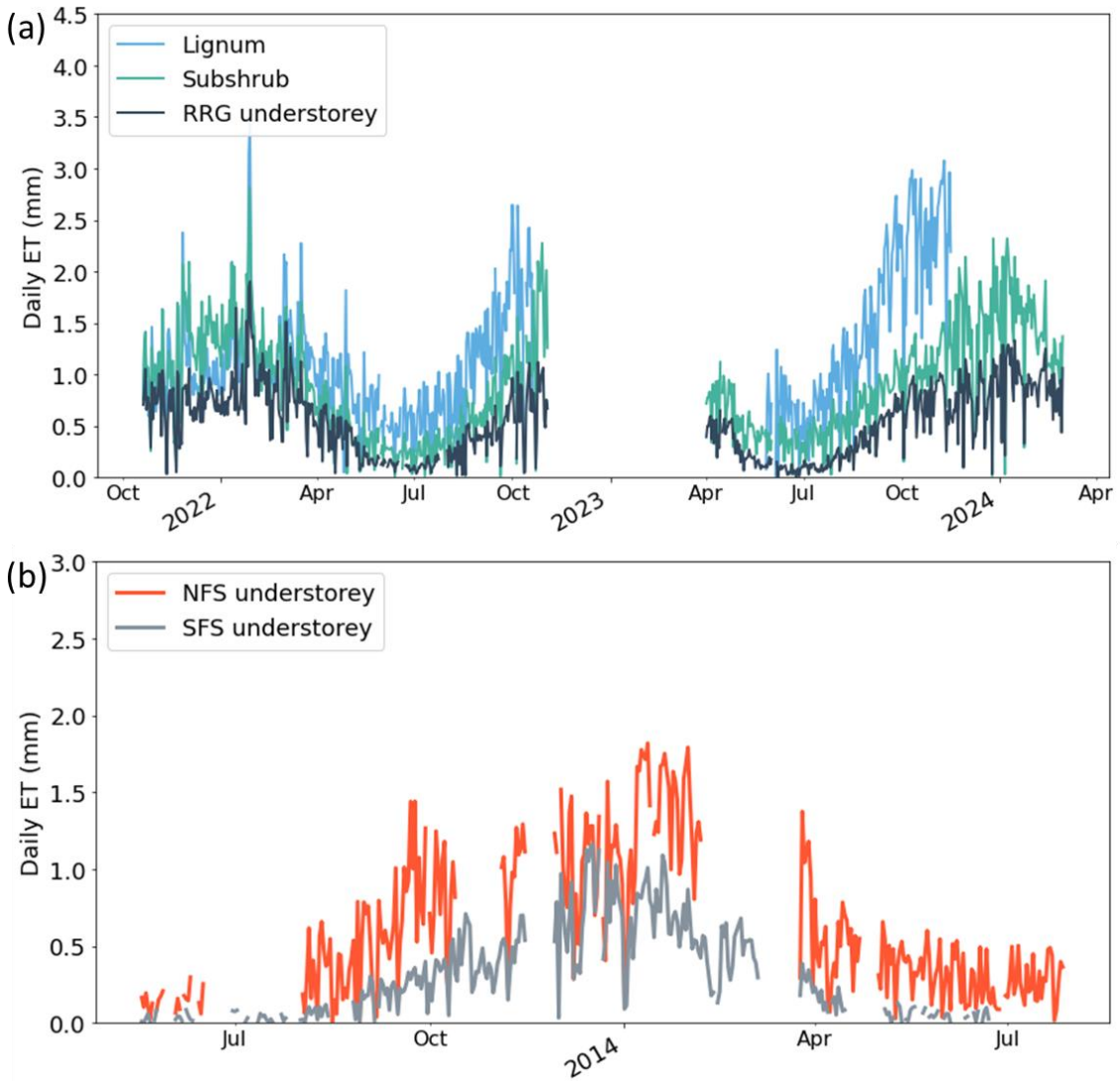

Figure 4.4 Daily ET at floodplain sites (a) and Mount Wilson sites (b) with the seasonal variations. The gaps indicate missing data.

4.3.2 Understorey surface temperature mapping and validation

The virtual scenes were generated with different solar elevation angles to simulate the drone thermal images. Table 4.2 shows the accuracy metrics of understorey temperature estimation with linear and logarithm regressions. Based on the result, the logarithmic regression was used in this analysis as it outperformed linear regression, except when the solar elevation angle was 90°, indicated by lower bias, MAE and RMSE. According to visual scene test result, the surface temperature estimation is more accurate at high solar elevation angles. Figure 4.5 presents the results of logarithmic regression used to estimate understorey temperature over six distinct days in the RRG understorey area.

Table 4.2 Mean Bias, MAE, RMSE, and R^2 of the Linear and Logarithmic Regression Model of understorey temperature under different solar elevation angles

Fitting methods	Solar elevation (°)	Mean bias	MAE	RMSE	R^2
Linear	90	-1.65	1.68	1.87	0.90
	80	2.73	2.76	3.12	0.76
	70	2.95	3.01	3.53	0.59
Logarithm	90	-1.79	1.90	2.18	0.85
	80	-2.31	2.41	2.76	0.76
	70	-1.83	2.23	2.65	0.59

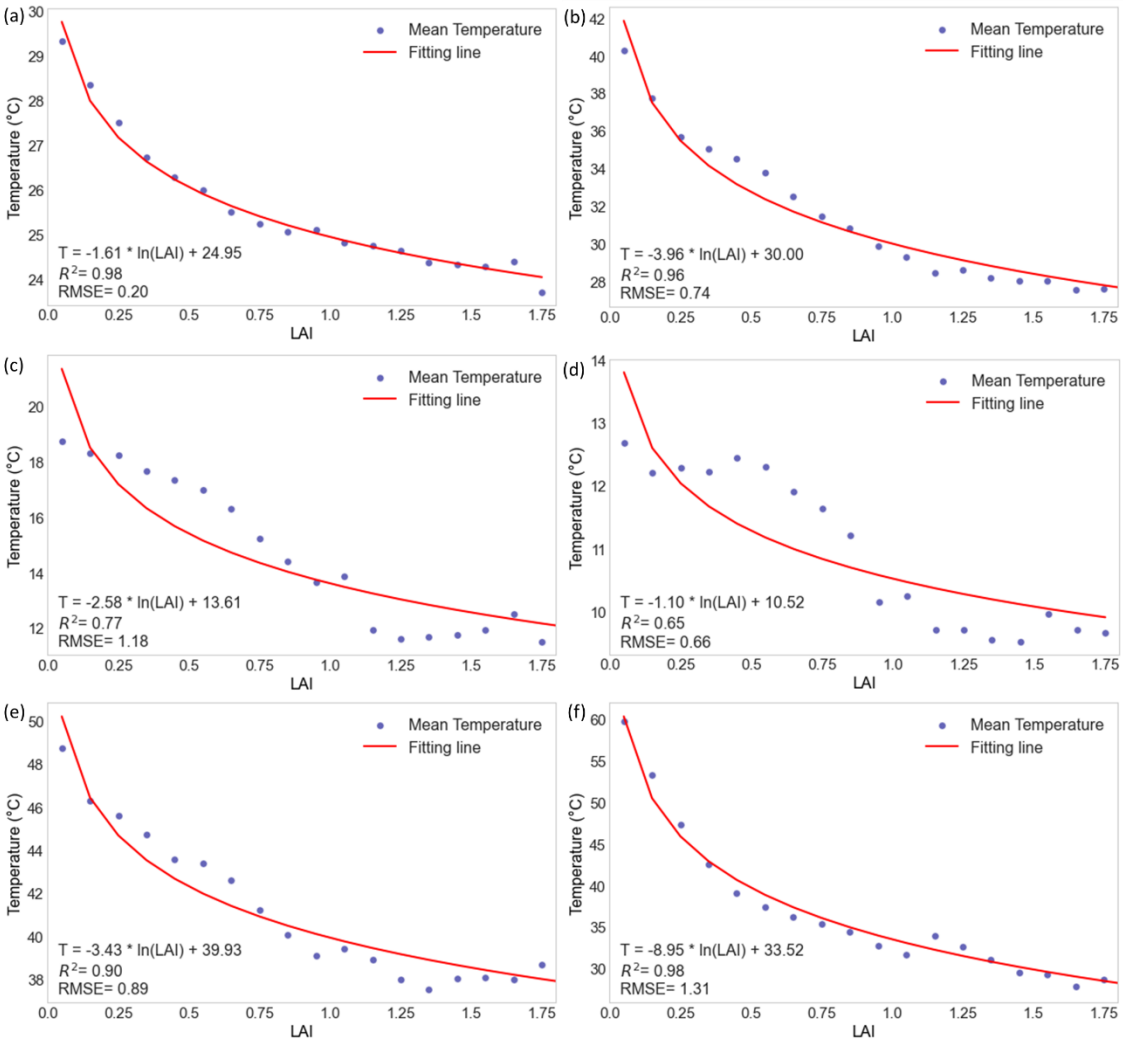

Figure 4.5 Logarithmic regression of understorey surface temperature and mean LAI (interval = 0.1). The thermal images were acquired on (a) March 4, 2022; (b) April 10, 2022; (c) May 7, 2022; (d) June 25, 2022; (e) September 13, 2023; and (f) November 17, 2023.

A comparison of the estimated and ground-measured understorey temperatures is presented in Figure 6. The surface temperature was estimated using a logarithmic regression model based on the thermal imagery (Figure 4.5(f)). The estimated surface temperature is closely correlated with the ground measurements, with R^2 of 0.75 and an RMSE of 2.38°C.

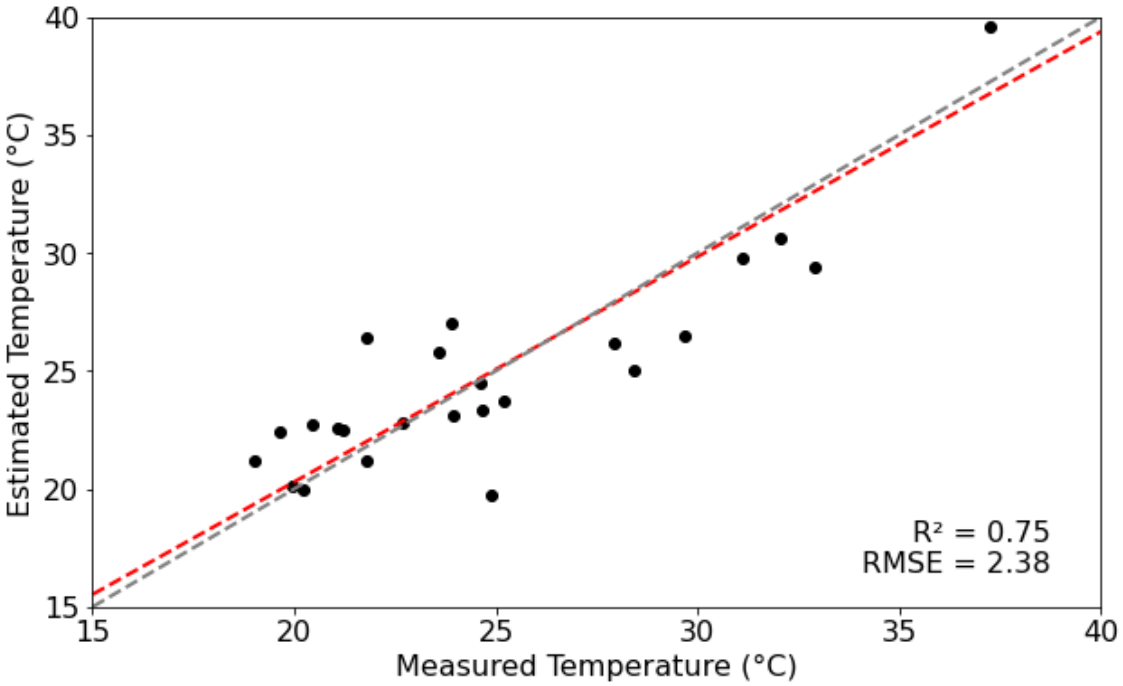

Figure 4.6 Estimated understorey surface temperature vs. ground measurements. The red dashed line is the fitted line, and the black dashed line is the 1:1 line.

4.3.3 ET mapping

Instantaneous ET maps are generated using the MEP model using all the available data from drone thermal surveys (Table 4.1) validated against measurements (Figure 4.7). The linear regression analysis conducted between the ET estimates derived from spatial data and the ET measurements obtained from field observations reveals that the data points are closely aligned with the 1:1 line, with an R^2 of 0.93. The regression slope is 0.90 and the intercept is 0.02. The strong correlation between the mapped ET and station observations illustrates the method's accuracy in representing ET variation spatially.

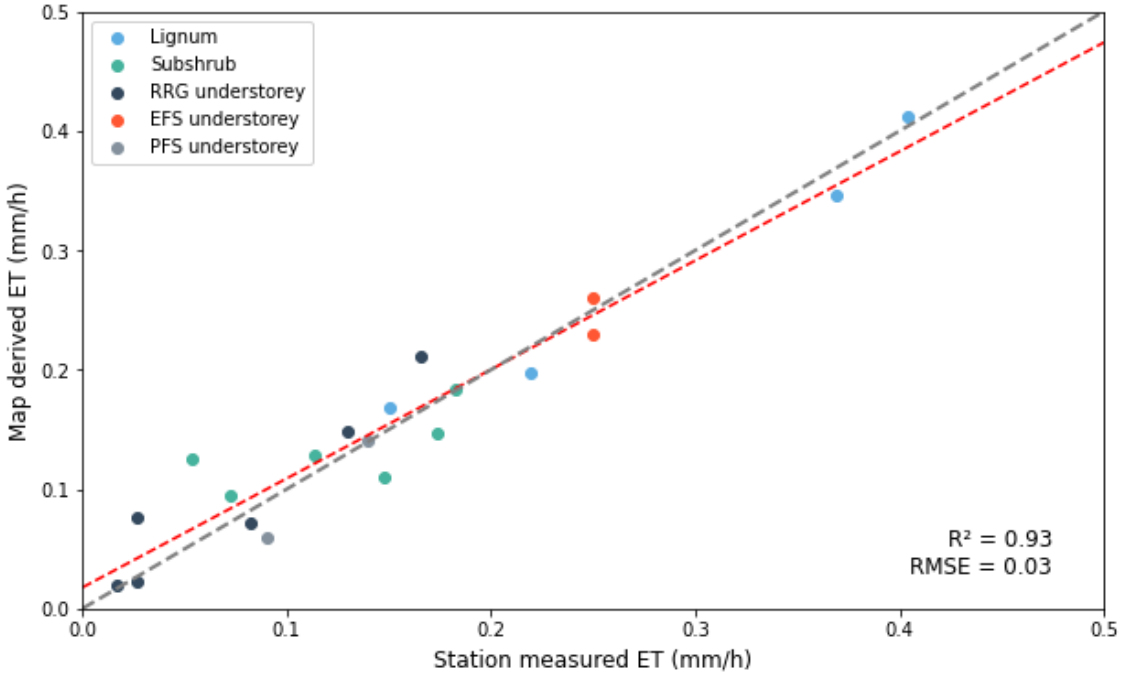

Figure 4.7 Drone based estimated ET vs. ground measurements. The red dashed line is the fitted line, and the black dashed line is the 1:1 line.

Figure 4.8 shows the ET maps for May 7, 2022, and September 13, 2023, of the RRG understorey, and the understorey ET maps for November 4, 2013, and November 18, 2013 with the corresponding probability density of open and understorey surfaces. The ET exhibits high spatial variability for both open and understorey surfaces. Generally, ET over understorey surface is lower than that over open surface due to reduced solar radiation. Differences of regional ET are evident at the Mt. Wilson site where the contrast between open and understorey surfaces is more pronounced than at the floodplain site due to sparse overstory vegetation at the RRG than at the Wilson site.

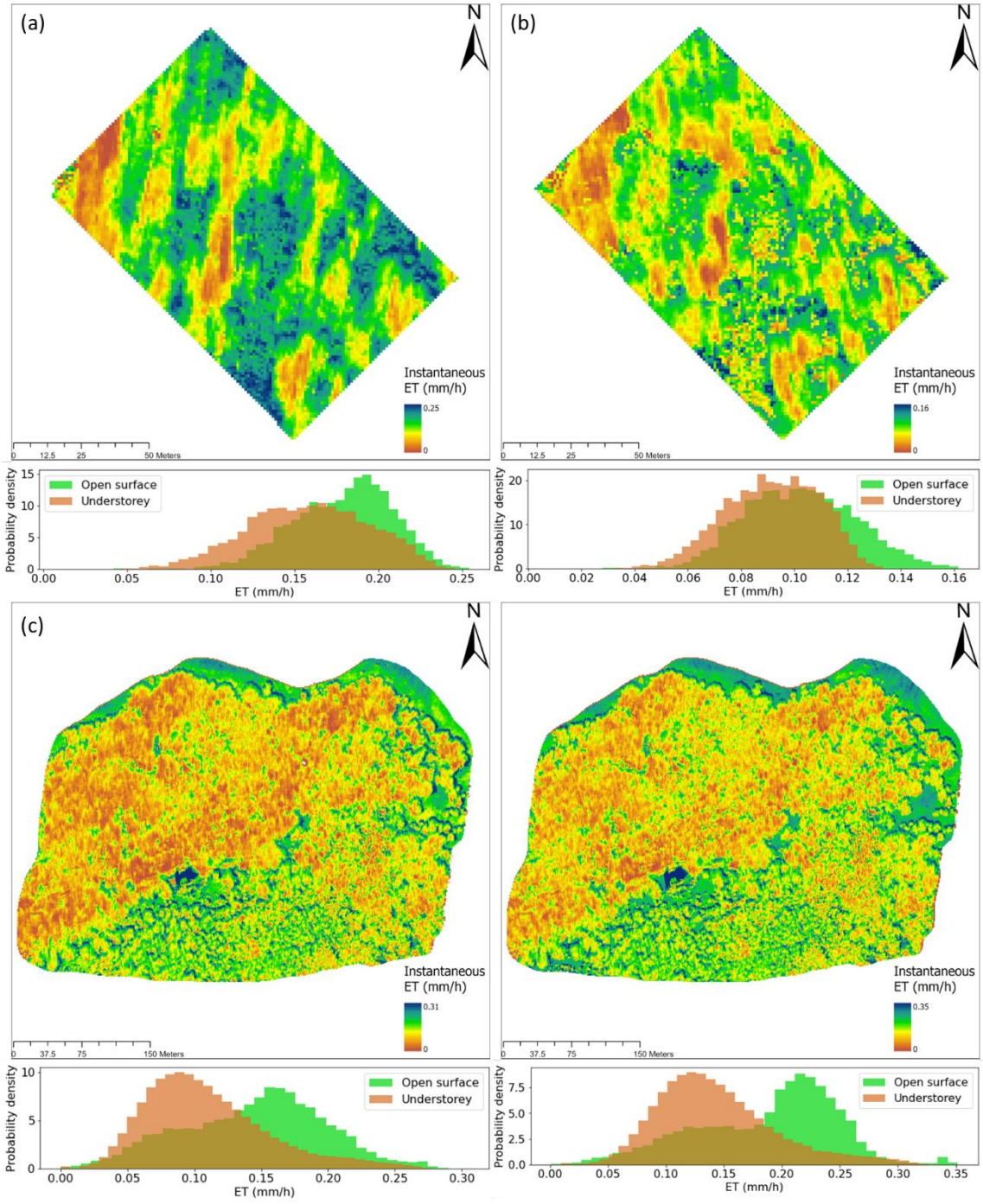

Figure 4.8 Spatial distribution of understorey instantaneous ET of RRG and Mount Wilson. (a) RRG, May 7, 2022; (b) RRG, September 13, 2023; (c) Mount Wilson, November 4, 2013; (d) Mount Wilson, November 18, 2013. Below is the probability density of open and understorey surfaces.

Figure 4.9 compares the monthly ET from station observations and mapping across various regions at Bookpurnong site. Monthly ET of Lignum and Subshrub areas has relatively low spatial variability before flooding events. Lignum maintained an average Standard Deviation (SD) of 0.64 mm/month and a Coefficient of Variation (CV) of 0.03, while Subshrub showed an average SD of 0.50 mm/month and a CV of 0.04. After the flooding, these areas experienced noticeable increases in variability, with mean SD and CV rising to 5.84 mm/month and 0.10 for Lignum, and 3.29

mm/month and 0.13 for Subshrub, respectively. The RRG understorey area consistently showed higher variability with an average SD of 4.92 mm/month and a CV of 0.29 throughout the study periods, suggesting that in open areas with low vegetation, such as Lignum and Subshrub, station measurements can generally represent the entire area due to minimal spatial variability in ET. The increased variability post-flooding highlights the potential limitations of station measurements in capturing the spatial differences of understorey, particularly in heterogeneous environments. This finding underlines the crucial role of detailed understorey ET mapping in understanding the spatial distribution of ET across different landscapes.

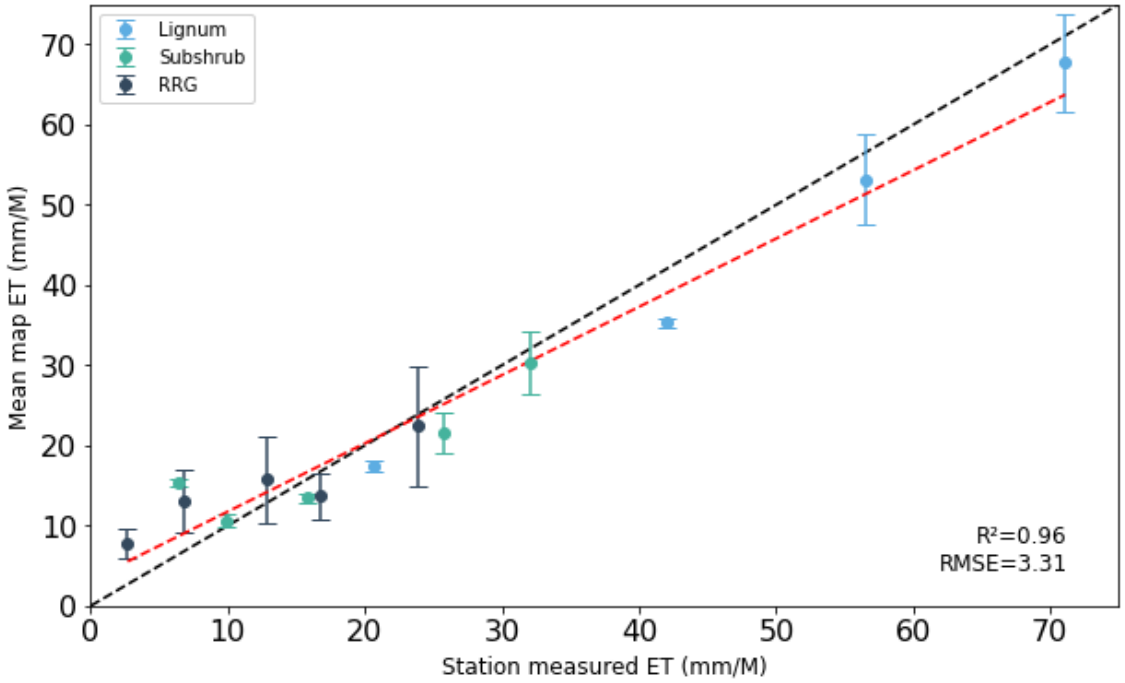

Figure 4.9 Scatter plot of station measured and mean monthly ET from the ET map. The error bars show the standard deviation of the map area. The red dashed line is the fitted line, and the black dashed line is the 1:1 line. For RRG site, only the understorey area (based on CHM) is calculated.

4.3.4 The impact of flooding on understorey ET

The Bookpurnong site was selected to examine the influence of flooding on surface. A severe River Murray flood occurred from late 2022 to early 2023. According to the upstream water level recorded at Lock 4 of the River Murray (https://riverdata.mdba.gov.au/lock-4-upstream), the Lignum site located at the lowest elevation among the stations was inundated from early October 2022. The Subshrub site was affected by rising water in November followed by the RRG site in December 2022. Water levels returned to normal by the end of March. According to the Bureau of Meteorology (BOM) records (http://www.bom.gov.au/), the monthly mean solar radiation from April to August showed minimal variation between 2022 and 2023 with an increase of less than 5% in

2023. In contrast, a notable increase of 20% in solar radiation was recorded in September and October of 2023 compared to the same months in 2022. This significant rise in solar radiation during these months could potentially lead to higher ET rates.

Figure 4.10 shows the changes of monthly ET before and after the flooding event (months with incomplete data are not shown). At the Lignum site, a significant increase in ET occurred after the flooding. The peak difference occurred between Septembers of the two years. About 40% more September ET was observed in 2023 (several months after the flood event) than in 2022.

At the Subshrub site, a distinctive pattern in ET change was observed following the flooding event. From April to September, ET increased from the corresponding months of the previous year with a peak change in July 2023 when ET increased by 50% from July 2022. Subsequently, this upward trend reversed. By October 2023, ET levels was lower than the previous year. Unlike the Lignum and Subshrub site, the RRG understorey exhibits very small changes in monthly ET before and after the flooding.

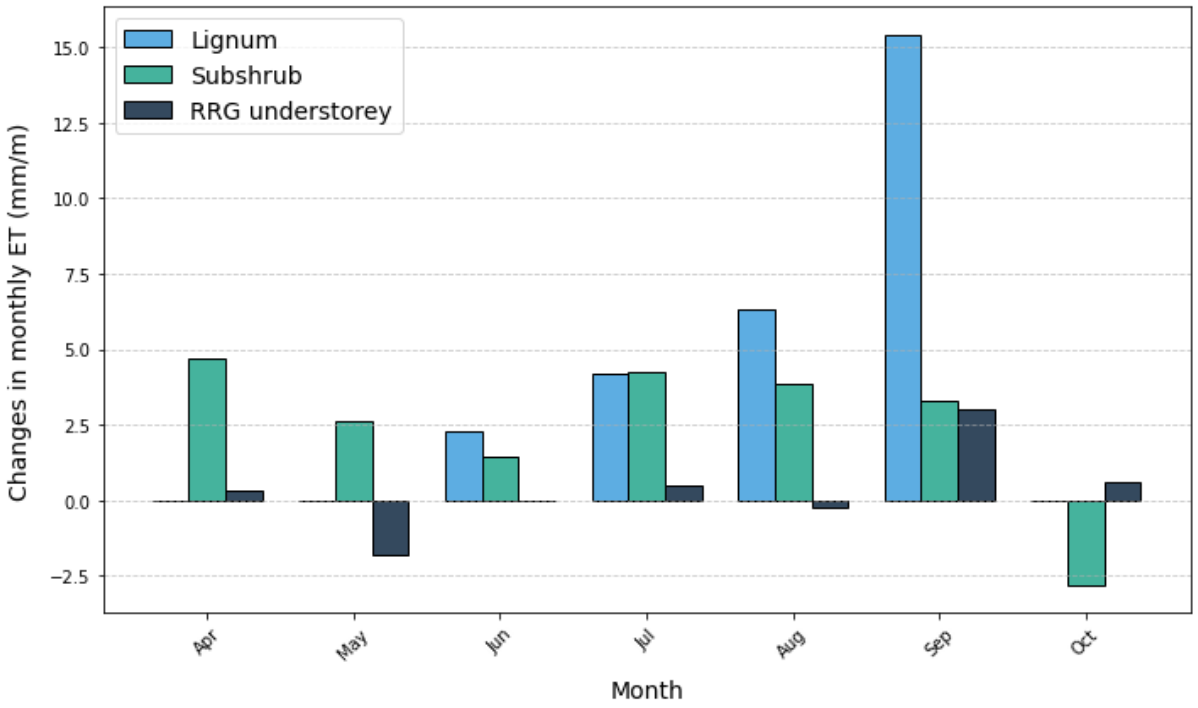

Figure 4.10 Change in monthly ET before and after the 2022-2023 Murray River flooding and months with incomplete data are not shown.

To assess the ET responses to the flood, it is crucial to examine spatial patterns in monthly ET maps. Due to the irregular timings of drone surveys before and after the flood event, directly comparing monthly ET maps was not feasible. As the map were generated at different month, Z-score normalization was applied to the monthly ET maps for May 2022 and September 2023

(Santana et al., 2018; Swetnam et al., 2021). A difference map was generated (Figure 4.11) to highlight the impact of flooding on the spatial variability of ET across different land cover types. Positive values on the difference map indicate areas where ET is above to the mean, suggesting regions potentially experiencing enhanced water availability or altered vegetation dynamics post-flooding. Conversely, negative values indicate areas with a decrease in ET, indicating reduced water availability or vegetation loss due to the flooding event.

In Figure 4.11 (a), the east part of Lignum area generally exhibits positive values (colour in red and orange) in contrast to the west part. Figure 4.11 (d) and (e) show that the Lignum cover surfaces exhibit negative difference values and the bare soil surface exhibit positive value. This spatial pattern implies high mortality rate of the Lignum plants, leading to reduced transpiration rates due to lower LAI. The high water availability post-flooding coupled with the emergent growth of grasses likely compensated the reduction of Lignum shrub transpiration, thereby sustaining higher total ET. During our drone survey period after the flooding, the main component of total ET in the Lignum area was soil evaporation of residual soil moisture left from the flooding.

Figure 4.11 (g) and (h) show a reverse pattern with shrub cover surfaces predominantly exhibiting positive differences attributing to the significant shrub growth due to increased water availability. According to the monthly rainfall data from BOM, the rainfall in June 2022 and June 2023 was 11.9 and 34.8 mm, respectively. The elevated soil moisture, due to both residual water from the flooding and the increased rainfall in 2023, was likely responsible for the MEP estimated ET changes between the two years. From August to October 2023, a significant reduction in rainfall was observed – only 50%, 5%, and 10% respectively of the previous year's levels. This decrease in rainfall led to reduced soil moisture and ET. The negative differences of the bare soil surface indicate a reduced water availability compared to pre-flooding stage, suggesting that the residual flooding water no longer exists in this area. This pattern suggests that the impact of the flooding on the Subshrub site was relatively short and that the ET dynamics at this area are more directly influenced by the precipitation input. As the surface soil water evaporated, transpiration from the newly grown shrubs became the dominant component of ET over this area.

For the RRG area, similar to the Subshrub area, the bare soil surface has negative values, suggesting that the soil moisture increase caused by the flooding does not affect ET after six months of flooding. No evident trend of understorey ET change after the flooding (Figure 4.10) implies that understorey ET is not limited by water availability but the solar radiation.

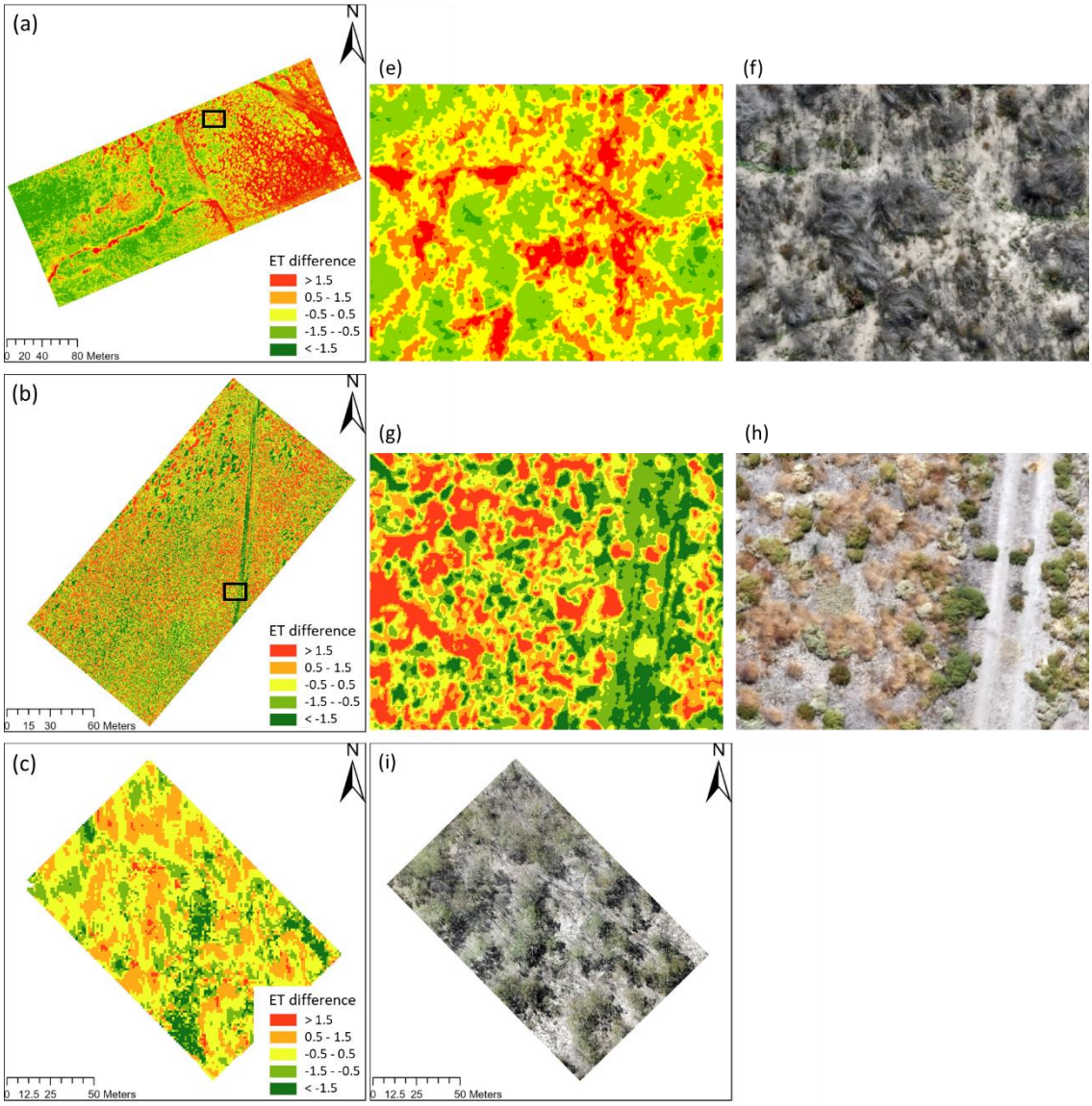

Figure 4.11 (a), (b), and (c) difference maps of the normalized post-flooding (September 2023) and pre-flooding (May 2022) ET for Lignum, Subshrub and RRG understorey area. (e) and (g) enlarged views. (f) and (h) RGB images for the enlarged area captured pre-flooding and post-flooding, respectively. (i) RGB image for RRG area on 2022/03/04.

As remote sensing imagery and flux towers quantify fluxes from the entire ecosystem (Scott et al., 2003; Linderman et al., 2004; Pisek et al., 2015; L. Li et al., 2020; Weerasinghe et al., 2020), directly comparing understorey ET independently from the rest of the ecosystem is challenging. To understand the impact of flooding on different vegetative layers within the woodland ecosystem, it is essential to examine the changes in the proportions of understorey ET relative to total ecosystem ET due to environmental fluctuations. The fraction of monthly understorey ET to total ecosystem ET for pre- and post-flood conditions in RRG site are calculated (Figure 4.12). Prior to the flooding event, the understorey ET consists of approximately 10-40% of the total ET. Seasonal variation of the understorey ET has low contribution to that of total ET during winter but makes up to 40% during early spring and autumn. Notably, the understorey ET fraction was significantly

reduced after the flooding event, which did not substantially change understorey ET (Figure 4.10). This reduction of the ET fraction can be attributed to an increase in the total ecosystem ET, likely driven by enhanced water availability. Different responses of ecosystem ET to flooding highlights the complexity of interactions within various components of ecosystem and their individual adaptations to environmental changes.

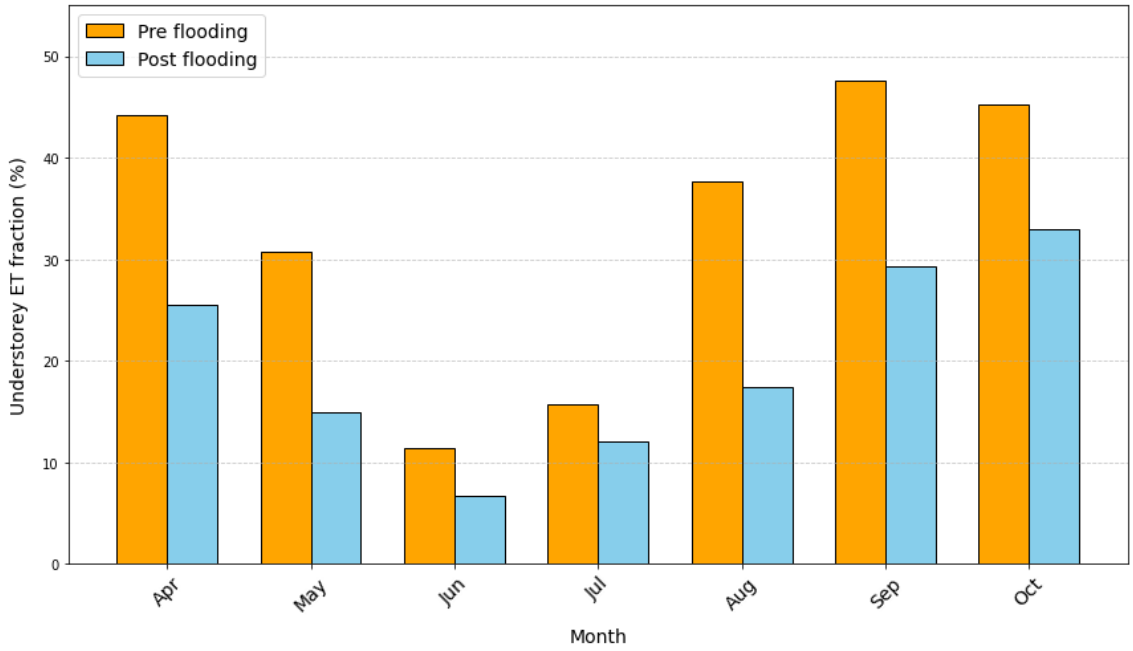

Figure 4.12 The understorey ET fraction of ecosystem ET at the RRG site from April to October.

4.3.5 The impact of topography on understorey ET

The Mount Wilson site was selected to examine the influence of topography on surface ET due to its complex topographical feature. Causal inference analysis was conducted to assess the direct impact of topographical variables on ET (Akbari et al., 2023). One of the variables of elevation, slope, or aspect (converted to sine and cosine components to represent east-west and north-south orientations)—was selected as the exposure variable, while the others along with LAI were treated as confounding variables to evaluate their causal relationship to ET. Figure 4.13 shows the exposure response curves (ERC) for different variables on November 18, 2013 to illustrate how understorey ET responds to changes of the exposure variables.

Elevation is shown to have minimal direct impact on ET, while slope and aspect orientation have pronounced effects. Understorey ET generally decreases with slope when orientation shifts towards east-facing aspects. This likely results from variations in the slope-controlled soil moisture retention capabilities and the sunlight exposure duration. As east-facing slopes receive sunlight primarily in the morning when temperatures are cooler, potentially reducing evaporative demand

compared to west-facing slopes which are sunlit in the hotter afternoon. The most substantial influence was observed in an orientation transition from the fact that ET over north-facing slope is approximately 0.1 mm higher than ET over south-facing slope indicates the sensitive response of understorey ET to aspect-induced microclimatic changes.

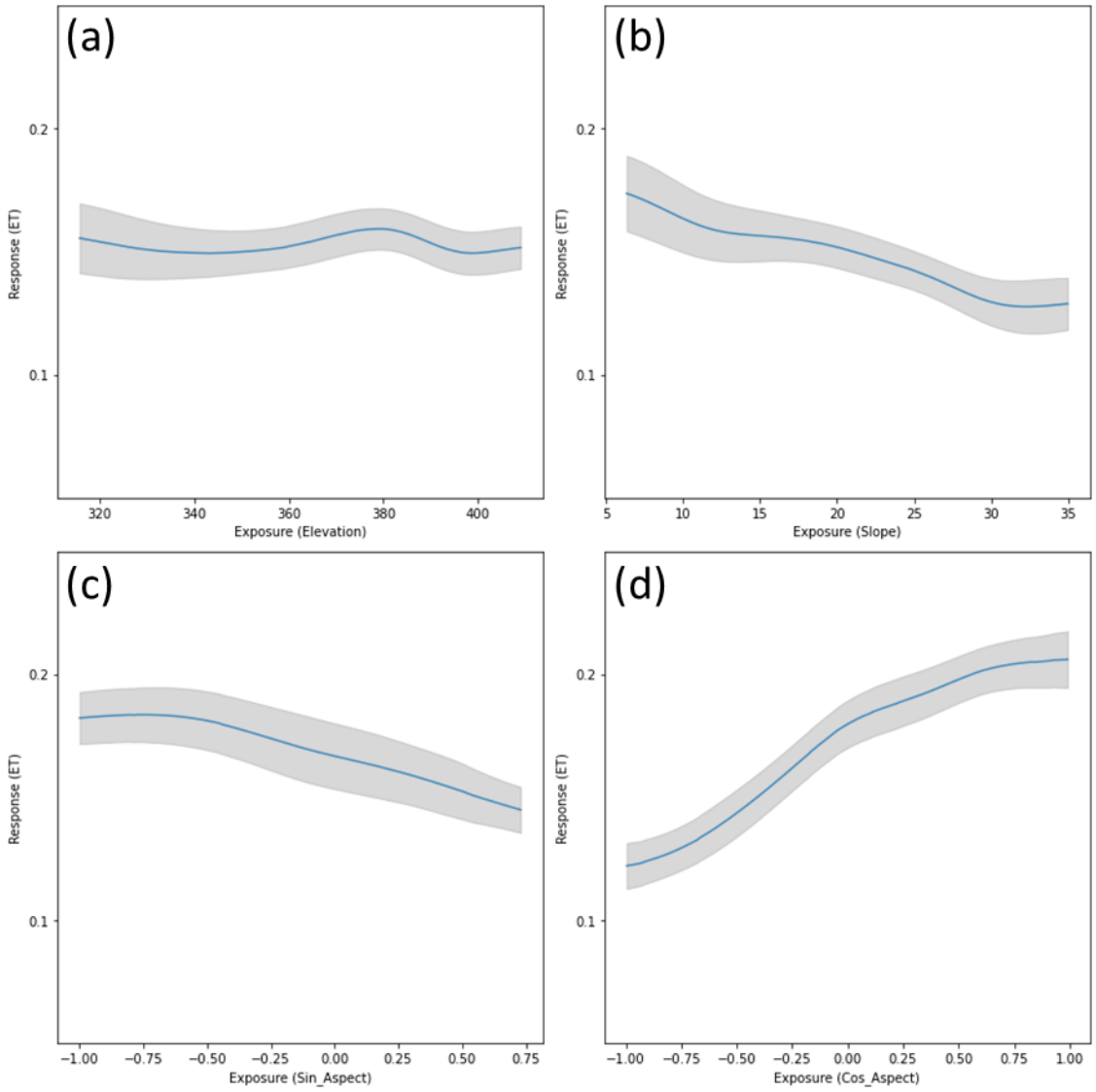

Figure 4.13 The Exposure Response Curves of spatially distributed understorey ET responses to different topographical factors (data from November 18, 2013; similar patterns observed on November 04, 2013 are not shown). The grey areas are the 95% confidence interval.

Figure 4.14 illustrates the fraction of understorey ET to total ecosystem ET similar to that in Figure 12. The understorey ET fraction is at its lowest during winter, around 30% at the EFS site and less than 10% at the PFS site. This fraction increases significantly in summer, exceeding 50% at the EFS site and reaching 25% at the PFS site. This finding demonstrates a substantial difference, with the EFS understorey contributing more to the total ET than the PFS.

Previous study finds that canopy transpiration in this region peaks in spring and drops to its lowest in late autumn and winter (H. Wang et al., 2024). It reflects an adaptive response that trees actively regulate their transpiration rates to optimize water use with changing environmental conditions, thus mitigating water stress. Our findings indicate that understorey ET peaks in summer and diminishes in winter, primarily driven by solar radiation. Higher ratio of understorey to total ET during the summer months implies higher sensitivity of tree to water stress during this period likely due to stomatal closure to reduce water loss (Gharun et al., 2013; Gharun et al., 2014). While H. Wang et al. (2024) reported similar annual total transpiration of the overstory canopies on both EFS and PFS, our analysis reveals significant differences in ET between these orientations at the understorey level. This finding highlights the spatial heterogeneity of understorey ET, emphasizing the importance of accurate ET mapping to better understand hydrological dynamics of complex terrains.

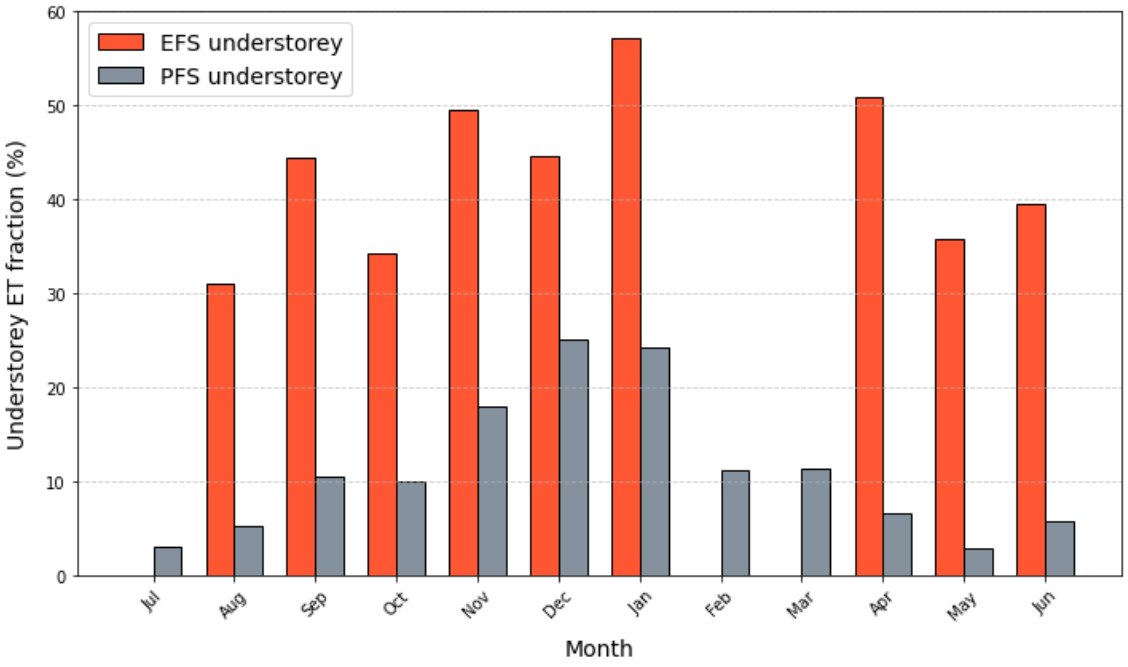

Figure 4.14 The understorey ET fraction of whole ecosystem ET of the Mount Wilson site, July 2013 - June 2014.

4.4 Conclusion

This study aimed to establish a robust method for estimating understorey surface ET using airborne thermal imagery and the Maximum Entropy Production (MEP) model, while investigating the contribution of understorey ET to total ecosystem ET in two typical settings and identifying influencing factors. By achieving these objectives, the research provides critical insights into the hydrological dynamics of woodland ecosystems and their implications for water management and ecological conservation.

The results demonstrate that understorey ET plays a significant role in ecosystem water dynamics, particularly during periods of high solar radiation and low precipitation. For the RRG site, the analysis revealed that the fraction of understorey ET to total ecosystem ET varies seasonally, peaking in summer due to increased evaporative demand and diminishing in winter when overstorey transpiration dominates. This highlights the sensitivity of understorey ET to solar radiation and its role as a compensatory mechanism when overstorey water use is limited by stomatal regulation during periods of water stress.

Spatial analysis at the Mount Wilson site highlights how topographical factors like slope and aspect influence understorey ET. These results demonstrate the variation in understorey ET across different terrains. The study also shows how flooding impacts open surface and understorey ET. After flooding, for the open surface, residual soil moisture initially boosted soil evaporation and shrub transpiration. As soil moisture decreased, ET became more dependent on rainfall. The understorey ET remains relatively stable before and after the flooding. These findings underline the role of extreme events in shaping woodland water dynamics.

In conclusion, this research establishes a comprehensive framework for quantifying understorey ET using high-resolution airborne thermal imagery and the MEP model. The findings from this study enhance our capacity to evaluate ecosystem water use and aid the development of more effective strategies of water resources management. This research contributes to improved ecohydrological modelling by improving our understanding of water consumption in forest and woodland ecosystems. One focus of future research is to achieve broader-scale ET monitoring and mapping using high-resolution thermal data from satellites.

4.5 References

Acharya, B. S., Bhandari, M., Bandini, F., Pizarro, A., Perks, M., Joshi, D. R., Wang, S., Dogwiler, T., Ray, R. L., & Kharel, G. (2021). Unmanned aerial vehicles in hydrology and water management: Applications, challenges, and perspectives. *Water Resources Research*, *57*(11), e2021WR029925.

Akbari, K., Winter, S., & Tomko, M. (2023). Spatial causality: A systematic review on spatial causal inference. *Geographical Analysis*, *55*(1), 56-89.

Allen, R. G., Pereira, L. S., Smith, M., Raes, D., & Wright, J. L. (2005). FAO-56 dual crop coefficient method for estimating evaporation from soil and application extensions. *Journal of irrigation and drainage engineering*, *131*(1), 2-13.

Allen, R. G., Tasumi, M., & Trezza, R. (2007). Satellite-based energy balance for mapping evapotranspiration with internalized calibration (METRIC)—Model. *Journal of irrigation and drainage engineering*, *133*(4), 380-394.

Anapalli, S. S., Fisher, D. K., Reddy, K. N., Wagle, P., Gowda, P. H., & Sui, R. (2018). Quantifying soybean evapotranspiration using an eddy covariance approach. *Agricultural Water Management*, *209*, 228-239.

Anderson, M. C., Kustas, W. P., Norman, J. M., Diak, G. T., Hain, C. R., Gao, F., Yang, Y., Knipper, K. R., Xue, J., & Yang, Y. (2024). A brief history of the thermal IR-based Two-Source Energy Balance (TSEB) model–diagnosing evapotranspiration from plant to global scales. *Agricultural and Forest Meteorology*, *350*, 109951.

Bastiaanssen, W. G., Menenti, M., Feddes, R., & Holtslag, A. (1998). A remote sensing surface energy balance algorithm for land (SEBAL). 1. Formulation. *Journal of Hydrology*, *212*, 198-212.

Carlson, T. N., Gillies, R. R., & Perry, E. M. (1994). A method to make use of thermal infrared temperature and NDVI measurements to infer surface soil water content and fractional vegetation cover. *Remote sensing reviews*, *9*(1-2), 161-173.

Chen, J. M., & Liu, J. (2020). Evolution of evapotranspiration models using thermal and shortwave remote sensing data. *Remote Sensing of Environment*, *237*, 111594.

Cheung, P. K., Jim, C. Y., & Hung, P. L. (2021). Preliminary study on the temperature relationship at remotely-sensed tree canopy and below-canopy air and ground surface. *Building and Environment*, *204*, 108169.

Doble, R., Simmons, C. T., & Walker, G. R. (2005). *Understanding spatial patterns of discharge in semi-arid regions using a recharge-discharge balance to determine vegetation health*. CSIRO Land and Water.

Feng, L., Liu, Y., Zhou, Y., & Yang, S. (2022). A UAV-derived thermal infrared remote sensing three-temperature model and estimation of various vegetation evapotranspiration in urban micro-environments. *Urban Forestry & Urban Greening*, *69*, 127495.

Gaulton, R., & Malthus, T. J. (2010). LiDAR mapping of canopy gaps in continuous cover forests: A comparison of canopy height model and point cloud based techniques. *International Journal of Remote Sensing*, *31*(5), 1193-1211.

Gharun, M., Turnbull, T. L., & Adams, M. A. (2013). Validation of canopy transpiration in a mixed-species foothill eucalypt forest using a soil–plant–atmosphere model. *Journal of Hydrology*, *492*, 219-227.

Gharun, M., Vervoort, R. W., Turnbull, T. L., & Adams, M. A. (2014). A test of how coupling of vegetation to the atmosphere and climate spatial variation affects water yield modelling in mountainous catchments. *Journal of Hydrology*, *514*, 202-213.

Gillies, R., Kustas, W., & Humes, K. (1997). A verification of the'triangle'method for obtaining surface soil water content and energy fluxes from remote measurements of the Normalized Difference Vegetation Index (NDVI) and surface e. *International Journal of Remote Sensing*, *18*(15), 3145-3166.

Guerschman, J. P., McVicar, T. R., Vleeshower, J., Van Niel, T. G., Peña-Arancibia, J. L., & Chen, Y. (2022). Estimating actual evapotranspiration at field-to-continent scales by calibrating the CMRSET algorithm with MODIS, VIIRS, Landsat and Sentinel-2 data. *Journal of Hydrology*, *605*, 127318.

Guerschman, J. P., Van Dijk, A. I., Mattersdorf, G., Beringer, J., Hutley, L. B., Leuning, R., Pipunic, R. C., & Sherman, B. S. (2009). Scaling of potential evapotranspiration with MODIS data reproduces flux observations and catchment water balance observations across Australia. *Journal of Hydrology*, *369*(1-2), 107-119.

Heidarian Dehkordi, R., Pelgrum, H., & Meersmans, J. (2022). High spatio-temporal monitoring of century-old biochar effects on evapotranspiration through the ETLook model: a case study with UAV and satellite image fusion based on additive wavelet transform (AWT). *GIScience & Remote Sensing*, *59*(1), 111-141.
Hoffmann, H., Nieto, H., Jensen, R., Guzinski, R., Zarco-Tejada, P., & Friborg, T. (2016). Estimating evaporation with thermal UAV data and two-source energy balance models. *Hydrology and Earth System Sciences*, *20*(2), 697-713.
Holzman, M. E., Rivas, R., & Piccolo, M. C. (2014). Estimating soil moisture and the relationship with crop yield using surface temperature and vegetation index. *International Journal of Applied Earth Observation and Geoinformation*, *28*, 181-192.
Hook, S. J., Gabell, A. R., Green, A. A., & Kealy, P. S. (1992). A comparison of techniques for extracting emissivity information from thermal infrared data for geologic studies. *Remote Sensing of Environment*, *42*(2), 123-135.
Hu, S., Zhao, C., Li, J., Wang, F., & Chen, Y. (2014). Discussion and reassessment of the method used for accepting or rejecting data observed by a Bowen ratio system. *Hydrological processes*, *28*(15), 4506-4510.
Iida, S. i., Ohta, T., Matsumoto, K., Nakai, T., Kuwada, T., Kononov, A. V., Maximov, T. C., van der Molen, M. K., Dolman, H., & Tanaka, H. (2009). Evapotranspiration from understory vegetation in an eastern Siberian boreal larch forest. *Agricultural and forest Meteorology*, *149*(6-7), 1129-1139.
Iida, S. i., Shimizu, T., Tamai, K., Kabeya, N., Shimizu, A., Ito, E., Ohnuki, Y., Chann, S., & Levia, D. F. (2020). Evapotranspiration from the understory of a tropical dry deciduous forest in Cambodia. *Agricultural and Forest Meteorology*, *295*, 108170.
Jia, C., Zhao, P., Wang, J., Deng, Y., Li, N., Wang, Y., & Miao, S. (2023). An application of the maximum entropy production method in the WRF Noah land surface model. *Journal of Geophysical Research: Atmospheres*, *128*(5), e2022JD037867.
Landuyt, D., De Lombaerde, E., Perring, M. P., Hertzog, L. R., Ampoorter, E., Maes, S. L., De Frenne, P., Ma, S., Proesmans, W., & Blondeel, H. (2019). The functional role of temperate forest understorey vegetation in a changing world. *Global Change Biology*, *25*(11), 3625-3641.
Li, L., Chen, J., Mu, X., Li, W., Yan, G., Xie, D., & Zhang, W. (2020). Quantifying understory and overstory vegetation cover using UAV-based RGB imagery in forest plantation. *Remote Sensing*, *12*(2), 298.
Li, N., Zhao, P., Wang, J., & Deng, Y. (2019). Estimation of surface heat fluxes over the central Tibetan Plateau using the maximum entropy production model. *Journal of Geophysical Research: Atmospheres*, *124*(13), 6827-6840.
Linderman, M., Liu, J., Qi, J., An, L., Ouyang, Z., Yang, J., & Tan, Y. (2004). Using artificial neural networks to map the spatial distribution of understorey bamboo from remote sensing data. *International Journal of Remote Sensing*, *25*(9), 1685-1700.
Liu, C., Zhang, X., & Zhang, Y. (2002). Determination of daily evaporation and evapotranspiration of winter wheat and maize by large-scale weighing lysimeter and micro-lysimeter. *Agricultural and Forest Meteorology*, *111*(2), 109-120.
Liu, W., Guan, H., Gutiérrez-Jurado, H. A., Banks, E. W., He, X., & Zhang, X. (2022). Modelling quasi-three-dimensional distribution of solar irradiance on complex terrain. *Environmental Modelling & Software*, *149*, 105293.
Mokari, E., Samani, Z., Heerema, R., Dehghan-Niri, E., DuBois, D., Ward, F., & Pierce, C. (2022). Development of a new UAV-thermal imaging based model for estimating pecan evapotranspiration. *Computers and Electronics in Agriculture*, *194*, 106752.
Nemani, R., Pierce, L., Running, S., & Goward, S. (1993). Developing satellite-derived estimates of surface moisture status. *Journal of Applied Meteorology and Climatology*, *32*(3), 548-557.
Pieters, A., Giese, M., Schmierer, M., Johnson, K., & Asch, F. (2022). Chamber-based system for measuring whole-plant transpiration dynamics. *Plant-Environment Interactions*, *3*(6), 243-253.
Pisek, J., Lang, M., & Kuusk, J. (2015). A note on suitable viewing configuration for retrieval of forest understory reflectance from multi-angle remote sensing data. *Remote Sensing of Environment*, *156*, 242-246.
Poon, P. K., & Kinoshita, A. M. (2018). Spatial and temporal evapotranspiration trends after wildfire in semi-arid landscapes. *Journal of Hydrology*, *559*, 71-83.

Qi, J., Xie, D., Yin, T., Yan, G., Gastellu-Etchegorry, J.-P., Li, L., Zhang, W., Mu, X., & Norford, L. K. (2019). LESS: LargE-Scale remote sensing data and image simulation framework over heterogeneous 3D scenes. *Remote Sensing of Environment*, *221*, 695-706.
Santana, N. C., de Carvalho Júnior, O. A., Gomes, R. A. T., & Guimarães, R. F. (2018). Burned-area detection in Amazonian environments using standardized time series per pixel in MODIS data. *Remote Sensing*, *10*(12), 1904.
Scott, R. L., Watts, C., Payan, J. G., Edwards, E., Goodrich, D. C., Williams, D., & Shuttleworth, W. J. (2003). The understory and overstory partitioning of energy and water fluxes in an open canopy, semiarid woodland. *Agricultural and Forest Meteorology*, *114*(3-4), 127-139.
Stannard, D. I., & Weltz, M. A. (2006). Partitioning evapotranspiration in sparsely vegetated rangeland using a portable chamber. *Water resources research*, *42*(2).
Sun, H. (2015). Two-stage trapezoid: A new interpretation of the land surface temperature and fractional vegetation coverage space. *IEEE Journal of Selected Topics in Applied Earth Observations and Remote Sensing*, *9*(1), 336-346.
Sun, Z., Wang, Q., Matsushita, B., Fukushima, T., Ouyang, Z., & Watanabe, M. (2009). Development of a simple remote sensing evapotranspiration model (Sim-ReSET): algorithm and model test. *Journal of Hydrology*, *376*(3-4), 476-485.
Swetnam, T. L., Yool, S. R., Roy, S., & Falk, D. A. (2021). On the use of standardized multi-temporal indices for monitoring disturbance and ecosystem moisture stress across multiple earth observation systems in the google earth engine. *Remote Sensing*, *13*(8), 1448.
Taheri, M., Mohammadian, A., Ganji, F., Bigdeli, M., & Nasseri, M. (2022). Energy-based approaches in estimating actual evapotranspiration focusing on land surface temperature: A review of methods, concepts, and challenges. *Energies*, *15*(4), 1264.
Ter Steege, H., Pitman, N. C., Sabatier, D., Baraloto, C., Salomão, R. P., Guevara, J. E., Phillips, O. L., Castilho, C. V., Magnusson, W. E., & Molino, J.-F. (2013). Hyperdominance in the Amazonian tree flora. *Science*, *342*(6156), 1243092.
Wang, H., Guan, H., Xu, X., Gao, L., Gutiérrez-Jurado, H. A., & Simmons, C. T. (2024). Topographic regulations on ecohydrological dynamics in a montane forest catchment and the implications for plant adaptation to environment. *Journal of Hydrology*, 131412.
Wang, H., Tetzlaff, D., & Soulsby, C. (2017). Testing the maximum entropy production approach for estimating evapotranspiration from closed canopy shrubland in a low-energy humid environment. *Hydrological processes*, *31*(25), 4613-4621.
Wang, J., & Bras, R. (2011). A model of evapotranspiration based on the theory of maximum entropy production. *Water resources research*, *47*(3).
Wang, J., & Bras, R. L. (2009). A model of surface heat fluxes based on the theory of maximum entropy production. *Water resources research*, *45*(11).
Wang, Y., & Fang, H. (2020). Estimation of LAI with the LiDAR technology: A review. *Remote Sensing*, *12*(20), 3457.
Weerasinghe, I., Bastiaanssen, W., Mul, M., Jia, L., & Van Griensven, A. (2020). Can we trust remote sensing evapotranspiration products over Africa? *Hydrology and Earth System Sciences*, *24*(3), 1565-1586.
Wolf, A., Saliendra, N., Akshalov, K., Johnson, D. A., & Laca, E. (2008). Effects of different eddy covariance correction schemes on energy balance closure and comparisons with the modified Bowen ratio system. *Agricultural and Forest Meteorology*, *148*(6-7), 942-952.
Wolf, S., Paul-Limoges, E., Sayler, D., & Kirchner, J. W. (2024). Dynamics of evapotranspiration from concurrent above-and below-canopy flux measurements in a montane Sierra Nevada forest. *Agricultural and forest Meteorology*, *346*, 109864.
Xu, D., Agee, E., Wang, J., & Ivanov, V. Y. (2019). Estimation of evapotranspiration of Amazon rainforest using the maximum entropy production method. *Geophysical Research Letters*, *46*(3), 1402-1412.
Yan, C., Xiang, J., Qin, L., Wang, B., Shi, Z., Xiao, W., Hayat, M., & Qiu, G. Y. (2023). High temporal and spatial resolution characteristics of evaporation, transpiration, and evapotranspiration from a subalpine wetland by an advanced UAV technology. *Journal of Hydrology*, *623*, 129748.
Yang, J., Li, B., & Shiping, L. (2000). A large weighing lysimeter for evapotranspiration and soil-water–groundwater exchange studies. *Hydrological processes*, *14*(10), 1887-1897.

Yang, Y., Scott, R. L., & Shang, S. (2013). Modeling evapotranspiration and its partitioning over a semiarid shrub ecosystem from satellite imagery: a multiple validation. *Journal of Applied Remote Sensing*, *7*(1), 073495-073495.
Yang, Y., Su, H., Zhang, R., Tian, J., & Li, L. (2015). An enhanced two-source evapotranspiration model for land (ETEML): Algorithm and evaluation. *Remote Sensing of Environment*, *168*, 54-65.
Yang, Z., Bai, P., & Li, Y. (2022). Quantifying the effect of vegetation greening on evapotranspiration and its components on the Loess Plateau. *Journal of Hydrology*, *613*, 128446.
Yepez, E. A., Williams, D. G., Scott, R. L., & Lin, G. (2003). Partitioning overstory and understory evapotranspiration in a semiarid savanna woodland from the isotopic composition of water vapor. *Agricultural and forest Meteorology*, *119*(1-2), 53-68.
Zhang, B., Kang, S., Li, F., & Zhang, L. (2008). Comparison of three evapotranspiration models to Bowen ratio-energy balance method for a vineyard in an arid desert region of northwest China. *Agricultural and Forest Meteorology*, *148*(10), 1629-1640.
Zhang, K., Kimball, J. S., & Running, S. W. (2016). A review of remote sensing based actual evapotranspiration estimation. *Wiley interdisciplinary reviews: Water*, *3*(6), 834-853.
Zhang, Z., Tian, F., Hu, H., & Yang, P. (2014). A comparison of methods for determining field evapotranspiration: photosynthesis system, sap flow, and eddy covariance. *Hydrology and Earth System Sciences*, *18*(3), 1053-1072.

5 DISSCUSION AND CONCLUSION

5.1 Summary of findings

This study focused on two primary aims: understanding the influence of topography on vegetation attributes and advancing methods for monitoring surface ecohydrological processes for semi-arid woodlands. The findings demonstrate that topographic factors, such as slope, aspect, and TPI, significantly affect both overstorey and understorey vegetation dynamics. Moreover, the development of robust methods for estimating understorey ET using the MEP model and high-resolution remote sensing provides novel insights into the spatial and temporal variability of ecohydrological processes. The key findings from each chapter are outlined below:

Chapter 2 presents an analysis of the relationships between vegetation attributes—such as tree height and NDVI—and fine-scale topographical factors within a semi-arid woodland environment. A primary finding of this research is that vegetation attributes exhibit significant sensitivity to topographic factors, particularly at a scale of 5–10 meters. This scale dependency highlights the importance of adopting high-resolution data and methods when modelling vegetation in heterogeneous landscapes. The research shows that the tree-based sampling method is superior to traditional pixel-based approaches, as it captures the spatial variability of vegetation attributes more accurately, leading to more reliable modelling results.

The thesis also emphasizes the significance of spatial non-stationarity in topography-vegetation relationships. Spatial non-stationarity refers to the phenomenon in which relationships between variables vary across space, rather than being consistent throughout a study area. Accounting for this variability is critical for accurately modelling vegetation attributes, as demonstrated by the superior performance of the MGWR model compared to traditional global models like SLR and RF. Although applying the model to unknown regions is challenging due to the locally fitted coefficients, the MGWR model's enhanced explanatory power and its ability to identify key variables that might be overlooked in global models highlight the value of adopting spatially adaptive techniques in ecohydrological research.

Key topographic drivers for vegetation attributes identified in this study include TPI and northness, both of which exhibit negative correlations with tree height. Similarly, NDVI is negatively correlated with TPI, slope, and northness, while eastness shows a positive correlation. These findings point to the pivotal role of topography-induced sunlight exposure and hydrological conditions in shaping vegetation attributes. For instance, areas with higher TPI (on ridges) and equator-facing slopes tend to support shorter trees with lower NDVI values. In contrast, east-facing slopes, which receive more morning sunlight, promote higher NDVI values, likely due to more favourable hydrological and microclimatic conditions in the morning.

Chapter 3 introduces a novel approach, the DST model, for simulating the spatial and temporal distribution of shortwave radiation in semi-arid woodlands. The DST model effectively captures the complex interactions between topography, canopy structure, and solar radiation, providing insights into how these factors influence the distribution of light energy at both the overstory and understorey levels.

One of the key findings from this chapter is the significant spatial variability in understorey radiation, which contrasts with the relatively uniform distribution of overstory radiation. This variability is largely driven by the interplay between slope aspects, with PFS receiving substantially less radiation than EFS. This difference is further exacerbated by the reduced shading effects from sparser overstory vegetation on EFS, which allows more sunlight to reach the understorey.

The implications of these findings are useful for understanding the microclimatic conditions that influence vegetation growth and water use in semi-arid woodlands. By quantifying the spatial distribution of radiation at multiple canopy levels, this research provides a foundation for more accurate ecohydrological modelling and supports the development of targeted reforestation strategies that account for the complex interactions between topography, radiation, and vegetation.

Chapter 4 focuses on the mapping of the spatial distribution of understorey ET and the factors that drive variability in water use across different parts of the catchments. By integrating the MEP model with airborne survey data, this chapter reveals substantial spatial heterogeneity in understorey ET, particularly in response to flood events and variations in topographic position. Topographic features, especially slope orientation, were found to significantly influence understorey ET. For instance, EFS generally exhibited higher ET rates compared to PFS due to increased incident solar radiation and warmer microclimatic conditions. It highlights the variations in incident radiation, such as differences in sunlight exposure and shading effects, play a crucial role in determining the microclimatic conditions that govern ET rates. Following flood events, surface ET responses varied significantly based on vegetation cover. Areas with dense overstory vegetation cover show less change of understorey ET than open surface. Moreover, the overstory and understorey layers exhibited distinct patterns of water use, indicating a complex interplay between different vegetation layers. The study finds that following flood events, the ET of overstory vegetation significantly increased, while understorey ET remained largely unchanged. This increase in overstory ET is likely due to the enhanced water availability, allowing larger trees with extensive root systems to uptake and transpire more water. In contrast, understorey ET did not exhibit significant post-flood changes, primarily because it is limited by available radiation. This differential response highlights the distinct roles that vegetation layers play in water dynamics within the catchment. All these findings help to understand the water use patterns of vegetation in semi-arid area.

Appendix A1 examines the use of the LandTrendr algorithm and Landsat time-series data for wildfire detection and post-fire recovery in semi-arid climates. The findings indicate that NDVI outperforms other indices for detecting burned areas in arid to semi-arid regions (290–400 mm annual precipitation), while NBR is more effective in humid areas (575 mm). However, monitoring post-fire recovery using remote sensing indices proves less reliable due to the variable responses of the understorey layer, underscoring the need for a deeper understanding of woodland 3D structure. These results provide guidance for optimizing wildfire detection and recovery monitoring tailored to specific climate conditions.

5.2 Discussion

5.2.1 Topographic effects on vegetation

The results from Chapter 2 indicate that both tree height and NDVI are significantly influenced by topographical factors, specifically TPI, northness, eastness, and slope. TPI and northness exhibited significant negative correlations with tree height, suggesting that trees tend to be taller in concave areas and on polar-facing slopes. NDVI, a proxy for vegetation health and density, was significantly influenced by northness (negative correlation), eastness (positive correlation), slope (negative correlation), and TPI (negative correlation). The significant negative correlation between TPI and both tree height and NDVI underscores the importance of landscape position in overstory development. Concave areas are more likely to accumulate soil moisture due to runoff and higher retention capacity, providing favourable conditions for tree growth and higher vegetation density (Yang et al., 2012; Sun et al., 2014). While slope orientation influences microclimatic conditions, its effect on overstory vegetation is not directly related to the difference of topography induced energy distribution. The results from Chapter 3 indicate that the radiation received by overstory canopies on equator-facing and polar-facing slopes is similar. This suggests that water availability, as influenced by topography, plays a critical role in overstory development on the slopes of different aspects.

Interestingly, at the Mount Wilson catchment, the TPI exhibited a significant correlation with overstory attributes, whereas the TWI did not. Previous studies demonstrated that topographic position and wetness indices are strongly associated with variations in tree height distribution. Specifically, the tallest trees were located in the lowest topographic positions with the highest wetness indices, while shorter trees were found in higher positions with lower wetness indices (Swetnam et al., 2015; Bałazy et al., 2019). While the representation of soil moisture by TWI may no longer be suitable at small scales (e.g. less than 10 m scale). In this scale, TPI can still effectively capture the soil moisture variation, which is in accordance with Araya et al. (2021). These results highlight the importance of considering the appropriate scale when modelling topography-vegetation interactions, addressing a key methodological gap.

Topography also significantly influences understorey ET by regulating both energy distribution and water availability. At the Mount Wilson site, understorey ET generally decreases with increasing slope. Steeper slopes enhance surface runoff and reduce soil moisture retention, thereby limiting water availability for understorey vegetation, as observed in similar studies where slope inclination affects evaporation dynamics by altering moisture distribution and increasing runoff on steeper gradients (Carey & Woo, 2001). Slope orientation exerts the strongest influence on the understorey, particularly on north- and south-facing slopes, by regulating the amount of incident radiation. These topographically driven variations in energy and water availability contribute to the observed spatial heterogeneity in understorey ET, advancing our understanding of how ecohydrological processes are influenced by topography.

Variations in understorey ET not only affect regional water availability but also influence soil properties, such as organic matter decomposition and $CaCO_3$ accumulation, particularly in semi-arid environments(Gutierrez‐Jurado et al., 2006; Sierra et al., 2015), which could directly impact plant growth and overall ecosystem functioning.

5.2.2 Timing and conditions for airborne thermal surveys for ET mapping

Conducting UAV thermal surveys at midday is considered optimal for several reasons. Firstly, image quality obtained during early morning and late afternoon flights is significantly reduced due to the low solar elevation angle. The low angle results in shadows cast by trees and topographical features in woodland areas, which can obscure details in the thermal imagery. These shadows introduce variations in thermal readings that complicating accurate data interpretation and analysis.

Secondly, midday conditions provide the strongest solar radiation which typically corresponds to the highest rates of ET when there is no water shortage, meaning that plants are actively transpiring. The increased solar input elevates the surface temperatures of non-vegetated areas more than those of vegetated areas due to differences in thermal properties and transpiration cooling effects. It could improve the detection of canopy surfaces against bare soil backgrounds and facilitates the identification of spatial patterns of vegetation water stress, if any are present.

Another significant challenge in thermal surveying is the presence of unstable sky conditions. Ideally, drone-based thermal imaging should be conducted under stable atmospheric conditions to ensure consistent and reliable data (Hoffmann et al., 2016; Elfarkh et al., 2023). However, constraints from limited drone availability, long-distance field sites, and unreliable weather forecasts can result in flights under less ideal conditions.

When clouds intermittently obstruct direct sunlight, there is a notable reduction in the energy input to the ground, leading to significant changes in the recorded temperatures by the thermal camera. This variation introduces abrupt changes in measured radiative temperatures over the imaged area, which can complicate the use of thermal imagery. To mitigate these issues, a correction

method has been developed and is detailed in Appendix 2, which adjusts for the effects of variable sky conditions and enhances the accuracy of thermal data interpretation.

5.2.3 Prediction of spatial distribution of vegetation attributes in natural catchments

The prediction of spatial distribution of vegetation attributes in natural catchments is critical for effective ecosystem management and conservation. Based on the findings from Chapter 2, several key insights emerge regarding the methodologies and factors influencing accurate spatial predictions.

The comparative analysis between SLR, MGWR, and RF models revealed that while machine learning approaches like RF can capture complex relationships within specific spatial regions, they are prone to overfitting and struggle with spatial generalizability. The SLR model, although simpler, demonstrated more consistent performance, particularly under spatial block sampling where spatial non-stationarity was prominent. The MGWR model, accounting for spatial non-stationarity, significantly improved explanatory power over global models, especially for attributes like NDVI that exhibit spatially varying relationships with topographic factors. Although the MGWR model excels in exploring and elucidating the intricate relationships between topographic factors and vegetation attributes, its applicability for spatial prediction in unknown regions remains limited. This limitation arises primarily because MGWR requires localized parameter estimates, which are derived from the specific spatial characteristics of the training dataset. To enhance the predictive capabilities of MGWR in uncharted areas, integrating it with spatial interpolation techniques such as kriging or combining it with machine learning algorithms could be a promising approach (Kumar et al., 2012; Yang et al., 2023). Such integration can potentially overcome the constraints of MGWR by providing more robust and transferable predictions across unknow regions.

For spatial prediction, another critical consideration is the 3D structure of vegetation layers, which can be altered by bushfires. The findings from Appendix A1 indicate that NDVI is more effective than other indices for detecting burned areas in semi-arid regions. However, the study also reveals that using remote sensing indices to monitor post-fire recovery is less reliable due to the complex and variable responses of the understorey layer. This variability highlights the limitations of traditional remote sensing indices, which often fail to capture the intricate vertical stratification and interactions within vegetation layers, especially in ecosystems heavily influenced by understorey dynamics.

Accurate spatial predictions of vegetation attributes enable targeted management practices, such as afforestation and reforestation efforts (Xie et al., 2008). Understanding the spatial distribution patterns facilitated by key topographic drivers allows for the optimization of resource allocation and the implementation of strategies that enhance ecosystem resilience (J. Wang et al., 2024). For instance, areas identified with favourable topographic conditions for tree growth can be prioritized

for planting, while regions prone to water stress can be managed to support drought resistant species.

5.3 Potential applications

5.3.1 Guidance for reforestation

Based on the integrated findings of this thesis, we can provide clear guidance for reforestation and ecological restoration strategies in semi-arid areas.

Firstly, assessing tree suitability is crucial for successful reforestation efforts (Chechina & Hamann, 2015; Chen et al., 2019). In the thesis, the results indicate that EFS have significantly higher understorey ET compared to PFS. In the dry season, understorey ET on EFS can account for more than 50% of the total ET, leading to reduced water availability in these areas, which further exacerbates water stress in the ecosystem. The findings of Chapter 2 reveal that the capacity of the landscape to sustain vegetation growth varies significantly and is influenced by topographic factors, making it predictable to some extent. PFS tend to support denser vegetation due to lower understorey ET and higher water availability, which promotes better tree growth and higher NDVI values. This suggests that, for reforestation efforts in semi-arid areas, prioritizing polar-facing slopes could be more effective in maintaining vegetation health and density. On the other hand, for EFS, where water stress and understorey radiation are higher, selecting drought-tolerant species would be essential to ensure successful reforestation. Therefore, in reforestation efforts in semi-arid areas, special attention should be given to species selection on EFS.

Secondly, understanding detailed ecosystem water consumption is essential for balancing water use between ecosystems and human needs (Azarnivand et al., 2020). A comparison of the annual average ET across different experimental sites reveals distinct patterns in water consumption. At the floodplain site, where the annual rainfall is approximately 250 mm, understorey ET reaches up to 190 mm per year, indicating that woodland ecosystems in this region exhibit high overall water consumption. Given this significant water use, reforestation efforts in areas with low rainfall should be carefully managed to minimize potential impacts on local hydrology and runoff (Hoek van Dijke et al., 2022). In the Mount Wilson region, where the average annual rainfall is approximately 700 mm, H. Wang et al. (2024) shows that the total overstory ET on the opposite slope is similar. Result in this study shows that the understorey ET rates for EFS and PFS are estimated at 260 mm and 130 mm per year, respectively. These findings suggest that understorey ET is relatively stable across different precipitation regimes. However, PFS sites have notably lower water consumption compared to EFS. From a water resource management perspective, afforestation in areas with higher precipitation appears more advantageous. Moreover, reforestation in PFS areas could further improve water use efficiency for its lower understorey water consumption. The study's insights align with recent research that afforestation amplifies spatiotemporal inequality in water

availability, increasing water availability in wetter regions while decreasing it in drier ones, underscoring the need to consider local precipitation conditions when planning reforestation to avoid exacerbating water scarcity (Xue et al., 2022; Zan et al., 2024).

5.3.2 Potential applications of the DST model

Beyond its primary application in calculating understorey ET in this study, the proposed DST model offers a multitude of additional uses that could potentially enhance ecological and environmental management practices.

Accurate mapping of solar radiation is pivotal for estimating photosynthetic activity and, consequently, carbon sequestration rates within forest ecosystems (Roxburgh et al., 2006; Ma et al., 2021). The DST model could be integrated with remote sensing data and ecosystem models to quantify the carbon uptake potential of different forest stands. By providing high-resolution solar radiation maps, the DST model enables the assessment of light availability, which directly influences photosynthesis and plant growth. This method could enhance the precision of carbon sequestration estimates and provides critical insights for effective forest management and climate change mitigation strategies.

In urban environments, the DST model could serve as a useful tool for optimizing the placement and selection of tree species within greenery infrastructure projects. By accurately mapping solar radiation across city landscapes, urban planners can optimize the locations for tree plantation that maximize shade cover to reduce urban heat island effects (Balany et al., 2020; Elbardisy et al., 2021; Ouyang et al., 2021). Furthermore, the DST model may be useful for the maintenance and monitoring of urban green spaces by offering insights into light availability, which is crucial for ensuring the health and growth of urban trees. This targeted approach could effectively enhance the functionality of urban forests.

The DST model could be instrumental in identifying thermal shelters for wildlife within forested and natural landscapes. By mapping areas with varying levels of solar radiation, the model can pinpoint microhabitats that provide cooler environments essential for species sensitive to heat stress. These thermal refuges are critical for maintaining wildlife health, particularly in regions experiencing increasing temperatures due to climate change (Elmore et al., 2017; Rakowski et al., 2019). Accurate identification of these region allows ecologists to protect and manage key habitats that support biodiversity and enhance ecosystem resilience. Additionally, the DST model can aid in the design of wildlife corridors and protected areas by ensuring that the thermal shelter zone is strategically located to facilitate species movement. This application is particularly important for species with limited mobility or those fragmented landscapes (Heller & Zavaleta, 2009; Krosby et al., 2010; Baguette et al., 2013).

5.4 Recommendations for future research

Chapter 2 provided insights into the relationships between a select set of vegetation attributes and topographical factors. Future research should aim to incorporate a broader spectrum of vegetation attributes, including diverse vegetation indices such as Enhanced Vegetation Index (EVI), Soil-Adjusted Vegetation Index (SAVI), and Normalized Difference Nitrogen Index (NDNI), which can provide a more nuanced understanding of vegetation health, density, and productivity. Structural parameters like canopy cover, tree diameter at breast height (DBH), and stem density offer deeper insights into forest structure and its relationship with topography. Additionally, studying both aboveground and belowground biomass, as well as biomass allocation patterns, can elucidate how different species allocate resources in response to topographical gradients. Moreover, incorporating seasonal variations into these studies is crucial, as vegetation attributes can exhibit significant temporal changes. Seasonal dynamics like vegetation phenology may alter the strength of relationships between vegetation and topographical factors. Studies that monitor these attributes across different seasons will provide a more comprehensive understanding of temporal influences on vegetation-topography interactions.

Despite the advancements, the study also shows limitations such as the inadequate performance of models for certain vegetation attributes like LAI and crown volume, which appear to be influenced by factors beyond topography, such as species composition and competition. Future research should integrate additional biotic and abiotic variables, including soil properties, species diversity, and climatic factors, to refine spatial predictions.

One significant challenge in forest structure analysis is the accurate detection and separation of individual trees from LiDAR data, particularly for species with irregular shapes such as eucalyptus. Currently, the manual separation process in this study is highly time-consuming and labour-intensive, limiting the scalability and efficiency of large-scale forest assessments. Traditional Individual Tree Detection (ITD) methods, such as watershed segmentation and region growing, often fall short when applied to trees with complex and irregular structure, as these algorithms struggle to delineate distinct tree crowns and trunks accurately. This limitation underscores the need for the development of automated ITD techniques tailored to handle the morphological diversity of different tree species. Future research should focus on leveraging advanced machine learning and deep learning algorithms, which have shown promise in enhancing the precision and efficiency of tree detection in structurally complex forest environments.

One of the primary constraints in applying the DST model to large-scale environments is its computational efficiency. As the spatial extent of the study area increases, the volume of data and the complexity of calculations required to accurately model understorey radiation grow substantially, potentially limiting the model's practicality for extensive applications. To address this challenge, future research should focus on integrating satellite-based data to model understorey

radiation. Satellite observations offer extensive coverage and high temporal resolution. However, leveraging satellite data necessitates the adaptation of the DST model to account for varying spatial resolutions and the inherent differences in data sources. As the scale of analysis shifts individual trees to pixels of mixed trees and inter-canopy space, the underlying physical processes influencing solar radiation distribution must be re-evaluated. Factors such as vegetation types, atmospheric conditions, and mixing pixels should be considered, requiring improvement of the existing model to maintain accuracy and reliability. Furthermore, optimizing the DST model for parallel processing and utilizing cloud-based computational resources could enhance its efficiency, enabling more rapid and large-scale application.

Chapter 4 highlighted the potential of high-resolution thermal data from satellites for large-scale ET monitoring. Future research in this domain should focus on several critical advancements. Firstly, method development for accurately separate ET contributions from overstory and understorey vegetation is essential for enhancing the precision of ET maps and improving our understanding of vertical water use dynamics within forest ecosystems. Additionally, increasing the temporal frequency of ET measurements by utilizing technology like geostationary satellites can capture diurnal and seasonal variations in ET, leading to more dynamic and responsive water resource management strategies. Furthermore, the integration of satellite-based thermal data with ground-based measurements and hydrological models is important for ET estimates. This combination ensures higher accuracy and reliability of ET maps by providing comprehensive datasets that account for both large-scale patterns and localized conditions, thereby facilitating more effective monitoring and sustainable management of water resources.

5.5 References

Araya, S. N., Fryjoff-Hung, A., Anderson, A., Viers, J. H., & Ghezzehei, T. A. (2021). Advances in soil moisture retrieval from multispectral remote sensing using unoccupied aircraft systems and machine learning techniques. *Hydrology and Earth System Sciences*, *25*(5), 2739-2758.

Azarnivand, A., Camporese, M., Alaghmand, S., & Daly, E. (2020). Modeling hydrological impacts of afforestation on intermittent streams. *Science of the Total Environment*, *728*, 138748.

Baguette, M., Blanchet, S., Legrand, D., Stevens, V. M., & Turlure, C. (2013). Individual dispersal, landscape connectivity and ecological networks. *Biological reviews*, *88*(2), 310-326.

Balany, F., Ng, A. W., Muttil, N., Muthukumaran, S., & Wong, M. S. (2020). Green infrastructure as an urban heat island mitigation strategy—a review. *Water*, *12*(12), 3577.

Bałazy, R., Kamińska, A., Ciesielski, M., Socha, J., & Pierzchalski, M. (2019). Modeling the effect of environmental and topographic variables affecting the height increment of Norway spruce stands in mountainous conditions with the use of LiDAR data. *Remote Sensing*, *11*(20), 2407.

Carey, S. K., & Woo, M. k. (2001). Spatial variability of hillslope water balance, Wolf Creek basin, subarctic Yukon. *Hydrological Processes*, *15*(16), 3113-3132.

Chechina, M., & Hamann, A. (2015). Choosing species for reforestation in diverse forest communities: social preference versus ecological suitability. *Ecosphere*, *6*(11), 1-13.

Chen, Y., Wu, B., Chen, D., & Qi, Y. (2019). Using machine learning to assess site suitability for afforestation with particular species. *Forests*, *10*(9), 739.

Elbardisy, W. M., Salheen, M. A., & Fahmy, M. (2021). Solar irradiance reduction using optimized green infrastructure in arid hot regions: A case study in el-nozha district, Cairo, Egypt. *Sustainability*, *13*(17), 9617.

Elfarkh, J., Johansen, K., Angulo, V., Camargo, O. L., & McCabe, M. F. (2023). Quantifying Within-Flight Variation in Land Surface Temperature from a UAV-Based Thermal Infrared Camera. *Drones*, *7*(10), 617.

Elmore, R. D., Carroll, J. M., Tanner, E. P., Hovick, T. J., Grisham, B. A., Fuhlendorf, S. D., & Windels, S. K. (2017). Implications of the thermal environment for terrestrial wildlife management. *Wildlife Society Bulletin*, *41*(2), 183-193.

Gutierrez-Jurado, H. A., Vivoni, E. R., Harrison, J. B. J., & Guan, H. (2006). Ecohydrology of root zone water fluxes and soil development in complex semiarid rangelands. *Hydrological Processes: An International Journal*, *20*(15), 3289-3316.

Heller, N. E., & Zavaleta, E. S. (2009). Biodiversity management in the face of climate change: a review of 22 years of recommendations. *Biological conservation*, *142*(1), 14-32.

Hoek van Dijke, A. J., Herold, M., Mallick, K., Benedict, I., Machwitz, M., Schlerf, M., Pranindita, A., Theeuwen, J. J., Bastin, J.-F., & Teuling, A. J. (2022). Shifts in regional water availability due to global tree restoration. *Nature Geoscience*, *15*(5), 363-368.

Hoffmann, H., Nieto, H., Jensen, R., Guzinski, R., Zarco-Tejada, P., & Friborg, T. (2016). Estimating evaporation with thermal UAV data and two-source energy balance models. *Hydrology and Earth System Sciences*, *20*(2), 697-713.

Krosby, M., Tewksbury, J., Haddad, N. M., & Hoekstra, J. (2010). Ecological connectivity for a changing climate. *Conservation Biology*, *24*(6), 1686-1689.

Kumar, S., Lal, R., & Liu, D. (2012). A geographically weighted regression kriging approach for mapping soil organic carbon stock. *Geoderma*, *189*, 627-634.

Ma, F., Zhang, F., Quan, Q., Wang, J., Chen, W., Wang, B., Zhou, Q., & Niu, S. (2021). Alleviation of light limitation increases plant diversity and ecosystem carbon sequestration under nitrogen enrichment in an alpine meadow. *Agricultural and forest Meteorology*, *298*, 108269.

Ouyang, W., Morakinyo, T. E., Ren, C., Liu, S., & Ng, E. (2021). Thermal-irradiant performance of green infrastructure typologies: Field measurement study in a subtropical climate city. *Science of the Total Environment*, *764*, 144635.

Rakowski, A. E., Elmore, R. D., Davis, C. A., Fuhlendorf, S. D., & Carroll, J. M. (2019). Thermal refuge affects space use and movement of a large-bodied galliform. *Journal of Thermal Biology*, *80*, 37-44.

Roxburgh, S., Wood, S., Mackey, B., Woldendorp, G., & Gibbons, P. (2006). Assessing the carbon sequestration potential of managed forests: a case study from temperate Australia. *Journal of Applied Ecology*, *43*(6), 1149-1159.

Sierra, C. A., Trumbore, S. E., Davidson, E. A., Vicca, S., & Janssens, I. (2015). Sensitivity of decomposition rates of soil organic matter with respect to simultaneous changes in temperature and moisture. *Journal of advances in modeling earth systems*, *7*(1), 335-356.
Sun, F., Lü, Y., Fu, B., Ma, Z., & Yao, X. (2014). Spatial explicit soil moisture analysis: pattern and its stability at small catchment scale in the loess hilly region of China. *Hydrological Processes*, *28*(13), 4091-4109.
Swetnam, T. L., Lynch, A. M., Falk, D., Yool, S., & Guertin, D. (2015). Discriminating disturbance from natural variation with LiDAR in semi-arid forests in the southwestern USA. *Ecosphere*, *6*(6), 1-22.
Wang, H., Guan, H., Xu, X., Gao, L., Gutiérrez-Jurado, H. A., & Simmons, C. T. (2024). Topographic regulations on ecohydrological dynamics in a montane forest catchment and the implications for plant adaptation to environment. *Journal of Hydrology*, 131412.
Wang, J., Xu, H., Yang, Q., Li, Y., Ji, M., Li, Y., Chang, Z., Qin, Y., Yu, Q., & Wang, X. (2024). Topographic Variation in Ecosystem Multifunctionality in an Old-Growth Subtropical Forest. *Forests*, *15*(6), 1032.
Xie, Y., Sha, Z., & Yu, M. (2008). Remote sensing imagery in vegetation mapping: a review. *Journal of Plant Ecology*, *1*(1), 9-23.
Xue, B., Wang, G., Helman, D., Sun, G., Tao, S., Liu, T., Yan, D., Zhao, T., Zhang, H., & Chen, L. (2022). Divergent hydrological responses to forest expansion in dry and wet basins of China: implications for future afforestation planning. *Water Resources Research*, *58*(5), e2021WR031856.
Yang, L., Wei, W., Chen, L., Jia, F., & Mo, B. (2012). Spatial variations of shallow and deep soil moisture in the semi-arid Loess Plateau, China. *Hydrology and Earth System Sciences*, *16*(9), 3199-3217.
Yang, W., Deng, M., Tang, J., & Luo, L. (2023). Geographically weighted regression with the integration of machine learning for spatial prediction. *Journal of Geographical Systems*, *25*(2), 213-236.
Zan, B., Ge, J., Mu, M., Sun, Q., Luo, X., & Wei, J. (2024). Spatiotemporal inequality in land water availability amplified by global tree restoration. *Nature Water*, 1-12.

APPENDIX
A1 SPATIOTEMPORAL DELINEATION OF BUSHFIRE IN SEMI-ARID AREA

Abstract

Understanding the wildfire extent and post-fire vegetation recovery is critical for fire and forest management. Remote sensing imagery is widely used in wildfire detection because it provides continuous and large-scale surface monitoring capability. In this study, we apply and evaluate the performance of the LandTrendr algorithm in wildfire detection across a semi-arid climate region with a marked precipitation gradient. The aims are to compare the performance of four spectral indices for the burned areas and post-fire recovery detection for different climate conditions and investigate the relationship between suitable model parameters and climate conditions. The results show that NDVI outperforms other indices, including NBR, in burned area detection for drier areas (annual precipitation <400 mm). Disturbance signal-to-noise ratio can serve as an indicator for suitable index selection for semi-arid areas. Although the performance in the detection of burned pixels varies among different indices, they are all suitable for delineating post-fire recovery except for the wet site (annual precipitation of 575 mm) where NBR displays the best performance. Parameter optimization results along the climate gradient show that climate conditions have a significant impact on suitable parameter selection. These findings provide guidance on vegetation wildfire detection in arid and semi-arid climates to support wildfire risk and forestry management.

A1.1 Introduction

Wildfires (or bushfires in Australia) are recurring natural disturbances that shape the structure and functions of terrestrial ecosystems. They cause vegetation mortality and reduce plant biomass and biodiversity within a short period (Seidl et al., 2014). Wildfires also affect the atmospheric chemistry and carbon budget by releasing carbon and trace gases such as nitrous oxide, contributing to climate warming (Arora & Boer, 2005). Conversely, post-fire recovery tends to sequester atmospheric carbon dioxide due to the high primary productivity and low levels of heterotrophic respiration of young growing forests (Barford et al., 2001; Masek et al., 2008). Understanding the effect of these processes is important for carbon budget modelling, wildfire susceptibility and probability mapping, and analysing the wildfire impact on wildlife habitat (McKendry et al., 2019; Iban & Sekertekin, 2022; Charizanos & Demirhan, 2023; Martínez-López et al., 2023). To this end, methods for accurately tracking wildfire-burned areas and post-fire recovery are needed.

Remote sensing technology provides time-series of earth observations, i.e. multispectral imagery at various spatial resolutions (Chuvieco et al., 2019), which has been extensively employed for wildfire disturbance detection. Previous studies found that the most significant changes in reflectance after a fire event are noticeable in the near-infrared (NIR) band and the short-wave

infrared (SWIR) band (García & Caselles, 1991; Trigg & Flasse, 2001). With a massive reduction of green leaves, the NIR reflectance decreases sharply immediately after a fire event, while the drying effect of the fire leads to an increase of SWIR reflectance (Chuvieco & Congalton, 1988; Ceccato et al., 2001). Some pioneer studies mapped burned areas based on the spectral change in the NIR band (Hitchcock & Hoffer, 1974; Hall et al., 1980). In order to utilize multispectral information, García and Caselles (1991) proposed a normalized NIR and SWIR reflectance difference, referred to as the normalized burn ratio (NBR). The NBR index proved to have the capacity to distinguish unburned and burned areas and became the most common remote sensing index for detecting burned areas (Key & Benson, 2006; Escuin et al., 2008; Lanorte et al., 2013; White et al., 2017).

Previous methods of wildfire detection were mainly based on comparing a specific spectral band or index of pre- and post-fire images, which is referred to as a bi-temporal approach (Epting et al., 2005). Although it is straightforward to perform, one potential problem with the bi-temporal approach is that it does not utilize multitemporal imagery to its full potential. This problem may limit its performance in burned area mapping and capacity in detecting surface condition changes with a long duration, such as in post-fire recovery processes (Hicke et al., 2006; Kennedy et al., 2010; Goodwin & Collett, 2014). In contrast to the bi-temporal approach, a time series approach can capture more detail in the dynamic changes of the Earth's surface. This method not only lends itself to automated image processing but also offers insights into different aspects of the disturbances, such as frequency and duration (Bourbonnais et al., 2017; Hislop et al., 2018; Nguyen et al., 2018). Kennedy et al. (2010) proposed the Landsat-based detection of Trends in Disturbance and Recovery (LandTrendr, denoted as LTR hereafter) that detects the abrupt change and recovery at a pixel level using the Landsat archive. Huang et al. (2010) proposed the Vegetation Change Tracker (VCT) algorithm for tracking forest disturbance history using the Landsat image time series. The Breaks for Additive Season and Trend (BFAST) algorithm adopts a decomposed image time series into the trend, season, and noise components to detect vegetation phenological change (Verbesselt, Hyndman, Zeileis, et al., 2010). Zhu et al. (2012) proposed the Continuous Monitoring of Forest Disturbance Algorithm (CMFDA) for abrupt forest change detection based on the Landsat archive. Based on CFMDA, an improved algorithm named Continuous Change Detection and Classification (CCDC) was developed, which extends the detecting object from forest to other land cover types and includes a slope component to detect gradual changes (Zhu & Woodcock, 2014). Table A1 lists these change-detecting algorithms and wildfire-related research.

LTR is a change detection algorithm designed for Landsat time series images that is useful for detecting long- and short-term disturbances (Kennedy et al. 2010). This method aims to detect the stable status and dramatic changes happening in an annual time series of spectral values or indices at a pixel level by using a time-segmentation method to fit the spectral trajectory into several piecewise functions. It has been widely used in wildfire detection for its capability to identify severe

and abrupt disturbances and to provide several important metrics, such as magnitude, change duration, and recovery rates, which are useful in characterizing fire events (Quintero et al., 2019; Rodman et al., 2021). For example, Kennedy et al. (2012) analysed the spatial and temporal patterns of wildfire and harvest disturbance in the Northwest Forest in the USA from the result of LTR. Viana-Soto et al. (2020) adopted LTR to derive trajectory metrics of two large wildfire events in pine forests in Spain from 1994 to 2018 and evaluated the post-fire recovery. Bright et al. (2019) used LTR to examine the post-recovery of NBR for wildfire events that occurred in western North America from 2000 to 2007. Kennedy et al. (2018) made the LTR algorithm available in the Google Earth Engine (GEE), a freely available satellite image platform for storage of extensive image data and cloud-based image processing (Gorelick et al., 2017). Quintero et al. (2019) evaluated the LTR algorithm for detecting burned areas in west-central Spain. Bonney et al. (2020) applied the LTR in GEE over Kangaroo Island, Australia, to monitor the bushfire history.

Table A1 A summary of wildfire detection studies based on time series approaches. Circled numbers are marked in Figure A1

Reference	Disturbance type	Method	Index	Vegetation type
Kennedy et al. (2010) ①	Wildfire, harvest, and insect-related mortality	LTR	NBR, NDVI, Wetness	Boreal forest, temperate forest, and shrub
Verbesselt, Hyndman, Newnham, et al. (2010)	Forest disturbance	BFAST	NDVI	Conifer forest
Huang et al. (2010)	Wildfire, logging, harvest, and urbanization	VCT	FZ	Temperate forest, mixed forest, shrub, and grassland
Kennedy et al. (2012) ②	Wildfire, harvest, and insect-related mortality	LTR	NBR	Conifer forest and dry forest
Zhu et al. (2012)	Forest disturbance	CMFDA	Spectral bands	Deciduous and evergreen forest
Zhu and Woodcock (2014)	Landcover change	CCDC	Spectral bands	Urban, agricultural field, and forest clearing
Watts and Laffan (2014)	Wildfire and flood	BFAST	EVI	Dry forest and shrubland
Meigs et al. (2016) ③	Wildfire and insect-related mortality	LTR	NBR	Conifer forest
X. Q. Fang et al. (2018)	Wildfire, harvest, and Insect-related mortality	BFAST	NDVI	Conifer forest
Novo-Fernandez et al. (2018)	Wildfire and insect-related mortality	VCT	Tasseled cap index	Temperate forest
Quintero et al. (2019) ④	Wildfire	LTR	NBR	Mediterranean forest and grassland
Bright et al. (2019)	Wildfire recovery	LTR	NBR	Conifer forest and mixed forest
Bonney et al. (2020) ⑤	Wildfire	LTR	NBR	Mediterranean forest and agricultural field
Viana-Soto et al. (2020) ⑥	Wildfire recovery	LTR	NBR	Mediterranean forest
Rodman et al. (2021) ⑦	Wildfire and insect-related mortality	LTR	NBR	Subalpine forest
Deng et al. (2021)	Wildfire and extreme events	BFAST	NDVI and EVI	Conifer forest and deciduous forest
Souza et al. (2021)	Wildfire and clearing	CCDC	EVI, NBR, NDVI, and other VI	Savanna and agricultural fields
Qiu et al. (2021)	Wildfire and recovery	VCT	FZ, EVI, NBR, NDMI, NDVI	Cold temperate forest
Wimberly et al. (2022) ⑧	Wildfire, and recovery	LTR	NDFI	Tropical forest
Zhang et al. (2022)	Wildfire, logging, and insect-related mortality	CCDC	Spectral bands	boreal forest and temperate forest

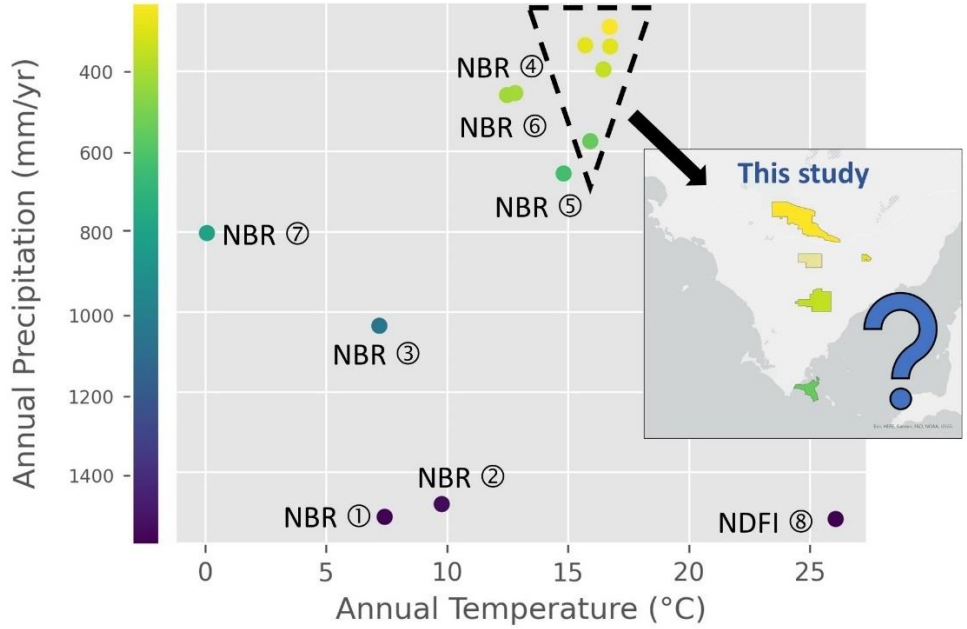

Figure A1.1 LTR-based wildfire-related studies mapped on the mean annual precipitation and temperature space. Circled numbers are associated with studies in Table 1. Our study areas are marked with a dash-line triangle. Climatic data are retrieved from the WorldClim database (Hijmans et al. 2005)

Accurate detection of the disturbance and recovery is largely dependent on the input time series data, which records the history of the land surface dynamic. The NBR index is considered the most sensitive spectral index in wildfire disturbance detection by utilizing both NIR and SWIR bands that reflect green vegetation and soil moisture. The NBR and dNBR (difference between pre- and post-fire NBR) have been widely used in burn scar and burn severity detection in the bi-temporal approach (Key & Benson, 2006; Veraverbeke et al., 2010; Edwards et al., 2013; Tran et al., 2018). For the time series approach, Kennedy et al. (2010) found the NBR is the most sensitive index in capturing disturbance for the diverse types of forest cover in the western United States. Cohen et al. (2010) performed a comparative test of using NBR and Tasseled Cap Wetness (TCW) for LTR, and confirmed that NBR is better than TCW in wildfire disturbance detection based on the forest in the States of Oregon and Washington, USA. Hislop et al. (2018) assessed the performance of several spectral indices in wildfire disturbance and recovery detection with multitemporal imagery in the eastern half of Victoria, Australia and found that NBR outperforms other indices (NDVI, SAVI NDMI and Tasseled Cap indices).

Most LTR-based investigations were conducted in areas with relatively high annual precipitation and adopted the NBR for wildfire detection (Table A1 and Figure A1). This raises the question of whether the NBR is still the first choice for disturbance detection in arid and semi-arid climates and vegetation cover. The distribution of biomes and plant functional types is largely determined by the climate conditions, including precipitation and temperature patterns (Guerschman et al., 2020).

From an ecological perspective, regions with lower precipitation tend to have sparse vegetation cover, reduced photosynthesis, and low biodiversity. These climate-dependent land cover features can be reflected differently in the spectral signals of different bands from remote sensing images. As a result, the relative performance of different spectral indices in the time series approaches (such as LTR) may vary with climate and vegetation cover conditions. By selecting the most appropriate index for a given region, the LTR algorithm can provide more accurate results that are meaningful in the context of the specific climate conditions of that region.

Cohen et al. (2018) proposed the disturbance to noise ratio (DSNR), which measures the signal strength of disturbance event relative to background noise in the time series data. Specifically, by using the DSNR, the study suggests that SWIR-based indices, such as NBR, outperform other indices in detecting forest disturbance across a diverse range of forest types in the USA. Further research is required to determine the effectiveness of the DSNR in index selection for semi-arid environments.

Another issue in applications of LTR is the parameterization. A set of default parameters is proposed after a test with a large number of disturbance events in western Oregon and Washington states (Kennedy et al., 2010; Kennedy et al., 2018). These default parameters are generally adopted in the LTR applications (Yang et al., 2018; Xiao et al., 2020; De Marzo et al., 2021; Gelabert et al., 2021; Rodman et al., 2021). Some studies suggest that the parameter should be optimized for better detection accuracy (Lombard et al., 2023). Yang et al. (2018) optimized the LTR parameters for mining detection by analyzing the NDVI characteristics. Bonney et al. (2020) tested the best index and parameters of LTR for the Kangaroo Island bushfires of 2019-2020. de Jong et al. (2021) used LTR for mangrove dynamic analysis and optimized three parameters: Max Segment, Recovery Threshold and Best Model Proportion for best fitting. Runge et al. (2022) optimized the LTR index and parameters for detecting rapid permafrost thaw disturbance. However, the underlying relationship between the parameters and climate conditions is still not fully understood. Investigating this relationship through sensitivity analysis can provide valuable insight into the factors that are most important for LTR parameterization and potentially improve the accuracy and reliability in land cover disturbance (e.g., wildfires) detection.

In this study, the LTR algorithm is applied to five conservation parks across Eyre Peninsula in South Australia to detect wildfires from 1990 to 2020. The objective of this study is to develop guidance for determining spectral index and parameters in LTR to delineate burned areas and post-fire recovery in semi-arid climates by answering the following questions:

(1) Is the NBR index, tested and applied mostly in humid and temperate climates, suitable for wildfire detection in semi-arid climates?

(2) If not, what spectral index is more suitable for semi-arid environments?

(3) Can we determine a suitable spectral index for LTR to detect wildfires in semi-arid regions using DSNR?

(4) Is there a climate-dependent relationship that is useful for LTR parameterization?

(5) What is the performance of different indices in detecting post-fire recovery in semi-arid climates?

A1.2 Study area and Method

A1.2.1 Study area and data

The study area is the Eyre Peninsula, located in the western part of South Australia (Figure A2). The climate over most of the area is characterized as Mediterranean, with hot and dry summers and mild and wet winters. A strong precipitation gradient exists from the south (575 mm/y) to the north (290 mm/y). The majority of the Eyre Peninsula has been cleared of native vegetation for farming wheat, barley, lupins, and canola, as well as for sheep and cattle livestock. Only the conservation parks are selected for further study (marked in black in Figure A2) to eliminate areas with strong anthropogenic disturbances such as harvesting and irrigation.

Table A2 presents the seasonality index and aridity index for each conservation park. The seasonality index measures the tendency of an area to have more rainfall in certain months or seasons (Markham, 1970). Its value ranges from 0 to 1, and a higher value indicates a strong seasonal precipitation. The aridity index is defined as the ratio of annual potential evapotranspiration to annual precipitation (Greve et al., 2019). It is widely used to characterize the aridity of an area and interannual variability of dryness. A higher aridity index value indicates a dryer climate condition.

As can be seen from Figure A2 and Table A2, Lincoln Park has the most typical Mediterranean climate among the conservation parks, with precipitation mostly occurring from June to August. The seasonality of the study areas gradually decreases towards the north. In Pinkawillinie Park, there is no obvious seasonal difference in precipitation. The aridity gradually increases from Lincoln Park to Pinkawillinie Park. The dominant vegetation type is *Eucalyptus mallee* for all conservation parks, according to the Forest dataset from the Australian Bureau of Agricultural and Resource Economics and Sciences (Committee, 2019) (Figure A3). '*Mallee*' is a unique Australian term for a range of eucalyptus trees that have multiple stems rising from an underground lignotuber.

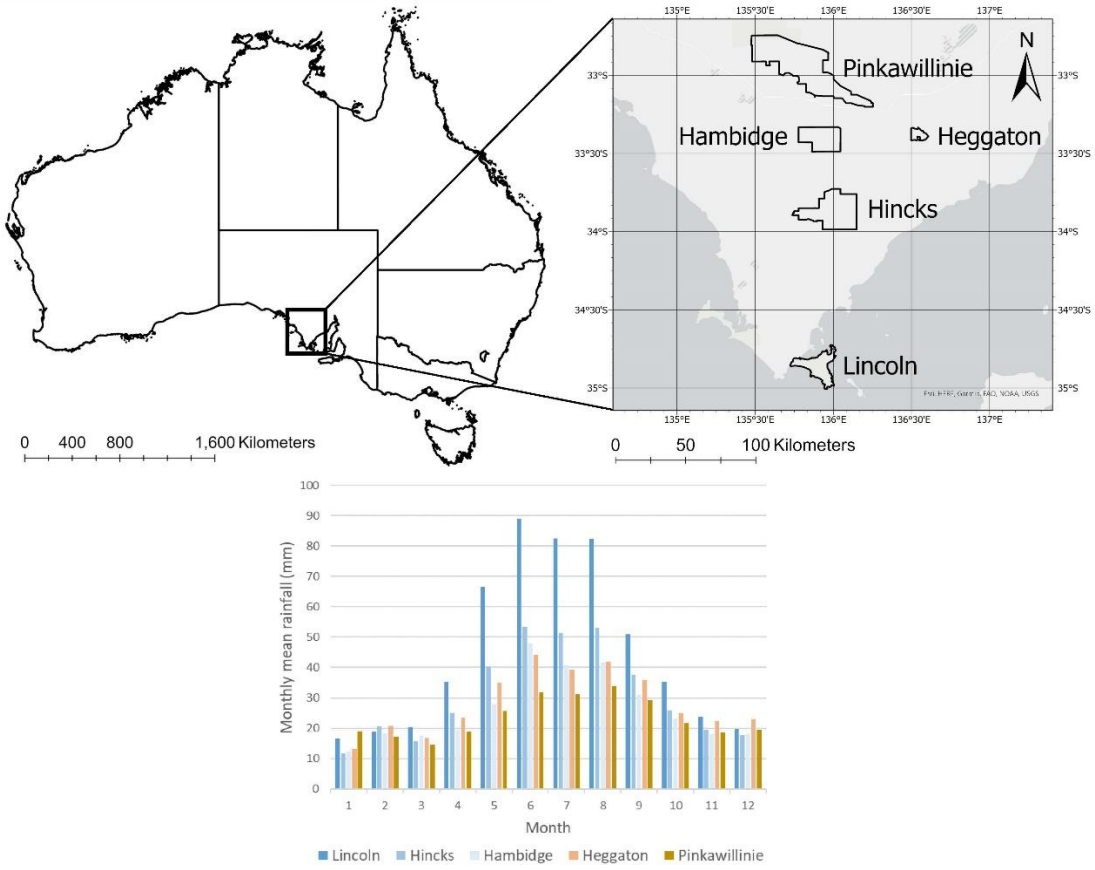

Figure A1.2 The geographical location of selected conservation parks in Eyre Peninsular and the monthly mean rainfall (2000 to 2020). The precipitation data from the nearest weather station are obtained from The Bureau of Meteorology, Australian Government (http://www.bom.gov.au/)

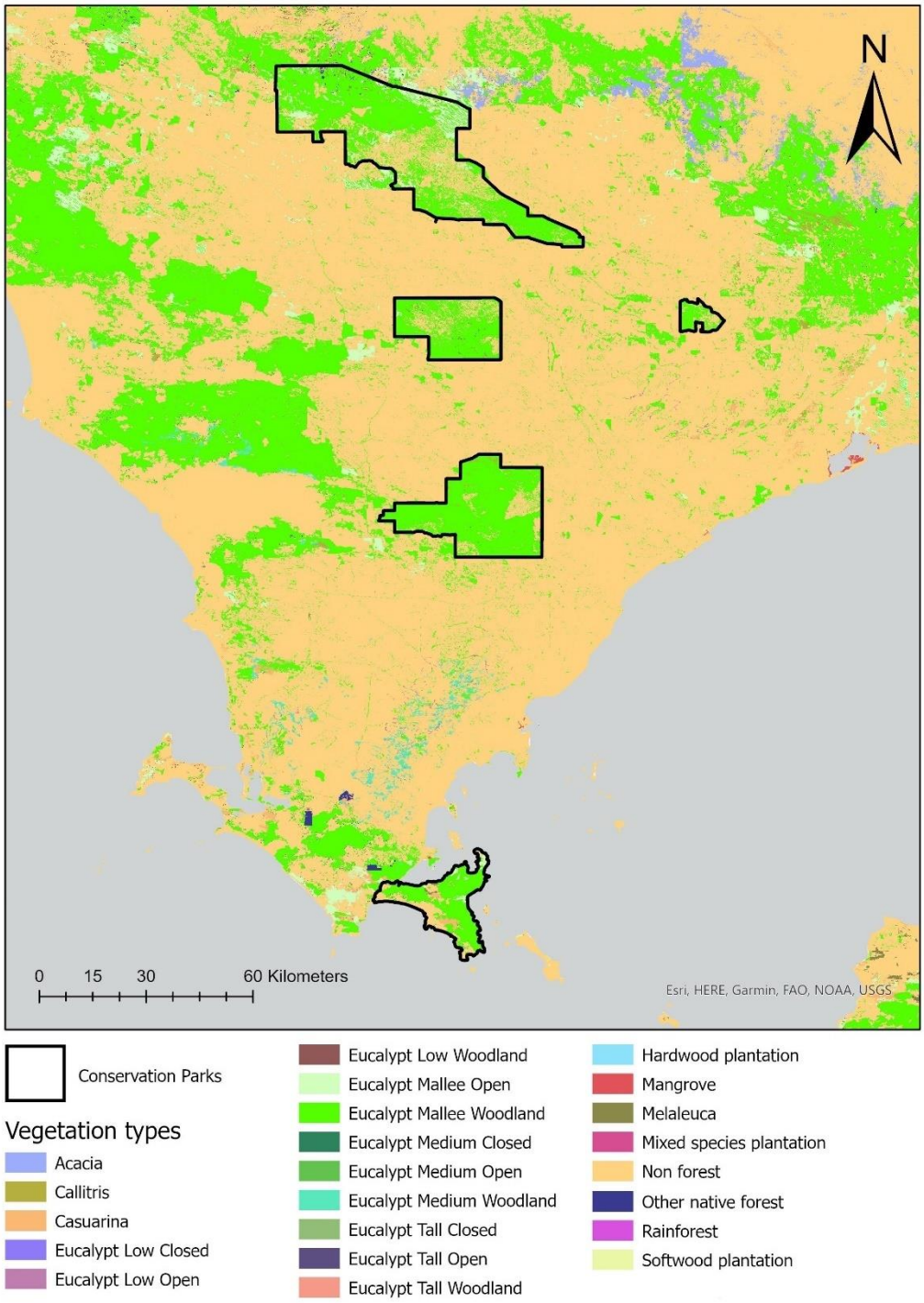

Figure A1.3 Forest types from Australian Bureau of Agricultural and Resource Economics and Sciences (ABARES)

Table A2 Seasonality and aridity indices of the study area. The potential evapotranspiration data used for aridity index calculation is derived from MOD16A2 from 2000 to 2014 (Mu et al. 2014)

	Lincoln	Hincks	Hambidge	Heggaton	Pinkawillinie
Seasonality index	0.40	0.32	0.27	0.23	0.17
Aridity index	3.05	5.24	6.06	7.75	7.76

The remote sensing data employed for this research include imagery of the Landsat Thematic Mapper (TM), Enhanced Thematic Mapper Plus (ETM+), and Operational Land Imager (OLI) sensors. They provide moderate resolution (30 m) earth imagery with acceptable temporal resolution (16 day's repeat cycle). Images from 1990 to 2020 are selected for the burned area and recovery detection. The growing season (1st June – 31st August) images are used to calculate the best-pixel composition based on medoid to reduce the seasonal variation. A CFMASK algorithm is employed to mask out cloud, shadow, and water bodies within multitemporal imagery (Zhu et al. 2015). The data preparation and LTR implementation are run in the Google Earth Engine platform (Gorelick et al. 2017; Kennedy et al. 2018).

The reference fire map is collected from the Department for Environment and Water, Government of South Australia (https://data.sa.gov.au/data/dataset/fire-history). This data records the fire date and burn scar mapping for the last 40 years in South Australia. The data are generated using different capture techniques with data sources, including aerial photography, multi-sensor satellite images and scientific fire reports. Table A3 shows the selected forest fire events that occurred in the conservation parks in Eyre Peninsula from 1990 to 2020.

Table A3 Summary of forest fire events from 1990 to 2020. The total areas from Lincoln Park to Pinkawillinie Park are 30,548, 67,847, 38,070, 6,504, and 135,784 hectares. Wildfires are naturally occurring fire. Prescribed burns are controlled events to reduce fuel loads

Location	Year	Fire type	Hectares burned
Lincoln Park	2001	Wildfire	10934
Lincoln Park	2009	Wildfire	219
Lincoln Park	2012	Prescribed Burn	434
Lincoln Park	2016	Prescribed Burn	904
Hincks Park	1999	Wildfire	3605
Hincks Park	2006	Prescribed Burn	1284
Hincks Park	2007	Wildfire	7799
Hincks Park	2009	Prescribed Burn	1710
Hincks Park	2011	Prescribed Burn	794
Hincks Park	2016	Prescribed Burn	353
Hincks Park	2017	Prescribed Burn	4642
Hambidge Park	2000	Wildfire	28492
Hambidge Park	2005	Wildfire	43
Hambidge Park	2018	Wildfire	31
Heggaton Park	1997	Wildfire	2642
Heggaton Park	2001	Wildfire	65
Heggaton Park	2006	Prescribed Burn	164
Pinkawillinie Park	1994	Wildfire	123
Pinkawillinie Park	2001	Wildfire	826
Pinkawillinie Park	2006	Wildfire	28154
Pinkawillinie Park	2010	Prescribed Burn	827
Pinkawillinie Park	2012	Prescribed Burn	2935
Pinkawillinie Park	2018	Wildfire	559

Fractional vegetation cover is an important parameter to express the functional and compositional attributes of forests (Chu and Guo 2014). The Digital Earth Australia Fractional Cover data are adopted for the purpose of post-fire recovery evaluation (https://dev.ecat.ga.gov.au/geonetwork/srv/api/records/145498). Fractional cover data distinguish three main fractions: 1) photosynthetic vegetation, including green leaves and grass; 2) non-photosynthetic vegetation, including branches, dry grass, and litter; 3) bare soil. Natural disturbances like wildfires can significantly alter forest structure, manifested by a decrease in the fraction of photosynthetic vegetation and an increase in the fraction of soil. With the restoration of forest structure, the fraction cover gradually recovers to the pre-fire stage. These data are used to verify the response of different indices to post-fire recovery.

A1.2.2 Methods

A1.2.2.1 Spectral indices and DSNR

Four common spectral indices for burned area detection in the literature (Table A1) including NBR, Normalized Difference Vegetation Index (NDVI), Normalized Difference Moisture Index (NDMI), and Enhanced Vegetation Index (EVI) are calculated from Landsat TM/ETM+/OLI based on the equations shown in Table A4. NBR is designed to distinguish burned and unburned areas by amplifying the different spectral responses of the NIR and SWIR2 bands of Landsat. NDVI utilizes the Red and NIR bands to assess the photosynthetic intensity of vegetation. EVI is designed to minimize the background and atmospheric noise effect on NDVI by adding the Blue band information. NDMI has similar spectral components as NBR but uses the Landsat SWIR1 band, which is more sensitive to vegetation moisture content.

The DSNR is the signal-to-noise ratio calculated for disturbance in the whole time series of observation. The signal is the amplitude of the disturbance event, and the noise is calculated as the root mean square error (RMSE) of the LTR estimates over the whole time series. $RMSE = \sqrt{\frac{\sum_{i=1}^{n}(\hat{y}_i - y_i)}{n}}$, where $\hat{y}$ is the LTR fitted index value, y is the observed index value, and n is the number of observations of the time series. Cohen et al. (2018) calculated the DSNR for several indices and spectral bands and found the result was well related to disturbance detection accuracy. The NBR index, which was the most accurate index in disturbance detection, had the highest DSNR values. This study aims to assess the effectiveness of DSNR in index selection for semi-arid climates.

Table A4 Selected spectral indices for time series analysis for LTR (Blue: Spectral reflectance of blue band with wavelength ranging from 450-510 nm; Red: Red band (640-670 nm), NIR: Near infrared band (850-880 nm); SWIR1: Shortwave infrared band 1 (1570-1650 nm); SWIR2: Shortwave infrared band 2 (2110-2290 nm))

Index	Formula	Related studies
Normalized Burn Ratio	$NBR = \frac{NIR - SWIR2}{NIR + SWIR2}$	Kennedy et al. (2010); Kennedy et al. (2012); Quintero et al. (2019); Qiu et al. (2021)
Normalized Difference Vegetation Index	$NDVI = \frac{NIR - Red}{NIR + Red}$	Verbesselt, Hyndman, Newnham, et al. (2010); X. Q. Fang et al. (2018)
Normalized Difference Moisture Index	$NDMI = \frac{NIR - SWIR1}{NIR + SWIR1}$	Souza et al. (2021)
Enhanced Vegetation Index	$EVI = 2.5 * \frac{NIR - Red}{NIR + 6 * Red - 7.5 * Blue + 1}$	Watts and Laffan (2014); Deng et al. (2021)

A1.2.2.2 LandTrendr

Figure A4 is an example of the LTR detection process. Black squares are the index values of a specified period (e.g., growing season) of each year, and the red line is the fitted spectral trajectory. By segmenting this trajectory, disturbance information can be identified at specific breakpoints—in this example, a wildfire occurred in 2001 is identified.

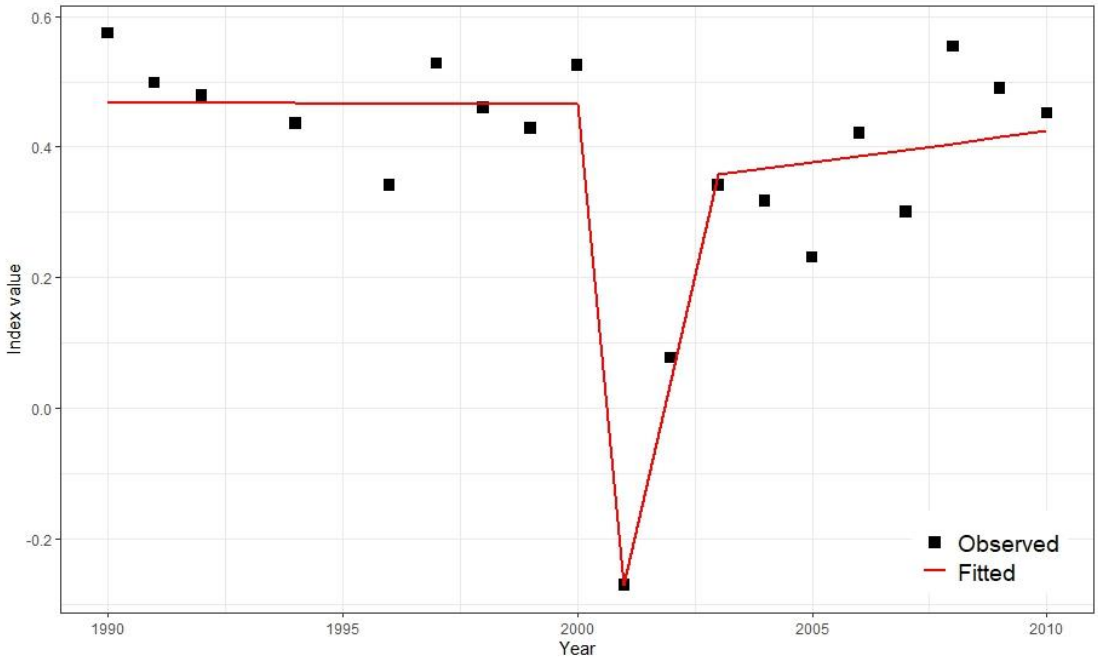

Figure A1.4 A conceptual graph of the LTR time-segmentation method (data extracted from Lincoln Park)

In the process of the LTR algorithm, the performance can be significantly impacted by the way in which the algorithm is tuned to the specific conditions of each region. Parameter calibration is needed in LTR applications as it is a parameter-sensitive algorithm (Quintero et al. 2019b). Table A5 lists all the parameters of LTR. Preliminary sensitivity tests in our study indicate that two parameters—Max Segments (MS) and Recovery Threshold (RT)—are especially critical for the algorithm's performance. They are selected for further evaluation.

MS defines the maximum number of segments used for fitting. RT (unit: yr-1 in this study) defines the threshold of the fast recovery event. A simple disturbance-recovery pattern usually consists of four phases (stable-decrease-recovery-stable). In that case, an MS value of 4 is appropriate to describe the temporal pattern and reduce the impact of noise in the time series. In a complex recovery situation, more segments may be required. RT has a value between 0 and 1. A higher value makes the model less likely to miss a fast recovery while more likely to cause a false positive error.

Table A5 LTR parameters, default values and the values to be evaluated

Parameters	Default	Evaluated value
Max Segments	6	4, 6, 8, 10
Spike Threshold	0.9	-
Vertex Count Overshoot	3	-
Prevent One Year Recovery	TRUE	-
Recovery Threshold	0.25	0.25, 0.5, 0.75, 1
Pval Threshold	0.05	-
Best Model Proportion	0.75	-
Min Observations Needed	6	-

A1.2.2.3 Accuracy evaluation

The data analysis is divided into two parts. The first part evaluates the detection accuracy of the burned area. According to the reference burned area mapping, the overall burned area is 104,352 hectares between 1990 and 2020, and the overlapping area is less than three thousand hectares. Considering that less than 5% of the burned area in our study area has experienced multiple burn events, we ignored this effect when evaluating the accuracy of the burned area. As a result, a pixel is classified as burned or unburned without considering temporal information and then compared to the reference burned map. Prescribed burns typically have a low to medium impact on forest structure (Nguyen et al., 2018). They are considered a form of fire disturbance in this study for the purpose of detecting burned areas. The producer's accuracy and user's accuracy are calculated to evaluate the omission and commission error, respectively. A high producer's accuracy value indicates low omission error (burned areas incorrectly labelled as unburned), and a high user's accuracy value indicates low commission error (unburned areas incorrectly labelled as burned) (Congalton 1991). Overall accuracy and Kappa coefficient are adopted to evaluate the detection accuracy. Overall accuracy is computed as a ratio between the number of correctly classified pixels and the total test samples. The Kappa coefficient is a relative measurement of accuracy that tells how much the classification result is better than a random classification (Congalton et al. 1983). Accuracy matrices are computed for all fire events that occurred within each conservation

park. The difference in the performance of overall accuracy and Kappa coefficient in this study is discussed in Section 1.3.1.

The second part of the data analysis is on the post-fire recovery. Five significant wildfire events with relatively large burned areas (2,642 – 28,492 hectares) are selected, one for each conservation park. Then, the mean fitted index values over the burned area are calculated and plotted as time series. A fraction cover map from Digital Earth Australia is used for comparison of the estimated recovery time. To remove the seasonal variation of the vegetation fraction, a time filter is applied, and only growing season data (June to August) are adopted. Mean values of fraction cover for each year are plotted to show the interannual variation of the vegetation status. A segmented linear regression is applied for noise suppression.

A1.3 Results

A1.3.1 Optimization of selected parameters for LTR

Four metrics are calculated to assess the sensitivity of different parameters. Among these, the kappa coefficient is selected to comprehensively evaluate the detection accuracy for different indices and parameter sets. Although overall accuracy can quantify the absolute accuracy of detection, it is not well-suited for evaluating the performance of various indices for LTR, which uses a binary classification system of 'burned' and 'unburned' values. The user’s accuracy is always higher than the producer’s accuracy for any study area and indices with the same parameter setting (Data not shown for simplicity). That means LTR tends to have a larger omission error than commission error. In other words, unburned pixels are less likely to be mistakenly identified as burned. In most cases, although the LTR does not effectively identify the burned pixels, the overall accuracy still maintains at a high level because the unburned pixels can be accurately identified. Thus, the Kappa coefficient, which measures the relative accuracy compared to random classification, is adopted to comprehensively evaluate the detection accuracy for different indices and parameter sets. Figure A5 shows that there is no obvious spatial pattern in Kappa for different study areas. That means the detection accuracy of LTR does not change with the wetness condition of the study areas. However, the selection of parameters is obviously affected by the precipitation gradient in the study area. In the wetter areas such as Lincoln and Hincks Park, a change in MS does not significantly affect Kappa. While RT affects the detection accuracy, especially when the value of RT is low, Kappa decreases significantly. In more arid areas, such as from Hambidge to Pinkawillinie Park, for most indices, an RT change does not obviously affect detection accuracy. In these regions, small MS values such as 4 are not suitable.

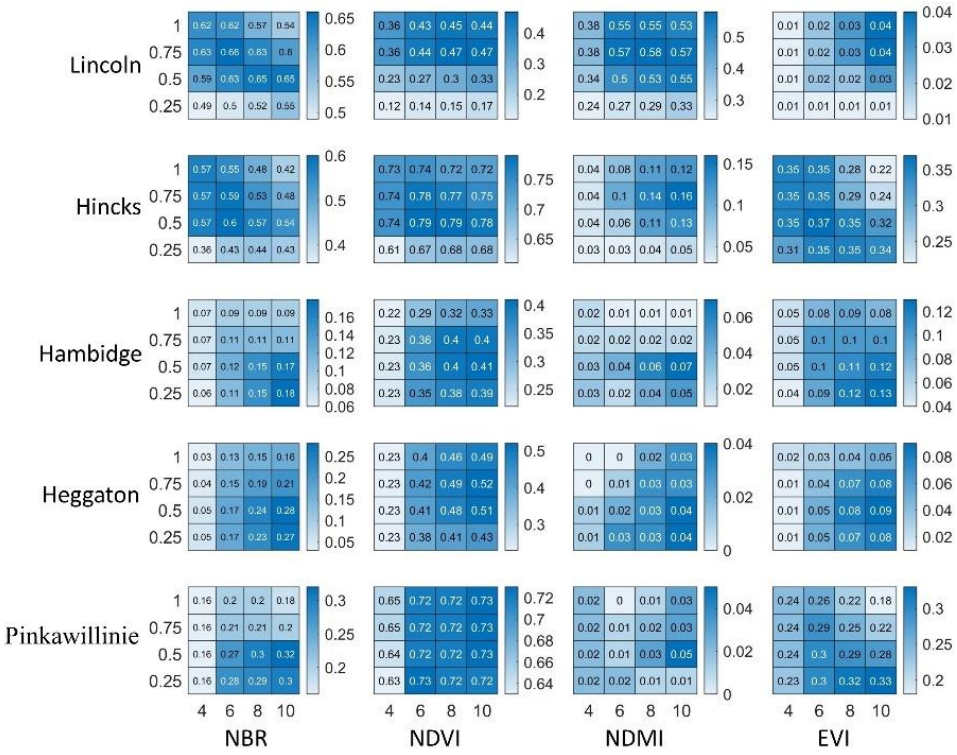

Figure A1.5 Kappa coefficient for different vegetation indices with different parameter sets. (Vertical axes denote Recovery Threshold and horizontal axes denote Maximum Segments)

A1.3.2 Comparison of selected spectral indices in burned area detection

In order to compare the effect of different indices on the LTR algorithm's ability to detect burned areas, the Kruskal-Wallis test is conducted to evaluate the differences in the Kappa coefficients, given that the assumptions of normality and homogeneity of variance are not met in the data. Results show that the Kappa does not follow the same distribution for different indices ($p<0.001$). The pairwise comparison results indicate that the distributions of all indices differ from each other ($p<0.001$) except for the group between NDMI and EVI ($p=0.06$). Figure A6 shows the overall accuracy and Kappa coefficient for each index with the optimized parameter set. The results show that NBR outperforms other indices at Lincoln Park, while NDVI has better performance than NBR at other sites. NDMI performs relatively well in Lincoln Park but not in other study areas, while EVI shows poor performance in all study areas. The above results indicate that the ability of the LTR algorithm to detect burned areas varies with the climatic conditions of the study area and the index used.

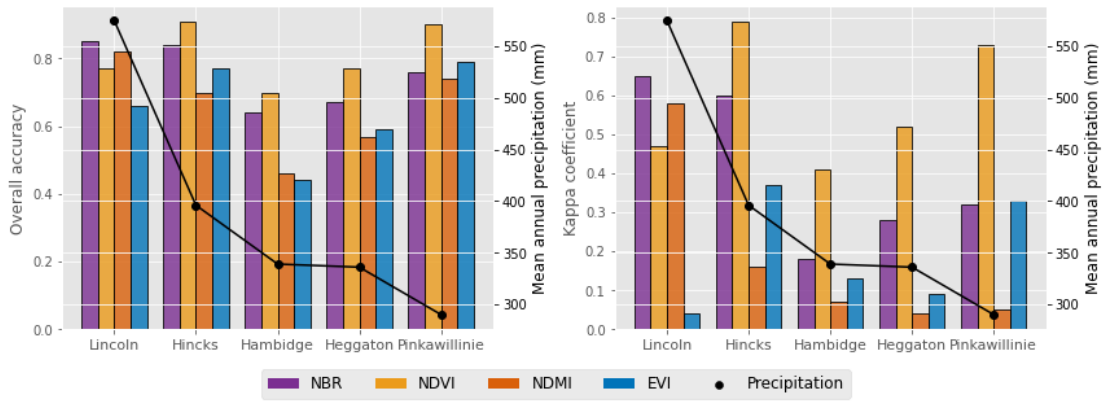

Figure A1.6 Overall accuracy and Kappa coefficient for different vegetation indices with the optimized parameter sets

DSNR is calculated within the burned area and plotted in Figure A7. In Lincoln Park, the DSNR of NBR is higher than that of other indices, followed by NDMI. For the rest of the conservation parks, DSNR of NDVI is generally larger than those of other indices. This result is closely related to the pattern of Kappa coefficients that high DSNR corresponds to high detection accuracy. Therefore, for a study area without reference data, suitable indices can be selected according to the difference in DSNR values. For some fires in the Hincks and Hambidge Park, high DSNR values of NDMI are observed, while the detection accuracy of NDMI in these areas is poor. However, this exception only occurs in very few fire events.

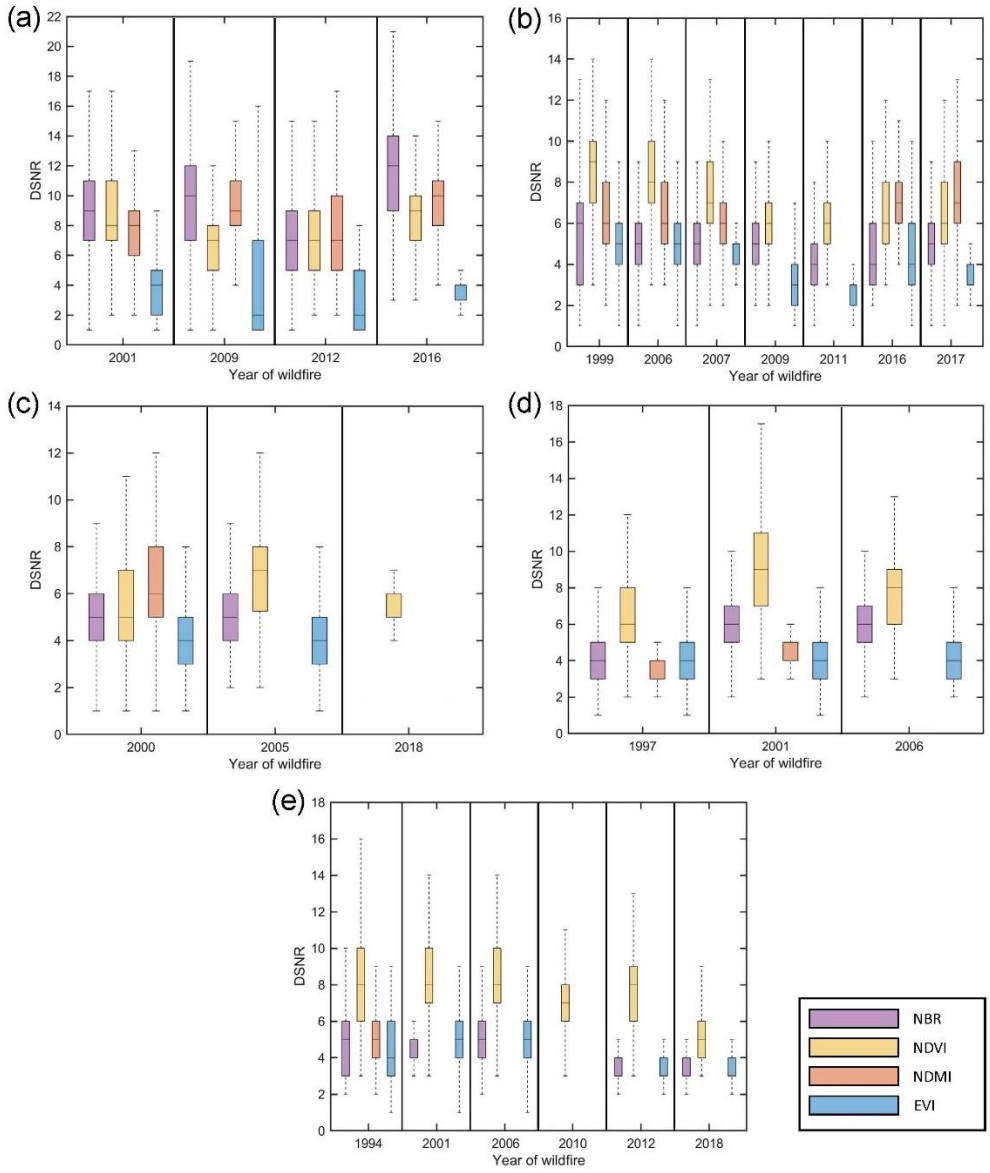

Figure A1.7 Disturbance To Noise Ratio of fire events across each conservation park. (a) Lincoln Park, (b) Hincks Park, (c) Hambidge Park, (d) Heggaton Park, and (e) Pinkawillinie Park. Missing values suggest no wildfires are detected

A1.3.3 Evaluation of post-fire recovery detection

Figure A8 shows the LTR fitted results for five significant fire events (Lincoln Park: 2001, Hincks Park: 2007, Hambidge Park: 2000, Heggaton Park: 1998, Pinkawillinie Park: 2006). As the EVI index is found to have poor performance in detecting burned areas in all conservation parks, it is not considered in recovery evaluation. The vegetation fraction cover of each burned area is used to validate the recovery period. To quantitatively evaluate the spectral index recovery, we calculate the amount of time for each index to restore to the pre-fire stage pixel by pixel (Figure A9). As can be seen from the vegetation fraction cover, Lincoln Park has experienced a rapid recovery after the 2001 fire, and it took six years for photosynthetic vegetation to fully return to the pre-fire stage. Figure A9 (a) suggests that only the NBR index correctly captures the recovery time. In Hincks and

Pinkawillinie Park, the fire happened in 2007 and 2006, and the post-fire recovery took nine and eight years, according to the vegetation fraction cover analysis, which is longer than in Lincoln Park. In Hambidge and Heggaton Park, fires happened in 2000 and 1998 and took 11 and 13 years to recover. This long recovery period is probably caused by the millennium drought from 1997 to 2009 (Van Dijk et al. 2013). The recovery time of the spectral index is also longer; according to Figure A9 (c) and (d), the recovery time estimated from all indices is roughly the same as for the vegetation fraction cover.

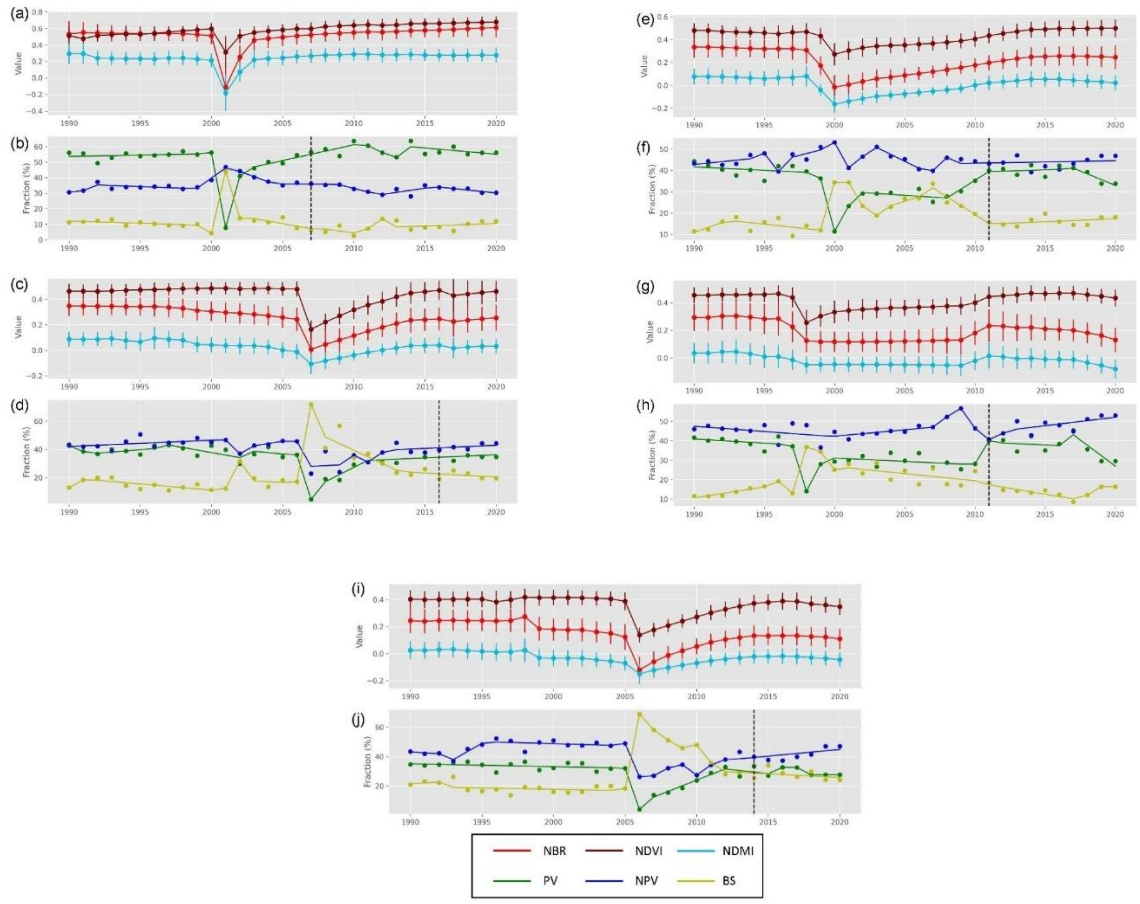

Figure A1.8 Time series value of different indices for five significant wildfire events for each conservation park and the time series fraction cover ((a) Lincoln Park, (b) Hincks Park, (c) Hambidge Park, (d) Heggaton Park, and (e) Pinkawillinie Park. PV, NPV and BS denote photosynthetic vegetation, non-photosynthetic vegetation, and bare soil). Vertical bars in the index value chart are the standard deviation. The solid line on the fraction cover is the result of piecewise regression for better visually distinguishing pre- and post-fire stages. For the photosynthetic vegetation fraction, the time when it first recovered to the pre-fire state is indicated by the dashed line

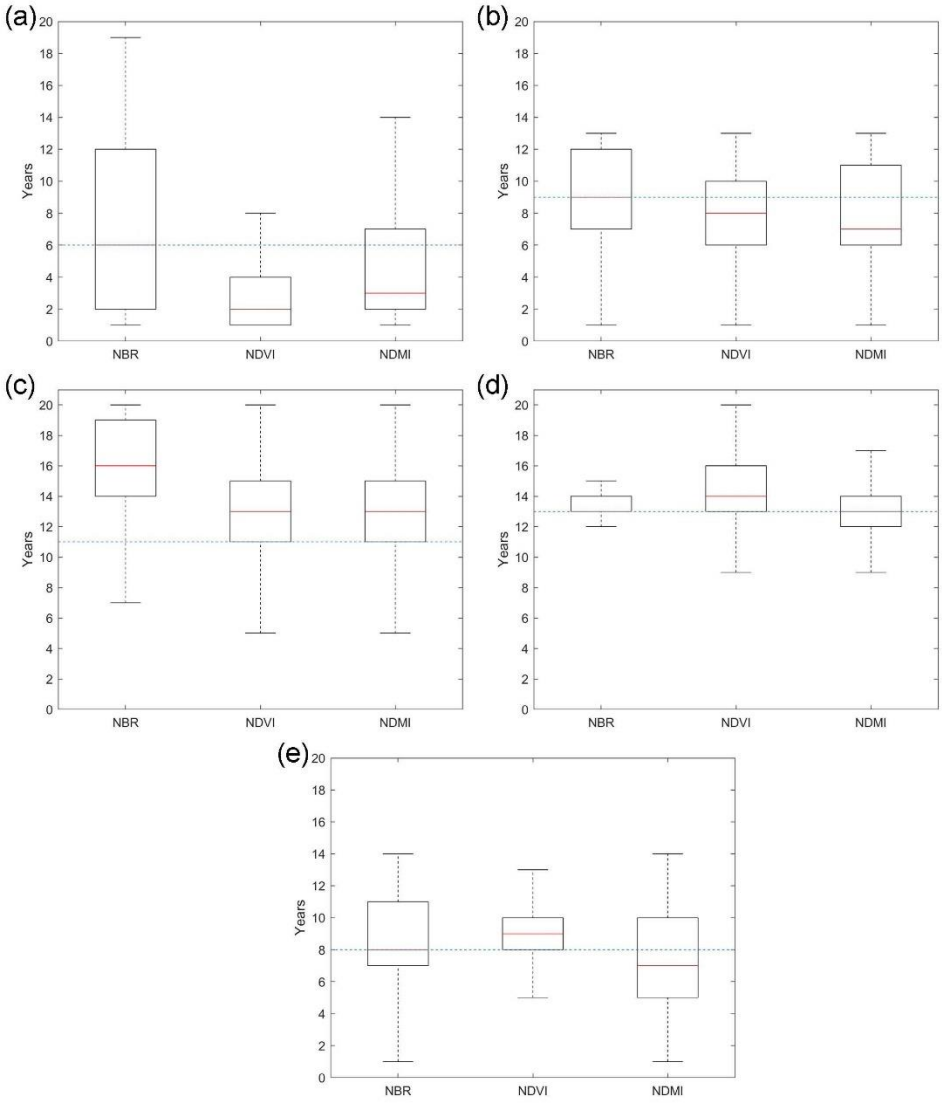

Figure A1.9 Statistics of the recovery period in years estimated from the NBR, NDVI and NDMI indices. (a) Lincoln Park, (b) Hincks Park, (c) Hambidge Park, (d) Heggaton Park, and (e) Pinkawillinie Park. The dashed line is the recovery year of the photosynthetic vegetation fraction

A1.4 Discussion

A1.4.1 Index suitability

The results of the index comparison indicate that the index suitability for detecting wildfires differs across areas with varying dryness conditions. As the vegetation type is similar across all study areas (eucalypt mallee woodland), the NBR index is the best performing index for Lincoln Park, with an annual rainfall of 575 mm/y, followed by the NDMI index. This result is consistent with the conclusions from Cohen et al. (2018) that the SWIR band has superior performance in disturbance detection. They also found that SWIR2 (2110-2290 nm) used in NBR is more sensitive to wildfire than the SWIR1(1570-1650 nm) band used in NDMI, which can also be observed from the accuracy evaluation. This conclusion is validated by several other research results from different

regions. Zhu and Woodcock (2014) demonstrated that NIR and SWIR bands have the biggest change when forest changes to other land cover types for a time series model. Quintero et al. (2019) applied the LTR algorithm in west-central Spain with a representative Mediterranean climate and found that NBR has a greater capacity to detect low-severity wildfires compared to NDVI. Souza et al. (2021) applied the CCDC algorithm in the Brazilian savanna for disturbance detection and found that SWIR-based indices like NBR perform best.

NBR does not perform as well for areas with relatively low precipitation. In Hincks to Pinkawillinie Park, the detection accuracies show a significant difference, and NDVI proves to have the best performance (with Kappa range from 0.41 to 0.79). For the other three indices, relatively high user's accuracy could be found for optimized parameters, but the producer's accuracy is low for most of the areas, indicating that the main error is misidentified burned pixels. One factor that may affect the accurate detection of the burned area is the magnitude of the disturbance. Figure A8 indicates that NBR has the maximum amplitude in wet areas while the amplitude of NDVI is higher in arid areas. This is consistent with the research of Epting et al. (2005), which proved that NBR is useful in burn severity detection only for forest areas and Tran et al. (2018) that NDVI has better performance in burn severity detection than NBR in areas with sparse vegetation density.

Another factor is the noise in the time series data. Kennedy et al. (2010) noticed that NBR is more susceptible to noise even if it is most sensitive in capturing the disturbance event. Compared to NDVI, which consists of the spectral reflectance of Red and NIR bands driven by photosynthetic pigments (such as chlorophyll and carotenoids) and structural features (leaf thickness, intercellular space, and dimensions), NBR is the combination of NIR and SWIR bands, while the latter one reflects the moisture content of soil and vegetation. This can be observed from Figure A8 that the time series NBR always have higher standard deviations than other indices. Thus, in semi-arid regions where vegetation growth is more sensitive to climatic conditions, NBR is more susceptible to noise due to precipitation temporal variation, which affects the observation of disturbances. We validate the DSNR proposed by Cohen et al. (2018) on its suitability for selecting a spectral index for disturbance detection under semi-arid climate conditions.

NDMI is only effective in wet areas, and EVI is underperforming in all study areas. The reasons for the low detection accuracy of these two indices are different. Standard deviation of the NDMI is at a low level, indicating that the time series is not affected much by noise. However, at the time of the fire, NDMI cannot accurately capture the disturbance signal, which is reflected in the low magnitude. The EVI index fluctuated significantly in the fire year, but large fluctuations can also be observed in years without a fire event, which affects the disturbance detection. As the blue band is more sensitive to atmospheric influences and less sensitive to most of the surface changes, it may not be suitable for disturbance detection because it introduces irrelevant noise (Zhu and Woodcock 2014; Zhu et al. 2020).

Following the approach of Afira and Wijayanto (2022), we further evaluated the index suitability using machine learning methods. The Random Forest and XGBoost algorithms are used to test the wildfire detection accuracy for the NBR and NDVI index based on the five significant fire events.

We build the classification model using pre- and post-fire NBR and NDVI data (NBRpre, NBRpost, NDVIpre, NDVIpost), dNBR and dNDVI as input. The feature importance is used to determine index suitability. The feature importance values derived from both Random Forest and XGBoost offer a quantitative measure of the influence of each input feature on the model's predictive accuracy. Specifically, Random Forest determines feature importance by assessing the reduction in the Gini impurity each time the feature is used for splitting across all trees in the ensemble. XGBoost computes feature importance based on the gain, which indicates the improvement in accuracy brought by a feature to the branches which it is on.

In each conservation park, both Random Forest and XGBoost consistently achieved high detection accuracies (above 0.9). However, a distinct variation in feature importance was observed across different regions. Similar to our earlier findings, dNBR is the predominant contributor in Lincoln Park. On the other hand, dNDVI is the most influential index for the other parks in both Random Forest and XGBoost models. This underlines the superior performance of NDVI over NBR in arid conditions, which is not only valid in time-series algorithms like LTR but also in machine-learning based bi-temporal burned area detection.

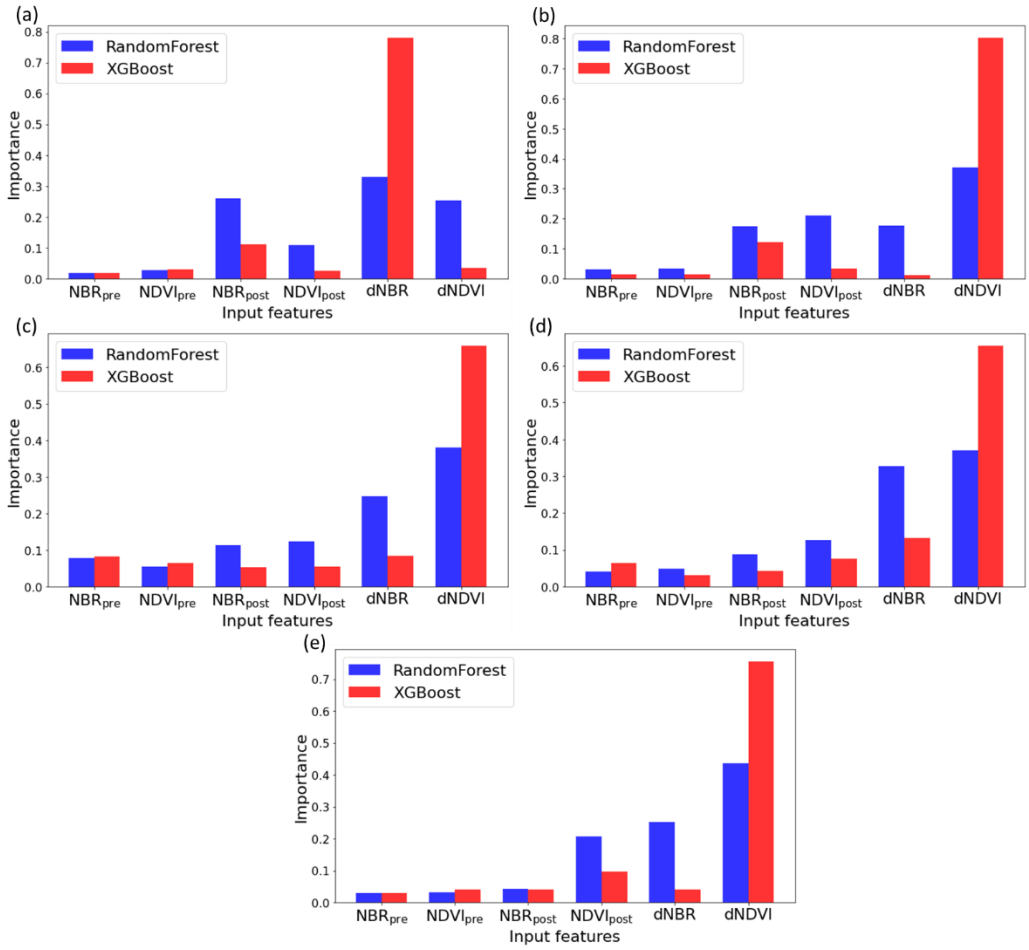

Figure A1.10 Feature importance of NBR and NDVI in the Random Forest and XGBoost modelling of burned pixels for one selected wildfire event in each of the five conservation parks: (a) Lincoln Park, (b) Hincks Park, (c) Hambidge Park, (d) Heggaton Park, and (e) Pinkawillinie Park

A1.4.2 Parameter sensitivity

Conservation parks are chosen for investigation in this study to avoid anthropogenic impacts on land cover changes, so forest fire is the primary disturbance type considered. In such cases, we find that the influence of the parameters on detection accuracy can be related to the climatic conditions. Parameter optimization results indicate that overall accuracy and Kappa are more sensitive to changes in RT in wetter study areas, while MS is more sensitive for drier areas. Differences in parameter selection may be explained by differences in post-fire recovery conditions affected by precipitation. For areas with high precipitation, good moisture condition leads to rapid post-fire recovery, so RT parameter must be set to a high value to avoid misinterpreting fire events as noise. In arid regions, recovery takes longer, and the recovery rates can change due to interannual precipitation variability. Thus, a higher MS is needed to better capture the index response to wildfire. Compared to the default parameters, the overall accuracy and kappa of optimized parameters can improve by up to 8.4% and 36.8%.

Considering that many previous studies generally used default parameters (De Marzo et al. 2021; Gelabert et al. 2021; Rodman et al. 2021; Xiao et al. 2020; Yang et al. 2018), we anticipate that this study can provide guidance for LTR algorithms for wildfire detection in semi-arid regions.

A1.4.3 Post-fire recovery

From the fraction cover trends of selected fire events in the study area, climatic conditions largely affect post-fire recovery, which is consistent with Meng et al. (2015). Extreme events such as the millennium drought from 1997 to 2009 also greatly affect recovery. We evaluated the post-fire recovery detection capabilities of NBR, NDVI, and NDMI. In relatively wet regions such as Lincoln Park, fraction cover returned to near pre-fire levels within a short period (2 years) but did not fully return to initial values until six years later. The average spectral index value in this region also rapidly recovered. Pixel-by-pixel statistics show that compared with other indices, the NBR takes longer to recover (median = 6), which is closer to the actual situation. The underestimation of recovery time by NDVI is very likely due to the rapid growth of herbaceous and shrub species in the relatively wet condition at the site and the high saturation characteristics of NDVI (Frazier et al. 2018).

For other study areas with dryer climates, the post-fire recovery estimated from all three indices shows great consistency with that inferred by the fraction cover data. No significant differences are found between indices. Noting that even fire events in arid regions are not well detected with NDMI due to low amplitudes, NDMI still provides a good estimation of post-fire recovery. This shows that even if there are a lot of omissions in the detection of fire areas, for those correctly identified pixels, the temporal changes of NDMI can still reflect the post-fire recovery well. In general, according to the fraction cover, the detection accuracy of different indices for recovery is consistent with the detection results of wildfire areas to a certain extent. That is, NBR is more accurate in the wet end of the study areas, while in other areas, the performance between different indices is not obvious. Previous post-fire recovery studies found that the applicability of spectral indices is different due to the different climatic conditions and vegetation types (Chen et al. 2011; Hao et al. 2022; Hislop et al. 2018; Nolè et al. 2022). As in wildfire risk management, post-fire recovery and wildfire area information are both required. The results from this study and previous studies suggest that the NBR index is suitable for an area of annual precipitation around 575 mm and above, and the NDVI index for areas with annual precipitation less than 400 mm.

A1.5 Conclusion

In this study, we applied the LTR algorithm and evaluated the capacity of the time series Landsat data in detecting wildfire areas and post-fire recovery in semi-arid regions with a significant climate gradient. Firstly, our result indicates the effectiveness of an index for burned area detection varies with climate conditions. NBR is more accurate in the humid end of the climate gradient examined

(575 mm), while NDVI outperforms other indices in arid and semi-arid regions (290 – 400 mm). Additionally, these findings are also valid for machine-learning-based bi-temporal burned area detection. DSNR is a suitable metric for selecting an appropriate index for wildfire area delineation. Secondly, the parameter optimization result suggests that the Max Segments and Recovery Threshold should be adjusted according to the climate prevailing in a region. In general, Recovery Threshold should be set to a higher value in wet areas, and the Max Segments should be higher for arid areas. Thirdly, the post-fire recovery detection with different indices does not significantly differ among different indices, except for the humid site where NBR proved to have better performance. This study provides guidance for selecting appropriate spectral index and applying LandTrendr for wildfire detection to support forestry management in semi-arid climates.

A1.6 References

Afira, N., & Wijayanto, A. W. (2022). Mono-temporal and multi-temporal approaches for burnt area detection using Sentinel-2 satellite imagery (a case study of Rokan Hilir Regency, Indonesia). *Ecological Informatics*, *69*, 101677.

Arora, V. K., & Boer, G. J. (2005). Fire as an interactive component of dynamic vegetation models. *Journal of Geophysical Research: Biogeosciences*, *110*(G2).

Barford, C. C., Wofsy, S. C., Goulden, M. L., Munger, J. W., Pyle, E. H., Urbanski, S. P., Hutyra, L., Saleska, S. R., Fitzjarrald, D., & Moore, K. (2001). Factors controlling long-and short-term sequestration of atmospheric CO2 in a mid-latitude forest. *Science*, *294*(5547), 1688-1691.

Bonney, M. T., He, Y., & Myint, S. W. (2020). Contextualizing the 2019–2020 Kangaroo Island Bushfires: Quantifying Landscape-Level Influences on Past Severity and Recovery with Landsat and Google Earth Engine. *Remote Sensing*, *12*(23), 3942.

Bourbonnais, M. L., Nelson, T. A., Stenhouse, G. B., Wulder, M. A., White, J. C., Hobart, G. W., Hermosilla, T., Coops, N. C., Nathoo, F., & Darimont, C. (2017). Characterizing spatial-temporal patterns of landscape disturbance and recovery in western Alberta, Canada using a functional data analysis approach and remotely sensed data. *Ecological Informatics*, *39*, 140-150.

Bright, B. C., Hudak, A. T., Kennedy, R. E., Braaten, J. D., & Khalyani, A. H. (2019). Examining post-fire vegetation recovery with Landsat time series analysis in three western North American forest types. *Fire Ecology*, *15*, Article 8. https://doi.org/10.1186/s42408-018-0021-9

Ceccato, P., Flasse, S., Tarantola, S., Jacquemoud, S., & Grégoire, J.-M. (2001). Detecting vegetation leaf water content using reflectance in the optical domain. *Remote Sensing of Environment*, *77*(1), 22-33.

Charizanos, G., & Demirhan, H. (2023). Bayesian prediction of wildfire event probability using normalized difference vegetation index data from an Australian forest. *Ecological Informatics*, *73*, 101899.

Chen, X., Vogelmann, J. E., Rollins, M., Ohlen, D., Key, C. H., Yang, L., Huang, C., & Shi, H. (2011). Detecting post-fire burn severity and vegetation recovery using multitemporal remote sensing spectral indices and field-collected composite burn index data in a ponderosa pine forest. *International Journal of Remote Sensing*, *32*(23), 7905-7927.

Chuvieco, E., & Congalton, R. G. (1988). Mapping and inventory of forest fires from digital processing of TM data. *Geocarto International*, *3*(4), 41-53.

Chuvieco, E., Mouillot, F., Van der Werf, G. R., San Miguel, J., Tanase, M., Koutsias, N., García, M., Yebra, M., Padilla, M., & Gitas, I. (2019). Historical background and current developments for mapping burned area from satellite Earth observation. *Remote Sensing of Environment*, *225*, 45-64.

Cohen, W. B., Yang, Z., Healey, S. P., Kennedy, R. E., & Gorelick, N. (2018). A LandTrendr multispectral ensemble for forest disturbance detection. *Remote Sensing of Environment*, *205*, 131-140.

Cohen, W. B., Yang, Z., & Kennedy, R. (2010). Detecting trends in forest disturbance and recovery using yearly Landsat time series: 2. TimeSync—Tools for calibration and validation. *Remote Sensing of Environment*, *114*(12), 2911-2924.

Committee, N. F. I. S. (2019). Australia's state of the forests report 2018.

Congalton, R. G. (1991). A review of assessing the accuracy of classifications of remotely sensed data. *Remote Sensing of Environment*, *37*(1), 35-46.

Congalton, R. G., Oderwald, R. G., & Mead, R. A. (1983). Assessing Landsat classification accuracy using discrete multivariate analysis statistical techniques. *Photogrammetric engineering and remote sensing*, *49*(12), 1671-1678.

de Jong, S. M., Shen, Y., de Vries, J., Bijnaar, G., van Maanen, B., Augustinus, P., & Verweij, P. (2021). Mapping mangrove dynamics and colonization patterns at the Suriname coast using historic satellite data and the LandTrendr algorithm. *International Journal of Applied Earth Observation and Geoinformation*, *97*, 102293.

De Marzo, T., Pflugmacher, D., Baumann, M., Lambin, E. F., Gasparri, I., & Kuemmerle, T. (2021). Characterizing forest disturbances across the Argentine Dry Chaco based on Landsat time series. *International Journal of Applied Earth Observation and Geoinformation*, *98*, 102310.

Deng, Y., Wang, M., Yousefpour, R., & Hanewinkel, M. (2021). Abiotic disturbances affect forest short-term vegetation cover and phenology in Southwest China. *Ecological Indicators*, *124*, Article 107393. https://doi.org/10.1016/j.ecolind.2021.107393
Edwards, A. C., Maier, S. W., Hutley, L. B., Williams, R. J., & Russell-Smith, J. (2013). Spectral analysis of fire severity in north Australian tropical savannas. *Remote Sensing of Environment*, *136*, 56-65.
Epting, J., Verbyla, D., & Sorbel, B. (2005). Evaluation of remotely sensed indices for assessing burn severity in interior Alaska using Landsat TM and ETM+. *Remote Sensing of Environment*, *96*(3-4), 328-339.
Escuin, S., Navarro, R., & Fernandez, P. (2008). Fire severity assessment by using NBR (Normalized Burn Ratio) and NDVI (Normalized Difference Vegetation Index) derived from LANDSAT TM/ETM images. *International Journal of Remote Sensing*, *29*(4), 1053-1073.
Fang, X. Q., Zhu, Q. A., Ren, L. L., Chen, H., Wang, K., & Peng, C. H. (2018). Large-scale detection of vegetation dynamics and their potential drivers using MODIS images and BFAST: A case study in Quebec, Canada. *Remote Sensing of Environment*, *206*, 391-402. https://doi.org/10.1016/j.rse.2017.11.017
Frazier, R. J., Coops, N. C., Wulder, M. A., Hermosilla, T., & White, J. C. (2018). Analyzing spatial and temporal variability in short-term rates of post-fire vegetation return from Landsat time series. *Remote Sensing of Environment*, *205*, 32-45.
García, M. L., & Caselles, V. (1991). Mapping burns and natural reforestation using Thematic Mapper data. *Geocarto International*, *6*(1), 31-37.
Gelabert, P., Rodrigues, M., de la Riva, J., Ameztegui, A., Sebastià, M., & Vega-Garcia, C. (2021). LandTrendr smoothed spectral profiles enhance woody encroachment monitoring. *Remote Sensing of Environment*, *262*, 112521.
Goodwin, N. R., & Collett, L. J. (2014). Development of an automated method for mapping fire history captured in Landsat TM and ETM+ time series across Queensland, Australia. *Remote Sensing of Environment*, *148*, 206-221.
Gorelick, N., Hancher, M., Dixon, M., Ilyushchenko, S., Thau, D., & Moore, R. (2017). Google Earth Engine: Planetary-scale geospatial analysis for everyone. *Remote Sensing of Environment*, *202*, 18-27.
Greve, P., Roderick, M., Ukkola, A., & Wada, Y. (2019). The aridity index under global warming. *Environmental Research Letters*, *14*(12), 124006.
Guerschman, J. P., Hill, M. J., Leys, J., & Heidenreich, S. (2020). Vegetation cover dependence on accumulated antecedent precipitation in Australia: Relationships with photosynthetic and non-photosynthetic vegetation fractions. *Remote Sensing of Environment*, *240*, 111670.
Hall, D. K., Ormsby, J. P., Johnson, L., & Brown, J. (1980). Landsat digital analysis of the initial recovery of burned tundra at Kokolik River, Alaska. *Remote Sensing of Environment*, *10*(4), 263-272.
Hao, B., Xu, X., Wu, F., & Tan, L. (2022). Long-Term Effects of Fire Severity and Climatic Factors on Post-Forest-Fire Vegetation Recovery. *Forests*, *13*(6), 883.
Hicke, J. A., Logan, J. A., Powell, J., & Ojima, D. S. (2006). Changing temperatures influence suitability for modeled mountain pine beetle (Dendroctonus ponderosae) outbreaks in the western United States. *Journal of Geophysical Research: Biogeosciences*, *111*(G2).
Hijmans, R. J., Cameron, S. E., Parra, J. L., Jones, P. G., & Jarvis, A. (2005). Very high resolution interpolated climate surfaces for global land areas. *International Journal of Climatology: A Journal of the Royal Meteorological Society*, *25*(15), 1965-1978.
Hislop, S., Jones, S., Soto-Berelov, M., Skidmore, A., Haywood, A., & Nguyen, T. H. (2018). Using landsat spectral indices in time-series to assess wildfire disturbance and recovery. *Remote Sensing*, *10*(3), 460.
Hitchcock, H., & Hoffer, R. (1974). Mapping a recent forest fire with ERTS-1 MSS data. Remote sensing of earth resources. Volume 3-Third Conference on Earth Resources Observation and Information Analysis System,
Huang, C., Goward, S. N., Masek, J. G., Thomas, N., Zhu, Z., & Vogelmann, J. E. (2010). An automated approach for reconstructing recent forest disturbance history using dense Landsat time series stacks. *Remote Sensing of Environment*, *114*(1), 183-198.

Iban, M. C., & Sekertekin, A. (2022). Machine learning based wildfire susceptibility mapping using remotely sensed fire data and GIS: A case study of Adana and Mersin provinces, Turkey. *Ecological Informatics*, *69*, 101647.
Kennedy, R. E., Yang, Z., & Cohen, W. B. (2010). Detecting trends in forest disturbance and recovery using yearly Landsat time series: 1. LandTrendr—Temporal segmentation algorithms. *Remote Sensing of Environment*, *114*(12), 2897-2910.
Kennedy, R. E., Yang, Z., Cohen, W. B., Pfaff, E., Braaten, J., & Nelson, P. (2012). Spatial and temporal patterns of forest disturbance and regrowth within the area of the Northwest Forest Plan. *Remote Sensing of Environment*, *122*, 117-133.
Kennedy, R. E., Yang, Z., Gorelick, N., Braaten, J., Cavalcante, L., Cohen, W. B., & Healey, S. (2018). Implementation of the LandTrendr algorithm on google earth engine. *Remote Sensing*, *10*(5), 691.
Key, C. H., & Benson, N. C. (2006). Landscape assessment (LA). *In: Lutes, Duncan C.; Keane, Robert E.; Caratti, John F.; Key, Carl H.; Benson, Nathan C.; Sutherland, Steve; Gangi, Larry J. 2006. FIREMON: Fire effects monitoring and inventory system. Gen. Tech. Rep. RMRS-GTR-164-CD. Fort Collins, CO: US Department of Agriculture, Forest Service, Rocky Mountain Research Station. p. LA-1-55*, *164*.
Lanorte, A., Danese, M., Lasaponara, R., & Murgante, B. (2013). Multiscale mapping of burn area and severity using multisensor satellite data and spatial autocorrelation analysis. *International Journal of Applied Earth Observation and Geoinformation*, *20*, 42-51.
Lombard, F., Soumaré, S., Andrieu, J., & Josselin, D. (2023). Mangrove zonation mapping in West Africa, at 10-m resolution, optimized for inter-annual monitoring. *Ecological Informatics*, *75*, 102027.
Markham, C. G. (1970). Seasonality of precipitation in the United States. *Annals of the Association of American Geographers*, *60*(3), 593-597.
Martínez-López, J., Bertzky, B., Robuchon, M., Bonet, F. J., & Dubois, G. (2023). Assessing habitat diversity and potential areas of similarity across protected areas globally. *Ecological Informatics*, *75*, 102090.
Masek, J. G., Huang, C., Wolfe, R., Cohen, W., Hall, F., Kutler, J., & Nelson, P. (2008). North American forest disturbance mapped from a decadal Landsat record. *Remote Sensing of Environment*, *112*(6), 2914-2926.
McKendry, I. G., Christen, A., Lee, S.-C., Ferrara, M., Strawbridge, K. B., O'Neill, N., & Black, A. (2019). Impacts of an intense wildfire smoke episode on surface radiation, energy and carbon fluxes in southwestern British Columbia, Canada. *Atmospheric Chemistry and Physics*, *19*(2), 835-846.
Meigs, G. W., Zald, H. S. J., Campbell, J. L., Keeton, W. S., & Kennedy, R. E. (2016). Do insect outbreaks reduce the severity of subsequent forest fires? *Environmental Research Letters*, *11*(4), Article 045008. https://doi.org/10.1088/1748-9326/11/4/045008
Meng, R., Dennison, P. E., Huang, C., Moritz, M. A., & D'Antonio, C. (2015). Effects of fire severity and post-fire climate on short-term vegetation recovery of mixed-conifer and red fir forests in the Sierra Nevada Mountains of California. *Remote Sensing of Environment*, *171*, 311-325.
Mu, Q., Zhao, M., & Running, S. (2014). Numerical Terradynamic Simulation Group MODIS Global Terrestrial Evapotranspiration (ET) Product (NASA MOD16A2/A3) Collection 5. *NASA Headquarters*.
Nguyen, T. H., Jones, S. D., Soto-Berelov, M., Haywood, A., & Hislop, S. (2018). A spatial and temporal analysis of forest dynamics using Landsat time-series. *Remote Sensing of Environment*, *217*, 461-475.
Nolè, A., Rita, A., Spatola, M. F., & Borghetti, M. (2022). Biogeographic variability in wildfire severity and post-fire vegetation recovery across the European forests via remote sensing-derived spectral metrics. *Science of the Total Environment*, *823*, 153807.
Novo-Fernandez, A., Franks, S., Wehenkel, C., Lopez-Serrano, P. M., Molinier, M., & Lopez-Sanchez, C. A. (2018). Landsat time series analysis for temperate forest cover change detection in the Sierra Madre Occidental, Durango, Mexico. *International Journal of Applied Earth Observation and Geoinformation*, *73*, 230-244. https://doi.org/10.1016/j.jag.2018.06.015
Qiu, J., Wang, H., Shen, W. J., Zhang, Y. L., Su, H. Y., & Li, M. S. (2021). Quantifying Forest Fire and Post-Fire Vegetation Recovery in the Daxin'anling Area of Northeastern China Using Landsat

Time-Series Data and Machine Learning. *Remote Sensing*, *13*(4), Article 792. https://doi.org/10.3390/rs13040792
Quintero, N., Viedma, O., Urbieta, I. R., & Moreno, J. M. (2019). Assessing Landscape Fire Hazard by Multitemporal Automatic Classification of Landsat Time Series Using the Google Earth Engine in West-Central Spain. *Forests*, *10*(6), Article 518. https://doi.org/10.3390/f10060518
Rodman, K. C., Andrus, R. A., Veblen, T. T., & Hart, S. J. (2021). Disturbance detection in landsat time series is influenced by tree mortality agent and severity, not by prior disturbance. *Remote Sensing of Environment*, *254*, 112244.
Runge, A., Nitze, I., & Grosse, G. (2022). Remote sensing annual dynamics of rapid permafrost thaw disturbances with LandTrendr. *Remote Sensing of Environment*, *268*, 112752.
Seidl, R., Rammer, W., & Spies, T. A. (2014). Disturbance legacies increase the resilience of forest ecosystem structure, composition, and functioning. *Ecological Applications*, *24*(8), 2063-2077.
Souza, A. A. D., Galvao, L. S., Korting, T. S., & Almeida, C. A. (2021). On a Data-Driven Approach for Detecting Disturbance in the Brazilian Savannas Using Time Series of Vegetation Indices. *Remote Sensing*, *13*(24), Article 4959. https://doi.org/10.3390/rs13244959
Tran, B. N., Tanase, M. A., Bennett, L. T., & Aponte, C. (2018). Evaluation of spectral indices for assessing fire severity in Australian temperate forests. *Remote Sensing*, *10*(11), 1680.
Trigg, S., & Flasse, S. (2001). An evaluation of different bi-spectral spaces for discriminating burned shrub-savannah. *International Journal of Remote Sensing*, *22*(13), 2641-2647.
Van Dijk, A. I., Beck, H. E., Crosbie, R. S., De Jeu, R. A., Liu, Y. Y., Podger, G. M., Timbal, B., & Viney, N. R. (2013). The Millennium Drought in southeast Australia (2001–2009): Natural and human causes and implications for water resources, ecosystems, economy, and society. *Water Resources Research*, *49*(2), 1040-1057.
Veraverbeke, S., Verstraeten, W. W., Lhermitte, S., & Goossens, R. (2010). Illumination effects on the differenced Normalized Burn Ratio's optimality for assessing fire severity. *International Journal of Applied Earth Observation and Geoinformation*, *12*(1), 60-70.
Verbesselt, J., Hyndman, R., Newnham, G., & Culvenor, D. (2010). Detecting trend and seasonal changes in satellite image time series. *Remote Sensing of Environment*, *114*(1), 106-115.
Verbesselt, J., Hyndman, R., Zeileis, A., & Culvenor, D. (2010). Phenological change detection while accounting for abrupt and gradual trends in satellite image time series. *Remote Sensing of Environment*, *114*(12), 2970-2980.
Viana-Soto, A., Aguado, I., Salas, J., & Garcia, M. (2020). Identifying Post-Fire Recovery Trajectories and Driving Factors Using Landsat Time Series in Fire-Prone Mediterranean Pine Forests. *Remote Sensing*, *12*(9), Article 1499. https://doi.org/10.3390/rs12091499
Watts, L. M., & Laffan, S. W. (2014). Effectiveness of the BFAST algorithm for detecting vegetation response patterns in a semi-arid region. *Remote Sensing of Environment*, *154*, 234-245. https://doi.org/10.1016/j.rse.2014.08.023
White, J. C., Wulder, M. A., Hermosilla, T., Coops, N. C., & Hobart, G. W. (2017). A nationwide annual characterization of 25 years of forest disturbance and recovery for Canada using Landsat time series. *Remote Sensing of Environment*, *194*, 303-321.
Wimberly, M. C., Dwomoh, F. K., Numata, I., Mensah, F., Amoako, J., Nekorchuk, D. M., & McMahon, A. (2022). Historical trends of degradation, loss, and recovery in the tropical forest reserves of Ghana. *International Journal of Digital Earth*, *15*(1), 30-51. https://doi.org/10.1080/17538947.2021.2012533
Xiao, W., Deng, X., He, T., & Chen, W. (2020). Mapping annual land disturbance and reclamation in a surface coal mining region using google earth engine and the landtrendr algorithm: a case study of the shengli coalfield in Inner Mongolia, China. *Remote Sensing*, *12*(10), 1612.
Yang, Y., Erskine, P. D., Lechner, A. M., Mulligan, D., Zhang, S., & Wang, Z. (2018). Detecting the dynamics of vegetation disturbance and recovery in surface mining area via Landsat imagery and LandTrendr algorithm. *Journal of Cleaner Production*, *178*, 353-362.
Zhang, Y. T., Woodcock, C. E., Chen, S. J., Wang, J. A., Sulla-Menashe, D., Zuo, Z. P., Olofsson, P., Wang, Y. T. J., & Friedl, M. A. (2022). Mapping causal agents of disturbance in boreal and arctic ecosystems of North America using time series of Landsat data. *Remote Sensing of Environment*, *272*, Article 112935. https://doi.org/10.1016/j.rse.2022.112935
Zhu, Z., & Woodcock, C. E. (2014). Continuous change detection and classification of land cover using all available Landsat data. *Remote Sensing of Environment*, *144*, 152-171.

Zhu, Z., Woodcock, C. E., & Olofsson, P. (2012). Continuous monitoring of forest disturbance using all available Landsat imagery. *Remote Sensing of Environment*, *122*, 75-91.
Zhu, Z., Zhang, J., Yang, Z., Aljaddani, A. H., Cohen, W. B., Qiu, S., & Zhou, C. (2020). Continuous monitoring of land disturbance based on Landsat time series. *Remote Sensing of Environment*, *238*, 111116.

A2 THERMAL IMAGE CORRECTION FOR UNSTABLE SKY CONDITION

Thermal infrared cameras detect the upward electromagnetic radiation from the Earth's surface in the longwave infrared spectrum. However, the radiative temperature measured by these sensors can be significantly impacted by variations in atmospheric conditions, particularly cloud cover. When clouds intermittently obscure direct solar insolation, there is a notable decrease in the incoming shortwave radiation reaching the surface, causing a rapid reduction in surface temperatures. This transient shading effect results in abrupt changes in the measured radiative temperature over the imaged area.

To mitigate the impact of this phenomenon, a histogram matching technique was implemented. This method adjusts the radiative temperatures in cloud-shaded regions to match the values expected under the clear-sky conditions observed in adjacent unshaded sections of the scene. First, a pixel-level segmentation technique was employed for initial automatic segmentation, followed by manual categorization of high and low-temperature segments based on average segment values. Edge-located segments were precisely identified using the lazy snapping method. The clear-sky subregions, unaffected by cloud cover and exhibiting consistently higher temperatures, were marked as reference zones for histogram matching. Subsequently, a histogram matching transformation was applied, ensuring that the temperature distribution in shaded areas aligns with that of the clear-sky references.

Figure 6 (a) and (b) show the influence of clouds on thermal imagery under fluctuating sky conditions. There is clear temperature gradient pattern can be found in Figure 6 (a) and (b) that the surface temperature suddenly decreases in certain areas. This pattern is attributed to the drone capturing some images under cloud cover, leading to anomalously low surface temperature readings and consequently, a skewed temperature distribution. Figures 6 (c) and (d) display the corrected thermal imagery, and figures 6 (e) and (f) illustrate histograms for reference, cloud-impacted, and corrected pixels. Compared to the raw images, the corrected images show an evenly distributed surface temperature, which could large reduce the uncertainty of ET caused by non-ET related temperature variation.

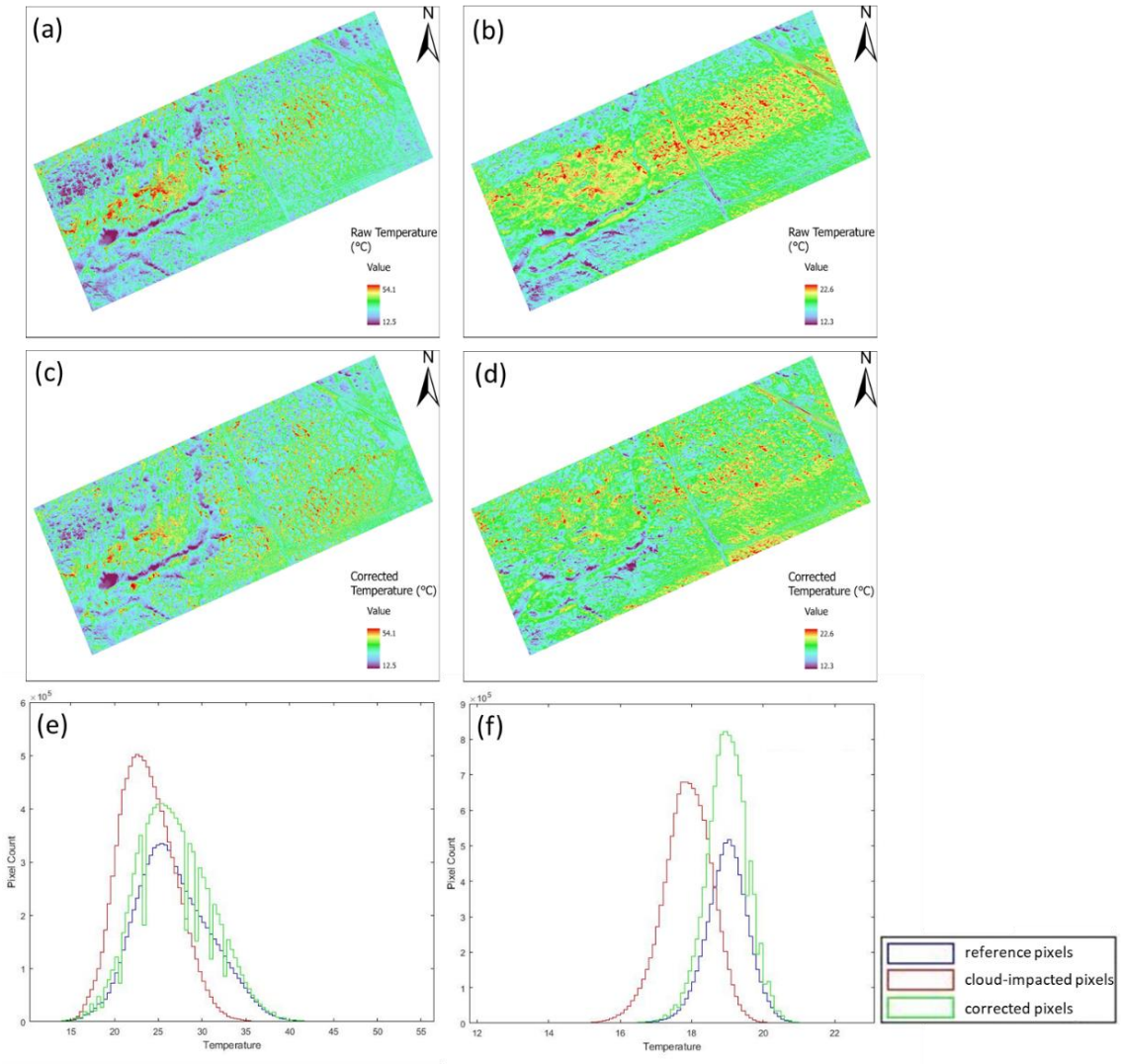

Figure A2.1 Thermal images of the Lignum site in Bookpurnong floodplain captured on 07/05/2022 at (a) 12:00 and (b) 17:00. (c) and (d) display the corrected thermal images corresponding to (a) and (b). (e) and (f) the histograms of pixel values before and after the correction.